Cloud Microphysics Investigations with the Cloudkite Laboratory

From Homogeneous Isotropic Turbulence towards Cloud Microphysics

Dissertation
FOR THE AWARD OF THE DEGREE
"Doctor rerum naturalium"
of the University of Göttingen

within the doctoral program Physics of Biological and Complex Systems
of the Göttingen Graduate Center for Neurosciences, Biophysics, and
Molecular Biosciences (GGNB)
of the Georg-August University School of Sciences (GAUSS)

submitted by
Marcel Schröder
from Arolsen, jetzt Bad Arolsen

Göttingen, 2023

Thesis Committee

Prof. Dr. Dr. h.c. Eberhard Bodenschatz
Department of Fluid Physics, Pattern Formation and Biocomplexity
Max-Planck-Institute for Dynamics and Self-Organization

Prof. Dr. Michael Wilczek
Theoretical Physics I
University of Bayreuth

Prof. Dr. Andreas Janshoff
Institute for Physical Chemistry
Georg August University of Göttingen

Members of the Examination Board

Referee: Prof. Dr. Dr. h.c. Eberhard Bodenschatz
Department of Fluid Physics, Pattern Formation and Biocomplexity
Max-Planck-Institute for Dynamics and Self-Organization

2nd Referee: Prof. Dr. Michael Wilczek
Theoretical Physics I
University of Bayreuth

Further members of the Examination Board:

Prof. Dr. Andreas Janshoff
Institute for Physical Chemistry
Georg August University of Göttingen

Prof. Dr. Dr.-Ing. habil. Andreas Dillmann
Institute of Aerodynamics and Flow Technology
German Aerospace Center

Prof. Dr. Stefan Klumpp
Institute for Nonlinear Dynamics
Georg-August-Universität Göttingen

Prof. Dr. Ulrich Parlitz
Biomedical Physics Group
Max-Planck-Institute for Dynamics and Self-Organization

Date of oral examination: 02.03.2023

Abstract

Clouds are crucial to the Earth's radiation budget and energy balance. Inadequately resolved cloud processes are a major source of uncertainty in weather forecasts and climate prediction. Due to their turbulent nature, cloud dynamics span a vast range of spatial and temporal scales from µm to km and ms to h, respectively. Together with phase transitions, the transport of heat and moisture as well as cloud droplet-turbulence interaction, the multiscale property of turbulence poses a huge challenge for unraveling cloud processes. Deployed by kite-stabilized and helium-filled aerostats, the so-called helikites, two specially designed instruments, the Max-Planck-Cloudkite + (MPCK+) and the mini-Max-Planck-Cloudkite (mini-MPCK), measure the atmospheric state and flow velocity as well as cloud microphysical properties. During EUREC^{4}A field campaign in the Caribbean from January to February 2020 above the Atlantic Ocean, both the MPCK+ and the mini-MPCK profiled the atmospheric boundary layer of the trade-wind region and sampled clouds. In this thesis, we report measurements of the energy dissipation rate and cloud droplet statistics in the trade-wind region.

The energy dissipation rate is one of the most fundamental turbulence characteristics and is estimated from one-dimensional velocity time-records. To benchmark different methods for estimating the energy dissipation rate, each method is compared to the ground-truth reference of direct numerical simulation (DNS) of stationary homogeneous isotropic turbulence at different Taylor-scale Reynolds numbers $74 \leq \mathrm{R}_\lambda \leq 321$. The impact of finite turbulence intensity and misalignment between the probe orientation and the mean flow direction is systematically studied and expressed by analytical expressions. Additionally, the effect of a finite averaging window and its R_λ dependence is captured by scaling arguments which are compared to hot-wire measurements from the Max Planck Variable Density Turbulence Tunnel with $147 \leq \mathrm{R}_\lambda \leq 5864$.

Both atmospheric turbulence and cloud droplet-turbulence interaction is investigated with the help of energy dissipation rate estimates from, in total, 197 h record of scientific data. This thesis examines the spatial distribution of cloud droplets in trade-wind cumuli, the onset of warm-rain initiation and the altitude dependence of the cloud droplet size distribution, which are analyzed based on 144 h of cloud droplet records. Furthermore, turbulence characteristics of the boundary layer, its stability and isotropy on inertial length scales are determined.

Contents

1 Introduction 1
1.1 Scope of the thesis . . . 1
1.2 Turbulent flows . . . 5
1.2.1 Equations of motion . . . 6
1.2.2 Reynolds number and Nature of Turbulence . . . 6
1.2.3 Reynolds decomposition and Mean-flow Equations . . . 8
1.2.4 Homogeneous Isotropic Turbulence . . . 9
1.2.5 The Atmospheric Boundary Layer . . . 16
1.2.6 Random Error of Time-Average . . . 19
1.3 Cloud microphysics . . . 22
1.3.1 Cloud Droplet Growth due to Condensation . . . 22
1.3.2 Cloud Droplet - Turbulence Interaction . . . 23

2 The Max-Planck-Cloudkites 27
2.1 Introduction . . . 27
2.2 Max Planck Cloudkite+ . . . 30
2.3 The mini-Max-Planck-CloudKite . . . 33
2.3.1 Design requirements . . . 33
2.3.2 Instrumentation . . . 35
2.3.3 Mechanical Design . . . 40
2.3.4 Operating the mini-MPCK remotely . . . 42
2.4 Performance assessment during in-situ measurements . . . 43
2.4.1 In-field Operation aboard RV Meteor . . . 43
2.4.2 Flight Properties and Platform Motion . . . 44
2.4.3 Comparison to Radiosonde measurements . . . 47
2.4.4 Flow Velocity Measurements and Turbulence characterization . 50
2.5 Discussions . . . 57
Appendix 2.A Revert Running Average . . . 60
Appendix 2.B Air temperature from speed of sound . . . 61
Appendix 2.C Wind tunnel experiment . . . 62
Appendix 2.D The micro-Max Planck Cloudkite . . . 62
Appendix 2.E Supplementary Figures . . . 64
Appendix 2.F Supplementary Tables . . . 66

3 Estimating the turbulent kinetic energy dissipation rate from one-dimensional velocity measurements in time 67
3.1 Introduction 68
3.2 Methods 70
  3.2.1 On Averaging, Reynolds Decomposition and Taylor's Hypothesis 70
  3.2.2 Preliminaries on Second-Order Statistics 72
  3.2.3 Estimating the Energy Dissipation Rate 73
  3.2.4 Simulations of homogeneous isotropic turbulence 78
  3.2.5 Variable Density Turbulence Tunnel 78
  3.2.6 Quantification of systematic and random errors 81
3.3 Results and Discussion 83
  3.3.1 Verification of the analytical methods and a first insight into their performance under ideal conditions 83
  3.3.2 Validity of Taylor's hypothesis and impact of random sweeping effects 86
  3.3.3 Probe Orientation 90
  3.3.4 Systematic and random errors due to finite averaging window size R 93
  3.3.5 Estimating the transient energy dissipation rate 100
3.4 Summary 103
Appendix 3.A Nomenclature 105
Appendix 3.B Supplementary Figures 107

4 Atmospheric Turbulence and Cloud Microphysics in the Trade-wind region 115
4.1 Atmospheric Turbulence Measurements at Constant Altitude 116
  4.1.1 Overview of M161 Flight 12 117
  4.1.2 Statistical Convergence in atmospheric turbulence 117
  4.1.3 Bulk Turbulence Characteristics of M161 Flight 12 120
4.2 Atmospheric Turbulence Characteristics of the Marine Boundary Layer 126
  4.2.1 Top of stably stratified Boundary Layers 126
  4.2.2 Stability of the Boundary Layer 128
  4.2.3 Turbulence Characteristics in the Trade-wind Boundary Layer . 130
4.3 Reynolds stress Anisotropy 136
  4.3.1 Graphical Representation of Reynolds stresses 136
  4.3.2 Anisotropy in high-R_λ flows 139
4.4 *In-situ* Measurements of Trade-wind Cumuli 142
  4.4.1 Turbulence Characteristics of Trade-wind Cumuli 148
  4.4.2 Statistics of Cloud Droplets in Trade-wind Cumuli 149
  4.4.3 Cloud Droplet Statistics in Precipitating Cloud 154
Appendix 4.A Protocol for Validity Flag 164
Appendix 4.B Effect of Filtering 166
Appendix 4.C Supplementary Tables 170
Appendix 4.D Supplementary Figures 172

5 Discussion and Outlook 175
5.1 Discussion 175
5.1.1 Turbulence Measurements in the Trade-wind Boundary Layer . 175
5.1.2 Cloud droplet statistics 179
5.2 Outlook 181
5.3 Summary 183

References 185

Curriculum Vitae 202

Chapter 1

Introduction

1.1 Scope of the thesis

On average, more than 45% of the Earth's surface and 68% of oceans are covered with clouds [1]. Clouds form in the Earth's atmosphere and can be classified in terms of visual appearance and altitude [2]. As an example, clouds near the planetary surface are known as fog whereas cauliflower-like cumulus clouds occur in an altitude range between 0 km to 2 km. In general, clouds can be described as multi-phase turbulent flows where cloud dynamics span a vast range of spatio-temporal scales [1, 3, 4]. In turbulence, energy is injected into the flow at large scales and, at small scales, energy is dissipated into heat at the energy dissipation rate ϵ, where the smallest relevant scales are known as the Kolmogorov scales [5].

The most frequent cloud type on the Earth is trade-wind cumuli (more than 32 %) over the sub-tropical ocean, which develop in the lowest few kilometers of the atmospheric boundary layer [1, 6]. Trade-wind cumuli are initiated by thermals that rise above an altitude level, where moist air condenses, the so-called lifting condensation level (LCL), and exist for several hours [1, 7, 8]. Often, shallow cumuli are only a couple of hundreds meter deep but they can grow up to the trade-wind inversion in case of strong enough buoyancy [9]. Trade-wind cumuli are isolated with larger regions absent of clouds leading to a recently measured cloud cover at cloud base of 3.5% [10]. They enhance the vertical heat and moisture transport [11], are coupled to global circulation [6, and references therein] and are crucial in the Earth's radiation budget [12, 13]. Regarding the latter, trade-wind cumuli reflect solar radiation and thereby cool the planet. The larger the area covered by shallow cumuli, the higher the fraction of reflected solar radiation. Primarily, uncertainty in climate prediction is caused by a lack of understanding of how these shallow cumulus clouds respond to global warming [14], which is usually modeled by the cloud fraction at the cloud base [9]. Recently, it has been shown that the climate sensitivity of shallow cumuli is low [9]. Instead, it is suggested that a deeper understanding of mesoscale circulation and its response to global warming is needed [9].

Despite the long history of research in the trades [e.g. 8, 15–18], the influence of turbulence on small-scale cloud processes still lacks detailed understanding. Especially, the rapid onset of precipitation in warm, i.e. ice-free, clouds within less than thirty minutes cannot be explained by evaporation-condensation processes only [19]. Warm rain forms in four steps. After the activation of cloud condensation nuclei in a super-saturated (cf. Sec. 1.3.1) environment, i.e. where relative humidity exceeds 100%, cloud droplets grow by condensation up to 15 µm during a time period of 30 min in typical cloud conditions with low super-saturation [20]. Cloud droplets larger than 40 µm in diameter further grow by gravitational collection where large cloud droplets sediment, collide and coalesce with smaller droplets [21]. However, it is not clear how cloud droplets transition the size gap of 15 µm to 40 µm in radius as neither condensational growth nor gravitational collection is effective [20]. This size gap is also known as the condensation-coalescence bottleneck. Warm-rain initiation concerns 31% of global and 72% of tropical rain [22] highlighting the fundamental importance of unraveling the relevant cloud processes.

The condensational growth rate of cloud droplets is proportional to the super-saturation [4]. In general, cloud droplets do not grow in homogeneous and constant conditions [20]. Instead, the large-scale temperature and super-saturation field inside clouds exhibit fluctuations caused by turbulent entrainment and mixing [4, 20]. These fluctuations cause the cloud droplets to grow by condensation or to decay by evaporation [3, 4]. Vice versa, these phase transitions impact the large-scale super-saturation and buoyancy by latent heat effects driving the turbulent flow [4]. Despite that the growth rate of cloud droplets decelerates with increasing diameter [23], a key ingredient for rain formation is the presence of large droplets. Hopping from one large eddy to another, cloud droplets experience different growth histories, which causes a broadening of droplet size distributions [20]. If a cloud droplet is advected always by strongly super-saturated eddies, this particular cloud droplet grows larger than the average.

A similar effect is known as convective ripening [24] where cloud droplets grow by condensation in ascending air parcels until reaching the cloud top. Due to the buoyancy reversal at the cloud top, the air parcel descends being dragged by cool air masses. In the cloud core, the air parcel is mixed with warm cloudy air again. If the time-scale of the mixing mechanism is much faster than the evaporation time scale, the cloud droplet does not evaporate and can continue growing in the subsequent updraft. It should be noted that convective ripening requires that the air parcel cools very slowly during the ascent and warms very fast during descent due to subsequent mixing. However, it is not yet fully understood how mixing processes are related to different scales of the turbulent flows partly due to the lack of *in-situ* measurements resolving sub-meter scales [4, 25].

Besides condensational growth, cloud droplets grow by collision-coalescence, which is affected by cloud droplet-turbulence interactions due to cloud droplet inertia [20, 26]. Cloud droplet inertia is non-dimensionally captured by the Stokes number St (cf. Sec. 1.3.2), which is a measure of how fast cloud droplet motions respond to changes in the ambient flow [4]. If St is finite, cloud droplets do not trace the flow anymore perfectly and are ejected from regions of high vorticity due to centrifugal forces inducing an inhomogeneous spatial cloud droplet distribution [26]. Emphasizing their importance, the spatial distribution of cloud droplets not only affects the collision rate but also the radiative properties of clouds [27]. However, *in-situ* measurements of cloud droplet spatial distribution resolving down to the smallest scales are rare [25]. If St is larger than 0.1, the inertial effects of cloud droplets become strong enough so that cloud droplet trajectories can intersect, which is known as the “sling effect”, causing high relative velocities of cloud droplets [28]. Both locally higher cloud droplet concentration and higher relative velocity of adjacent cloud droplets cause enhanced collision rates [29].

In typical turbulent cumulus clouds with a cloud depth of $\sim 1\,\mathrm{km}$ and cloud droplet radius $\sim 10\,\mu\mathrm{m}$, the collision rate due to droplet inertia is on the order of $1 \times 10^{-6}/\mathrm{s}$ whereas the rate of gravitational collection is two orders of magnitude larger, i.e. $\sim 1 \times 10^{-4}/\mathrm{s}$ [26]. The probability of a cloud droplet to grow to a rain droplet is estimated to be on the order of 10^{-7}, which, considering a cloud droplet of radius $10\,\mu\mathrm{m}$, involves about 125 collision-coalescence events with cloud droplets of the same size to grow up to $50\,\mu\mathrm{m}$ in radius [26]. Hence, the initiation of rain is related to rare and localized events resulting in the runaway growth of cloud droplets [26, 30]. In general and independent of the underlying mechanism, the runaway growth of cloud droplets is crucial to the onset of precipitation. It is therefore of utmost interest to determine these runaway processes and to quantify their occurrence frequency [26].

To investigate such cloud processes, it is necessary to resolve the turbulent flow down to the smallest scales as well as the spatial distribution of cloud droplets. Advantageously in direct numerical simulation (DNS), the entire flow field is fully resolved. To simulate cloud dynamics for clouds with a typical depth $L \sim 1000\,\mathrm{m}$, a characteristic velocity scale $u \sim 1\,\mathrm{m/s}$ and smallest relevant scales $\eta_K \sim 1\,\mathrm{mm}$, a DNS of 10^{18} grid points has to be run for a time period of at least $l/u \sim 10\,\mathrm{min}$ [31], which is computationally very expensive, if not possible at all. In the DNS of a turbulent flow with $\mathrm{R}_\lambda = 1300$, the simulated time period is about 20 times the Kolmogorov time scale τ_K [32]. Therefore, DNS is well-suited for investigating small-scale processes [4]. Large-eddy simulations are able to simulate large-scale processes but suffer from the parameterization of scales smaller than the grid size ranging from $5\,\mathrm{m}$ to $100\,\mathrm{m}$ [33–35].

Laboratory experiments are able to reproduce turbulent flows with Taylor-scale Reynolds numbers, a measure for the separation of large and small scales, as high as observed in the atmosphere [36, e.g.]. However, in laboratory experiments, the largest scale is $L \sim 1\,\mathrm{m}$ being much smaller than in the atmosphere (e.g. cloud depth ranging from $100\,\mathrm{m}$ to $1000\,\mathrm{m}$). Therefore, turbulent flows at high-Reynolds number are usually generated by increasing the energy dissipation rate ϵ, which is equivalent to decreasing the smallest scales ($\eta_K \propto \epsilon^{-1/4}$). As a consequence, the role of gravity compared to fluid accelerations, which is captured by the fluid Froude number $\mathrm{Fr} \propto \eta_K^{-3/4}$, is underestimated compared to atmospheric flows. Hence, it is difficult to reproduce realistic atmospheric conditions in laboratory experiments. Therefore, *in-situ* measurements are necessary in order to investigate atmospheric flows and cloud processes.

In this thesis, airborne measurements of atmospheric turbulence and inside clouds are conducted with two specially developed instruments, the Max Planck Cloudkite + (MPCK+) and the mini-Max Planck Cloudkite (mini-MPCK). The MPCK+ is equipped with a combined holography and Particle Image Velocimetry system [37]. Both the MPCK+ and mini-MPCK count and size cloud droplets with the help of cloud droplet probes. Furthermore, they comprise several instruments to measure relative wind speed and fluid properties such as air temperature. Both instruments are carried by tethered helium-filled and kite-stabilized balloons ("helikites"). Helikites provide a high degree of mobility and guarantee high spatio-temporally resolved measurements down to mm-scales due to the low relative wind speed $\sim 10\,\mathrm{m/s}$ (cf. Sec. 2.1). During the EUREC^{4}A (Elucidating the role of cloud-circulation coupling in climate) field campaign [38], the MPCK+ and mini-MPCK profiled the atmosphere and sampled clouds whereby the helikites are launched from both the research vessel (RV) Maria S. Merian and RV Meteor. Due to their scientific instrumentation and high spatial resolution, both instruments promise unique data sets of clouds and the cloud-free atmosphere, which can serve as the basis for many research questions [37].

One of the most important goals is to measure the cloud droplet distribution in space with the help of the MPCK+ and mini-MPCK, thereby quantifying inhomogeneities and proving the existence of regions inside clouds devoid of cloud droplets. These regions are referred to as *cloud voids* and are related to strong and long-living vortices expelling cloud droplets due to centrifugal forces [39]. Furthermore, cloud droplet sizing instruments aboard the MPCK+ and mini-MPCK allow for recording droplet size distributions both in non-precipitating and precipitating clouds in order to quantify the droplet size distribution, which affects cloud droplet inertia. The cloud droplet measurements are complemented by turbulence measurements in order to assess the importance of inertial and gravitational effects, which are captured by the Stokes number and non-dimensional settling velocity Sv, respectively [4]. Both St and Sv as well as many turbulence characteristics are based on the energy dissipation rate. As explained in detail below (cf. Chapter 3), the energy dissipation rate is estimated from one-dimensional time-records of the relative wind speed invoking Kolmogorov's phenomenology from 1941 [5].

In addition to cloud microphysical measurements, the MPCK+ and mini-MPCK are able to measure vertical profiles, e.g. of temperature and wind in the atmospheric boundary layer. Notably, the atmospheric boundary layer is considered to be the lowest $100\,\mathrm{m}$ to $3000\,\mathrm{m}$ of the Earth's atmosphere [40]. As mentioned below, the static stability of the atmospheric boundary layer depends on the vertical gradient of the *virtual potential temperature* (cf. Eq. (1.53)). A stably stratified boundary layer suppresses the vertical motion of the fluid and an unstable boundary layer enhances the vertical motion of the fluid impacting the vertical transport of heat and moisture [40]. In principle, atmospheric turbulence can also be driven by shear, a non-vanishing mean wind gradient [40]. The relative importance of shear and stratification is captured by the Richardson number [40, 41]. Quantifying Richardson numbers from profiles of mean wind and virtual potential temperature in combination with turbulence length scales thus hints at the turbulent state and stability of the atmospheric boundary layer. Based on this, one can evaluate the possibility of how far vertical transport processes take place. As vertical heat and moisture transport is important for clouds being initiated above thermals [7], it can be anticipated that the presence of clouds is related to the stability of the boundary layer and its turbulent state.

To summarize, this work focuses on investigations of atmospheric turbulence and cloud microphysics dealing with the following questions:

- How are cloud droplets in trade-wind cumuli distributed in space? Do cloud voids exist in trade-wind cumuli?
- What is the role of cloud droplet inertia and gravity in non-precipitating and precipitating clouds?
- How does the cloud droplet size distribution vary with altitude and from cloud edge to cloud core?
- What are the characteristic turbulence features of trade-wind cumuli and how do they differ from the cloud-free environment, e.g. in the sub-cloud layer or between clouds?
- Does the stability of the boundary layer allow for the presence of turbulence?
- Is the assumption of statistically local isotropic turbulence valid? Hence, is it justified to estimate the energy dissipation rate based on Kolmogorov's phenomenology?
- How accurately can the energy dissipation rate be estimated given various experimental limitations?

After outlining the scope of the thesis, the most relevant concepts of turbulence and cloud microphysics are introduced in Chapter 1. Both the MPCK+ and mini-MPCK are presented in Chapter 2. In Chapter 3, the performance of energy dissipation rate estimates under various experimental limitations is assessed. Results from atmospheric turbulence and cloud microphysical measurements are presented in Chapter 4 and discussed in Chapter 5.

1.2 Turbulent flows

As mentioned before, clouds are highly turbulent. Therefore, the equations of fluid motion, a phenomenological description of turbulence and fundamental turbulence characteristics are shortly introduced in this section. Most of the content is following textbooks [5, 42]. If not mentioned otherwise, the fluid is assumed to be free of particles and to consist of dry air only. In addition, it is assumed that the fluid is continuous and behaves like a Newtonian fluid fulfilling [42]

$$\tau_{ij} = \rho\nu \left(\frac{\partial u_i}{\partial x_j} + \frac{\partial u_j}{\partial x_i} \right) , \tag{1.1}$$

where τ_{ij} is the stress tensor, ρ the density and ν the kinematic viscosity. Hence, the shear stresses of Newtonian fluids are proportional to the kinematic viscosity in Newtonian fluids. If equations are written in the component form, Einstein's convention (i.e. summation over repeated indices) is implied.

1.2.1 Equations of motion

Conservation of Mass

As mass is not destroyed or created, mass is conserved. The conservation of mass can be expressed in terms of the continuity equation [5]

$$\frac{\partial \rho}{\partial t} + \frac{\partial(\rho u_i)}{\partial x_i} = 0\,, \tag{1.2}$$

where u_i is the i-component of the three-dimensional velocity field $\boldsymbol{u}(\boldsymbol{x}, t)$. Equation (1.2) reduces to $\partial u_i/\partial x_i = 0$ for an incompressible fluid.

Newton's second law

Neglecting external forces like gravity, a fluid parcel of volume δV and density ρ is accelerated by body forces and surface forces [5]. The latter is due to viscosity and can be captured by the symmetric stress tensor $\tau_{ij} = \tau_{ji}$ [42]. The body force results from the net force that pressure exerts on all surfaces of that fluid parcel and applying Gauss' theorem [42]. Then, the equations of motion of a fluid parcel read [5]

$$\frac{Du_i}{Dt} = \frac{\partial u_i}{\partial t} + u_j \frac{\partial u_i}{\partial x_j} = \underbrace{-\frac{1}{\rho}\frac{\partial p}{\partial x_i}}_{\text{pressure gradient}} + \underbrace{\nu \frac{\partial^2 u_i}{\partial x_j \partial x_j}}_{\text{viscous force}} , \tag{1.3}$$

equations are given by Eq. (1.2) and (1.3). This set of equations cannot be solved in general due to its non-linearity in $u_j \frac{\partial u_i}{\partial x_j}$, non-locality of the pressure gradient and the dissipative nature of the viscous stresses [42]. In the absence of viscous forces, the fluid parcel moves against the pressure gradient, i.e. from regions of high pressure to low pressure.

1.2.2 Reynolds number and Nature of Turbulence

To better compare the relative importance of viscous stress to inertial forces, it is helpful to write Eq. (1.3) in a non-dimensional form [5]. Capturing the typical velocity and length scales of the flow by $\tilde{u}$ and $\tilde{L}$, respectively, the non-dimensional form of Eq. (1.3) reads:

$$\frac{D\bar{u}_i}{D\bar{t}} = -\frac{\partial \bar{p}}{\partial \bar{x}_i} + \underbrace{\frac{\nu}{\tilde{L}\tilde{u}}}_{1/Re} \frac{\partial^2 \bar{u}_i}{\partial \bar{x}_j \partial \bar{x}_j} , \tag{1.4}$$

where $\bar{u}_i = u_i/\tilde{u}$, $\bar{t} = t\tilde{u}/\tilde{L}$, $\partial/\partial\bar{x}_i = \tilde{L}\partial/\partial x_i$, $\bar{p} = p/(\rho\tilde{u}^2)$ and Re the Reynolds number. The Reynolds number can be interpreted as a measure between inertial and viscous forces:

$$Re = \frac{\text{inertial forces}}{\text{viscous forces}} = \frac{\rho \tilde{u}^2 \tilde{L}^2}{\mu \tilde{L} \tilde{u}} = \frac{\tilde{u}\tilde{L}}{\nu} , \tag{1.5}$$

where $\mu = \rho\nu$ is the dynamic viscosity. If $Re < 1$, viscous forces dominate over inertial forces and the flow is laminar. In the other limit, $Re \gg 1$, the dynamics of the flow are controlled by inertial forces. Of course, this view is simplified because it does not take into account the effect of boundaries, initial conditions or stratification. However, due to the low kinematic viscosity of (dry) air $\mathcal{O}(\nu) \sim 1 \times 10^{-5}\,\mathrm{m^2/s}$ at typical atmospheric conditions (air temperature of 20 °C at 1000 hPa), the Reynolds number is usually high for finite $\tilde{u}$ and $\tilde{L}$ so that the flow is turbulent in general.

Turbulent flows are omnipresent in daily life and expose themselves by whirls in a river or at a waterfall, twisted smoke plumes from a chimney or in the cauliflower-like appearance of cumulus clouds. These examples of a turbulent flow come along with a higher rate in mixing and transport of heat, moisture and momentum compared to laminar flows [5]. Two realizations of a turbulent flow are never identical due to their strong dependence on initial conditions. Turbulent flows are coined by their chaotic, multi-scale, intermittent and dissipative nature [5, 42].

A helpful quantity in describing the nature of turbulence is the vorticity $\boldsymbol{\omega} = \nabla \times \boldsymbol{u}$, which is a measure of the angular velocity of the fluid [42]. Re-expressing the Navier-Stokes equations in terms of the vorticity for constant-density flows yields [5]:

$$\frac{D\boldsymbol{\omega}}{Dt} = \nu\nabla^2\boldsymbol{\omega} + \boldsymbol{\omega} \cdot \nabla\boldsymbol{u} . \tag{1.6}$$

The first term on the right-hand side is due to the local diffusion of vorticity due to viscous forces on the fluid parcel, which is why vorticity acts locally [42]. Considering the second term on the right-hand side, the velocity gradient tensor $\nabla\boldsymbol{u}$ can either compress or stretch fluid parcels. Hence, due to the conservation of angular momentum, vorticity is enforced (weakened) by a finite strain if $\nabla\boldsymbol{u}$ causes stretching (compression) of that fluid parcel. This effect is known as *vortex stretching* [5, 42].

With the help of vorticity and depending on its shape, a single whirl in a river can be understood as a blob, sheet or tube of vorticity, which is often known as a *turbulent eddy* [42]. Due to the local character of vorticity, these eddies are coherent over a certain time and associated with a typical length scale l. Extending the idea of eddies on a cumulus cloud, its appearance is due to the complex arrangement of numerous eddies of different sizes evolving in time and space, where small eddies are embedded in larger eddies [5]. These eddies are coupled to the local velocity field, which compresses or stretches the vortices. Turbulence can hence be regarded as a complex cluster of intertwined vortices obeying Eq. (1.6) [42].

1.2.3 Reynolds decomposition and Mean-flow Equations

The most basic statistical quantity of a turbulent velocity field $u_i(\boldsymbol{x}, t)$ is its mean U_i. According to Reynolds, the velocity field can be decomposed into its mean U_i and the fluctuating part u_i' [5]:

$$u_i = U_i + u_i' \,. \tag{1.7}$$

Invoking Reynolds decomposition, the Navier-Stokes equations can be rewritten in terms of the mean-momentum or Reynolds equations by [5]

$$\frac{\partial U_i}{\partial x_i} = 0 \,, \tag{1.8}$$

$$\begin{aligned} \frac{\partial U_i}{\partial t} + U_j \frac{\partial U_i}{\partial x_j} &= -\frac{1}{\rho}\frac{\partial \langle p \rangle}{\partial x_j} + \nu \frac{\partial^2 U_i}{\partial x_j \partial x_j} - \frac{\partial \langle u_i' u_j' \rangle}{\partial x_j} \\ &= \frac{1}{\rho}\frac{\partial}{\partial x_j}\left[-\langle p \rangle \delta_{ij} + \underbrace{\nu\rho \frac{\partial \langle U_i \rangle}{\partial x_j}}_{\text{viscous stress}} - \rho \underbrace{\langle u_i' u_j' \rangle}_{\text{Reynolds stress}} \right] . \end{aligned} \tag{1.9}$$

The Reynolds stress tensor is hence given by co-variances of velocity fluctuations $\langle u_i' u_j' \rangle$, which is symmetric, i.e. $\langle u_i' u_j' \rangle = \langle u_j' u_i' \rangle$, and has non-negative eigenvalues [5]. The diagonal components are called "normal stresses" and the off-diagonal components are called " shear stresses" [5]. Furthermore, the turbulent kinetic energy k is defined in terms of the trace of the Reynolds stress tensor, i.e. [5]

$$k \equiv \frac{1}{2}\langle \boldsymbol{u}' \cdot \boldsymbol{u}' \rangle = \frac{1}{2}\langle u_i' u_i' \rangle \,. \tag{1.10}$$

Together with the continuity equation, Eq. (1.8), there are four equations but 10 unknowns (U_i, $\langle p \rangle$ and $\langle u_i' u_j' \rangle$). Hence, the Reynolds equations are unclosed and can only be solved if the Reynolds stresses are known (or modeled) [5].

Anisotropy

The Reynolds stress tensor can also be decomposed into an isotropic part $\frac{2}{3}k\delta_{ij}$ and a deviatoric part a_{ij} [5].

$$\begin{aligned} a_{ij} &\equiv \langle u'_i u'_j \rangle - \frac{2}{3}k\delta_{ij} \,, \\ \Rightarrow b_{ij} &= \frac{a_{ij}}{2k} = \frac{\langle u'_i u'_j \rangle}{\langle u'_l u'_l \rangle} - \frac{1}{3}\delta_{ij} \,, \end{aligned} \tag{1.11}$$

where b_{ij} is the normalized anisotropy tensor. The isotropic component $\frac{2}{3}k$ can be included in an effective mean pressure so that the momentum is transported only by the anisotropic components a_{ij} [5].

1.2.4 Homogeneous Isotropic Turbulence

In the following, the characteristic length scale of a fully turbulent flow is denoted by $\mathcal{L}$ and the velocity scale by $\mathcal{U}$. It is assumed that the Reynolds number $Re = \mathcal{U}\mathcal{L}/\nu$ is very high.

A turbulent flow consists of eddies of multiple sizes. Energy is injected at the largest scales $L < \mathcal{L}$, which is why this range is called energy-containing range, and which is practically realized by a stirring process or boundary effects. As an example, in clouds, the energy is injected mostly by buoyant and shear instability [2, 4]. At the smallest scales of the turbulent flow, where viscous forces are comparable to or larger than inertial forces, kinetic energy is dissipated into heat. The range of scales in between the energy-injection scale and the dissipation range is dominated by inertial forces only and is known as the inertial sub-range [5]. According to the picture of the turbulent energy cascade introduced by Richardson, energy is transferred from larger eddies to smaller eddies by the breakup of eddies [5].

In the atmosphere, large eddies are generally anisotropic, e.g. due to stratification or topography. Due to its chaotic nature, Kolmogorov postulated that small eddies of a turbulent flow are independent of large eddies, hence the energy-injecting mechanism, [5] leading to

Kolmogorov's hypothesis of local isotropy:

"At sufficiently high Reynolds numbers, the small-scale turbulent motions ($l \ll \mathcal{L}$) are statistically isotropic. "

In consequence, the statistics of small eddies is universal. As kinetic energy is dissipated into heat by viscous effects, it is plausible to assume that two parameters determine the statistics of small eddies, the viscosity of the fluid and the rate at which energy is transferred from large to small eddies. In equilibrium, this transfer rate is approximately equal to the energy dissipation rate ϵ, at which kinetic energy is dissipated due to viscous effects. This motivates [5] **Kolmogorov's first similarity hypothesis:**

"In every turbulent flow a sufficiently high Reynolds number, the statistics of small-scale motions ($l < L$) have a universal form that is uniquely determined by ν and ϵ."

In this range of scales, viscous forces are important suggesting that the Reynolds number associated with these scales l are on the order of one or smaller. Based on dimensional arguments, there is only one set of length, time and velocity scales that can be formed by ϵ and ν only. These scales are known as the Kolmogorov scales [43]:

$$\eta_K = \left(\frac{\nu^3}{\epsilon}\right)^{1/4}, \tag{1.12}$$

$$\tau_K = \left(\frac{\nu}{\epsilon}\right)^{1/2}, \tag{1.13}$$

$$u_K = (\nu\epsilon)^{1/4}, \tag{1.14}$$

where η_K, τ_K and u_K are the Kolmogorov length, time and velocity scale, respectively. The Reynolds number associated with the Kolmogorov scales is equal to one: $Re(\eta_K) = \frac{\eta_K u_K}{\nu} = 1$. The notion of "similarity" is due to the fact that the small-scale statistics are statistically identical if they are scaled by the Kolmogorov scales [5].

In contrast to the smallest eddies with $Re(\eta_K) = 1$, the scale-dependent Reynolds number $Re(l)$ is still large for eddies in the inertial sub-range with $\eta_K \ll l \ll L$. Intuitively, viscous effects play a minor role suggesting for

Kolmogorov's second similarity hypothesis:

"In every turbulent flow a sufficiently high Reynolds number, the statistics of the motions of scale l in the range $\eta_K \ll l \ll L$ have a universal form that is uniquely determined by ϵ, independent of ν."

It is not possible to define length, time and velocity scales from only ϵ. However, eddies of characteristic length scale l have characteristic time and velocity scales of [5]:

$$u(l) = (\epsilon l)^{1/3}, \tag{1.15}$$

$$\tau(l) = \left(\frac{l^2}{\epsilon}\right)^{1/3} = \frac{l}{u(l)}, \tag{1.16}$$

$$\Rightarrow \epsilon = \frac{u(l)^3}{l} = \frac{u(l)^2}{\tau(l)}, \tag{1.17}$$

where the last step is explained below and where $u(l)$ is the characteristic velocity and $\tau(l)$ the characteristic time scale. $\tau(l)$ is also known as the eddy turnover time. Considering the energy injection scale L, the characteristic velocity scale $u(L)$ is similar to the root mean square (RMS) of the velocity fluctuations u':

$$u' = \sqrt{\frac{1}{3}\langle u_i' u_i' \rangle}. \tag{1.18}$$

In homogeneous isotropic turbulence, the RMS velocity fluctuations u' are equal to the RMS fluctuations of the longitudinal velocity denoted by $\sigma_{u_1'}$.

Furthermore, considering the picture of the energy cascade, kinetic energy is transferred from eddies with a characteristic length scale larger than l to smaller ones. Assuming that this energy transfer is across eddies of size l, the rate of energy transfer across these eddies is $\sim u(l)^2/\tau(l)$, hence being constant and independent l within the inertial sub-range [5]. In consequence, within the concept of the energy cascade, the rate of energy transfer from the energy injection scale L to eddies of the inertial sub-range with characteristic l is equal to the rate at which energy dissipates by viscous effects, i.e. ϵ [5].

However, it is still unclear how the energy is distributed among eddies of different sizes. A useful quantity is the energy spectrum function $E(\kappa)$ capturing how much energy is contained in eddies of a characteristic size l where $\kappa = 2\pi/l$ is a wavenumber. $E(\kappa)$ contains information on the fully-resolved three-dimensional velocity field, which is difficult to experimentally measure. However, $E(\kappa)$ can be defined in terms of a one-dimensional energy spectrum $E_{11}(\kappa)$, as given by Eq. (3.10) in Sec. 3.2.2, which can be obtained from measurements of $u_1(\boldsymbol{x}, t)$, the $\boldsymbol{e}_1$-component of the velocity field. Assuming statistically stationary homogeneous isotropic turbulence, $E(\kappa)$ can be obtained by

$$E(\kappa) = \frac{1}{2}\kappa^3 \frac{\mathrm{d}}{\mathrm{d}\kappa}\left(\frac{1}{\kappa}\frac{\mathrm{d}E_{11}(\kappa)}{\mathrm{d}\kappa}\right) . \tag{1.19}$$

According to Kolmogorov's second similarity hypothesis, inertial-range statistics are uniquely governed by ϵ. Hence, the energy spectrum function is expected to be a function of ϵ and κ only. Dimensional analysis yields the famous -5/3 - scaling of the spectrum in the inertial sub-range [5]

$$E(\kappa) = C_K \epsilon^{2/3} \kappa^{-5/3} , \tag{1.20}$$

where $C_K \approx 1.5$ is the universal Kolmogorov constant. It should be noted that the turbulent kinetic energy k is obtained by integrating over $E(\kappa)$ all wavenumbers [5]

$$k = \int_0^\infty \mathrm{d}\kappa \, E(\kappa) . \tag{1.21}$$

Similarly, the energy dissipation rate can be spectrally expressed as [5]

$$\epsilon = 2\nu \int_0^\infty \mathrm{d}\kappa \, \kappa^2 E(\kappa) . \tag{1.22}$$

As $E(\kappa)$ is monotonically decreasing in the inertial sub-range and the dissipation range, Eqs. (1.21) and (1.22) reveal that most of the turbulent kinetic energy is stored in the large eddies while most of the energy is dissipated at small scales [5].

As Kolmogorov described the phenomenology of the Richardson cascade theoretically in 1941 [43, 44], this theory is usually referred to as K41 in the following.

Correlation functions

One of the most basic second-order statistics is the two-point velocity covariance tensor (compare Sec. 3.2.2). Here, we assume statistically stationary homogeneous isotropic turbulent flow with vanishing mean, i.e. $\boldsymbol{u}(\boldsymbol{x},t) = \boldsymbol{u}'(\boldsymbol{x},t)$ as well as $\langle u_1'^2 \rangle = \langle u_2'^2 \rangle = \langle u_3'^2 \rangle = \langle u'^2 \rangle$, and that all averages are invariant under rotations of the coordinate system. The two-point velocity covariance tensor is defined as [e.g. 5, 45, 46]

$$\begin{aligned} R_{ij}(\boldsymbol{r}) &= \langle u_i'(\boldsymbol{x}+\boldsymbol{r},t) u_j'(\boldsymbol{x},t) \rangle \,, && (1.23) \\ &= \langle u'^2 \rangle \left(g(r)\delta_{ij} + [f(r) - g(r)] \frac{r_i r_j}{r^2} \right) && (1.24) \end{aligned}$$

where Eq. (1.24) is due to isotropy and $f(r) = R_{11}(r)/R_{11}(0)$ is the longitudinal autocorrelation function. The transverse autocorrelation function $g(r)$ is uniquely defined in terms of $f(r)$ by [5]

$$g(r) = f(r) + \frac{1}{2} r \frac{\partial f(r)}{\partial r} \,. \tag{1.25}$$

Notably, $f(0) = g(0) = 1$. Let the longitudinal direction of the flow be parallel to the $\boldsymbol{e}_1$-direction of the chosen coordinate system. Then, $R_{11}(r) = \langle u'^2 \rangle f(r)$, $R_{22}(r) = R_{33}(r) = \langle u'^2 \rangle g(r)$, and the off-diagonal components are zero [5].

Descriptively, the correlation functions are a measure of how the velocity field is correlated over a separation of $\boldsymbol{r}$. The length, over which the flow can be considered to be correlated is the integral length scale, which is defined as [5]

$$\begin{aligned} L_{11} &= \int_0^\infty \mathrm{d}r' f(r') \,, && (1.26) \\ L_{22} = L_{33} &= \int_0^\infty \mathrm{d}r' g(r') && (1.27) \\ & && (1.28) \end{aligned}$$

where L_{11} is the longitudinal integral length scale and L_{22} as well as L_{33} are the transverse integral scales. In homogeneous isotropic turbulence, $L_{22} = L_{33} = L_{11}/2$ holds [5]. The integral scales are characteristic to large eddies so that L_{11} can also be estimated by a scaling argument [47]:

$$L_{11} = C_\epsilon \frac{\langle u_1'^2 \rangle^{3/2}}{\epsilon} \,. \tag{1.29}$$

where $C_\epsilon \approx 0.5$ is the dissipation constant. In homogeneous isotropic turbulence at high Reynolds numbers, the integral scale is related to the energy injection scale L by $L_{11}/L \approx 1/2$ [5]. In the atmosphere, L corresponds to the energy injection scale, e.g. length scale of convection rolls in a convective boundary layer such as the boundary layer depth [41]. Hence, the integral scale should be approximately half of the boundary layer depth if the boundary layer is assumed to be isotropic. Similarly and for completeness, the integral time scale T_{11} is given by

$$T_{11} = C_\epsilon \frac{\langle u_1'^2 \rangle}{\epsilon} = \frac{L_{11}}{\langle u_1'^2 \rangle^{1/2}} \,. \tag{1.30}$$

In addition to integral scales, another length scale can be derived from autocorrelation functions that is intermediate between the Kolmogorov length scale η_K and the integral scales at high Reynolds numbers. This length scale is known as the Taylor micro-scale and is obtained by [5]

$$\lambda_f = \left(-\frac{1}{2} \frac{\partial^2 f(0)}{\partial r^2} \right)^{-1/2} \,, \tag{1.31}$$

$$\lambda_g = \left(-\frac{1}{2} \frac{\partial^2 g(0)}{\partial r^2} \right)^{-1/2} \,, \tag{1.32}$$

$$\tag{1.33}$$

where λ_f is the longitudinal and λ_g the transverse Taylor micro-scale. In homogeneous isotropic turbulence, λ_f and λ_g can be expressed as [5]

$$\lambda_f = \sqrt{\frac{30 \nu u'^2}{\epsilon}} \,, \tag{1.34}$$

$$\lambda_g = \sqrt{\frac{15 \nu u'^2}{\epsilon}} \,, \tag{1.35}$$

$$\tag{1.36}$$

invoking $\epsilon = 15\nu \langle (\partial u_1' / \partial x_1)^2 \rangle$, which will be introduced below. In homogeneous isotropic turbulence, $\lambda_f / \lambda_g = \sqrt{2}$. Moreover, one can define a Reynolds number, the Taylor micro-scale Reynolds number, with the help of the Taylor micro-scale [5]

$$\mathrm{R}_\lambda = \frac{\lambda_g u'}{\nu} = \sqrt{\frac{15 u'^4}{\epsilon \nu}} \tag{1.37}$$

$$\sim \sqrt{15} \frac{\epsilon^{1/6} L_{11}^{2/3}}{\nu^{1/2}} \tag{1.38}$$

which is based on λ_g and where u' is substituted by $u' \sim (L_{11}\epsilon)^{1/3}$. Defining a large-eddy Reynolds number by $Re_L = k^{1/2} L / \nu$ with $L \equiv k^{3/2}/\epsilon$, the separation of scales between the energy-containing eddies and the dissipative scales grows with Re_L as [5]

$$\frac{L}{\eta_K} = Re_L^{3/4} \,. \tag{1.39}$$

In atmospheric flows, where a typical length scale is $\mathcal{O}(L) \sim 100\,\mathrm{m} - 1000\,\mathrm{m}$ and $\eta_K \approx 1\,\mathrm{mm}$ (cf. Chapter 4), a well-pronounced inertial sub-range, for example in second-order structure functions, is expected.

Structure functions

Kolmogorov's phenomenology is also expressed in terms of velocity structure functions, i.e. moments of velocity increments separated by a separation vector $\boldsymbol{r}$ [43]. As mentioned before, we consider a velocity field $\boldsymbol{u}(\boldsymbol{x}, t)$ with vanishing mean, i.e. $\boldsymbol{u}(\boldsymbol{x}, t) = \boldsymbol{u}'(\boldsymbol{x}, t)$. The second-order velocity structure function tensor is given by the covariance tensor of velocity increments [5, 42]

$$D_{ij}(\boldsymbol{r}) = \Big\langle \left[u_i'(\boldsymbol{x}+\boldsymbol{r}, t) - u_i'(\boldsymbol{x}, t)\right] \Big[u_j'(\boldsymbol{x}+\boldsymbol{r}, t) - u_j'(\boldsymbol{x}, t)\Big] \Big\rangle \,. \tag{1.40}$$

In homogeneous isotropic turbulence, the diagonal components of the velocity fluctuation covariance tensor are equal to each other, i.e. $\langle u_1'^2 \rangle = \langle u_2'^2 \rangle = \langle u_3'^2 \rangle = \langle u'^2 \rangle$, and it is assumed that all averages are invariant under rotations of the coordinate system (compare Sec. 3.2.2). Then, the second-order velocity structure function tensor depends only on the separation vector $\boldsymbol{r}$ [5]

$$D_{ij}(\boldsymbol{r}) = D_{NN}(r)\delta_{ij} + \left[D_{LL}(r) - D_{NN}(r)\right] \frac{r_i r_j}{r^2} \,, \tag{1.41}$$

where $D_{LL}(r)$ is the longitudinal and $D_{NN}(r)$ the transverse structure function. Let the longitudinal direction of the flow be parallel to the $\boldsymbol{e}_1$-direction of the chosen coordinate system. Then, the longitudinal second-order structure function $D_{11}(r)$ is related to $f(r)$ by [e.g. 5, 42]

$$D_{11}(r\boldsymbol{e}_1) = D_{LL}(r) = \langle (u_1'(\boldsymbol{x} + r\boldsymbol{e}_1, t) - u_1'(\boldsymbol{x}, t))^2 \rangle = 2\langle u'^2 \rangle (1 - f(r)) \,. \tag{1.42}$$

Considering separations $L \gg r \gg \eta_K$ in the inertial sub-range and taking Kolmogorov's second similarity hypothesis into account, the only possibility to match the units of $D_{LL}(r)$ ($\mathrm{m}^2/\mathrm{s}^2$) is given by [5]

$$D_{LL}(r) = C_2(\epsilon r)^{\zeta_2} \,, \tag{1.43}$$

where $\zeta_2 = 2/3$ and $C_2 \approx 2$ [5]. Furthermore, $\partial D_{ij}(\boldsymbol{r})/\partial r_i = 0$ in incompressible, zero-mean flows with $\partial u_i'/\partial x_i = 0$. In homogeneous isotropic turbulence, the transverse structure function $D_{NN}(r)$ can hence be expressed as a function of $D_{LL}(r)$ only by [5]

$$D_{NN}(r) = D_{LL}(r) + \frac{1}{2} r \frac{\partial}{\partial r} D_{LL}(r) \,. \tag{1.44}$$

Then, $D_{ij}(\boldsymbol{r})$ can be expressed in the inertial sub-range as [5]

$$D_{ij}(\boldsymbol{r}) = C_2(\epsilon r)^{2/3} \left(\frac{4}{3}\delta_{ij} - \frac{1}{3}\frac{r_i r_j}{r^2} \right) \,. \tag{1.45}$$

At last, it should be noted that not only do many length scales depend on the variance of the velocity fluctuations but also many length scales such as the integral length scale as well as the Taylor micro-scales.

The Energy Dissipation Rate

In the framework of K41 and the energy cascade, the energy dissipation rate is a fundamental quantity in turbulence. Turbulent kinetic energy is dissipated into heat at the smallest scales of the flow by friction. Here, the rate of energy dissipation will be introduced with the help of an energy budget equation for a fluid parcel of a fixed volume and density ρ.

To derive a budget equation for the energy density, the Navier-Stokes equations, Eq. (1.3), are multiplied with $\boldsymbol{u}$, which yields [42]

$$\frac{\partial u^2/2}{\partial t} = -\nabla \cdot \left[\left(\frac{u^2}{2} + \frac{p}{\rho}\right) \cdot \boldsymbol{u}\right] + \frac{\partial}{\partial x_j}\left(2\nu u_i S_{ij}\right) - \underbrace{2\nu S_{ij} S_{ij}}_{\epsilon_0 \geq 0}\,, \tag{1.46}$$

where $S_{ij} = (\partial u_i/\partial x_j + \partial u_j/\partial x_i)/2$ is the strain-rate tensor and $u^2/2$ the turbulent kinetic energy per unit mass of the fluid. The first term on the right-hand side (rhs) of Eq. (1.46) is due to the convection of energy across the boundary of the fluid parcel. In addition, the work of fluid parcel deformation due to pressure forces and viscous stress at the boundary of the fluid parcel is captured by the second and third term, respectively [42]. The last term on the right-hand side of Eq. (1.46) is the only term, which is non-negative, hence acting as a global sink. We can identify this term with the instantaneous energy dissipation rate per unit mass [42]

$$\epsilon_0 = 2\nu S_{ij} S_{ij}\,. \tag{1.47}$$

However, Kolmogorov's phenomenology from 1941 is based on the volume-averaged mean energy dissipation rate, which is given by

$$\epsilon \equiv \langle \epsilon \rangle = \langle \epsilon_0 \rangle = \langle 2\nu S_{ij} S_{ij} \rangle\,. \tag{1.48}$$

In homogeneous isotropic turbulence, this equation simplifies to [5]

$$\langle \epsilon \rangle = \nu \left\langle \frac{\partial u_i}{\partial x_j} \frac{\partial u_i}{\partial x_j} \right\rangle = 15\nu \left\langle \left(\frac{\partial u_1}{\partial x_1}\right)^2 \right\rangle\,, \tag{1.49}$$

where the rhs equation can be applied to one-dimensional time-records of the longitudinal velocity in order to estimate the mean energy dissipation rate.

Refined similarity hypotheses

Kolmogorov's phenomenology from 1941 relates velocity statistics to the mean energy dissipation rate. However, it can be anticipated that the energy dissipation rate depends on local velocity gradients considering, e.g., Eq. (1.47), which are strongly fluctuating resulting in heavy tails of their probability distribution functions (PDF) [5, 42, 48]. The strong fluctuations being localized in the flow is attributed to the phenomenon of intermittency, which Kolmogorov accounted for in his refined similarity hypothesis [5].

Kolmogorov restated the first and second similarity hypothesis in 1962 by conditioning velocity statistics on the locally volume-averaged energy dissipation rate. In his refined similarity hypothesis, Kolmogorov defines the locally volume-averaged energy dissipation rate field [49]

$$\langle \epsilon_0(\boldsymbol{x},t)\rangle_R = \frac{3}{4\pi R^3}\iiint_{\mathcal{V}(R)} \epsilon_0(\boldsymbol{x}+\boldsymbol{r},t)\mathrm{d}\boldsymbol{r}\,. \tag{1.50}$$

which were assumed to be log-normally distributed [5]. A consequence is that the scaling exponents of the structure functions change [5]

$$\zeta_n = \frac{1}{3}n\left(1-\frac{1}{6}\mu(n-3)\right)\,, \tag{1.51}$$

where $\mu = 0.25$ is the intermittency exponent resulting in $\zeta_2 = 2/3 + 1/36$ being referred to as K62-scaling in the following.

1.2.5 The Atmospheric Boundary Layer

The purpose of this section is to introduce the definition of the virtual potential temperature θ_v and the Richardson number, which are both important quantities for characterizing the stability of the atmospheric boundary layer. In addition, this section is meant to emphasize the dynamic structure of the lower atmospheric boundary, i.e. of the sub-cloud layer and the cloud layer. The interested reader is kindly referred to [e.g. 40, 41, 50, 51] for more information on atmospheric boundary layers. In particular, the focus is on marine boundary layers.

The Earth's topography poses a boundary to the atmospheric flow where the lowest part, say up to an altitude of 3000 m, is influenced by processes at this boundary. Therefore, the unaffected part of the Earth's atmosphere is called the *free atmosphere* and the region below, the affected part by boundary processes on time scales of an hour or less is the boundary layer [40]. Boundary layers above the ocean are known as marine boundary layers. Marine boundary layers develop slowly in time because, at the bottom, the sea surface temperature is approximately constant over the diurnal cycle due to strong mixing in the oceanic top layers as well as the large heat capacity of water [40]. In marine boundary layers, forcing is mainly due to frictional drag, heat transfer and phase transitions such as condensation and evaporation manifesting themselves in the presence of clouds (cf. Fig. 1.1). Therefore, one can divide the boundary layer into a sub-cloud layer and a cloud layer as shown in Fig. 1.1. Both frictional drag leading to wind shear as well as thermals of rising warmer air drive turbulence in the atmospheric boundary layer. The largest eddies of the turbulent flow scale with the boundary layer depth h [40]. As turbulence is orders of magnitude more effective in transporting heat or moisture, e.g., than diffusivity, the evolution of boundary layers is coupled to turbulence [40]. The evolution of the sub-cloud layer depth can be captured by a mass budget at the cloud base comprising (i) dry and warm air entrainment in the sub-cloud layer denoted by E in Fig. 1.1, (ii) large-scale vertical motion W and (iii) the vertical mass flux M at cloud base due to convection [9, e.g.].

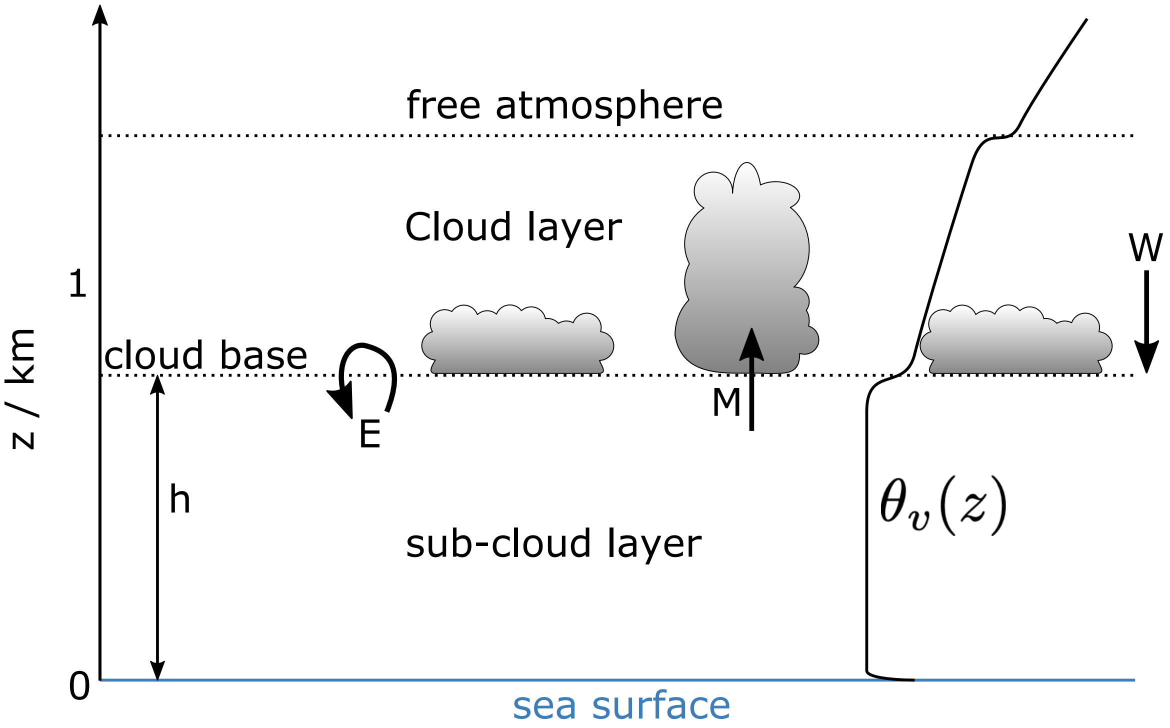

Figure 1.1 Sketch of the atmospheric boundary layer and main physical processes affecting its depth h. $\theta_v(z)$ is the virtual potential temperature as a function of altitude z. E, M and W are the top entrainment velocity, M is the convective mass flux out of the sub-cloud layer and W is the large-scale vertical velocity at $z = h$, respectively.

Warm air is less dense than colder air due to thermal expansion causing air parcels to rise that are warmer than the environment. These air parcels are positively buoyant. In the atmosphere, the temperature of vertically moving air parcels also changes (adiabatically) because of pressure changes. This effect is compensated by the so-called potential temperature for dry air [2]

$$\theta = T \left(\frac{p}{p_0}\right)^{(1-\gamma)/\gamma} , \tag{1.52}$$

where γ is the adiabatic constant of dry air and $p_0 = 1000\,\mathrm{hPa}$ is the reference pressure. However, the atmosphere is not dry. Instead, air comprises liquid water, ice and water vapor where the latter is less dense than air. Here, we focus on unsaturated air so that ice and liquid water are not taken into account. In this context, one can define a re-scaled potential temperature at which the density of dry air would equal that of moist air. This temperature is the so-called virtual potential temperature [2, 41]

$$\theta_v = \theta(1 + 0.61q)\,, \tag{1.53}$$

where $q = \rho_v/\rho$ is the specific humidity with the water vapor density ρ_v and the dry air density ρ. It is apparent from Eq. (1.53) that $\theta_v \leq \theta$ so that the virtual potential temperature is always larger than the potential temperature resulting in larger buoyancy.

Static stability of boundary layers is usually expressed in terms of buoyancy. If an air parcel is vertically shifted in altitude and relaxes back into its original position due to buoyant forces, the boundary layer is considered to be statically stable. In case the virtual potential temperature of a vertically shifted air parcel is identical to the ambient, the ambient air is statically neutral. Otherwise, if buoyant forces cause the air parcel to further move away from its original position, the boundary layer is statically unstable. Static stability expresses itself in a positive vertical gradient of $\theta_v(z)$. Turbulent mixing in the sub-cloud layer causes $\theta_v(z)$ to be constant with height resulting in a so-called mixed layer. More precisely, $\theta_v(z)$ is the mean temperature from cooler air parcels at the bottom and warmer air parcels at the top of the mixed layer. The homogenized $\theta_v(z)$-profile causes a sharp increase in $\theta_v(z)$ at the top of the mixed layer, which is statically stable and known as temperature inversion. Hence, the atmospheric boundary layer is usually topped by a stably stratified layer.

In a stably stratified boundary layer, vertical motions of air parcels are prone to buoyant restoring forces, which consequently suppress vertical motions [40]. Besides being buoyancy-driven, turbulence in the boundary layer is also generated by wind shear. It is hence possible that the effect of vertical shear is stronger than stratification. The gradient Richardson number quantifies the relative importance of stratification and vertical wind shear and can be expressed as [40, p.176 ff]

$$\mathrm{Ri} = \frac{\frac{g}{\langle\theta_v\rangle_z}\frac{\partial\langle\theta_v\rangle_z}{\partial z}}{\left(\frac{\partial\langle U_1\rangle_z}{\partial z}\right)^2 + \left(\frac{\partial\langle U_2\rangle_z}{\partial z}\right)^2}\,, \tag{1.54}$$

where g is gravity, $\langle\cdot\rangle_z$ a vertical average and U_1, U_2 the horizontal mean wind components. It has been shown that flows are turbulent for $\mathrm{Ri} < \mathrm{Ri}_c \approx 0.25$ where Ri_c is the critical Richardson number. For $\mathrm{Ri} > 1$, turbulent static stability of the atmosphere suppresses vertical turbulent motions [40, 52, and references therein]. The different regimes are summarized in Table 1.1.

In practice, vertical gradients are approximated by finite differences, which yields the bulk Richardson number [40, p.176 ff]

$$\mathrm{Ri} = \frac{g}{\langle\theta_v\rangle}\frac{\Delta\langle\theta_v\rangle_z/\Delta z}{\left(\Delta\langle U_1\rangle_z/\Delta z\right)^2 + \left(\Delta\langle U_2\rangle_z/\Delta z\right)^2}\,, \tag{1.55}$$

where Δ is the difference across altitude. Note that the critical Richardson number is only valid for the gradient Richardson number [40]. Reasonable Richardson numbers

Regime	characteristics
$\mathrm{Ri} < 0$	unstable stratification, turbulent
$0 < \mathrm{Ri} < 0.25$	stable stratification, turbulent
$0.25 < \mathrm{Ri} < 1$	turbulent
$\mathrm{Ri} > 1$	stable stratification, non-turbulent

Table 1.1 Atmospheric Stability and presence of turbulence in different regimes of the gradient Richardson number Ri_G. Values are taken from [52].

in the atmosphere are $\mathcal{O}(\mathrm{Ri}) \sim 10$ [41].

At last, the energy dissipation in turbulent flows is related to viscosity (cf. Eq. (1.47), as an example). Due to stratification, the density and air temperature is a function of altitude affecting the viscosity of the fluid. The density of moist air and dynamic viscosity η is obtained using CoolProp [53]. Then, the kinematic viscosity can be calculated by

$$\nu = \eta/\rho\,, \tag{1.56}$$

where ρ is the density and η the dynamic viscosity.

1.2.6 Random Error of Time-Average

It is evident from section 1.2.4 that many turbulence characteristics, such as the turbulent kinetic energy, the mean energy dissipation rate ϵ or longitudinal integral scale L_{11}, depend on the variance of longitudinal velocity fluctuations $\langle u_1'^2\rangle$. Considering one-dimensional velocity measurements in time in the streamwise direction of a statistically stationary turbulent flow, the variance of velocity fluctuations $\langle u_1'^2\rangle$ is defined by $\langle u_1'^2\rangle_\tau = \langle (u_1(t) - \langle u_1(t)\rangle_\tau)^2\rangle_\tau$ where τ is the duration of the averaging window. This implies that the accuracy of $\langle u_1'^2\rangle$ depends on the accuracy of the time-averaged longitudinal velocity $\langle u_1(t)\rangle_\tau$. For an infinitely long averaging window with $\tau \to \infty$ and assuming a statistically stationary turbulent flow, the time-averaged velocity *converges* to the mean velocity with $\lim_{\tau\to\infty}\langle u_1\rangle_\tau = \langle u_1\rangle = U$. In this case, the one-dimensional time-record of the velocity is *ergodic*. More detailed information about averages is presented in section 3.2.1.

In simulations or laboratory experiments, it is possible to approximate such statistically stationary and homogeneous turbulence. Consequently, longer runtime of the simulations or longer measurement periods in laboratory experiments improves the convergence of velocity statistics. In contrast, atmospheric turbulence is influenced by the diurnal cycle and large-scale variability ("synoptic conditions"). Under many atmospheric conditions, this large-scale variability is expressed by the so-called *spectral gap* in the power spectrum of one-dimensional velocity fluctuations at frequencies $\sim 1/\mathrm{h}$ [e.g. 40, 54]. Hence, the upper bound on a suitable averaging window is $\sim 1\,\mathrm{h}$ [55]. Thus, the question arises of how *accurately* the mean velocity and variance of velocity fluctuations can be determined.

At first, the random error of mean velocity estimates is derived. Considering one-point velocity time-records of a stationary turbulent flow, the mean velocity can be estimated by time averaging. For a finite averaging window τ, the time-average of a one-dimensional velocity time-record is defined by [e.g. 41]

$$\langle u_1 \rangle_\tau = \frac{1}{\tau} \int_0^\tau \mathrm{d}t u_1(t) \,. \tag{1.57}$$

The random error can be captured in terms of the estimation variance as given by [41]

$$\left\langle (\langle u_1(t) \rangle_\tau - U)^2 \right\rangle = \left\langle \left(\frac{1}{\tau} \int_0^\tau \mathrm{d}t u_1(t) - U \right)^2 \right\rangle = \left\langle \left(\frac{1}{\tau} \int_0^\tau \mathrm{d}t u_1'(t) \right)^2 \right\rangle \,, \tag{1.58}$$

where U is the true mean velocity of the flow and $u_1'(t) = u_1(t) - U$ according to Reynolds averaging. In the case of stationary turbulence, equation (1.58) can be rewritten in terms of the longitudinal auto-correlation (coefficient) function $\rho(t-s) = \langle u_1'(t) u_1'(s) \rangle / \langle u_1'^2 \rangle$ by [e.g. 41]

$$\left\langle (\langle u_1(t) \rangle_\tau - U)^2 \right\rangle = \frac{\langle u_1'^2 \rangle}{\tau^2} \int_0^\tau \mathrm{d}t \int_0^\tau \mathrm{d}s \, \rho(t-s) \,. \tag{1.59}$$

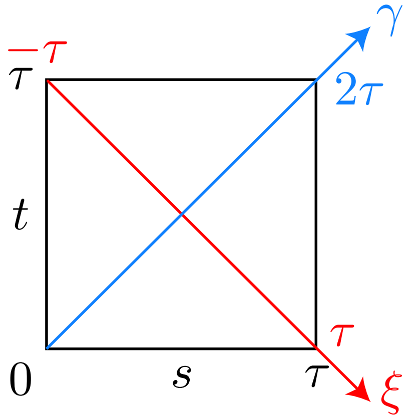

Figure 1.2 Visualization of substitution by $\xi = t - s$ and $\gamma = t + s$ to reduce Eq. (1.59) to a single integral in terms of initial integration variables t and s where τ denotes the averaging window.

Assuming that $u_1'(t)$ is ergodic and stationary, $\rho(t-s)$ is symmetric and can be described by one variable only [56]. Hence, the previous double integral, Eq. (1.59), can be simplified to a single integral by substituting $\xi = t - s$ and $\gamma = t + s$ [41]. Taking into account that $t, s \in [0, \tau]$, it follows that $\xi \in [-\tau, \tau]$ and $\gamma \in [0, 2\tau]$ as shown by Fig. 1.2 [1]. Furthermore, the integration boundaries need to be determined. Integrating

---

[1] Personal communication Michael Wilczek

ξ from $-\tau$ to τ poses a condition on γ. To illustrate this, γ can be expressed in terms of ξ by (i) $\gamma = 2t - \xi$ or (ii) $\gamma = 2s + \xi$. Considering the case $s = t = \tau$ on the line $\xi = 0$ and recalling that $\gamma \in [0, 2\tau]$, the latter is only fulfilled for (i) $0 \leq \xi \leq \tau$ or (ii) $-\tau \leq \xi \leq 0$, respectively. For the maximum available range of γ along the line $\xi = 0$, where $s = t$, the above conditions lead to $\gamma = 2t - |\xi|$ due to symmetry so that the upper limit of the integral over γ is given by $2\tau - |\xi|$. Similarly, for $s = t = 0$ at opposite ends of the line $\xi = 0$, (i) $\gamma = -\xi$ or (ii) $\gamma = +\xi$, which leads to the lower integration boundary $\gamma = |\xi|$ due to $0 \leq \gamma \leq 2\tau$. Then, Eq. (1.59) can be written as

$$\begin{aligned}
\left\langle \left(\langle u_1(t) \rangle_\tau - U \right)^2 \right\rangle &= \frac{1}{2} \frac{\langle u_1'^2 \rangle}{\tau^2} \int_{-\tau}^{\tau} \mathrm{d}\xi \int_{|\xi|}^{2\tau - |\xi|} \mathrm{d}\gamma \rho(\xi) \\
&= \frac{\langle u_1'^2 \rangle}{\tau^2} \int_{-\tau}^{\tau} \mathrm{d}\xi (\tau - |\xi|) \rho(\xi) \\
&= \frac{2\langle u_1'^2 \rangle}{\tau^2} \int_{0}^{\tau} \mathrm{d}\xi (\tau - \xi) \rho(\xi) \,, \\
&= \frac{2\langle u_1'^2 \rangle}{\tau} \int_{0}^{\tau} \mathrm{d}\tau \left(1 - \frac{\xi}{\tau} \right) \rho(\xi) \,, \qquad (1.60)
\end{aligned}$$

where the second-last equation follows from the symmetry of $\rho(\xi)$ in ξ. Given that the integral time scale T_{11} exists and is finite, Eq. (1.60) yields for $\tau \to \infty$ [41]

$$\left\langle \left(\langle u_1(t) \rangle_\tau - U \right)^2 \right\rangle \approx \int_0^\infty \mathrm{d}\xi \rho(\xi) = \frac{2\langle u_1'^2 \rangle T_{11}}{\tau} \,. \qquad (1.61)$$

Equation (1.61) is the estimation variance of the mean velocity U due to a finite averaging window τ. In relative terms, i.e. considering $\langle (\langle u_1(t) \rangle_\tau - U)^2 / U^2$, this equation shows that the estimation variance increases with turbulence intensity $\sqrt{\langle u_1'^2 \rangle}/U$ and integral time scale T_{11}. The averaging variance decreases with the averaging window τ motivating the importance of long averaging windows.

Secondly, one can derive a systematic error for estimating the variance of a stationary and ergodic velocity time-record [56, 57]. Considering a velocity fluctuation time record with vanishing (ensemble) mean, i.e. $\langle \langle u_1'(t) \rangle_\tau \rangle = 0$, the variance estimate based on the averaging window τ reads [e.g. 56]

$$\langle u_1'^2 \rangle_\tau = \frac{1}{\tau} \int_0^\tau \mathrm{d}t \left(u_1'(t) - \langle u_1'(t) \rangle_\tau \right)^2 = \frac{1}{\tau} \int_0^\tau \mathrm{d}t_1 \left(u_1'(t_1) - \frac{1}{\tau} \int_0^\tau \mathrm{d}t_2 u_1'(t_2) \right)^2 . \qquad (1.62)$$

On average, Eq. (1.62) yields [e.g. 56]

$$\begin{aligned}
\Big\langle \langle u_1'^2 \rangle_\tau \Big\rangle &= \left\langle \frac{1}{\tau} \int_0^\tau \mathrm{d}t \, \left(u_1'(t) - \langle u_1'(t)\rangle_\tau\right)^2 \right\rangle \\
&= \left\langle \frac{1}{\tau} \int_0^\tau \mathrm{d}t u_1'^2(t_1) - 2u_1'(t)\langle u_1'(t)\rangle_\tau + \langle u_1'(t)\rangle_\tau^2 \right\rangle \\
&= \langle u_1'^2 \rangle \frac{1}{\tau} \int_0^\tau \mathrm{d}t - 2 \left\langle \left(\frac{1}{\tau} \int_0^\tau \mathrm{d}t u_1'(t) \right)^2 \right\rangle + \left\langle \left(\frac{1}{\tau} \int_0^\tau \mathrm{d}t u_1'(t) \right)^2 \right\rangle \\
&= \langle u_1'^2 \rangle - \left\langle \left(\frac{1}{\tau} \int_0^\tau \mathrm{d}t u_1'(t) \right)^2 \right\rangle \\
&= \langle u_1'^2 \rangle - \frac{2\langle u_1'^2 \rangle T_{11}}{\tau} \, , \qquad (1.63)
\end{aligned}$$

where$\langle u_1'^2 \rangle$ is the true variance. In consequence, the estimation variance of the mean velocity (Eq. (1.61)), which can be regarded as a random error, causes a systematic underestimation of the variance. From Eq. (1.63), we can also estimate the relative systematic error of the variance estimate, which is given by Eq. (3.41) and used in Sec. 3.3.4.

To summarize, I define $\langle u_1(t) \rangle_\tau$ to be converged if the estimation variance of the mean, Eq. (1.61), is much smaller than the variance for $\tau \gg T_{11}$. I define $\langle u_1'^2 \rangle_\tau$ to be converged if the systematic error is much smaller than the random error, which are both defined by Lenschow, Mann, and Kristensen in [56] for $\tau \gg T_{11}$.

1.3 Cloud microphysics

This work focuses on warm clouds, which are free of ice. Hence, warm clouds are particle-laden flows, where the air temperature is warmer than 0 °C and water is either in the liquid or vapor phase. Here, before introducing important parameters with respect to cloud droplet-turbulence interaction, some aspects of cloud droplet growth are summarized. For more detailed information, the interested reader is kindly referred to [4, 21, 23, 26].

1.3.1 Cloud Droplet Growth due to Condensation

Cloud droplets initiate in super-saturated environments when water vapor condenses on a cloud condensation nucleus (CCN), which are aerosols such as sea salt particles in marine environments. After being activated, cloud droplets can grow up to $\delta_p \sim 30\,\mu\mathrm{m}$ by condensation the growth rate for an isolated droplet is given by [4, 23]

$$\frac{\mathrm{d}d_p}{\mathrm{d}t} = \gamma \frac{2s}{d_p} \, , \qquad (1.64)$$

where $s = e/e_s - 1$ is the super-saturation, e the vapor pressure, e_s the saturation vapor pressure and γ a function of ambient pressure and temperature. In consequence of the inverse relationship between droplet diameter and the growth rate (in terms of d_p), the droplet size distribution tends towards narrow distribution with increasing mean droplet diameter $\bar{d}_p$ around $\bar{d}_p$ [4]. This is also captured by a time-evolution equation for the droplet size distribution [23]. In unsaturated air, where $s < 0$, the droplet diameter decreases with time. The evolution of the saturation field can be captured by [4]

$$\frac{\mathrm{d}s}{\mathrm{d}t} = Au_3 - \frac{s}{\tau_s}\,, \tag{1.65}$$

where A is a temperature-dependent thermodynamic variable, u_3 is the vertical velocity, $\tau_s \propto (n\bar{d}_p)^{-1}$ is the phase relaxation time, n the cloud droplet number concentration and $\bar{d}_p$ the mean droplet diameter. The first term in Eq. (1.65) describes adiabatic cooling (heating) due to ascent (descent) [4]. The second term represents the change in s due to droplet growth. On the one hand, condensation (evaporation) transfers water vapor (liquid water) into liquid water (water vapor). On the other hand, latent heat release heats (cools) the ambient air coupling to the supersaturation [4]. It should be noted that Eqs. (1.64) and (1.65) apply in the cloud core and do not account for fluctuations of supersaturation, e.g. due to mixing. It has been shown that cloud droplets can be activated even in, on average, sub-saturated air [58].

Besides the mean droplet diameter, another central quantity for quantifying clouds emerged in the brief summary above - the cloud droplet number concentration being defined as [59]

$$n = N/V\,, \tag{1.66}$$

where N is the total number count of cloud droplets and V is the sampling volume. In many cloud probing instruments, e.g. cloud droplet probes, the sampling volume is given by $V = uA\Delta t$ where u is the relative wind speed, A is the measurement cross-sectional area and Δt is the sampling time interval. Similarly, the number concentration can be defined for each diameter bin by

$$n(d_i \leq d_p < d_{i+1}) = N(d_i \leq d_p < d_{i+1})/V\,, \tag{1.67}$$

where $N(d_i \leq d_p < d_{i+1})$ is the number count of droplets in the diameter range d_i to d_{i+1}.

1.3.2 Cloud Droplet - Turbulence Interaction

The following considerations are not only valid for cloud droplets but also for other (spherical) particles in a turbulent flow. Some notions refer to particles in general (e.g. particle relaxation time). Hence, in the scope of this thesis, cloud droplets and particles both refer to cloud droplets.

Cloud droplets are dispersed in turbulent flows obeying the Navier-Stokes equations (Eqs. (1.3) and (1.2)). Several forces act on a cloud droplet in a turbulent environment, among which are viscous drag, gravitational settling, added mass and the Basset-Boussinesq force [26, 60]. As cloud droplet diameters are on the order of $\mathcal{O}(d_p) \sim 10\,\mu\mathrm{m}$, they are much smaller than the Kolmogorov length scale of the turbulent flow $\mathcal{O}(\eta_K) \sim 1\,\mathrm{mm}$. Furthermore, the density of ambient air is much smaller than the density of liquid water ($\rho \ll \rho_l$, where ρ is the air density and ρ_l is the density of liquid water). Taking into account both limits for cloud droplets, the equation of motion of cloud droplets can be modeled in terms of gravity and Stokes drag [26]

$$\dot{\boldsymbol{u}}_p = \frac{1}{\tau_p}(\boldsymbol{u}(\boldsymbol{x},t) - \boldsymbol{u}_p) + \boldsymbol{g}\,, \tag{1.68}$$

where τ_p is the particle relaxation time, which is defined as [26]

$$\tau_p = \frac{2}{9}\frac{(d_p/2)^2}{\nu}\frac{\rho_l}{\rho}\,, \tag{1.69}$$

where ν is the kinematic viscosity. The particle relaxation time is a measure for how fast the cloud droplet kinematics respond to changes in the flow $\boldsymbol{u}(\boldsymbol{x},t)$. The relevant time scale for changes at small scales of the flow is the Kolmogorov time scale τ_K, Eq. (1.13). A comparison of the particle relaxation time and the Kolmogorov time yields the Stokes number [26]

$$\mathrm{St} = \tau_p/\tau_K\,. \tag{1.70}$$

The Stokes number is a measure for the inertia of cloud droplets. If $\mathrm{St} \ll 1$, particles behave like tracers. If $\mathrm{St} \gg 1$, the finite particle inertia causes particles to move relative to the ambient flow $\boldsymbol{u}(\boldsymbol{x},t)$. For $0.1 \lesssim \mathrm{St}$, cloud droplets can be slung out of strong vortices, which is known as the “sling effect” [28]. The sling effect can cause cloud droplet trajectories of nearby droplets to cross each other increasing the chance for cloud droplet collisions [28]. Due to intermittency and the relation to strong vortices, sling events occur more frequently in high R_λ turbulent flows [61]. Experimentally, it has been found that cloud droplets with $\mathrm{St} \gtrsim 0.1$ are inhomogeneously distributed in space leading to cloud voids [39] and clustering [62].

In still air, i.e. $\boldsymbol{u}(\boldsymbol{x},t) = 0$, the cloud droplet is accelerated by gravity only. With the initial condition $\boldsymbol{u}_p(t=0) = 0$, the cloud droplet velocity can be integrated to $\boldsymbol{u}_p = \boldsymbol{u}_T(1 - \exp(-t/\tau_p)$ with $\boldsymbol{u}_T = \tau_p\boldsymbol{g}$. To compare the impact of gravitational settling to cloud droplet inertia, the terminal velocity u_T is related to the Kolmogorov velocity scale u_K, Eq. (1.14). This velocity ratio yields the non-dimensional settling velocity parameter [4]

$$\mathrm{Sv} = \frac{u_T}{u_K}\,. \tag{1.71}$$

In a cloud with $\langle\epsilon\rangle \sim 1 \times 10^{-2}\,\mathrm{W/kg}$, $\nu \sim 1.5 \times 10^{-5}\,\mathrm{m^2/s}$ and $d_p \sim 30\,\mathrm{\mu m}$, the Stokes number $\mathrm{St} \sim 0.07$ is smaller than the non-dimensional settling velocity parameter $\mathrm{Sv} \sim 1.4$ highlighting the importance of gravity [4].

Collision-Coalescence

Cloud droplets can not only grow by condensation but also by collision-coalescence, which is crucial for the rapid onset of precipitation in warm clouds but is also related to rare events [26, 63]. As an example, droplet growth due to gravitational collection occurs at a rate of $\sim 1 \times 10^{-4}/\mathrm{s}$ for a collector droplet with $d_p = 12.5\,\mathrm{\mu m}$ in a background of $10\,\mathrm{\mu m}$-droplets assuming that 3% of geometric collisions lead to coalescence [26]. Geometrically, collision-coalescence requires two droplets with diameters d_1 and d_2 to be within a sphere of diameter $D = d_1 + d_2$ [26]. In addition to geometric constraints, hydrodynamic droplet-droplet interactions and surface properties must allow for coalescence [4]. Taking the three previous requirements into account, the collection kernel, which is the important quantity for determining collision-coalescence rates, can be written as [4]

$$K_{12} = \Gamma_{12} E(d_1, d_2)\,, \tag{1.72}$$

where $E(d_1, d_2)$ is the collision efficiency [64, e.g.] and Γ_{12} the collision kernel. The collision kernel Γ_{12} is proportional to D^2 and to the relative velocity of two droplets so that it is enhanced in case of intersecting trajectories of nearby cloud droplets [4, 26]. Furthermore, Γ_{12} is enhanced in the case of clustered cloud droplets resulting in shorter inter-particle distances [26]. Note that not all geometric collisions, i.e. where two droplets are closer than $D/2$, lead to coalescence in practice. This is because of a disturbance flow that one droplet induces in the neighborhood of another droplet [4]. To overcome this flow perturbation, cloud droplets must be horizontally closer than $D/2$ resulting in the collision efficiency $E(d_1, d_2) = y_c^2/(d_1/2 + d_2/2)^2$ where y_c is the critical inter-droplet distance for coalescence [4, e.g.].

Chapter 2

The Max-Planck-Cloudkites

In this chapter, I introduce three instruments of the Max Planck Cloudkite Observatory that are relevant to this thesis. These instruments, the Max Planck Cloudkite+ (MPCK+), the mini-Max Planck Cloudkite (mini-MPCK) and the micro-Max Planck Cloudkite (micro-MPCK) are specially developed to provide insight into cloud microphysics from the large atmospheric scales $\sim 100\,\mathrm{m}$ down to the Kolmogorov scale, which is a fraction of $1\,\mathrm{mm}$. This chapter is organized as follows: first, I motivate the need for balloon-borne measurements and shortly present the MPCK+. Afterwards, I introduce the mini-MPCK in terms of requirements, scientific instrumentation, mechanical design and in-field operation in Secs. 2.3.1 to 2.3.4. In Sec. 2.4, exemplary data from the operation during the EUREC^{4}A field campaign is shown which serves as the basis to assess the performance of the mini-MPCK. This chapter is closed with a discussion and outlook with respect to a revised version of the mini-MPCK in Sec. 2.5.

It is planned to submit parts of this section as an instrument paper on the Mini-MPCK to the journal Atmospheric Measurement Techniques. Gholamhossein Bagheri, Eberhard Bodenschatz and I conceived and designed the Mini-MPCK. Gholamhossein Bagheri and I assembled the Mini-MPCK. Gholamhossein Bagheri, Freja Nordsiek, Antonio Ibañez Landeta and I wrote the control software. Eberhard Bodenschatz, Gholamhossein Bagheri, Freja Nordsiek, Oliver Schlenczek, Johannes Güttler, Antonio Ibañez Landeta and I performed *in-situ* measurements and collected the data, which was supported by Marcel Meyer, Andreas Kopp, Andreas Renner and Artur Kubitzek. Mechanical parts and electronics were developed in collaboration with and manufactured by the in-house machine shop and scientific electronics, respectively.

2.1 Introduction

Clouds determine the energy balance of the Earth's atmosphere, its radiation budget and the hydrological cycle [12, 13]. The lack of detailed understanding of clouds is a main source of uncertainty in weather forecasting and climate modeling [65, and references therein]. It is not yet quantitatively understood how rain is initiated in

---

[0] Interested readers are referred to [37] for detailed information.

warm, i.e. ice-free, clouds and how warm rain initiation is connected to the cloud's surroundings [20, 26]. One of the most prevailing questions in climate modeling concerns the sensitivity of trade-wind cumuli to changes in environmental conditions [6]. In general, clouds are dispersed droplets or ice particles in a turbulent flow spanning a wide range of spatial and temporal scales from micrometers to km and milliseconds to hours [3]. At small scales, cloud particles interact with the flow and grow or decay due to localized fluctuations of temperature and humidity [4, 23]. At intermediate scales, entrainment and mixing is generated by turbulence [66]. Both small-scale and intermediate-scale processes are coupled to large scales of the cloud via buoyancy and drag forces [67].

The multiscale properties of the turbulent flow with typical Taylor-scale Reynolds numbers $\mathcal{O}(10^4)$ in combination with moisture and temperature transport, phase transitions, and inertial particle dynamics present a challenge for modeling and parameterization in large-eddy simulations (LES), e.g. [4, 68–73]. A fully-resolved direct numerical simulation (DNS) does not rely on parameterizing small-scale processes but demands 10^{18} grid points for a time period of at least 10 min in order to capture the cloud evolution over at least one characteristic eddy turn-over time [31]. Even nowadays, this approach is still far beyond any computational power which is why recent numerical approaches combine DNS and LES [70]. Laboratory experiments provide a controlled and steady environment reaching atmospheric Taylor-scale Reynolds numbers although they do not reproduce atmospheric conditions in their complexity [among others 36, 74, 75]. This is why atmospheric field measurements serve as needed compliments to simulations and laboratory experiments [76–78].

Trade-wind cumuli dynamically evolve during their life cycle, which is related to turbulent processes such as entrainment and mixing [33, 79]. Entrainment and mixing processes have been described by the transition length scale from inhomogeneous to homogeneous mixing $l^* \sim \epsilon^{1/2}\tau_{\mathrm{react}}^{3/2}$ where ϵ is the mean energy dissipation rate inside the cloud and τ_{react} the time scale of the phase change such as cloud droplet evaporation or the super-saturation time scale. In highly turbulent clouds with $\epsilon \sim 10^{-2}\,\mathrm{W/kg}$ and $\tau_{\mathrm{react}} \sim 1\,\mathrm{s}$ [80], the transition length scale was found $l^* \sim 0.1\,\mathrm{m}$. To resolve these entrainment and mixing processes of (trade-wind) cumulus clouds and to assess the impact on the cloud droplet size distribution, highly resolved measurements in time and space of both turbulence and cloud droplets are needed [29].

While *in-situ* measurements on towers or mountain tops guarantee the best spatio-temporal resolution, ground-based measurements are fixed in location, limited in altitude and experimental sites on mountain tops are affected by topography [54, 81–84]. Despite that remote sensing is able to characterize the large-scale environment, it is limited in resolution and needs *in-situ* measurements for calibration [85–87]. Radiosondes lifted by weather balloons provide valuable insight into the vertical structure of the atmospheric boundary layer and high flexibility with respect to the launching location [e.g. 88–90]. However, they are not suitable for cloud evolution studies because they are advected by the atmospheric flow and cannot be kept at constant altitude.

In contrast, aircraft-borne measurements are nearly fully uncorrelated with the atmospheric flow due to a high relative wind speed ($\mathcal{O}(100\,\mathrm{m/s})$ and are conducted within the atmospheric boundary layer, i.e. far away from the topography. On the one hand, Taylor's hypothesis (introduced in Sec. 3.2.1) is advantageously fulfilled. On the other hand, the high relative wind speed impedes high spatial resolution in the millimeter to decimeter scale [52]. The relative wind speed of unmanned aerial vehicles (UAV) and helicopters ($\sim 20\,\mathrm{m/s}$) is lower than that of aircraft although helicopters are usually not allowed to enter clouds due to safety regulations [91, 92]. Therefore, *in-situ* measurements are limited to cloud tops unless the cloud is shallow [8, 92]. Furthermore, helicopter-borne measurements usually require a minimal relative wind speed in order to keep the instrument out of the rotor's downdraft. During nighttime, both helicopters and aircraft have major safety issues when flying at low altitude above ground. Furthermore, aircraft, helicopters and unmanned aerial vehicles have a limited operation time due to battery capacity so probing the atmospheric boundary layer over the diurnal cycle is usually not possible [93, 94].

Tethered aerostats and kites can be operated in windy and calm atmospheric conditions and they probe the atmospheric boundary layer below, inside and above clouds if allowed by the net lift. They are able to measure at a constant altitude, vertically profile the atmospheric boundary layer along the ascends and descends or, combining the two previous flight strategies, perform staircase flights. In particular, they are used to measure atmospheric turbulence, cloud microphysics, solar radiation and fluxes of heat moisture and momentum up to a few km above Mean Sea Level (MSL) [94–104]. However, tethered aerostats can only be operated in moderate wind conditions up to $\mathcal{O}(10\,\mathrm{m/s})$ [e.g. 98]. In the past, aerostats have been deployed from research vessels proving the high mobility of this experimental approach [e.g. 105]. Compared to aircraft, the operation of balloons is fairly inexpensive [104]. The spatio-temporal resolution of balloon-borne measurements is ~ 10 times higher than that of aircraft for comparable sampling rates thanks to the low relative wind speed of $\mathcal{O}(1\,\mathrm{m/s}) - \mathcal{O}(10\,\mathrm{m/s})$. The measurement duration is only limited by disk space or battery capacity [106].

Here, we use specially developed scientific instruments, the Max-Planck-Cloudkite + (MPCK+), the mini-Max-Planck-CloudKite (mini-MPCK), and the micro-Max-Planck-Cloudkite (micro-MPCK) to characterize atmospheric turbulence and cloud microphysics with high spatial and temporal resolution down to the micro-meter scale. Being relatively lightweight instruments, they are deployed by tethered helium-filled and kite-stabilized balloons ("helikites", manufactured by Allsopp Helikites Ltd). During the EUREC^{4}A field campaign in the Caribbean from January to February 2020, the mini-MPCK was operated on RV Meteor and RV Maria S. Merian over the Atlantic Ocean during day and night with a flight duration up to 15 h. The MPCK+ was deployed on RV Maria S. Merian and the micro-MPCK on RV Meteor. Compared to aircraft, helicopters, or satellites, their operation is inexpensive. To minimize flow distortions by the helikite, the mini-MPCK can be mounted on the main line 50 m below the helikite.

In this chapter, I introduce all three specially developed scientific instruments while concentrating on the mini-MPCK. Regarding the mini-MPCK, the principal ideas on the design and our choices in the instrumentation are presented in Sec. 2.3. Then, we assess the performance of the mini-MPCK with the help of first data records from the EUREC^{4}A field campaign and comparisons of redundant measurements in Sec. 2.4. Finally, we will provide an outlook on design improvements in Sec. 2.5.

2.2 Max Planck Cloudkite+

Climate models and weather predictions still suffer from an insufficient understanding of cloud processes such as moist convection and cloud formation [65]. The vast range of spatio-temporal scales of atmospheric and cloud dynamics, which is due to its turbulent nature, is a major challenge in resolving such processes [3]. However, turbulence is conjectured to be at the core of many small-scale processes in clouds such as mixing and rain initiation in warm clouds [19, 26]. Fundamental questions are:

- How does turbulent mixing due to turbulent entrainment inside a cloud evolve as a function of time and space? Is the mixing predominantly homogeneous or inhomogeneous?
- How does turbulence affect relative droplet velocity statistics and distribution of droplets in space?
- If globally present in clouds, how important is mixing and inertial clustering?
- How do cloud microphysics vary in time and space?

Providing answers to these questions by *in-situ* measurements requires the smallest relevant scales of the turbulent flow and cloud features to be resolved. Therefore, the Mobile Cloud Observatory (MCO) specially developed an airborne scientific instrument, the Max Planck Cloudkite+ (MPCK+) as shown in Fig. 2.1. The interested reader is referred to [37] for a detailed description of both the helikite, the MPCK+ and the operational procedure whereas only a short summary is presented here.

The MPCK+ is specially developed for measuring atmospheric turbulence and cloud microphysical quantities simultaneously. Therefore, the MPCK+ is equipped with instruments that measure cloud droplet sizes, shape and spatial distributions as well as the atmospheric state (air temperature and relative humidity) and wind (Fig. 2.1). The remotely controlled MPCK+ is powered by a battery that lasts for about 30 min with all imaging instruments running and several hours with only non-imaging instruments running. The imaging instruments are the Particle Image Velocimetry (PIV) and holography system (Fig. 2.1), which sample 1.6 L/s and 1.7 L/s of air, respectively. Decisive for the MPCK+ design is to fully capture the coupling between cloud microphysics and turbulence. This is why the overlap of sampling volumes between, especially, the holography (droplet sizes and three-dimensional spatial distributions) and the PIV (two-dimensional droplet velocities and two-dimensional droplet spatial distribution) is crucial. This overlap is illustrated in Fig. 2.1 by the green

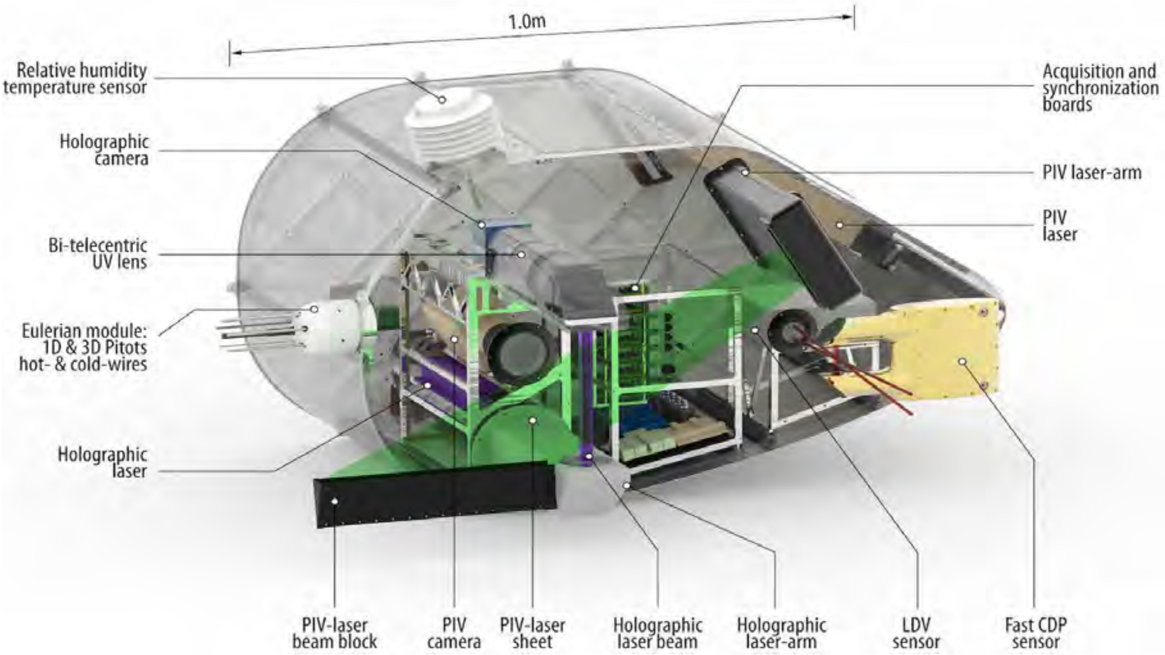
1.0m
Relative humidity temperature sensor
Holographic camera
Bi-telecentric UV lens
Eulerian module: 1D & 3D Pitots hot- & cold-wires
Holographic laser
Acquisition and synchronization boards
PIV laser-arm
PIV laser
PIV-laser beam block
PIV camera
PIV-laser sheet
Holographic laser beam
Holographic laser-arm
LDV sensor
Fast CDP sensor

Figure 2.1 Visualization of the Max Planck Cloudkite + (MPCK+) and its main scientific instruments: the combined holography and PIV unit. The PIV is operated at 15 Hz with a probing volume of 23 cm × 15 cm × 0.3 cm (green laser sheet) whereas the holography is operated at 75 Hz with a probing volume of 1.5 cm × 1.5 cm × 10 cm (violet laser column). The Fast Cloud Droplet Probe (Fast CDP) measures cloud droplet sizes in the range 1.5 µm to 50 µm. The Laser Doppler Velocimetry sensor (LDV) was not operated during EUREC^{4}A . The wind speed is measured by a pitot tube at 100 Hz. Fluctuations of the wind speed and air temperature are measured by a hot- and cold-wire, respectively, at ~ 10 kHz. Relative humidity and air temperature are measured at < 10 Hz.

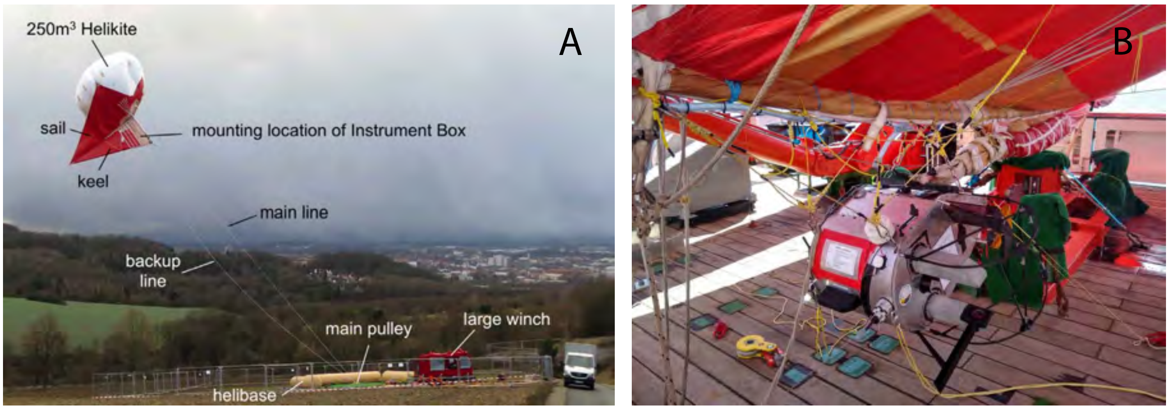

Figure 2.2 The 250 m^3 helikite at the airfield next to the Max Planck Institute for Dynamics and Self-organization (A) and at the rear of RV Maria S. Merian during EUREC^{4}A (B). A: Besides the scientific instrumentation, the main components of the setup are the winch, the main line, the backup line and the 250 m^3 helikite. Initially, it was planned to mount the MPCK+ at the keel of the 250 m^3 helikite. B: The MPCK+ is hang from the 250 m^3 helikite at the front during EUREC^{4}A .

laser sheet (PIV, wavelength 532 nm) and violet laser column (Holography, wavelength 355 nm).

The MPCK+ is carried by a tethered helikite consisting of a 250 m^3 helium-filled balloon and a kite where the keel is 15 m long (Fig. 2.2). The helikite can lift a net payload of 50 kg at an altitude of 1 km above mean sea level (MSL). At the airfield next to the Max Planck Institute for Dynamics and Self-organization (Fig. 2.2A), the 250 m^3 helikite is held by a main tether (“main line”) and a backup tether (“backup line”). The main tether is guided by a main pully and spooled by a large winch, which is anchored to the ground. Originally, the MPCK+ was planned to be mounted at the keel of the 250 m^3 helikite. During the EUREC^{4}A field campaign, the MPCK+ was hung from the helikite at the front in order to simplify the attachment and de-attachment process (Fig. 2.2B). Being an airborne instrument that is pulled by a research vessel, it is possible to sample individual clouds of interest with the MPCK+. Another advantage of tethered aerostats is the low relative wind speed. Together with the high sampling rate of the imaging instruments, the low relative wind speed allows for measurements of cloud features at very high spatio-temporal resolution while the smallest resolved scales are comparable to the Kolmogorov scales of the turbulent flow. As an example, the cloud edge can be resolved with an accuracy below the low decimeter scale at relative wind speeds of $\sim 10\,\mathrm{m/s}$. Furthermore, it is possible to continuously sample the cloud volume with both PIV and holography if the relative wind speed $< 1\,\mathrm{m/s}$.

To summarize, the MPCK+ is a mobile instrument that can be operated in remote regions of the globe. The MPCK+ is equipped with a, to my knowledge and up to now, unique PIV/holography combination to acquire highly resolved measurements inside clouds. The MPCK+ measurements allow for unraveling cloud droplet - turbulence interactions, e.g. the existence of spatial clustering, which is crucial for understanding rain formation in warm clouds and their radiative characteristics.

2.3 The mini-Max-Planck-CloudKite

The mini-Max-Planck-Cloudkite (mini-MPCK) is a scientific instrument, which is specially developed to characterize atmospheric turbulence inside clouds and in the cloud-free atmosphere, as well as to measure cloud droplets. The mini-MPCK is designed to answer the following questions:

- How do environmental conditions such as the diurnal cycle, surface temperature, surface structure or temperature profiles affect atmospheric turbulence?
- What is the energy dissipation rate inside clouds and at the cloud edge?
- How do large-scale circulation interact with cloud-scale processes and how do they influence cloud microphysics?
- How are cloud droplets spatially distributed?
- What are the key differences between precipitating and non-precipitating clouds in terms of turbulence characteristics?
- How much does moist convection affect the formation and evolution of clouds?
- How do phase changes affect moist convection?

In this section, we will first explain the design requirements for the mini-MPCK that follow from the questions above. Then, we will shortly report on the scientific instrumentation, the mechanical design and the operation of the mini-MPCK.

2.3.1 Design requirements

Characterizing atmospheric turbulence and cloud microphysics requires measurements of various quantities. Under both cloud-free and cloudy conditions, the mini-MPCK is designed to measure the wind vector, wind speed variations, air temperature, and relative humidity, as well as cloud microphysical quantities and droplet numbers and diameters. To relate turbulence and cloud microphysical measurements to environmental conditions, static air pressure, air temperature and relative humidity have to be recorded. Furthermore, high spatio-temporally resolved measurements of relative humidity and air temperature (RHT) are not only crucial to measure vertical RHT profiles but also to measure heat and moisture transport in the atmosphere or to determine the evolution of supersaturation inside clouds [e.g. 51, 58, 107]. For all measurements, basic quantities are the time and location of the measurement. As an example, vertical profiles of thermodynamic quantities require the altitude of the platform. As each sensor measures in the platform frame of reference, they have to be converted into the earth frame of reference. As an example, it is important to rotate the wind vector and wind speed measurements from the platform frame of reference into the earth frame of reference as the wind velocity and wind speed measurement are relative to the platform motion, as mentioned in Sec. 2.3.2. Therefore, accurate platform position, velocity, orientation (roll, pitch and yaw) and angular velocity measurements are needed, too. The instrument is designed for redundant measurements using independent measurement principles (e.g., wind measurements using sonic and pressure-based anemometry) to identify systematic errors by the measurement principle.

Measuring the air temperature and relative humidity inside clouds and in the atmosphere is challenging because of the particle-laden environment and radiation. Impinging droplets potentially moisturize the RHT sensors. In the case of unheated RHT sensors, the RHT measurement of air is useless until the sensor is dry. Further challenges arise from salt contamination which is likely in marine boundary layer measurements after 5 min to 60 min exposure and which causes the sensors to remain wet down to $\approx 30\%$ relative humidity [108]. Note that the relative humidity is a monotonically decreasing function of the air temperature which is why the bias in the air temperature measurement also affects the relative humidity. If the instrument and the RHT sensors are exposed to radiation, the instrument and RHT sensors heat up. In consequence, the temperature measurement is overestimated and the RH measurement underestimated due to the thermal mass of the instrument as well as the sensor and heat exchange with the ambient air. Therefore, the RHT sensors need protection against radiation and cloud droplets, which still ensures sufficient ventilation.

The mini-MPCK is supposed to characterize atmospheric turbulence and cloud microphysical parameters by *in-situ* measurements being deployed on a helikite (Fig. 2.3). The helikite is held by the main tether, which is inclined to about 45° in equilibrium. The main line is rolled up on a winch which is anchored to the ground thereby holding the helikite in place. There are two possibilities to lift the mini-MPCK by a helikite. On the one hand, the mini-MPCK can be attached to the helikite directly. On the other hand, as shown in Fig. 2.3, the mini-MPCK can be attached to the main tether at the center of mass which minimizes the flow distortion by the helikite. This way, it is ensured that the mini-MPCK is balanced. Conducting air-borne *in-situ* measurements with a helikite results in three important requirements. First, the mini-MPCK must be sufficiently light so that the helikite still provides enough lift to reach cloud altitudes, i.e. flight altitudes higher than 900 m above ground. In the case of the 75 m^3 helikite, the static lift at sea level is 35 kg (114 kg for a 250 m^3 helikite). Second, to achieve an accurate measurement of higher-order wind velocity statistics, the mini-MPCK must be able to measure at least 30 min at an eddy turnover time of $\sim$ 10 min in the sub-cloud layer [56]. Much longer measurements of at least 12 h duration are required to capture the diurnal cycle of the boundary layer and clouds. Hence, the capacity of the battery must be larger than 22 Ah because the power consumption of the mini-MPCK is 50 W when the CDP2 is constantly running. Note that the maximal power consumption of the CDP2 can be as high as 120 W temporally. Third, the sensor and control electronics need a waterproof housing against dust, splash water, and water droplets.

The mini-MPCK runs autonomously and without remote control. In the field, we want to get instantaneous information on multiple measurement quantities, e.g. the mean relative wind speed, flight altitude and location for flight safety to just name a few. These parameters are helpful to maneuver the helikite according to the chosen flight strategy. If necessary, we also need to access the mini-MPCK remotely for manual operation once it is in the air. For this reason, a radio link is needed as indicated by the wifi symbol in Fig. 2.3.

2.3.2 Instrumentation

As mentioned above, the mini-MPCK is designed primarily for the characterization of cloud microphysics and atmospheric turbulence. Table 2.1 gives an overview of the sensors installed in the mini-MPCK. All measured quantities except cloud droplet diameter d_p, droplet number N_p, droplet interval time Δt_p, acoustic temperature T_{acoustic}, wind vector $\boldsymbol{u}$, and liquid water content LWC are measured with at least two different sensors. Here, we give an overview of our choice of scientific sensors. The main requirements were serial interface to be compatible with the Max-Planck-Cloudkite Protocol (Sec. 2.3.4), voltage range 3 V to 23 V, a compact design and low weight and power device.

Wind vector and speed

The three-dimensional wind vector $\boldsymbol{u} = \boldsymbol{v}_p - \boldsymbol{v}$ relative to the platform, where $\boldsymbol{v}_p$ is the platform velocity and $\boldsymbol{v}$ the flow, is required by a sonic anemometer (hereafter referred to as “sonic”). Here, we use the uSonic3 Class A MP manufactured by Metek GmbH at a sampling rate of 30 Hz. Advantageously, it measures the vertical velocity in the platform frame of reference directly by 3 independent measurement paths, hence attaining a high accuracy of the vertical velocity. The accuracy of the wind measurement decreases with the angle of attack due to shadow effects of the transducers [109]. We also shortened the sonic in order to save weight and to shrink the mini-MPCK. In consequence, we had to sacrifice orientation data by the sonic. Furthermore, the electronics were rearranged so that they occupied less space.

The relative wind speed $u = |\boldsymbol{v}_p - \boldsymbol{v}|$ is measured by the Pitot Static System PSS-8$^{\text{TM}}$manufactured by Simtec AG (hereafter called “PSS8”) with a sampling rate of 100 Hz. Assuming that the platform is always aligned with the predominant wind direction, which is chosen to be the $\boldsymbol{e}_1$-direction, $u = \sqrt{u_1^2 + u_2^2 + u_3^2} \approx u_1$ in the platform frame of reference if $u_1 \ll u_{2,3}$.The measurement error of the dynamic pressure due to misalignment between the sensor and the mean wind direction is below 2.5% for angles of attack (or side slip) between ±25°. The relative wind speed is further measured by a hot-wire anemometer (55P16 miniature wire probe, mini-CTA, Dantec Dynamics) at a sampling rate of 8×10^3 Hz. The analog signals are converted to digital signals by a LabJack T7 OEM.

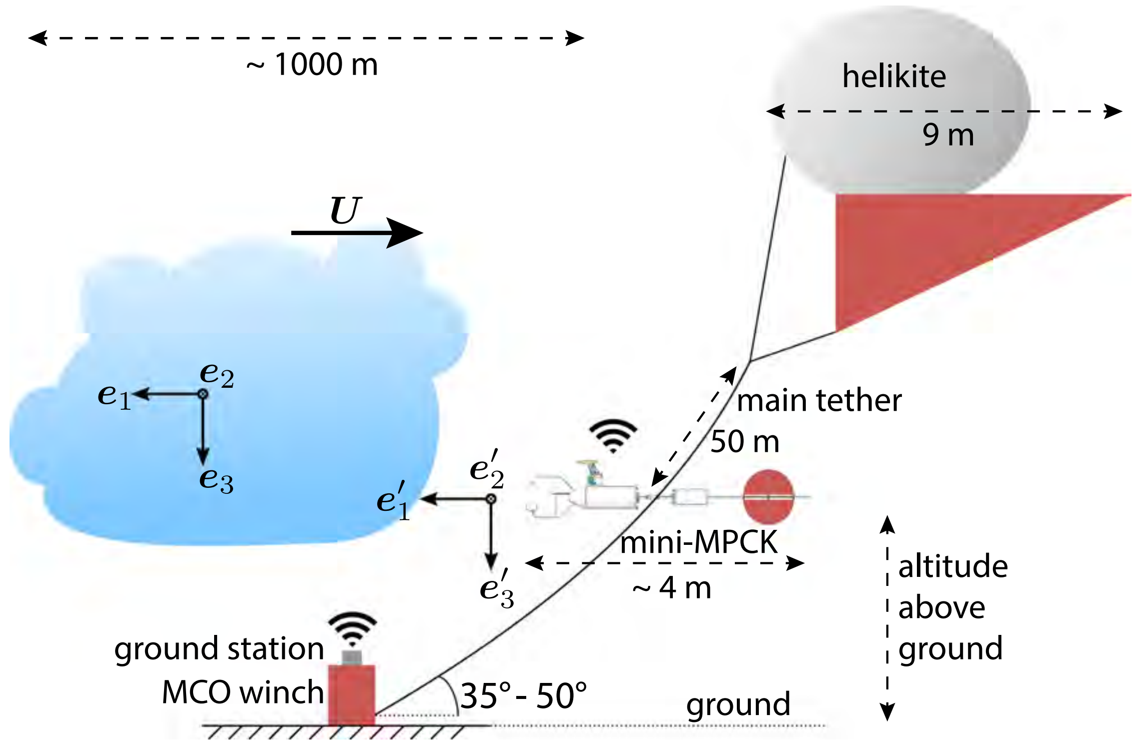
~ 1000 m
helikite
9 m
$\boldsymbol{U}$
$\boldsymbol{e}_1$
$\boldsymbol{e}_2$
$\boldsymbol{e}_3$
$\boldsymbol{e}'_1$
$\boldsymbol{e}'_2$
$\boldsymbol{e}'_3$
main tether
50 m
mini-MPCK
~ 4 m
altitude
above
ground
ground station
MCO winch
35° - 50°
ground

Figure 2.3 Overview of operating the mini-MPCK in the field. The winch of the Max Planck Observatory (MCO) is anchored to the ground, e.g. the deck of a research vessel in case of remote measurements from a research vessel on the ocean. The helikite ($75\,\mathrm{m}^3$ or $250\,\mathrm{m}^3$) is held by the main tether, which is rolled up by the winch. At maximal pull, the line is inclined by about 45° as drag and lift of the helikite balance tension of the main tether. The mini-MPCK carries all scientific instruments, records data inside clouds and cloud-free atmosphere in the platform frame of reference ($\boldsymbol{e}'_i$ where $i \in \{1,2,3\}$) and is supposed to orient itself to the mean wind $\boldsymbol{U}$ in the earth frame of reference ($\boldsymbol{e}_i$ where $i \in \{1,2,3\}$). The mini-MPCK is attached to the main tether 50 m below the helikite. The mini-MPCK is connected to the ground station via two radio links (433 MHz and 2.4 GHz). The sketch is unrealistically scaled for better visibility. The wifi symbol is copied from Keynote.

Category	Instrument	Manufacturer	Quantity	Range	Acquisition rate [Hz]	Annotations
Cloud droplets	Cloud Droplet Probe 2 UAV	Droplet Measurement Technologies, Inc.	d_p	2 µm to 50 µm	2	U from 10 m/s to 250 m/s
			N_p		2	lower bound of LWC
			Δt_p	up to 256 particles	1×10^6	
wind	mini-CTA	Dantec Dynamics	u'	> 0.2 m/s	8×10^3	$k_{\max}\eta_K \gtrsim 1$, bandwidth 10 kHz
	uSonic3 Class A MP	Metek GmbH	$\boldsymbol{u}$	0 m/s to 40 m/s	30	max. sampling rate 50 Hz
			T_{acoustic}	−40 °C to 60 °C	30	
	Pitot Static System PSS-8™	Simtec AG	u	0 m/s to 89.5 m/s	100	
			T	−60 °C to 70 °C		$\tau \sim 4\,\mathrm{s}@U10\,\mathrm{m/s}$
			p	238 hPa to 1080 hPa		
Relative humidity and air temperature	HMP7	Vaisala	T	−70 °C to 180 °C	0.2	$\tau \sim 15\,\mathrm{s}$
			RH	0 % to 100 %	0.2	
	AM2315	AOSONG	T	−70 °C to 180 °C	1	$\tau \sim 5\,\mathrm{s}$
			RH	0 % to 100 %	1	
	BMP388	Adafruit	T	−40 °C to 85 °C	1	$\tau \sim 0.005\,\mathrm{s}$
			p	300 hPa to 1250 hPa	1	sampling rate ≤ 200 Hz
position and orientation	Ellipse-N	SBG-Systems	s, θ, ϕ	0° to 360°	200	bandwidth magnetometer 110 Hz
			lat, lon, alt		200	
	ZED-F9P	u-blox		lat, lon, a	1	sampling rate ≤ 25 Hz
	BNO 055	Adafruit	ψ, θ, ϕ	0° to 360°	100	bandwidth magnetometer 20 Hz

Table 2.1 Instrumentation of the mini-MPCK. The measurement quantities are: cloud droplet diameter d_p, cloud droplet number count N_p, cloud droplet inter-arrival time Δt_p, wind vector $\boldsymbol{u}$, acoustic temperature T_{acoustic}, wind speed u (and wind speed fluctuations u'), temperature T, relative humidity RH, pressure p, platform orientation angles (roll ψ, pitch θ, yaw ϕ), platform position (latitude lat, longitude lon, GPS altitude, a) and liquid water content LWC. Both the webcam and the LWC probe were not operated (n.o.) during EUREC^{4}A field campaign. $k_{\max}$ is the largest resolved wavenumber, η_K is the Kolmogorov length scale, τ is the time constant (i.e. the response time for reaching 63% of the actual air temperature T), U the mean wind speed.

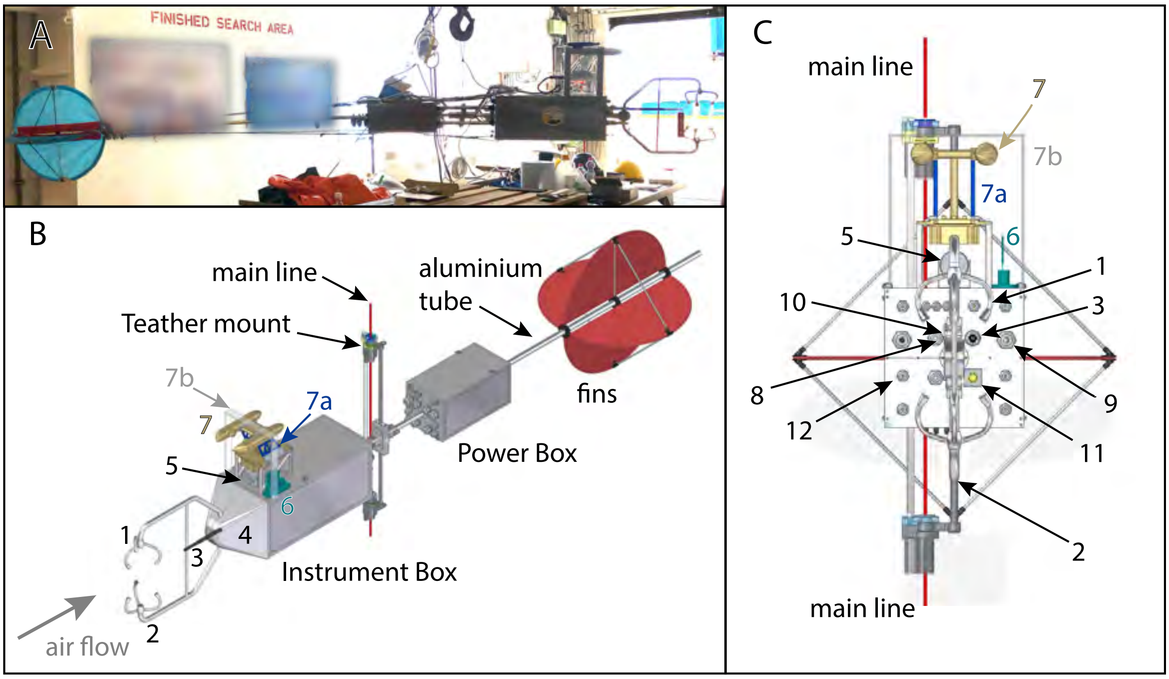
A
FINISHED SEARCH AREA
B
main line
aluminium tube
Teather mount
7b
7a
7
5
fins
Power Box
6
1
4
3
Instrument Box
air flow
2
C
main line
7
7b
7a
5
6
1
10
3
8
9
12
11
2
main line

Figure 2.4 The mini - Max Planck CloudKite (mini-MPCK). (A) The mini-MCPK is on RV Maria S. Merian during the EUREC^{4}A - ATOMIC field campaign in the Caribbean January to February 2020. Posters showing the members of the ship's and scientific crew are blurred to protect privacy. (B) Schematic view of the mini-MPCK consisting of an Instrument Box, Power box, fins, a centered aluminum tube, a tether moint and the main line. (C) Front perspective to visualize the sensor arrangement. The mini-MPCK is equipped with a sonic anemometer (1), a hot-wire anemometer (2), a pitot tube (3), a webcam (5), a liquid-water-content probe (6), three temperature and relative humidity sensors (8, 9, 11), an orientation sensor (10) and a UFT probe (12). Temperature and relative humidity sensors are shielded by the nose (4). The cloud droplet probe (7) is supported by aluminum structures (7a) and protected by a frame (7b).

Temperature and Relative Humidity

Here, we use the HMP 7 manufactured by Vaisala to record the air temperature (PT 100) and relative humidity (capacitive measurement) at a sampling frequency of 0.2 Hz. Supplementary RHT measurement is conducted with AOSONG AM2315 at 1 Hz. The AOSONG RHT sensors are calibrated as explained in [37]. The air temperature is further measured by the PSS8 temperature sensor (PT-100) at 100 Hz and by the BMP388 (Bosch, Adafruit) at 1 Hz. The uSonic3 Class A MP manufactured by Metek GmbH ("sonic") is able to measure the air temperature with a sampling frequency of 30 Hz indirectly via the measurement of the speed of sound in air as explained in Sec. 2.B.

Cloud Droplets

The Cloud Droplet Probe 2 UAV (CDP2) from Droplet Measurement Technologies Inc. is used to measure the size and number density of cloud droplets (2 µm to 50 µm in diameter) with a sampling rate of 2 Hz. The CDP2 also provides the cloud droplet inter-arrival time of up to 256 particles per sampling interval with a 1 µs temporal resolution. Due to the low relative wind speed, more than 99% of the totally measured particles is also recorded as particle-by-particle data (PbP-data) in typical shallow cumulus conditions with a cloud droplet number concentration of $\sim 100/\mathrm{cm}^3$ and mean relative wind $U \sim 10\,\mathrm{m/s}$. The CDP2 requires a wind speed between 10 m/s to 250 m/s. The measurement principle of the CDP2 is based on the forward scattering of a laser beam (wavelength 658 nm) by crossing cloud particles. The scattered light is projected through a 50/50 beam splitter onto two photodetectors (a qualifier and a sizer), where the detected intensity is used to size the particles. A disadvantage is that the CDP2 is not able to measure the velocity of the particles. However, the CDP2 is lightweight ($\approx 1.8\,\mathrm{kg}$ including power and data cables) and consumes $\lesssim 48\,\mathrm{W}$. Combining the droplet counts with the relative wind speed measurements, we obtain the droplet density $n = N_p/(\langle u\rangle A\Delta t)$, where $\langle u\rangle$ is the average relative wind speed, $A = 0.24\,\mathrm{mm}^2$ is the laser beam cross-section, and Δt is the sampling interval. It is possible to calculate the LWC using N_p and d_p. However, the LWC will most likely be underestimated since droplets smaller than 2 µm and larger than 50 µm will not be detected.

Position and Orientation

In addition to the time of measurement, it is essential to determine the platform position, orientation and rotation. To meet this demand, the mini-MPCK is equipped with an INS (Inertial Navigation System), which is a combination of a GNSS (Global Navigation Satellite System) and IMU (Inertial Measurement Unit). Here, we use an SBG Ellipse-N (manufactured by SBG Systems) containing an accelerometer, a gyro, a magnetometer, a pressure sensor and a single-band GNSS. Due to its sensor fusion logic, the SBG Ellipse-N is able to calculate angular velocities in real-time. The SBG position,velocity, orientation and angular velocities are sampled at 200 Hz.

Advantageously, it is very light (47 g) and small (46 x 45 x 24 mm). The SBG is the origin of the platform frame of reference which is why all momentum arms are given relative to the SBG Ellipse-N.

The SBG Ellipse-N GNSS position and velocity is backed up by the SparkFun GPS-RTK2 (sampling rate 1 Hz), which is equipped with a u-blox ZED-F9P together with a u-blox multiband antenna (ANN-MB Multi-band ANN-MB-00-00). Platform orientation and acceleration are additionally acquired by the BNO055 (Adafruit) at 100 Hz. The barometric altitude is redundantly recorded by the PSS8 (at 100 Hz)and the BMP388 (at 1 Hz).

2.3.3 Mechanical Design

The mini-Max Planck CloudKite (mini-MPCK) carries the scientific instrumentation as well as controllers and electronics, which enable the operation. A side view of the mini-MPCK on RV Maria S. Merian during the EUREC^{4}A field campaign as well as the instrument design is shown in Fig. 2.4. The mini-MPCK consists of two boxes. The instrument box houses all scientific sensors except for the backup GNSS (u-blox ZED-F9P). The scientific sensors are located at the upstream end of the mini-MPCK. They are placed as close as possible to each other in order to measure the same eddies on sub-meter scales. The maximal separation between all scientific sensors is between the sonic and the CDP2, which is $\approx$ 62 cm relative to the center of the measurement volume. The nose of the instrument reduces the pressure distortion close to the scientific sensors. The nose part further protects the RHT sensors against cloud droplets while ventilation is guaranteed by an array of holes. Furthermore, the nose is colored white to protect the sensors from radiative heating. The power box houses the battery, the power distribution electronics and the backup GNSS (u-blox ZED-F9P). Both boxes are connected by an axial aluminum tube. As the power box, fins (50 cm in diameter) and tether-mount can be shifted on the aluminum tube, it is possible to place the tether-mount in the center of mass. The instrument box, power box and fins are clamped to the aluminum tube. The tether-mount is fixed to the aluminum tube by grub screws in order to prevent a reduction of the mechanical stability of the aluminum tube.

To protect the electronics against water and dust, both sides of the power and instrument box have to be sealed while still remaining accessible, e.g. for maintenance. Therefore, all covers for the foreseen windows are circumferenced by a ridge. Analogously, all windows are framed by a marine silicon-filled groove. The sealing is accomplished by pressing the cover onto the marine silicon-filled groove frame by numerous screws. The feed-throughs for cables are tightened around each cable and, additionally, glued to the surface of the aluminum plate with silicon glue.

In addition, the instrument should orient itself in the mean wind direction so that the measured flow is not disturbed by the instrument itself. The alignment can be achieved by mounting the instrument below the kite-stabilized balloon. This can be done by using dyneema lines that connect the foreseen loops (eyelets) at the instrument box with hooks attached to the helikite's keel. If the flow distortion by the balloon has

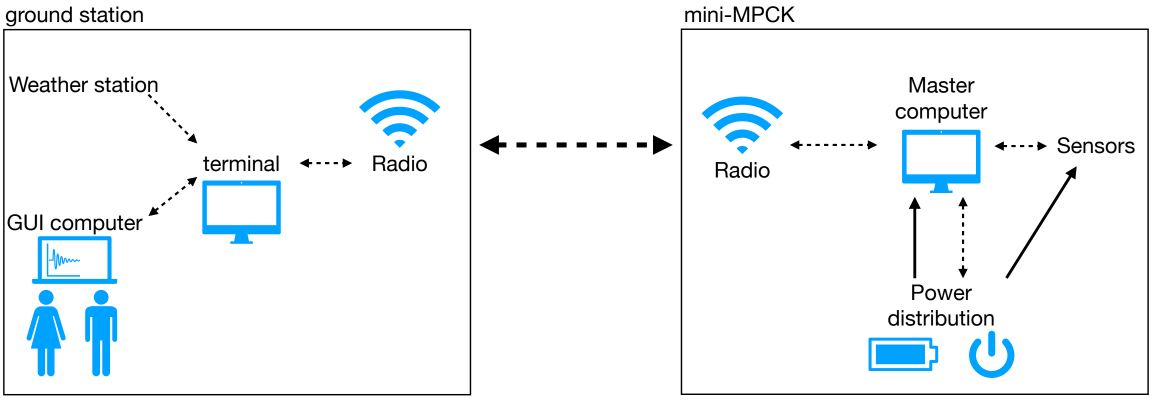

Figure 2.5 Schematic overview of the communication network. On the ground, the weather station sends meteorological data to the terminal in order to observe the local weather and electrical field. The terminal routes commands from the GUI computer to the mini-MPCK. The GUI computer also monitors meteorological data sent by the mini-MPCK via the radio-link. The mini-MPCK is controlled by the master computer. The master computer not only records the data acquired by the sensors, it also sends commands to the power distribution unit in order to provide the sensors with power. The power distribution unit comprises safety electronics for the battery, too, in order to prevent the battery to be under-charged. Dashed arrows correspond to a data link and solid arrows to a power connection. Symbols are taken from Keynote.

to be avoided, the instrument can be mounted on the main line, e.g. 50 m below the balloon. This approach asks for a combination of two additional features. The first feature is the tail of the instrument consisting of fins and a prolongation. The fins provide the aerodynamic force to orient the instrument into the mean wind direction where the prolongation enhances the momentum arm, hence improving the stabilization. The second feature is the line mount, which needs to allow for at least 180° of rotational freedom in the horizontal direction. As the line of the helikite stabilizes at an angle of ≈ 45° against the vertical in windy conditions, the tether-mount has to further allow for at least ≈ 90° so that the instrument can align itself in the vertical direction, too. To achieve a stable balance around the horizontal axis, the mini-MPCK is attached to the main line at its center of mass.

Finally, the mini-MPCK is a mobile and flexible instrument, which should be practical and easy to operate and to handle. In total, the mini-MPCK is shorter than 4 m and its weight amounts to ≈ 29 kg including the tether-mount. Therefore, it is short and light enough to be maneuvered in laboratories and on the deck of a research vessel by a reasonable number of persons. It should be noted that the mini-MPCK is designed independently of the carrying platform. In principle, if the tether-mount is exchanged by another mounting system, the mini-MPCK can also be operated from towers.

2.3.4 Operating the mini-MPCK remotely

In the field, we need instantaneous information on multiple measurement quantities, e.g. the mean relative wind speed, flight altitude, location for flight safety and for realizing the flight strategy. We also need to access the mini-MPCK remotely once it is in the air in order to operate it manually. For that reason, we implemented a network that comprises a ground station, the (airborne) mini-MPCK and a radio link as shown in Figs. 2.3 and 2.5. The central part of the ground station is the so-called terminal that monitors flight information of the airborne mini-MPCK and the electrical field to detect thunderstorms as lightning strikes impose a huge danger to operators near the main tether and to the experimental setup. On MSM89, the terminal also mapped the line tension of the main tether, which was measured by a tensiometer.

The Max-Planck-CloudKite Protocol (MPCK-P) handles the communication between the ground station and the mini-MPCK. More precisely, the terminal routes commands from the GUI computer to the airborne mini-MPCK and multiple measurement quantities from the airborne mini-MPCK to the GUI computer via the radio link. The radio link is established by radio modules of the ground station and radio modules on the mini MPCK platform. The primary communication link is the XBee (Zigbee-Module – 802.15.4 XBee ZB SMT manufactured by DIGI) at a frequency of 2.4 GHz with an antenna provided by TE Connectivity Laird (RF ANT 2.4GHZ/5.5GHZ WHIP TILT). The backup communication link is established by the RFM9x LoRa 433 MHz radio module (with an antenna from Antenova, model SREI038-S9P), which is connected to the power controller in the power box of the mini-MPCK.

The MPCK-P also handles the serial communication between the master computer (here DA1100 Series Rugged Embedded Computer manufactured by Cincoze) and the sensors where the measurement data are recorded as a function of computer time. To simplify the interface, we decided on serial communication (RS 232, RS 422, and RS 485) whenever possible. In addition, the master computer sends commands to the power controller (Arduino Feather M0 with 433 MHz LoRa Radio Module) setting the relais for providing the sensors with power. As most of the scientific sensors are “power-on”, they boot automatically and send data to the master computer via the serial interface. Usually, the mini-MPCK is operated in full acquisition mode, i.e. all connected sensors are switched on by default. In manual mode, each relais can be switched on or off. The entire system can be rebooted.

The backup radio link provides an essential safety feature as it permanently sends the GPS position to the terminal via the radio link. Importantly, the backup GPS (Zed-F9P) is read by the power controller. As the power controller is powered by a 3V backup battery, it continues to work independently of the master computer or the main battery. Even if the master computer or main battery fails, the power controller sends the GPS position to the terminal. A more detailed description of the communication network and radio links is presented in [37].

Research Cruise	Flight ID	UTC time takeoff	UTC time landing	duration [HH:MM]
RV Maria S. Merian (MSM89)	7	2020-02-05 12:43:00	2020-02-05 20:42:00	07:59
	10	2020-02-09 21:54:55	2020-02-10 18:43:00	20:48
	13	2020-02-13 01:05:32	2020-02-13 19:11:15	18:05
	15	2020-02-14 23:37:00	2020-02-15 19:06:43	19:29
	17	2020-02-16 10:28:00	2020-02-16 18:34:00	08:06
	19	2020-02-17 12:41:00	2020-02-17 18:11:00	05:30
RV Meteor (M161)	1	2020-01-24 21:38:40	2020-01-24 22:16:36	00:37
	3	2020-01-27 18:15:36	2020-01-27 20:55:58	02:40
	4	2020-01-28 15:17:14	2020-01-28 18:16:30	02:59
	5	2020-01-30 13:20:11	2020-01-30 18:38:02	05:17
	6	2020-01-31 01:54:00	2020-01-31 06:26:06	04:32
	7	2020-02-02 01:20:00	2020-02-02 13:00:00	11:40
	8	2020-02-03 17:15:44	2020-02-04 04:47:06	11:31
	9	2020-02-05 18:08:26	2020-02-06 13:00:00	18:51
	10	2020-02-06 13:24:30	2020-02-06 19:06:32	05:42

Table 2.2 Flight overview for the two mini-MPCKs on RV Maria S. Merian (MSM89) and RV Meteor (M161) during the EUREC^{4}A field campaign. The duration is the time from takeoff to landing. On RV Meteor, flight 2 did not record any data due to power failure. Flights 1 to 6, 8, 9, 11, 12, 14, 16, 18, and 20 on MSM89 were conducted with the Max Planck CloudKite + (MPCK+). During flight 11 on M161, which is not shown in the overview, the 75 m^3 helikite including the mini-MPCK were lost in strong wind gusts. Flight 12 on M161 was conducted with the micro-MPCK, which is not subject of this article.

2.4 Performance assessment during in-situ measurements

The mini-MPCK was deployed on two different platforms during the EUREC^{4}A field campaign, namely on a 250 m^3 helikite on RV Maria S. Merian and on a 75 m^3 helikite on RV Meteor [6, 38]. We briefly explain the working principle of the setup and present exemplary data records from the mini-MPCK research flights. In total, we performed eight research flights on RV Meteor (M161) and six on RV Maria S. Merian (MSM89) as shown in Table 2.2. On M161, the mini-MPCK primarily profiled the atmospheric boundary layer to characterize its turbulence while the crew on MSM89 prioritized measurements inside clouds. Hence, different flight strategies were performed.

2.4.1 In-field Operation aboard RV Meteor

In this section, we want to explain how measurements were conducted with the mini-MPCK on M161. The procedure is slightly different from the flight operation on MSM89 [37]. Figure 2.6A shows the 75 m^3 helikte aboard RV Meteor (M161) during the EUREC^{4}A field campaign in its "parking" position downstream of the research vessel. The helikite is held in place by the main tether. The perspective from the deck of RV Meteor is presented in Fig. 2.6B. The MCO winch controls the length of the main tether that is guided by a line guidance system. Its dimensions are chosen such that the main tether cannot tangle with the A-frame of RV Meteor or ship masts or antennas even at a tether inclination angle of $\approx 45°$.

During the launching and landing process, two more winches are needed because the mini-MPCK has to be (de-)attached to the main tether. Because of the structural stiffness, it is neither possible to pull the tether-mount through the line guiding system nor the mini-MPCK which is connected to the main tether as mentioned above. This problem is solved by the so-called "handling winch", which is connected to a support line being connected to the helikite directly. The handling winch serves to bring the helikite closer to the deck without pulling on the main tether. The other additional winch is located at the top bar of the A-frame. This winch pulls the main tether towards the MCO winch with the help of an additional pully so that the mini-MPCK can be easily connected (disconnected) to (from) the main tether during the launching (landing) process on the deck. Notably, the A-Frame is tilted towards the MCO winch as much as possible in order to generate more space for the process.

When the mini-MPCK is attached to the main tether, i.e. in flight, the flight altitude is regulated by controlling the length of the main tether with the help of the MCO winch. For flights 9 and 10 on M161, we used a mooring winch of RV Meteor instead. The general landing and launching procedure remained the same, though. Both on RV Meteor and RV Maria S. Merian, we profited from remote sensing instruments that could give us information on the cloud base and from radiosondes regarding the air temperature profiles [e.g. 38, 88]. This information was useful for the choice of flight strategy.

2.4.2 Flight Properties and Platform Motion

Airborne measurements with an aerostat like the helikites are flexible in operation. Not only are they capable of constant altitude flights, which is necessary when sampling mainly clouds, but they are also capable of atmospheric profiling. A combination of the two capabilities results in the staircase altitude profile. This flight strategy is advantageous for measuring (vertical) fluxes in the atmospheric boundary layer. Since the fluxes decrease linearly with altitude, two sufficiently long flight segments with constant altitude in the sub-cloud layer are sufficient to determine the flux profile [56, 110]. Since the cloud base is variable in height, it is safe to choose the highest flight distance in the sub-cloud layer at least 100 m below the cloud base. As mentioned earlier, the cloud base was known a priori based on the remote sensing instruments (radar) during our ship-based measurements during the EUREC^{4}A field campaign.

The primary purpose of the mini-MPCK on RV Meteor was to characterize atmospheric turbulence and measure vertical fluxes in the sub-cloud layer. Clouds were sampled whenever they were present and the dynamic lift of the helikite was sufficient to reach altitudes of 800 m above mean sea level (MSL). Therefore, we performed staircase flights, as exemplified by the barometric altitude record in Fig. 2.7A. The mean altitude of the constant altitude $\langle z_{\mathrm{PSS8}} \rangle_T$ flights is shown by the black dashed lines, where PSS8 refers to the pitot tube. The standard deviation of barometric altitude during constant altitude flight segments increases from 5 m for low altitudes

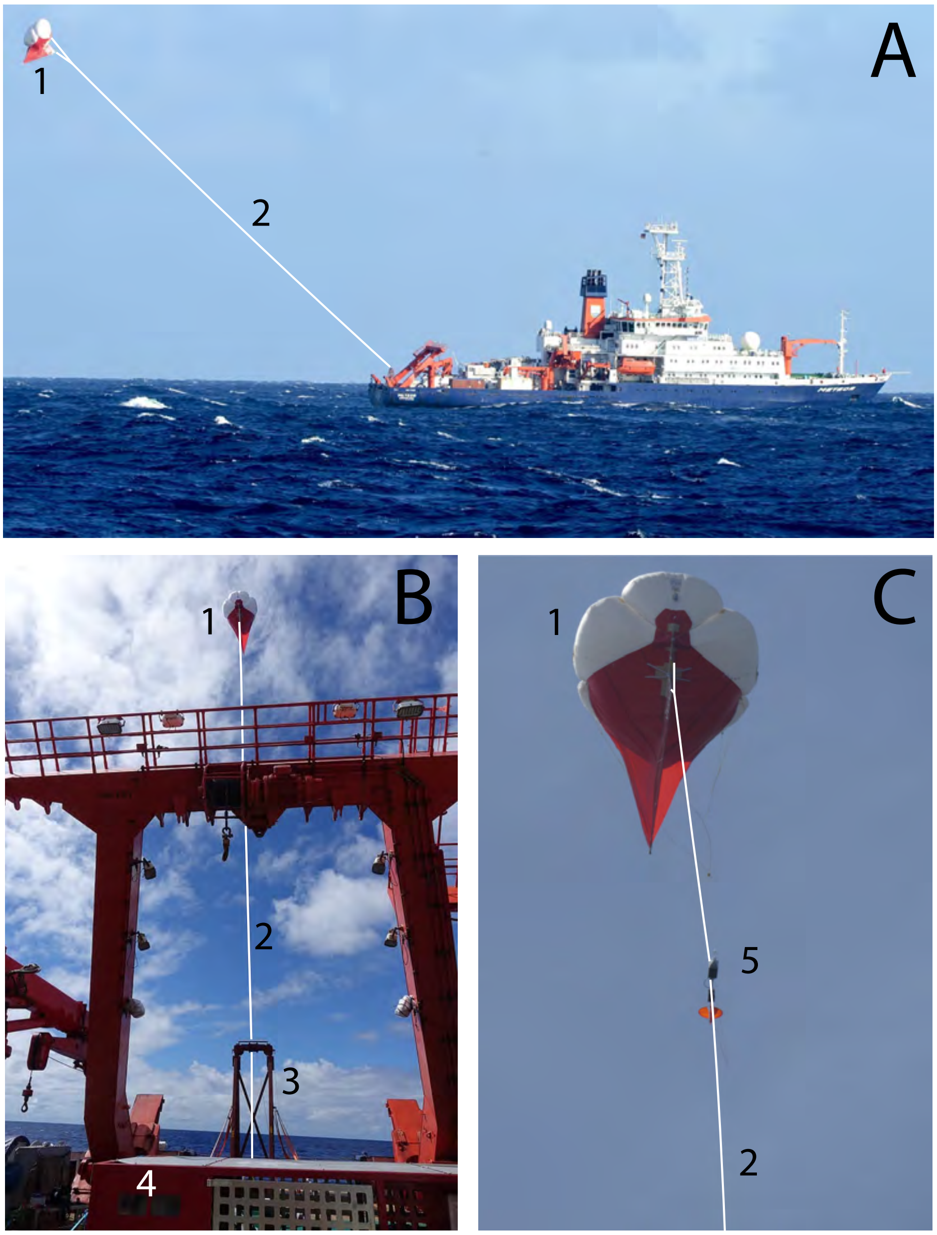

Figure 2.6 The Helikite launched aboard the RV Meteor during the EUREC^{4}A - ATOMIC field campaign in the Caribbean January to February 2020. (A) Side view of the 75 m^3 Helikite (1) in its parking position at 50 m altitude above MSL. The Helikite is anchored to the rear of RV Meteor by the main line (2). (B) Perspective from the deck of RV Meteor. The Helikite (1) is connected to the winch (4) via the main line (2). The line guiding system (3) prevents the line from entangling in the ship's structures such as the A-frame or various cranes. (C) The Helikite (1) lifts the mini-MPCK being attached to the main line (2).

$\approx 200\,\mathrm{m}$ above MSL to 25 m for high altitudes of $\approx 1\,\mathrm{km}$ above MSL. Cloud events, i.e., when the number of cloud particles N_d is greater than 30 0.5 s, are represented by blue dots. The inset of Fig. 2.7A shows a map where the position of the mini-MPCK is represented by red dots in terms of latitude and longitude. An overview of the flight time per altitude is shown in Fig. 2.7B. The lowest flight segment is at about 200 m above MSL, while the highest flight segment is concentrated at about 800 m above MSL, since this was the maximum altitude we could reach at the beginning of EUREC^{4}A in low wind conditions. Between flight segments, the mean ascent speeds are in the range of 0.18 m to 0.28 m, as shown in the left panel of Fig. 2.17. The mean descent rate is in the range of $-0.15\,\mathrm{m/s}$ to $-0.35\,\mathrm{m/s}$, with the slower descent rates due to the lower spooling speed of the RV Meteor mooring winch (dashed line) compared to the MCO winch (dashed line) in the right panel of Fig. 2.17.

The mini-MPCK on RV Maria S. Merian concentrated on cloud microphysical measurements. Therefore, the flight altitude was adjusted to be inside the cloud layer based on information gained by remote sensing. As an example, the altitude profile of flight 19 on RV Maria S. Merian (MSM89) is shown in Fig. 2.7C where the first clouds were encountered at $\sim 600\,\mathrm{m}$ and $\sim 1000\,\mathrm{m}$ above MSL. As the flight strategy was different, the total flight time per altitude accumulates at $\sim 800\,\mathrm{m}$ and $\sim 1200\,\mathrm{m}$ above MSL as shown in Fig. 2.7D.

We conducted airborne measurements with a kite-stabilized, helium-filled balloon, which orients itself to the mean wind direction with the help of a keel. Hence, the balloon is moving in the turbulent flow. As the mini-MPCK is not mounted on, e.g., a fixed mast, it is also prone to platform motions. If the mini-MPCK is mounted on the pre-tensioned main tether due to the aerodynamic drag, the system corresponds mechanically to a damped and driven pendulum. If the damping due to the tension of the main tether is low, the driving force exerted by balloon motions can excite pendulum motions of the mini-MPCK. The pendulum motion of the mini-MPCK on RV Meteor is visualized in Fig. 2.8A by the power spectral density of the roll rate PSD($\dot{\psi}$) which corresponds to angular accelerations. Notably, the tension on the main tether was low due to the limited lift of the $75\,\mathrm{m}^3$ helikite which is why the damping of the pendulum motion was small. We suggest that the pendulum motion of the mini-MPCK results in an oscillation around its equilibrium position (i.e. the connection to the tether-mount) at a frequency of $\sim 0.1\,\mathrm{Hz}$ due to the aerodynamic drag of the fins. The tether-mount itself allows for horizontal and vertical rotation as explained above so that oscillations are generally not dampened. The inset of Fig. 2.8A shows the correlation of $f_{\max}$ on the mean wind speed U per flight where $f_{\max}$ is the frequency of the global maximum of PSD($\dot{\psi}$) as indicated by dots.

In contrast, the tension of the main tether of the $250\,\mathrm{m}^3$ was much higher ($< 1\,\mathrm{t}$) on RV Maria S. Merian. On MSM 89, the mini-MCPCK was attached to the main tether only on flight 7. For all the other flights on MSM89, the mini-MPCK was mounted below the balloon on more than 4 attachment points. This is why PSD($\dot{\psi}$) for flight 7 also exhibits higher frequency modes as shown in Fig. 2.8B. All other flights (flights 10, 13, 15, 17, 19) decay after their global maximum at roughly 1 Hz. Thus, mounting the mini-MPCK below the main balloon not only shifted the global maximum of PSD($\dot{\psi}$) to higher frequencies, it also hindered higher-frequency oscillations, e.g. at $\approx 10\,\mathrm{Hz}$. The inset of Fig. 2.8B shows no correlation between $f_{\max}$ and the mean wind speed per flight.

The platform motion also affects the angle of attack $\alpha = \arcsin\left(\frac{u_3}{u}\right)$ where $u = \sqrt{u_1^2 + u_2^2 + u_3^2}$ and angle of sideslip $\beta = \arcsin\left(u_2/\sqrt{u_1^2 + u_2^2}\right)$, where $u_{1,2,3}$ are given in the platform frame of reference with the platform North (1), platform East (2) and platform Down (3). Both α and β are ideally close to 0°. Figure 2.9 shows α and β for M161 (A, B) and MSM89 (C,D) for each flight of the mini-MPCK. Considering M161 on RV Meteor, the angle of attack α (Fig. 2.9A) is reasonable for all flights but flights 1, 5 and 6. Flight 1 was a test flight where the static lift of the helikite was insufficient in wind-still conditions. As a result, the mini-MPCK could not be lifted out of the wake of RV Meteor and did not achieve to follow the turbulent flow. In flight 5, the CDP2 exerted a torque that the clamping mechanism on the rod could not withstand. As a result, the instrument was turned by ≈ 45°. Similarly, the box was still not stable against rotation on the rod in flight 6 even without CDP2. From flight 7 on, we strengthened the clamping mechanism with an additional improvised clamp. This attempt was successful and was even stable when the CDP2 was flown as well in flight 9 and 10. The angle of sideslip β (Fig. 2.9) differs significantly from 0° for each flight. This is due to the twist in the main tether and the limited horizontal rotational freedom of 270° only. It happened that the mini-MPCK was blocked on one end of the tether-mount even though we tried to clamp the tether-mount to the main tether with the largest dynamical range possible. Considering MSM89, α is only distributed around 0° in the case of flight 7, when the mini-MPCK was attached to the main line, and flights 10 and 13. The angle of sideslip is non-ideal in any flight despite that the mini-MPCK is mounted to the helikite. The angle of sideslip β is also affected by the mounting configuration (Fig. 2.9D) where flight 7 (tether-mount) differs from the other flights (10-19) where the mini-MPCK is hung from the main spare of the $250\,\mathrm{m}^3$ helikite. We attribute these differences to both the mounting configuration and the different dimensions of the helikite and the mini-MPCK. Due to its larger size, the helikite reacts to larger scales of the turbulent flow compared to the mini-MPCK. Hence, the helikite is more inertial in reaction to the main flow and is advected by much larger scales only. During the advection motions, the mini-MPCK does not necessarily point into the mean wind.

2.4.3 Comparison to Radiosonde measurements

During the EUREC^{4}A field campaign, radiosondes (Vaisala RS41-SGP) profiled the atmospheric boundary layer to measure thermodynamical quantities such as air temperature and relative humidity [88]. Likewise, altitude profiles of such thermodynamical quantities can be obtained from mini-MPCK measurements as it is also equipped with meteorological sensors to measure the air temperature and relative humidity as a function of the flight altitude, as mentioned above. Although the RHT sensors are

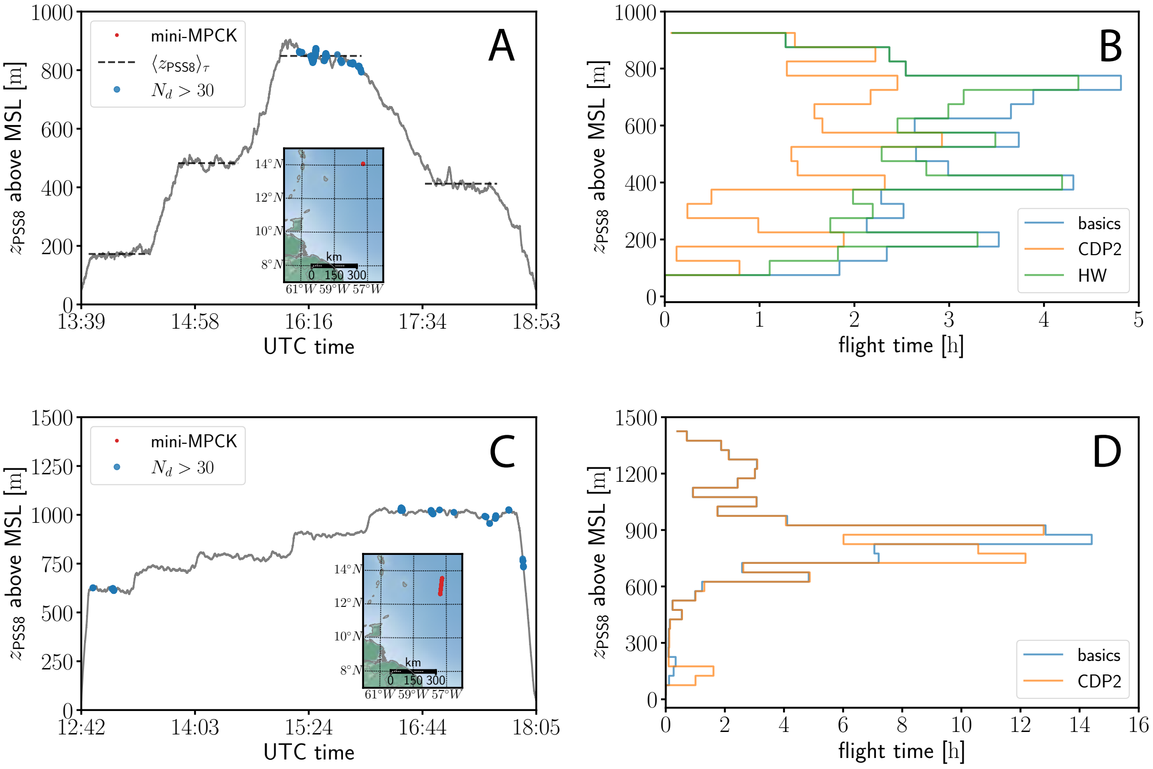

Figure 2.7 Flight strategies visualized by time series of barometric altitudes of the mini-MPCK (A) for flight 10 during M161 on RV Meteor and (C) flight 19 during MSM89 on RV Maria S. Merian. The barometric altitude is recorded as a function of time by the PSS8 (z_{PSS8}, grey line). The measurement location in terms of latitude and longitude is upstream of Barbados as shown by the red dots in the inset map of (A) and (C). Constant altitude legs with mean altitude $\langle z_{\mathrm{PSS8}} \rangle_\tau$ are highlighted by the black dashed line in (A) where τ is the duration of each flight leg. The mini-MPCK traversed several clouds as shown by the number counts of cloud droplets measured by the CDP2 exceeding 30 counts per 0.5 s. (B) and (D) present the overview of total flight time per altitude for M161 on RV Meteor and MSM89 on RV Maria S. Merian, respectively. The bin size is chosen to be 50 m. "basics" comprise the Metek, PSS8, HMP7, AM2315, BMP388, SBG, BNO055 and ZED-F9P. HW is the hot-wire.

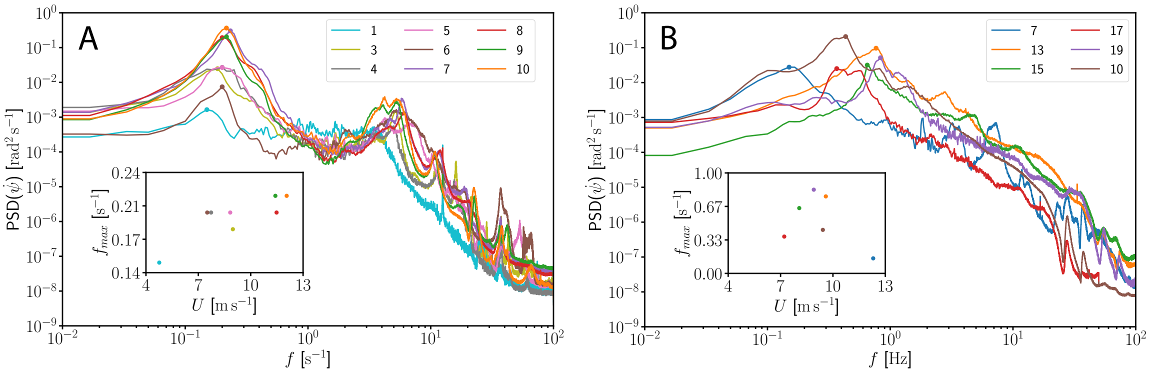

Figure 2.8 Spectral properties of the platform motion are captured by the power spectral density (PSD) of platform roll rate $\dot{\psi}$ in frequency space for all flights on RV Meteor (A) and on RV Maria S. Merian (B). The PSD($\dot{\psi}$) is block-averaged for time windows of 60 s. f_{max} corresponds to the location of the global maximum of PSD($\dot{\psi}$) being illustrated by the dots. The inset shows the frequency of maximal PSD($\dot{\psi}$) against the global mean velocity U.

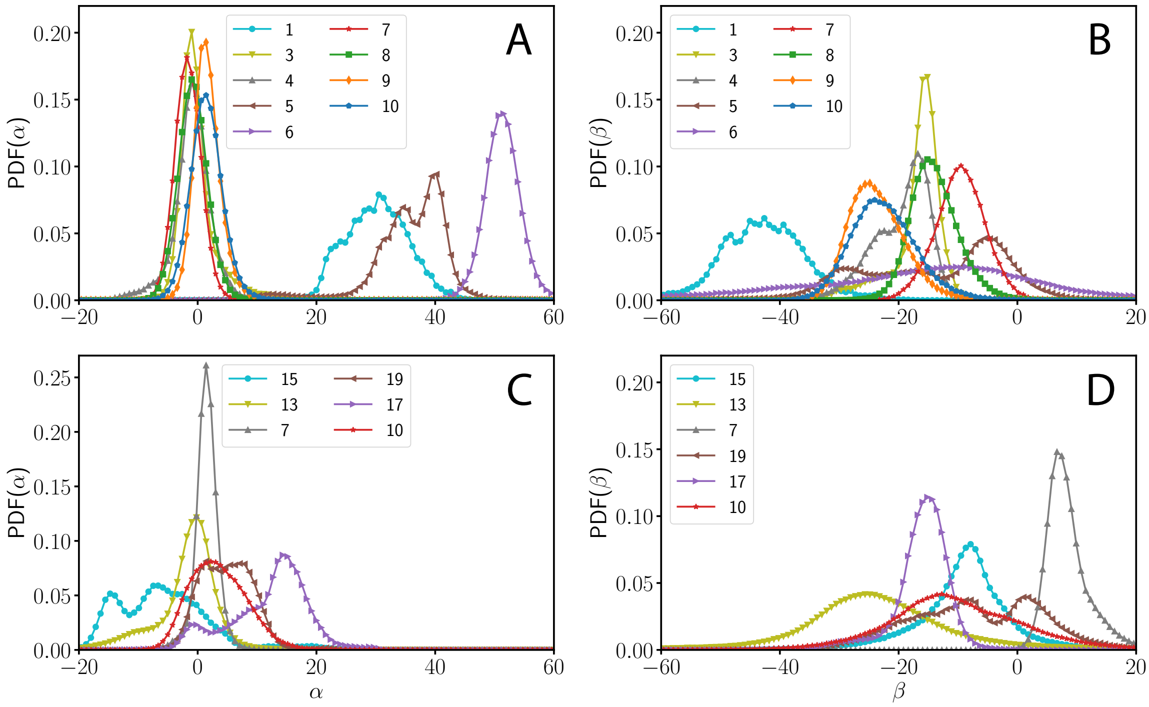

Figure 2.9 Angle of attack α and angle of sideslip β measured by the Metek sonic anemometer for the mini-MPCK on RV Meteor (A, B) and the mini-MPCK on RV Maria S. Merian (C, D). Ideally, i.e. in case of alignment to the mean wind direction, both PDF(α) and PDF(β) are distributed around 0 m/s. The α-axis is clipped from -20° to 60° and the β-axis is clipped from -60° to 20° to optimize visibility.

mounted in plastic feed throughs due to the lower thermal conductivity compared to the aluminum housing, the thermal mass of the instrument biases the air temperature and relative humidity measurement. While the relative humidity is a monotonic function of air temperature, the absolute humidity is not. Hence, the absolute humidity measurement is accurate provided that the ventilation of the RHT sensors is sufficient and radiative errors are negligible and no droplets hit the RHT sensors. Furthermore, the acoustic temperature measurement is the least affected temperature measurement of the mini-MPCK. Neglecting radiative errors, the air temperature is derived from first principles via the speed of sound of air which can be converted into air temperature for a given absolute humidity [111] as explained in Sec. 2.B.

Here, we use altitude profiles of the air temperature and relative humidity measured by the mini-MPCK to compare with three radiosonde measurements during flight 10 on RV Meteor (M161) as shown in Fig. 2.10A. On average, the mini-MPCK air temperature is 0.06 K higher than the radiosonde (compare Fig. 2.10B). The accuracy of the radiosonde is 0.3 K in soundings (below 16 km altitude above MSL) and the accuracy of the AM2315 is between 0.1 K to 1 K. Thus, the altitude profile of the mini-MPCK and all three radiosondes agrees well in the limit of accuracy of the measurements. Between 50 m to 700 m altitude above MSL, the vertical air temperature gradient measured by the mini-MPCK is -0.95 K per 100 m and the air temperature gradient measured by the radiosondes is -0.98 K per 100 m. The vertical gradient of the air temperature is close to the adiabatic lapse-rate of air temperature, which suggests a well-mixed boundary layer. The reverse conversion is shown in Figs. 2.10 where the speed of sound c is obtained from radiosonde measurements. As the mini-MPCK air temperature was slightly higher than the radiosonde air temperature, the opposite is true for the speed of sound. At last, the comparison of the relative humidity is shown in Figs. 2.10E and F. On average, the mini-MPCK and radiosonde relative humidity profiles deviate by 0.04% (absolute). However, the longer flight duration enables the mini-MPCK to measure more variability in relative humidity as illustrated by altitudes from 750 m to 900 m where two radiosondes measure a 10% change and the mini-MPCK 20%-30% change in relative humidity. This significant change in relative humidity is coincidental with a drop in air temperature. This is usually a sign of entrainment of cold and dry air from the free troposphere. Further analysis is needed to explore this event. In summary, the mini-MPCK compares statistically very well with measurements from radiosondes for flight 10 on M161.

2.4.4 Flow Velocity Measurements and Turbulence characterization

The primary measurement goal of the mini-MPCK is the characterization of atmospheric turbulence. For this reason, we first want to validate the velocity measurement itself. To quantify the systematic error of the flow velocity measurement due to the boundary of the instrument box, we performed measurements at different mean velocities 1 m/s to 11.5 m/s and locations, i.e. measurement volumes of different sensors, in the open-end

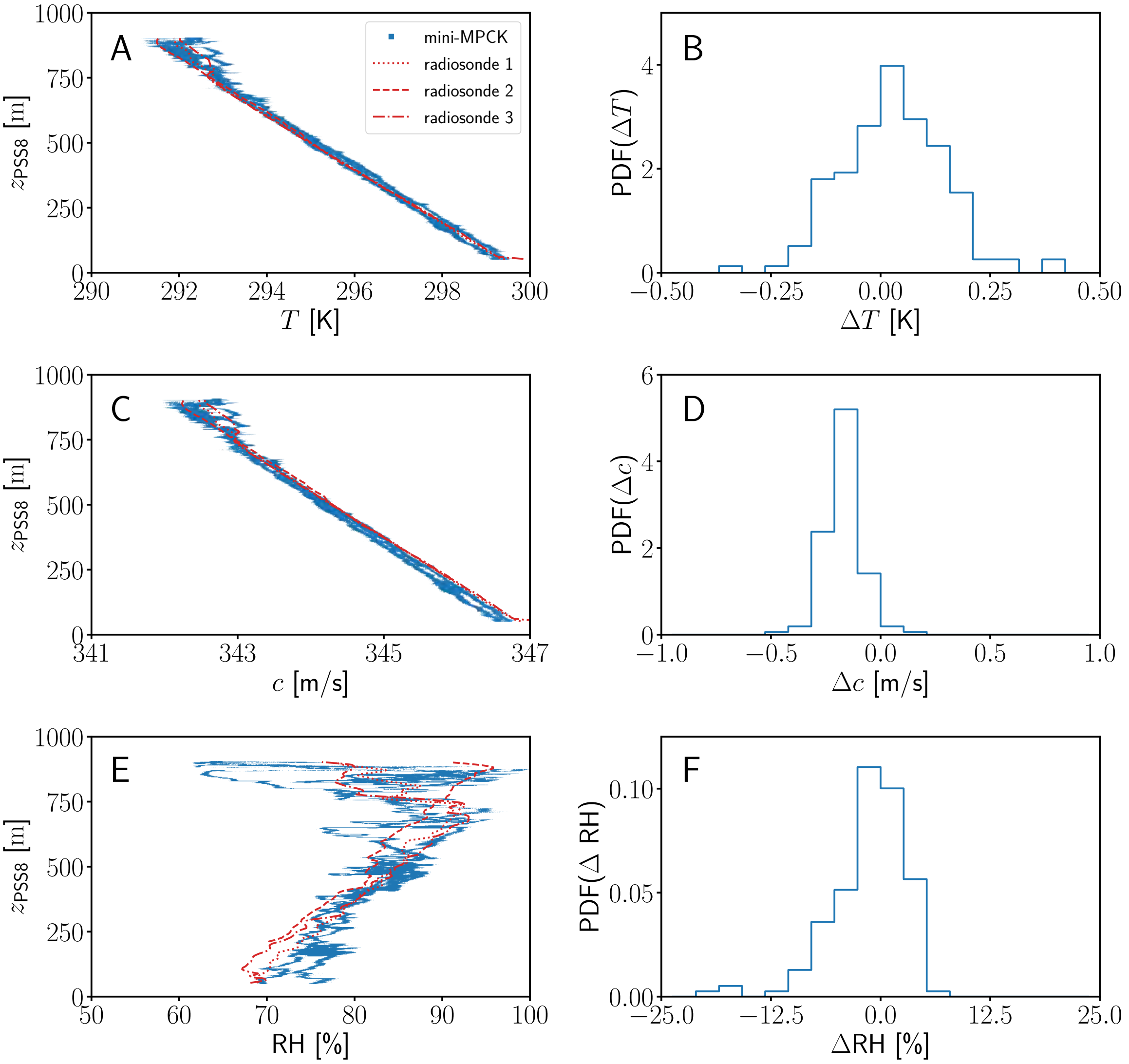

Figure 2.10 Comparison of the T, c and RH measurements with the help of the mini-MPCK to three radiosondes (radiosonde 1: 14:44 UTC, radiosonde 2: 16:19 UTC, radiosonde 3: 18:44 UTC) that were launched from RV Meteor during the duration of flight 10 of M161 [88]. The altitude profiles are shown in panels A, C and E whereas the PDFs of the differences ΔT (B), Δc (D) and ΔRH (F) quantify the deviation of mini-MPCK barometric altitude profiles from the ones measured by radiosondes 1 to 3. The large discrepancies in the relative humidity are due to cloud events and entrainment of dry air.

Prandtl wind tunnel as shown in Fig. 2.18. We used a 1:4 model of the mini-MPCK and measured the mean velocities with a pre-calibrated off-the-shelve hot-wire (Testo 405i with 0.01 m/s resolution and 0.1 m/s accuracy). which was hand-held. The ratio of the mean wind speed measured at a specific location U_m and the mean speed in the wind tunnel U_∞ is shown in Fig. 2.11A. The error bars represent the variability during the measurement period. U_∞ is determined 0.5 m upstream of the model sonic. As the ratio is close to 1, the shape of the instrument only slightly distorts the pressure field affecting the velocity measurement. As it was difficult to keep the hot-wire calm and in an optimal orientation for high U_∞, these ratios are most likely overestimated. As no significant trend is recognizable, we obtained the correction factors for the wind velocity measurement by averaging all ratios but the one at the highest U_∞.

The wind speed is measured with the PSS8 static pitot tube and with the Metek sonic anemometer. The comparison of the PSS8 wind speed measurement to the Metek wind speed measurement is shown in Fig. 2.11C and D for the mini-MPCK on RV Meteor (M161) and RV Maria S. Merian (MSM89). The error bars are given by one standard deviation. As mentioned before, the instrument box during flight 5 and 6 was rotated by 45° around the aluminum tube. Due to the sub-optimal orientation, it cannot be expected that the PSS8 and Metek show a good agreement. For all other flights, linear fits yield on average a slope of 0.988 ± 0.001 with an interception of $0.241\,\mathrm{m/s} \pm 0.694\,\mathrm{m/s}$ (average Pearson correlation coefficient 0.927 ± 0.034). During MSM89, the PSS8 wind speed signal exhibited unphysical oscillations with an amplitude of 30 m/s in some cases. Hence, all wind measurements were excluded where $|u_{\mathrm{Metek}} - u_{\mathrm{PSS8}}| > 3\sigma_{u_{\mathrm{Metek}}}$ with the standard deviation of the Metek wind speed $\sigma_{u_{\mathrm{Metek}}}$. Linear fits of the remaining flights yield an average slope of 1.013 ± 0.001 and 0.181 ± 0.828 (average Pearson correlation coefficient 0.845 ± 0.117). Taking into account the accuracy of the Metek (1.5%, e.g. 0.15 m/s at mean wind speed of 10 m/s) and the PSS8 (0.15 m/s at 0 °C angle of attack), the mini-MPCK is able to measure the wind speed accurately in the field.

During EUREC^{4}A, the PSS8 firmware runs a running average on the wind speed measurements. The default averaging window length was set to 8 points, which corresponds to 80 ms at a sampling rate of 100 Hz. Unfortunately, we did not switch the running average off. Mathematically, the running average is a convolution of a boxcar with the wind speed time record, which corresponds to a product of the Fourier-transformed wind speed measurement and boxcar (sinc-function) in Fourier space. Hence, the averaging affects the power spectrum as shown by the blue curve in Fig. 2.11B. The power spectra are obtained by the Welch method for a window of 30 min [112]. The power spectrum of the original PSS8 wind speed time record is distorted in the inertial range for frequencies larger than 1 Hz. The peak around 0.2 Hz is presumably due to the platform motion of the mini-MPCK, which has been explained in Sec. 2.4.2. The running average can be principally reverted in Fourier space, which causes singularities due to the sinc-devision. In real space, the running average can be recursively reverted as explained in Sec. 2.A. The resulting power spectral density follows the -5/3-scaling, which is predicted by the Kolmogorov phenomenology from

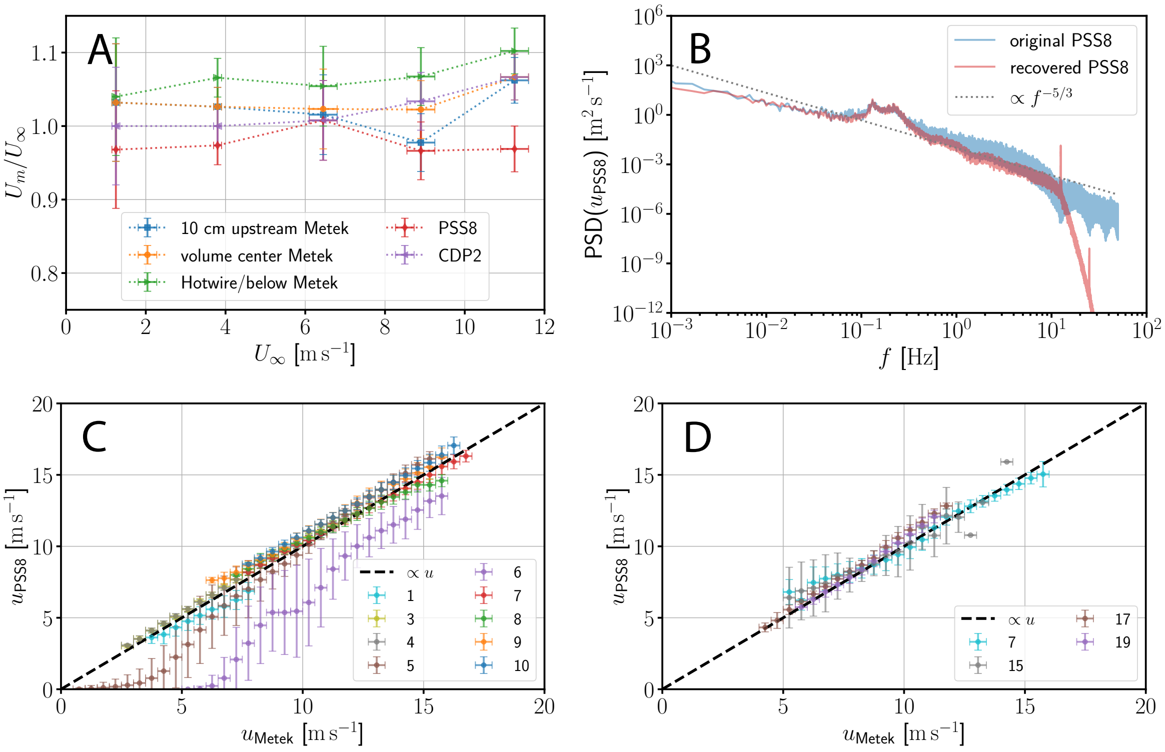

Figure 2.11 Windtunnel measurements (A) and comparison of relative wind speed measurements (C, D) by the sonic anemometer and the pitot tube. (A) The average wind speed was measured by a calibrated hotwire (Testo 405i). The mean wind speed in the wind tunnel U_∞ was measured in the center of its cross section. Then, the wind speed U_m measured by the mini-MPCK is determined at all relevant measurement locations. At the highest mean wind speed, the measurement is inaccurate as it was not possible to hold the sensor calmly in place. (B) Power spectral density of original and recovered PSS8 wind speed measurement. The expected K41 scaling $f^{-5/3}$ is shown by the gray dotted line. The lower plots show the measurements of the Metek sonic anemometer and the PSS8 pitot tube of mean wind speed all flights of M161 on RV Meteor (C) and MSM89 on RV Maria S. Merian (D) during the EUREC^{4}A field campaign.

1941 [44]. Although the recursive approach is numerically more stable compared to Fourier space, there are still peaks at harmonics of 12.5 Hz. Hence, the PSS8 wind speed measurement has to be filtered at 12 Hz at most.

We use the filtered PSS8 wind speed time record to turbulence characteristics such as the energy dissipation rate, from which we infer the most relevant turbulence length scales, e.g. the Kolmogorov length scale η_K or the integral length scale L_{11}. Invoking K41, the mean energy dissipation rate is estimated by a fit in the inertial range of the longitudinal second-order structure function $D_{LL}(r)$:

$$D_{LL}(r) = \left\langle (u_1(x+r) - u_1(x))^2 \right\rangle , \tag{2.1}$$

where *longitudinal* refers to the mean wind direction $\boldsymbol{U}/|\boldsymbol{U}|$. Longitudinal second-order

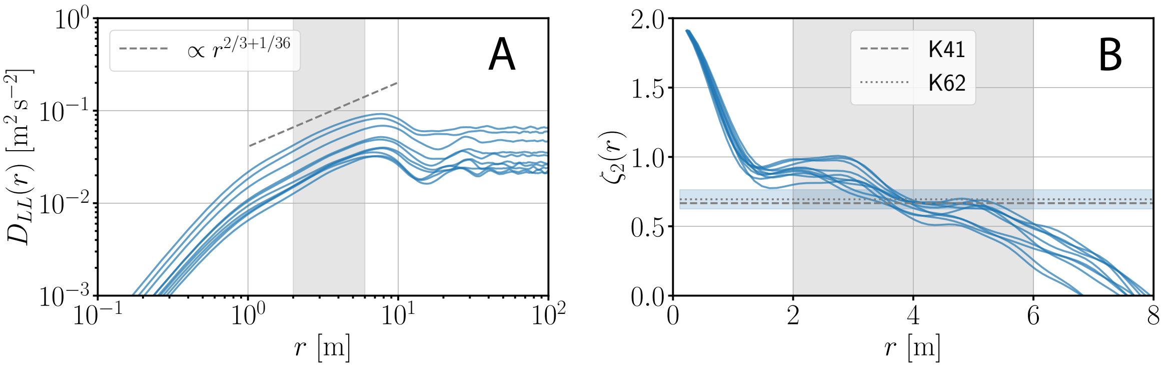

Figure 2.12 Longitudinal second-order structure functions $D_{LL}(r)$ measured by the PSS8 static pitot tube on mini-MPCK for flight 10 on RV Meteor (M161) during EUREC^{4}A. (A) $D_{LL}(r)$ are computed for averaging windows of 30 min. The wind speed is low-pass filtered with a cutoff at 12 Hz and high-pass filtered with a cutoff at 0.5 Hz using a 4th-order butterworth filter. The gray dashed line sketches the expected r-scaling from Kolmogorov's refined phenomenology from 1962. The gray shaded area is the fit range for estimating the mean energy dissipation rate. (B) Local scaling exponents $\zeta_2(r)$ of $D_{LL}(r)$ for r ranging from 0 m to 8 m. The blue shaded region is the 10% environment or the K62-scaling exponent $\zeta_2 = 2/3+1/36$ and the gray shaded region represents the fit-range. The K41-scaling exponent is $\zeta_2 = 2/3$.

structure functions $D_{LL}(r)$ measured by the PSS8 static pitot tube on mini-MPCK for flight 10 on RV Meteor (M161) during EUREC^{4}A is shown in Fig. 2.12A for averaging windows of 30 min. The wind speed is low-pass filtered with a cutoff at 12 Hz and high-pass filtered with a cutoff at 0.5 Hz using a 4th-order Butterworth filter due to the platform motion and recovery, respectively. The gray dashed line sketches the expected r-scaling from Kolmogorov's refined phenomenology from 1962 [49]. The fit range ($r \in [2\,\mathrm{m}, 6\,\mathrm{m}]$) is sketched by the gray-shaded region. Figure 2.12B shows the local scaling exponent of $\zeta_2(r) = \mathrm{d}\log D_{LL}(r)/\mathrm{d}\log r$ where the fit range is shown by the gray-shaded region. The 10% environment is shown by the blue-shaded region. Both K41 and K62 scaling exponents are drawn by the dashed and dotted lines, respectively. Averaged over the fit range and for all time windows, the mean scaling exponent is 0.74 ± 0.06 (mean ± standard deviation). Neglecting all time windows with a larger deviation than 10% from the K62-prediction, the mean scaling exponent is 0.71 ± 0.03. Given that the PSS8 wind speed time record is even not corrected for platform motion, the measured mean scaling exponents are very close to the K62 prediction ($2/3 + 1/36$). Thus, our approach is able to reproduce the K62 scaling for estimating the mean energy dissipation rate.

The altitude profile of the mean energy dissipation rates $\langle\epsilon_{I2}\rangle_T$, which are obtained from $D_{LL}(r)$ based on 30 min time windows, is shown in Fig. 2.13A. The error bars are given by the random error due to the finite averaging window [113]. Energy dissipation rates are drawn in gray if the mean scaling exponent does not deviate by more than 10% from the K62 prediction. Otherwise, the mean energy dissipation rate is shown in red, which occurs in $\sim 37\%$ of all time windows. In the altitude range of

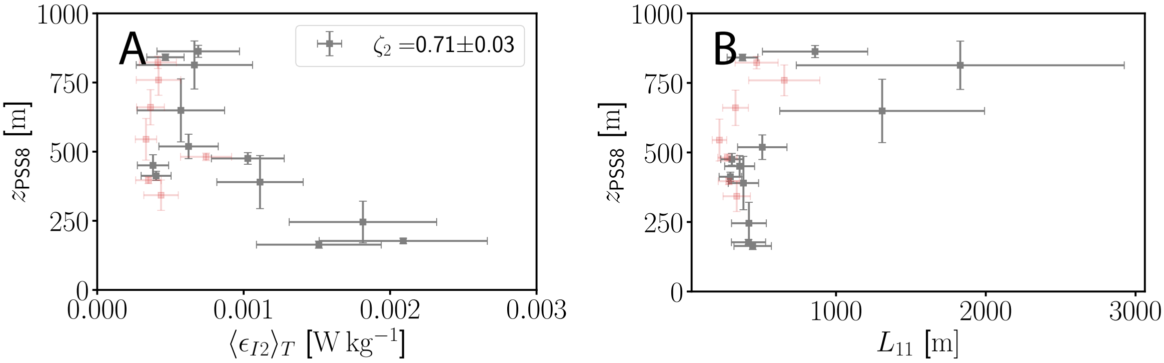

Figure 2.13 (A) Mean energy dissipation rate altitude profile. The mean energy dissipation rate are estimated from $D_{LL}(r)$ obtained for time windows of 30 min. (B) Longitudinal integral length scale L_{11} altitude profile where L_{11} is obtained via Eq. (1.29).

250 m to 1000 m above MSL, $\langle\epsilon_{I2}\rangle_T$ does not vary significantly suggesting a well-mixed boundary layer. Using the mean energy dissipation rates $\langle\epsilon_{I2}\rangle_T$ and the variance $\sigma_{u_1}^2$ of the low-pass filtered PSS8 wind speed, the integral length scale can be estimated by $L_{11} = C_\epsilon \sigma_{u_1}^3 / \langle\epsilon_{I2}\rangle_T$. The altitude profile of the estimated longitudinal length scale L_{11} is shown in Fig. 2.13B where the error bars are given by Gaussian error propagation considering the error in $\langle\epsilon_{I2}\rangle_T$ only and $C_\epsilon = 0.7$ as in grid turbulence [47]. In the well-mixed region of the boundary layer, the integral length scale is 300 m to 400 m. There are two outliers with $L_{11} \approx 1300$ m and $L_{11} \approx 1700$ m which is probably due to a dry and cold air entrainment event of the troposphere (compare also Figs. 2.10A and E at $z_{\mathrm{PSS8}} \sim 650$ m and $z_{\mathrm{PSS8}} \sim 900$ m, respectively). Both $\langle\epsilon_{I2}\rangle_T$ and L_{11} are reasonable as L_{11} is half the energy injection scale in isotropic turbulence [5]. Assuming that the energy is injected by large convective rolls, the energy injection scale is approximately given by the depth of the sub-cloud layer, which is ~ 800 m above MSL for flight 10 on M161.

Ideally, in order to measure in the direction of the longitudinal velocity, the mini-MPCK should always point in the direction of the mean velocity field while sampling the turbulent flow. In practice, the mini-MPCK reacts to scales of the velocity field that are comparable to the size of the components of the mini-MPCK, e.g. the fins. Hence, the mini-MPCK rather points in the direction of a low-pass filtered velocity field. It is expected that the mini-MPCK performs relatively stronger adjustment motions in high turbulence intensities. To demonstrate the capability of the mini-MPCK to characterize turbulence, we model the mini-MPCK as a virtual probe that points into the direction of a low-pass filtered, three-dimensional velocity field. This is realized by re-projecting the velocity time record of each virtual probe on the low-pass filtered velocity field. Thereby, this approach assumes a vanishing instantaneous directional adjustment time neglecting vortex shedding and its moment of inertia. It further neglects lateral adjustment motions of the helikite causing an overestimation of the variance $\langle u_1'^2\rangle$ of $15\% - 30\%$ [114]. In consequence, the virtual probes act like perfect weather vanes and are subsequently denoted by “weather vane”-like velocity measurement. We chose a

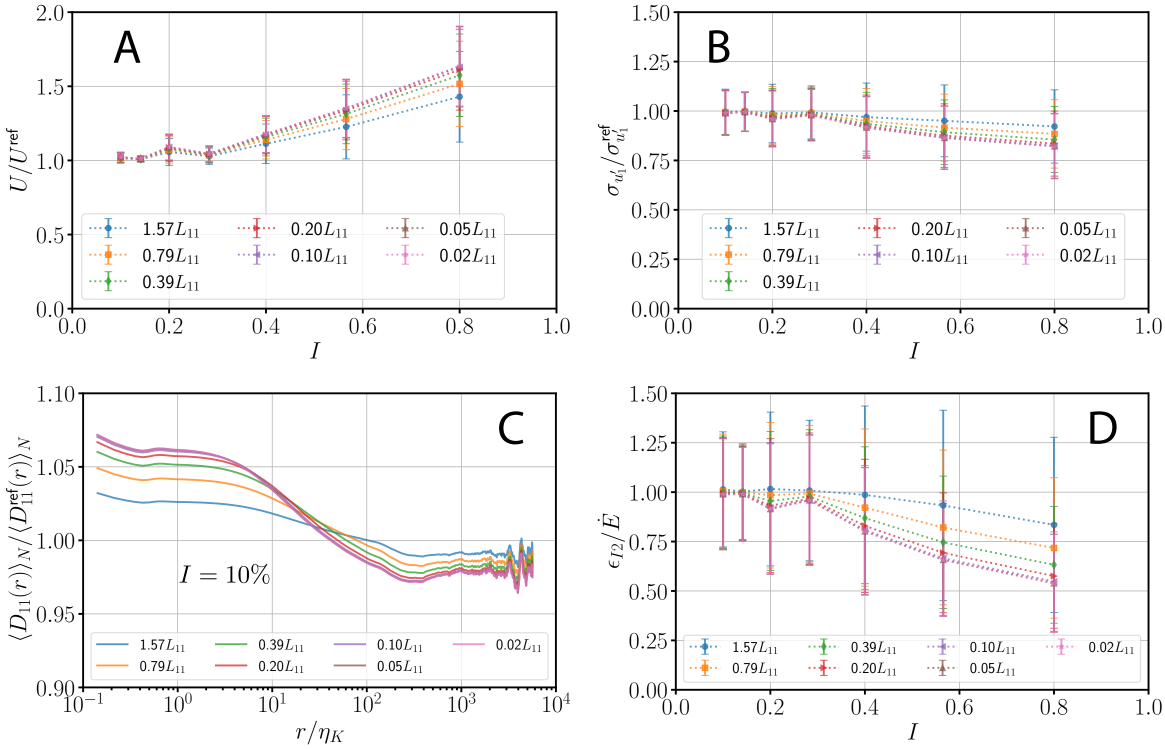

Figure 2.14 Ratio of the mean wind speed U (A), root mean square velocity fluctuations $\sigma_{u_1'}$ (B), second-order structure functions $D_{11}(r)$ (C) and the mean energy dissipation rate ϵ_{I2} (D) obtained from measurements by "weather vane"-like virtual probes relative to a reference measurement by uniformly moving virtual probe. The reference measurement is denoted by "ref". DNS of homogeneous isotropic turbulence are run for turbulence intensities $I = 0.1 - 0.8$ and seven different filter scales, which are expressed in terms of the longitudinal length scale L_{11} of the flow. Data points are given by ensemble averages and the error bars are given by the standard deviation of the ensemble.

range of spectral cutoffs to assess the importance of the ratio between the integral scale and the scale of eddies to which the mini-MPCK reacts. The DNS of homogeneous isotropic turbulence is seeded with 1000 virtual probes sampling the three-dimensional velocity field [115]. To capture the effect of the turbulence intensity, each virtual probe samples the flow with a given mean speed but randomly chosen direction where the root mean square velocity fluctuation $\sigma_{u'}$ of the DNS is fixed. Velocity time-records by virtual probes with constant mean velocity serve as the reference measurement.

Both the reference as well as the "weather vane"-like measurements are analyzed. The reference values of the mean wind speed U^{ref}, root mean square velocity fluctuations $\sigma_{u_1'}^{\text{ref}}$ and second-order longitudinal structure function $D_{11}^{\text{ref}}(r)$ are obtained from the reference measurement of each virtual probe according to the analysis procedure in [113]. The energy injection rate $\dot{E}$ serves as a reference for the mean energy dissipation rate estimate ϵ_{I2}. Similarly, the mean wind speed U, root mean square velocity fluctuations $\sigma_{u_1'}$ and second-order longitudinal structure function $D_{11}(r)$ are obtained from the “weather vane”-like measurement of each virtual probe according to the analysis procedure in [113]. The ratio of “weather vane”-like measurements to reference measurements captures the effect of adjustment motions where a value of 1 implies a vanishing impact of adjustment motions.

Figure 2.14 shows the ensemble-averaged ratios of the measured mean velocity U/U^{ref} (Fig. 2.14A), the root mean square velocity fluctuations $\sigma_{u_1'}/\sigma_{u_1'}^{\mathrm{ref}}$ (Fig. 2.14B), the second-order structure function $D_{11}(r)/D_{11}^{\mathrm{ref}}(r)$ for typical atmospheric turbulence intensity $I = 10\%$ (Fig. 2.14C) and the mean energy dissipation rate obtained from the longitudinal second-order structure function $\epsilon_{I2}/\dot{E}$ (Fig. 2.14D). Error bars are given by the ensemble standard deviation. L_{11} is estimated from the DNS directly according to $L_{11} = \pi E_{11}(0)/(2\sigma_{u_1'}^2)$ [5]. Assuming typical the integral length scales of atmospheric flows $\sim 200\,\mathrm{m}$ and given the length of the mini-MPCK $\sim 4\,\mathrm{m}$, the mini-MPCK corresponds to the pink line ($0.02L_{11}$). Taking into account that Taylor’s frozen field hypothesis is only valid for $I \leq 25\%$, it is expected that each considered quantity (U, $\sigma_{u_1'}$, $D_{11}(r)$, ϵ_{I2}) deviates significantly from the reference for $I = 25\%$. However, at smaller turbulence intensities $I \leq 25\%$, the effect of the adjustment motion on the considered quantities is small for all filter scales. In the case of $0.02L_{11}$, $D_{11}(r)$ is overestimated for small scales and under-estimated for large scales. In consequence, the inertial range scaling exponent will be lower than the K62 prediction. Finally, we conclude the mini-MPCK is well suited for characterizing atmospheric turbulence.

2.5 Discussions

In this section, we review the in-field performance of the mini-MPCK during EUREC^{4}A. We especially shed light on the measurement of the wind velocity, fluxes and RHT as well as the tether-mount, operational inconveniences and structural stability. Furthermore, we report on the revised mini-MPCK and implied improvements.

Wind measurements in particle-laden turbulent flows, such as inside clouds, are difficult due to the presence of cloud particles. For example, impinging cloud droplets cause spikes in the hot-wire wind fluctuation measurement [116] due to droplet evaporation. In addition, cloud droplets, especially rain droplets, can clog the holes of the Pitot tube and impede the measurement of static pressure and total pressure. In contrast, wind measurements using sonic anemometry, which relies on measuring the speed of sound in (dry) air, are not significantly affected by cloud droplets [117]. Considering marine, shallow cumulus clouds, the liquid water content is $\sim 0.1\,\mathrm{g/m^3}$. The sonic measurement volume is about $1 \times 10^{-3}\,\mathrm{m^3}$, so the volume fraction of water to the measurement volume is $\sim 10^{-7}$. Despite the fact that the speed of sound in liquid water is about $4c$, where c is the speed of sound in dry air, it is plausible that the influence of liquid water on the sound wind measurements is small in the case of marine shallow cumuli. This consideration also shows the importance of redundancy through different measurement principles.

Platform motions not only pose a challenge for measuring the wind speed but also for measuring the vertical velocity in the Earth frame of reference, which is a critical quantity to measure vertical fluxes. The mini-MPCK is equipped with a sonic that measures the vertical velocity by three independent, vertically oriented measurement paths directly if the measurement paths are perfectly aligned with the vertical direction in the Earth frame of reference. Therefore, it is not possible to determine vertical fluxes from the mini-MPCK data records during EUREC^{4}A without proper platform motion and orientation corrections. Up to now, the data assimilation and sensor fusion is not enough progressed to deal with the drift in the platform yaw angle and the noise in the Euler angle rates.

To accurately characterizing atmospheric turbulence, the mini-MPCK should point always in the mean wind direction. This is the ideal alignment reducing the flow distortion by the instrument itself and ensuring to measure the longitudinal direction of the flow. However, on RV Meteor, the mean angle of sideslip was significantly deviating from 0° for most flights of the mini-MPCK. This is due to a combination of a twisted main tether and limited rotational freedom of 270° in the horizontal plane, which blocked the mini-MPCK in aligning itself with the horizontal mean flow direction. Hence, the tether-mount proved to be not ideal. On RV Maria S. Merian, the mini-MPCK was mounted below the balloon. Despite that the balloon is orienting itself to the mean flow direction, the mini-MPCK is still oscillating which is why the angle of sideslip is non-zero in the platform frame of reference. During a land-based campaign in Finland, which took place in September 2022 in Pallas, a similar instrument (winddart) was hung from the main tether of the $250\,\mathrm{m}^3$ helikite by a $10\,\mathrm{m}$ long line. This configuration was very stable without oscillatory motions because the coupling of balloon motions to the platform is weaker compared to a tether-mount. In the future, on land-based campaigns, the mini-MPCK will be hung from the main tether, too. Unfortunately, this approach was not operational on the ocean because of the vertical inclination of the main tether and instrument landing on the deck. However, the mini-MPCK is able to characterize atmospheric turbulence even without the corrections for platform motions as explained in Sec. 2.4.4.

Radiation, salt contamination and impinging water droplets are a challenge for atmospheric *in-situ* RHT measurements. Heat change due to radiative effects can be minimized by the use of (white) shields, which is done by the white nose of the mini-MPCK. However, good ventilation of the RHT sensors is critical for point-like measurements of air temperature and relative humidity. Therefore, ventilation holes are drilled in the enclosing white nose shield. Impinging droplets can be avoided by arranging the ventilation holes relative to the sensors such that the sensors are most likely not hit by inertial particles. Furthermore, it should be avoided to put a sensor in the dead-water region of the flow through nose part. Here, we bypass the problem of ventilation by using the acoustic temperature to obtain the air temperature and relative humidity (Secs. 2.4.3 and 2.B). This approach also minimizes the effect of the thermal mass of the housing and heat conduction by the sensor mounts in the nose part of the mini-MPCK. To cope with salt contamination of wire-based temperature or capacitive humidity measurements, the sensors should be frequently rinsed with distilled water. However, the data would not be usable until the sensor dried again. To our knowledge, there is no way to fully avoid salt contamination in marine environments.

During the EUREC4^{4}A field campaign, the mini-MPCK was not sufficiently convenient to operate. As an example, the instrument box had to be fully opened at one side at least to maintain, e.g., the hot-wire. In addition to opening the window, the data acquisition board (labjack) had to be unscrewed so that the mini-CTA is accessible. Likewise, for every battery exchange, the power box had to be fully opened. For these reasons, the instrument box shall be modulized so that accessing instruments is easier. In addition, the side windows are now closed by a clamp mechanism that is much faster and easier to open or close. Furthermore, in order to simplify the re-charging process, adequate power plugs are planned to be outside of the power box so that charging is possible without opening the power box.

In addition to the operational difficulties, the instrument box was not stable against axial rotations around the aluminum tube. Furthermore, high-frequency oscillations at frequencies higher than 1 Hz are visible in PSD($\dot{\psi}$) as shown in Fig. 2.8. These oscillations might partially be explained by vortex shedding. Assuming a Strouhal number $Sr = fL/u$ and choosing $u \sim 10\,\mathrm{m/s}$ (mean velocity), $L \sim 24\,\mathrm{cm}$ (edge length of instrument box), the frequency of vortex shedding is $\sim 8\,\mathrm{Hz}$. Another reason for high-frequency oscillations is the insufficient stiffness of the aluminum tube.

We addressed and solved the problems during EUREC^{4}A by revising the mini-MPCK, which results in the so-called mini-MPCK 2.0 (Fig. 2.15). While the concept of two balanced boxes (i.e. instrument and power box) was adopted from the prototype mini-MPCK, the mini-MPCK2.0 has a more aerodynamic oval shape in order to reduce the pressure distortion at the nose. The vortex shedding is reduced by an aerodynamic shield covering the box suspension between the instrument and power box and a cone-shaped tail downstream of the power box. To improve the velocity data, the stiffness of the aluminum box is increased by a specially designed suspension and a foreseen mount for the hot-wire. In the future, the mini-MPCK 2.0 is equipped with more sensors. First, the LWC-300 probe from Droplet Measurement Technologies Inc. provides a direct measurement of the LWC in the range of $0\,\mathrm{g/m^3}$ to $3\,\mathrm{g/m^3}$. The LWC-300 probe consists of a hot cylinder with a constant overheat temperature that evaporates impinging cloud particles. Furthermore, the absolute humidity will be optically measured by Licor 7500-DS. The Licor 7500-DS will be mounted next to the sonic so that moisture fluxes can be properly measured. We also consider developing a lightweight chilled mirror to measure the dew point, hence relative humidity, accurately also in cloudy conditions.

The mini-MPCK is able to measure atmospheric turbulence even without complex platform motion corrections if the most dominant modes of the platform motion are high-pass filtered. Cloud microphysical measurements and atmospheric state measurements are successfully measured by the mini-MPCK. Vertical flux measurements are currently not possible as the wind vector needs to be corrected for platform motion. Therefore, either better orientation sensors and adequate conversion to Earth frame of reference or a different mounting strategy is needed. Due to its low power consumption, we consider the mini-MPCK an ideal scientific instrument to conduct balloon-borne measurements

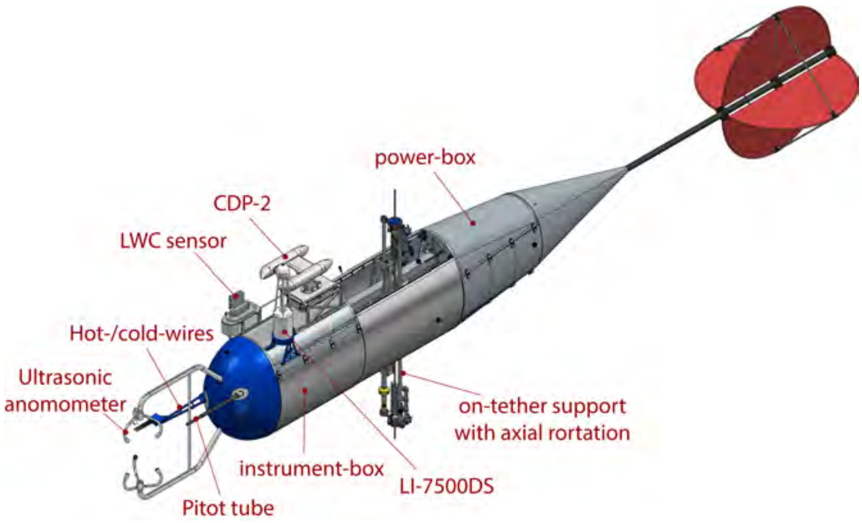

Figure 2.15 The revised mini-MPCK 2.0 with an aerodynamic cover shielding the suspension between the instrument box and power box and a cone-shaped tail to reduce vortex shedding.

across the diurnal cycle. Despite that, even more requirements will be fulfilled by the mini-MPCK 2.0., the mini-MPCK is an easy-to-operate and flexible instrument that can be operated not only on land-based towers but also balloon-borne in very remote regions of the oceans.

Appendix 2.A Revert Running Average

The PSS8 system comprises a pitot tube, the so-called air data computer and a PT100 temperature sensor. The pitot tube records the static pressure p_s and total pressure p_t in time. The PT100 temperature sensor measures the air temperature T. The air data computer performs a running average over 8 data points by default so that

$$p_t(t_{i+1}) = \frac{1}{N} \sum_{j=i-N}^{i} p_t(t_j)\,. \tag{2.2}$$

The running averages for T and p_s follow by substituting T and p_s in Eq. (2.2). Given the sampling frequency of 100 Hz, the running average of p_t corresponds to a convolution of p_t with a boxcar of a time period of 80 ms. In consequence, the Fourier transform of the boxcar, the sinc funcion, also appears in the power spectral density. However, the running average of N data points can be reverted for all but the first N data points of the p_t-time series:

$$\tilde{p}_t(t_{i-N}) = N p_t(t_{i+1}) - \sum_{j=i-N+1}^{N} p_t(t_j)\,. \tag{2.3}$$

Assuming that the variability in T and p_s is negligible on time scales below 100 ms, the wind speed can be obtained using the Bernoulli equation

$$u = \sqrt{\frac{2p_d}{\rho}}\,, \tag{2.4}$$

where $p_d = \tilde{p}_t - p_s$ and ρ is the air density. Invoking the ideal gas law for dry air and using the PSS8 air temperature T and static pressure p_s, the density of dry air is given by:

$$\rho = \frac{M}{R}\frac{p_s}{T}\,, \tag{2.5}$$

where $R = 8.314\,462\,618\,\mathrm{J/(K\,mol)}$ is the universal gas constant and $M = 28.965 \times 10^{-3}\,\mathrm{kg/mol}$ is the molar mass of dry air.

Appendix 2.B Air temperature from speed of sound

In principle, the sonic measures the run time of sound pulses between at least two transducers. From the distance between transducers and the run time, the wind component parallel to the measurement path and the speed of sound can be obtained [118]. The speed of sound c can be converted into air temperature [111]:

$$T_\mathrm{s} = \frac{c^2}{\gamma_\mathrm{d} R_\mathrm{d}}\,, \tag{2.6}$$

where $\gamma_\mathrm{d} = C_\mathrm{pd}/C_\mathrm{vd}$ is the ratio of specific heat at constant pressure C_pd to the specific heat at constant volume C_vd for dry air and R_d is the gas constant for dry air. Here, the sonic temperature T_s is obtained under the assumption of dry air. In reality, both R and γ depend on humidity. Taking into account humidity, the air temperature of moist air as a function of T_s is given by [111]:

$$T = T_s \frac{\xi(1+\chi_\mathrm{w})[1+(C_\mathrm{vw}/C_\mathrm{vd})\chi_w]}{(\xi+\chi_w)[1+(C_{pw}/C_{pd})\chi_w]}\,, \tag{2.7}$$

where χ_w is the water mixing ratio, $\xi = M_w/M_d = 0.622$ the molar mass ratio of water vapor to dry air. Technically, Zhou et al. refer to closed-path eddy-covariance systems. Here, the water mixing ratio is obtained from the AOSONG AM2315 air temperature and relative humidity measurement. To calculate $\chi_w = \rho_w/\rho_d$, the water vapor density is obtained by $\rho_w = f\rho_w^\mathrm{sat}\mathrm{RH}$ where $f = 1.0016 + 3.15 \times 10^{-6}\,\mathrm{hPa}/p_s - 0.074\,\mathrm{hPa}/p_s$ is the water enhancement factor [119] and ρ_w^sat is the density of saturated water vapor [120, Eq. (3)]. The dry air density is obtained from Eq. (2.5). Additionally, the PSS8 static pressure is low-pass filtered at 0.05 Hz in order to suppress static pressure variations due to platform motion. At last, we use χ_w and T, Eq. (2.7), to calculate the relative humidity of ambient air.

Appendix 2.C Wind tunnel experiment

We performed wind tunnel measurements with a 1:4 model of the mini-MPCK in order to determine deviations of the wind speed at different sensors from the true mean wind speed U_∞. Therefore, we mounted the model mini-MPCK on a frame of aluminum profiles such that the model is central with respect to the cross-section of the wind tunnel. Thereby, we minimize wall effects by the wind tunnel. Similar to the mini-MPCK on M161, the model is mounted to a rod but with a locked tether-mount. This means that the model did not align itself with the mean flow which is why the model needs to be manually aligned to the mean flow direction prior to the wind speed measurement.

Appendix 2.D The micro-Max Planck Cloudkite

After the loss of the mini-MPCK on M161 during flight 11 due to strong winds, we built a minimal instrument package from spare parts, the so-called micro-Max Planck Cloudkite (micro-MPCK). The micro-MPCK is a scientific instrument for measuring atmospheric turbulence. The micro-MPCK and the experimental setup aboard RV Meteor are shown in Fig. 2.16. The micro-MPCK is equipped with a Pitot Static System PSS-8™ manufactured by Simtec AG ("PSS8") to sample the relative wind speed $u_1(t)$ and air temperature T at a frequency of 100 Hz. During the EUREC^{4}A field campaign, the micro-MPCK was deployed by a 34 m^3 helikite with a static lift of 14 kg during M161 Flight 12 on RV Meteor (Fig. 2.16). The micro-MPCK was strapped to the keel of the helikite, as shown in Fig. 2.16A.

During flight 12, the main tether was the meteor line (manufactured by Rudolf Seldis GmbH & Co. KG) with a diameter of 14 mm and a weight of 1.1 kg per 10 m line. Since the total length of this line was only ~ 400 m, the maximal achievable flight altitude was limited to ~ 150 m above MSL due to the line inclination $\gtrsim 45°$ in windy conditions. The launching and landing procedure of the micro-MPCK was similar to the mini-MPCK on RV Meteor (see Sec. 2.3.4). The micro-MPCK was deployed by the 34 m^3 helikite being anchored to the ship directly to perform long-term measurements in the boundary layer (Fig. 2.16B). This data can be compared to other wind measurements aboard RV Meteor although it is not considered in the scope of this thesis.

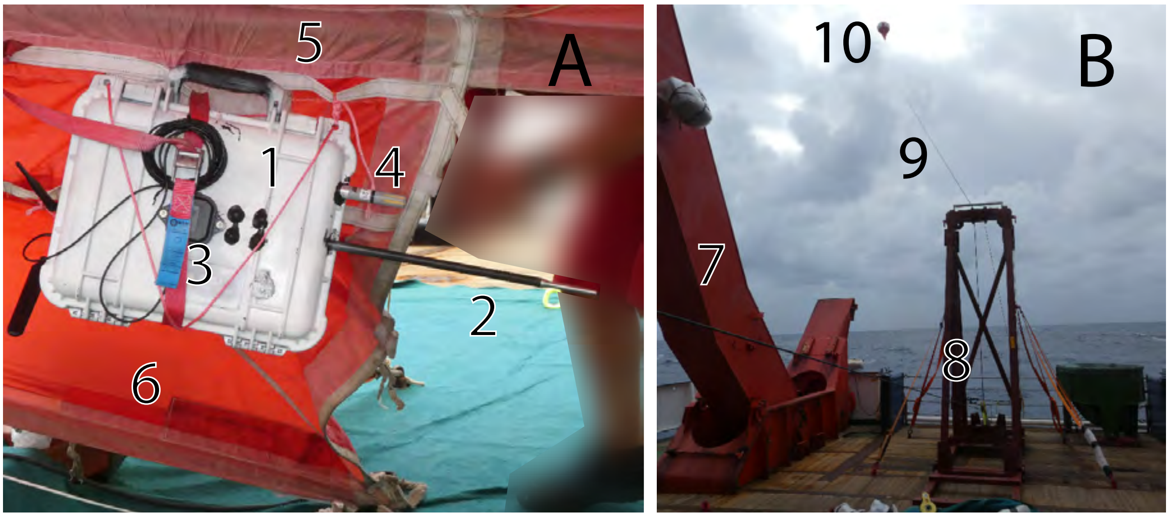

Figure 2.16 The micro-MPCK (1) aboard RV Meteor during EUREC^{4}A field campaign. A: The micro-MPCK is equipped with a PSS8 pitot tube (2), a u-blox multiband antenna (3) and an AM2315 RHT sensor (4). The GPS antenna (3) is glued to the outside of the micro-MPCK Peli case in order to receive a better GPS signal. The micro-MPCK is strapped to the keel (6) below the main spare (5) of a 34 m^3 helikite (10). The original picture is blurred where a person is partially shown in order to guarantee privacy. B: The main tether (9) anchors the helikite to RV Meteor where the main tether is guided by the line guiding system (8). The line guiding system is located between the side arms of the A-frame (7).

Appendix 2.E Supplementary Figures

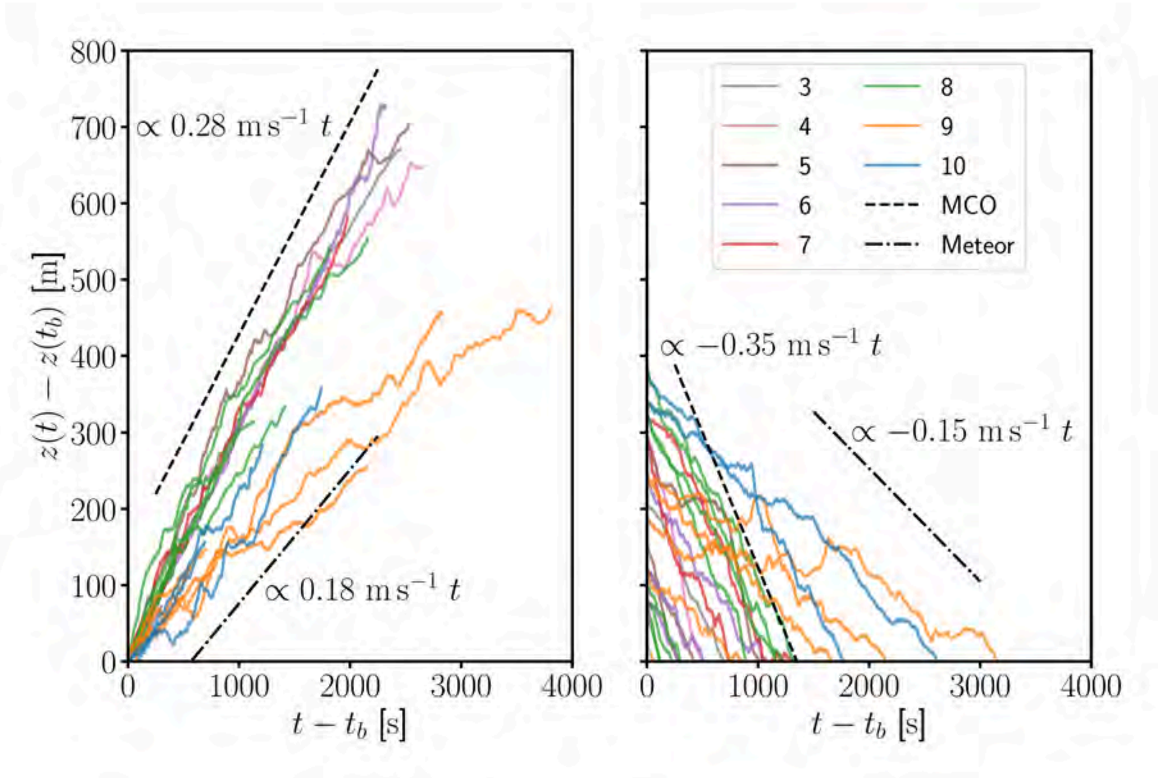

Figure 2.17 Barometric altitude difference as a function of time for the mini-MPCK on RV Meteor (M161) for all ascents (left panel) and for all descents (right panel). The barometric altitude is recorded with the PSS8. The time is given relative to the begin time t_b of each ascent or descent. Similarly, the altitude time record $z(t)$ is given relative to the barometric altitude $z(t_b)$ at the begin of each ascent or descent. The average ascent and descent rates are obtained by linearly fitting the altitude time series. The dashed lines in both panels comprise all flights (flight ID 1 - 8) that where conducted with the winch of the Mobile Cloud Observatory (MCO) whereas the dash-dotted lines comprise the flights 9 and 10 being conducted from a mooring winch of RV Meteor.

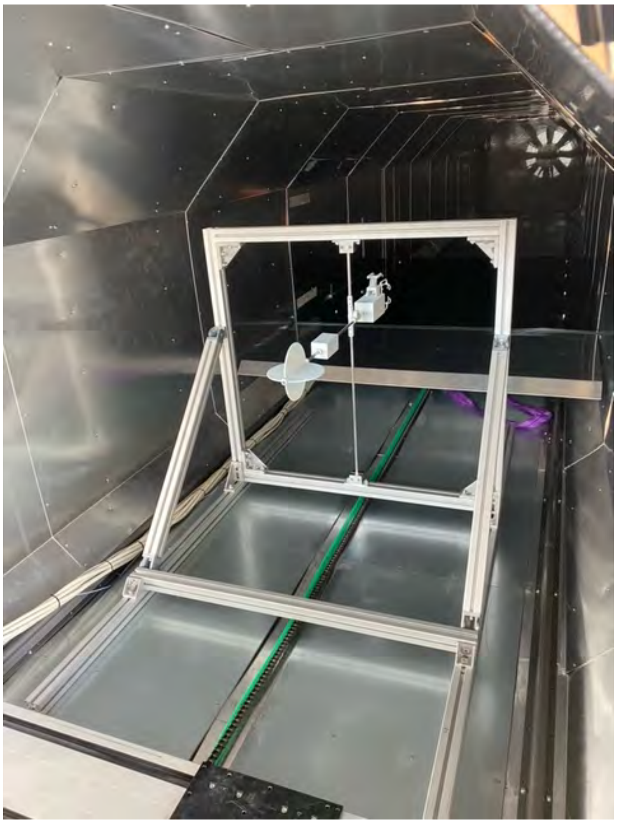

Figure 2.18 The 1:4 mini-MPCK model in mounted to a frame off aluminum profiles inside the Prandtl tunnel. In the background, the fan is visible. The mini-MPCK is close to the outlet and points to the mean wind direction.

Appendix 2.F Supplementary Tables

Symbol	Definition	Unit
a	GPS altitude above MSL	m
d_p	cloud droplet diameter	m
N_p	cloud droplet number count	#
Δt_p	cloud droplet inter-arrival time	s
$\boldsymbol{u}$	relative wind vector	m/s
u	relative wind speed	m/s
u'	relative wind speed fluctuations	m/s
T	temperature	K
T_{acoustic}	acoustic temperature	K
RH	relative humidity	%
p	pressure	hPa
ψ	roll	°
θ	pitch	°
ϕ	yaw	°
lat	GPS latitude	°
lon	GPS longitude GPS	°
$\boldsymbol{v}_p$	platform velocity	m/s
$\boldsymbol{v}$	wind velocity	m/s
LWC	liquid water content	g/m^3

Table 2.3 Nomenclature of quantities that are used in the scope of this work.

Chapter 3

Estimating the turbulent kinetic energy dissipation rate from one-dimensional velocity measurements in time

In general, the energy dissipation rate is a central turbulence characteristics. In the scope of this work, the energy dissipation rate is obtained from time records of the longitudinal velocity inside clouds and in the cloud-free atmosphere. While the energy dissipation rate can be directly obtained from the velocity gradient tensor in DNS, it is difficult to measure the energy dissipation rate in-situ. A similar but shortened version of this section is submitted as an article to Atmospheric Measurement Techniques.

The article reviews different methods applicable to different ranges and evaluates their performance in homogeneous isotropic turbulence. It also provides an assessment of various experimental limits and imperfections such as misalignment between the sensor and mean flow direction, turbulence intensity and the effect of finite averaging windows. Analytical expressions for all error sources are presented. In addition, the article elaborates the possibility of estimating a transient energy dissipation rate. This article is the basis for subsequent analysis of *in-situ* measurements and, hence, of great importance for this work. Without this article, I could not determine the accuracy neither of the energy dissipation rate estimates nor for all parameters that depend on the energy dissipation rate.

I conceptualized the study together with Eberhard Bodenschatz, Michael Wilczek, and Gholamhossein Bagheri. I further developed, validated and ran the analysis code. Together with Tobias Bätge and Michael Wilczek, I theoretically modeled the systematic and random errors due to experimental limitations/ imperfections. Together with Eberhard Bodenschatz, Michael Wilczek, and Gholamhossein Bagheri, I analyzed and interpreted the data. Furthermore, I wrote the initial draft, proofread and edited the manuscript.

3.1 Introduction

Turbulence is fundamental to many natural and engineering processes, such as transport of heat and moisture in the Earth's atmosphere [e.g. 29, 50, 55, 121, 122], wind energy conversion [123], entrainment and mixing [e.g. 8, 124–129], and warm rain initiation [e.g. 4, 23, 26, 130], to name just a few. In three-dimensional turbulence, the kinetic energy is typically injected into the flow at the largest scales and successively transferred to smaller eddies by means of the direct energy cascade. At the smallest scales characterized by the Kolmogorov length scale (or the dissipation scale) η_K, kinetic energy is dissipated by viscous effects at the energy dissipation rate ϵ. The energy dissipation rate ϵ is one of the most fundamental quantities in turbulence and is used to estimate many relevant features of a turbulent flow, such as the Kolmogorov length scale η_K, the Taylor microscale λ [5], the Taylor-scale Reynolds number R_λ and, by means of dimensional estimates, the energy injection scale.

The instantaneous energy dissipation field $\epsilon_0(\boldsymbol{x}, t)$ is highly intermittent with strong small-scale fluctuations [5, 42, and references therein], which are at the core of the intermittency problem in turbulence [48, 131, 132]. It also plays an important role in turbulent mixing in reacting flows [e.g. 125, 133, 134] or turbulence-induced rain initiation in warm clouds [4]. $\epsilon_0(\boldsymbol{x}, t)$, however, is extremely difficult to measure experimentally as it requires the complete knowledge of the three-dimensional velocity field at high temporal and spatial resolution.

Apart from the instantaneous dissipation field $\epsilon_0(\boldsymbol{x}, t)$, the energy dissipation in a turbulent flow can be statistically described by either the local or global mean energy dissipation rate which are both important. Local volume averages of the instantaneous dissipation field $\langle\epsilon\rangle_R$ and related surrogates, e.g. longitudinal, transverse or asymmetric components of $\epsilon_0(\boldsymbol{x}, t)$, still capture intermittent effects of turbulence [135, 136, and references therein]. The local volume averages of the dissipation field converge to the global mean energy dissipation rate $\langle\epsilon\rangle$ for infinitely large averaging volumes. $\langle\epsilon\rangle$ can be used to describe the statistics of homogeneous and locally isotropic turbulence based on the Kolmogorov's phenomenology (K41) [43]. However, even if the global mean energy dissipation rate $\langle\epsilon\rangle$ is known with a low uncertainty, it is of great value to know how locally averaged dissipation rates $\langle\epsilon\rangle_R$ deviate from the global mean energy dissipation rate $\langle\epsilon\rangle$.

For a statistically stationary homogeneous isotropic (SHI) turbulent flow, $\langle\epsilon\rangle$ can be estimated from time-dependent single-point one-dimensional velocity measurements through different methods, such as longitudinal or transverse velocity gradients [137–140, among others], inertial-range scaling laws comprising the famous 4/5 law [43, 44], counting zero-crossings of the velocity fluctuation time series [141, 142] or dimensional arguments [e.g. 143–145]. These methods usually invoke Taylor's hypothesis to map temporal signals onto spatial signals, which requires a *sufficiently small* turbulence intensity. The turbulence intensity is defined as the ratio of the root mean square velocity fluctuations $\sigma_{u'}$ to the mean velocity U. When all of these criteria are met, single-point velocity measurements with hot-wire anemometers at a high temporal resolution have been shown to be suitable for accurately estimating the global energy dissipation rate [138, 139, 146, 147]. However, *ideal* SHI and low-intensity turbulent flows are rarely encountered in natural turbulent flows, such as those in the atmospheric boundary layer.

In such non-stationary and inhomogeneous flows, the global mean energy dissipation rate $\langle\epsilon\rangle$ alone is not representative as the characteristics of turbulent flows can be highly time- and space-dependent even at the energy injection scales. As a result, one needs to calculate a local $\langle\epsilon\rangle_\tau$ and $\langle\epsilon\rangle_R$, respectively, based on velocity statistics for a *properly chosen* averaging window τ in time or R in space, which is short enough for resolving the temporal or spatial variations but also long enough to obtain statistically representative values with *acceptable* systematic and/or random errors [e.g. 55, 56]. Therefore, a conflict arises with respect to the averaging time between resolving small-scale features of a turbulent flow and statistical convergence under non-stationary and inhomogeneous conditions.

In the case of atmospheric flows, in-*situ* measurements made via airborne [8, 52, 131, 140, 148–150, e.g.] as well as ground-based [54, 87, 151, 152, e.g.] platforms typically can only resolve the coarse-grained time series of the local mean energy dissipation rate $\langle\epsilon\rangle_\tau$. However, since there is no high-resolution three-dimensional velocity measurement available during such in-*situ* measurements to serve as the ground-truth, it remains unclear how large the errors in estimating the coarse-grained time series of the local mean energy dissipation rate are due to individual choices of the averaging window. In the absence of a ground-truth reference, the comparison between different methods exposes large deviations [54, 140, 142, 153]. As an example, Wacławczyk et al. [153] found deviations of about 5%-50% for estimating the mean energy dissipation rate depending on the method and averaging windows using synthetic data modeled via von Karman spectrum. Another example is the work of Akinlabi et al. [154], who found that estimates of mean energy dissipation rate by one-dimensional longitudinal velocity can differ by a factor of 2 to 3 from those calculated using DNS, depending on the method used.

Our literature review indicates that a systematic investigation is still needed to fully understand how the choice of averaging window, analysis methods, turbulence intensity and large-scale random flow velocities can influence estimating the mean energy dissipation rate and its deviations from the instantaneous energy dissipation rate. To this end, we systematically benchmark different techniques available in the literature using fully resolved DNS of statistically stationary, homogeneous, isotropic turbulence. Since the full dissipation field is available from DNS, this approach provides ground-truth reference for comparisons to the various estimation techniques. To bridge the gap between typical R_λ of DNS and atmospheric flows, we use high-resolution measurements of the longitudinal velocity components of the Variable Density Turbulence Tunnel [36, 147, 155] at various Taylor Reynolds number R_λ between 140 and 6000. The impact of turbulence intensity, large-scale random sweeping velocities, size of averaging window, Reynolds number and also possible experimental imperfections, such as anemometer misalignment are investigated in detail. Our work aims to be a step towards the goal of extracting the time-dependent energy dissipation rate from non-ideal naturallyoccurring turbulent flows mitigating the impact of non-ideal features of the flow, e.g., anisotropy or inhomogeneity. In Sect. 3.2, we first define the central statistical quantities and the individual methods for estimating the energy dissipation rate in detail. An analysis of the individual methods including discrepancies, errors due to finite turbulence intensity, and alignment errors are discussed in Sect. 3.3 followed with a summary of our findings.

3.2 Methods

Let $\boldsymbol{u}(\boldsymbol{x},t) = u_1(\boldsymbol{x},t)\boldsymbol{e}_1 + u_2(\boldsymbol{x},t)\boldsymbol{e}_2 + u_3(\boldsymbol{x},t)\boldsymbol{e}_3$ denote the three-dimensional velocity vector of the turbulent flow, where $\boldsymbol{x} = x_1\boldsymbol{e}_1 + x_2\boldsymbol{e}_2 + x_3\boldsymbol{e}_3$ are the components of the Cartesian coordinate system and t is the time. We assume that the streamwise direction of the global-mean flow $\boldsymbol{U}$ is in the direction of $\boldsymbol{e}_1$ such that $\boldsymbol{U} = U\boldsymbol{e}_1$ is (by definition) constant in space and time. We refer to $\boldsymbol{e}_1$ as the *longitudinal* direction and the components normal to that, i.e. $\boldsymbol{e}_2$ and $\boldsymbol{e}_3$, as the *transverse* directions of the flow. As mentioned earlier, many experimental setups record only a one-dimensional flow velocity at one location and as a function of time. We consider this one-dimensional velocity time record to be in the longitudinal flow direction unless otherwise stated. In the following, we first introduce different averaging principles that can be used to analyze turbulence statistics and Taylor's frozen hypothesis, and then present the commonly used methods for extracting the energy dissipation rate. A preliminary introduction of the basic statistical description of turbulent flows is provided in the appendix (Sec. 3.2.2) for the sake of completeness.

3.2.1 On Averaging, Reynolds Decomposition and Taylor's Hypothesis

Most methods used to retrieve the dissipation rate require spatially resolved velocity statistics although the velocity is recorded only at a single point and as a function of time in many experiments. Therefore, prior to estimating the energy dissipation rate, the one-dimensional velocity time-record should be first mapped onto a spatially resolved velocity field. This is achieved by invoking Taylor's hypothesis, which requires a Reynolds decomposition of the velocity time-record by separating the velocity fluctuations from the mean velocity. To perform the Reynolds decomposition, we first have to clarify what is meant by the mean velocity.

Generally, we have to distinguish between the global mean velocity $\boldsymbol{U} = \langle \boldsymbol{u}(\boldsymbol{x},t)\rangle = U\boldsymbol{e}_1$, which is independent of time and space since $\boldsymbol{u}(\boldsymbol{x},t)$ is assumed to be statistically stationary and homogeneous, the volume-averaged velocity $\langle \boldsymbol{u}(\boldsymbol{x},t)\rangle_R$ over a sphere of radius R, the time-averaged velocity $\langle \boldsymbol{u}(\boldsymbol{x},t)\rangle_\tau$ over a time interval τ, and the ensemble-averaged velocity $\langle \boldsymbol{u}(\boldsymbol{x},t)\rangle_N$ over N realizations [5, 41, among others]. In this work, $\langle\cdot\rangle$ denotes the global mean, i.e. for infinitely large averaging windows in time or space. Implicitly, $\langle \boldsymbol{u}(\boldsymbol{x},t)\rangle_R = 3/(4\pi R^3)\iiint_0^R \mathrm{d}\boldsymbol{x}\, u(\boldsymbol{x},t)$ and $\langle \boldsymbol{u}(\boldsymbol{x},t)\rangle_\tau = \frac{1}{\tau}\int_{-\tau/2}^{\tau/2}\mathrm{d}t'\boldsymbol{u}(\boldsymbol{x},t')$ are, respectively, local volume and time averages as both R and τ are typically finite. In the limit of $R, \tau \to \infty$, $\langle \boldsymbol{u}(\boldsymbol{x},t)\rangle_R$ and $\langle \boldsymbol{u}(\boldsymbol{x},t)\rangle_\tau$ tend to $\vec{U}$. For repeatable experiments where identical experimental conditions are guaranteed, $\langle \boldsymbol{u}(\boldsymbol{x},t)\rangle_N$ tends to $\boldsymbol{U}$ when $N \to \infty$.

Here we define the mean of a one-dimensional velocity time-record in the longitudinal direction by

$$U_\tau = \langle u_1(t)\rangle_\tau = \frac{1}{\tau}\int_{-\tau/2}^{\tau/2} \mathrm{d}t' u_1(t') \,, \tag{3.1}$$

such that $U = \lim_{\tau\to\infty} U_\tau$ where τ is the *averaging window*. It should be noted that the global mean of the transverse velocity will be equal to zero, i.e. $\langle u_{2,3}(t)\rangle_\tau = 0$ when $\tau \to \infty$, since here it is assumed that they are orthogonal to the mean flow direction.

According to the Reynolds decomposition, the longitudinal velocity time record is composed of the mean velocity U and the random velocity fluctuation component $u_1'(t) = u_1(t) - U$ so that the mean of the longitudinal velocity fluctuations $\langle u_1'(t)\rangle = 0$. This is also true for other components of the velocity.

In certain circumstances, it is possible to map $u_1'(t)$ from time to space coordinates by applying the Taylor's (frozen-eddy) hypothesis [41, 156], which relates temporal and spatial velocity statistics. Taylor argues that eddies can be regarded as *frozen* in time if they are passing the probing volume much faster than they evolve in time. This is the case if the turbulence intensity $I = \sigma_{u_1'}/U$ is much smaller than the unity, i.e. $I \ll 1$, where $\sigma_{u_1'} = \langle u_1'^2\rangle^{1/2}$ is the Root-Mean-Square (RMS) velocity fluctuation. Then, the series of time lags $\Delta t = t - t_0$ relative to the start time t_0 is mapped onto a distance vector with $\boldsymbol{x} = \boldsymbol{x}_0 + U\Delta t\, \boldsymbol{e}_1$ [156] where $\boldsymbol{x}_0$ is the initial position at time t_0. This approach is found to be reliable for $I \lesssim 0.25$ [54, 157, 158] while it has been shown to fail when $I > 0.5$ [159]. The application of Taylor's hypothesis is inaccurate in case of large-scale variations of the velocity fluctuation field comparable to the mean velocity, which are known as "random sweeping velocity" [160, 161] and which can be approximated by the turbulence intensity [158]. Complicating the estimation of the mean velocity, random sweeping causes the mean energy dissipation rate to be consistently overestimated [137, 162].

One way to cope with non-stationary velocity time records is to evaluate the mean velocity for a subset of this signal. If the averaging time τ is finite, the time average U_τ may differ from the mean velocity U causing a systematic bias in the subsequent data analysis. The estimation variance of the time average U_τ can be analytically expressed as [5, 41, among others]

$$\langle (U_\tau - U)^2\rangle \approx \frac{2\langle u_1'^2\rangle T}{\tau} \,, \tag{3.2}$$

where T is the integral time scale and $\langle u_1'^2\rangle$ the variance of the velocity time series. Notably, the size of the averaging window has to be large enough such that it fulfills $\langle u_1'(t)\rangle_\tau \approx 0$ to apply the Reynolds decomposition. This expression can be converted to space invoking Taylor's hypothesis.

3.2.2 Preliminaries on Second-Order Statistics

As discussed in detail below, the mean energy dissipation rate can be related to second-order statistics of the velocity field, either in terms of velocity gradients or in terms of velocity increments. In any case, the two-point velocity covariance tensor turns out to be the central quantity of interest, from which the second-order structure function tensor, the spectral energy tensor and the velocity gradient covariance tensor can be obtained.

In the following, we assume zero-mean SHI turbulence so that two-point quantities depend only on the separation vector $\boldsymbol{r}$, all averages are invariant under rotations of the coordinate system, and the mean squared velocity fluctuation is identical for all velocity components, i.e. $\langle u'^2 \rangle = \langle u_1'^2 \rangle = \langle u_2'^2 \rangle = \langle u_3'^2 \rangle$. We provide an overview of the most relevant definitions, their notation and conventions. This section does not explicitly discuss the effect of the averaging window, but the definitions presented can be applied to windowed inputs with no or straightforward modifications.

Under the given assumptions, the two-point velocity covariance tensor takes the form [e.g. 5, 45, 46]

$$R_{ij}(\boldsymbol{r}) = \langle u_i'(\boldsymbol{x}+\boldsymbol{r},t) u_j'(\boldsymbol{x},t) \rangle = \langle u'^2 \rangle \left(g(r)\delta_{ij} + [f(r) - g(r)] \frac{r_i r_j}{r^2} \right) , \tag{3.3}$$

where $f(r) = R_{11}(r)/R_{11}(0)$ and $g(r) = f(r) + r\partial_r f(r)/2$ are the longitudinal and transverse autocorrelation functions, respectively, with $f(0) = g(0) = 1$. Notably, if one chooses $\boldsymbol{r} = r\boldsymbol{e}_1$, $R_{11}(r) = \langle u'^2 \rangle f(r)$, $R_{22}(r) = R_{33}(r) = \langle u'^2 \rangle g(r)$, and all other components vanish [e.g. 5]. As a remarkable consequence, $R_{ij}(\boldsymbol{r})$ is uniquely defined by $f(r)$ in isotropic turbulence. As mentioned below, the integral length scale as well as the Taylor microscale are determined by $f(r)$ [5].

Analogously, a covariance tensor can be defined for velocity increments, i.e. the second-order velocity structure function tensor [5, 42]

$$D_{ij}(\boldsymbol{r}) = \langle [u_i'(\boldsymbol{x}+\boldsymbol{r},t) - u_i'(\boldsymbol{x},t)] \left[u_j'(\boldsymbol{x}+\boldsymbol{r},t) - u_j'(\boldsymbol{x},t) \right] \rangle \tag{3.4}$$

$$= D_{NN}(r)\delta_{ij} + [D_{LL}(r) - D_{NN}(r)] \frac{r_i r_j}{r^2} . \tag{3.5}$$

The longitudinal second-order structure function $D_{11}(r)$ is related to $f(r)$ by [e.g. 5, 42]

$$D_{11}(\boldsymbol{r} = r\boldsymbol{e}_1) = D_{LL}(r) = \langle (u_1'(\boldsymbol{x}+r\boldsymbol{e}_1,t) - u_1'(\boldsymbol{x},t))^2 \rangle = 2\langle u'^2 \rangle (1 - f(r)) . \tag{3.6}$$

As explained below, measuring the longitudinal second-order structure function $D_{LL}(r)$, the mean energy dissipation rate can be inferred from the inertial-range scaling of the longitudinal structure function (cf. Eq. (3.15)).

Furthermore, the velocity gradient covariance tensor can also be defined in terms of the velocity covariance tensor

$$R_{ijkl}(\boldsymbol{r}) = \left\langle \frac{\partial u'_i(\boldsymbol{x},t)}{\partial x_k} \frac{\partial u'_j(\boldsymbol{x},t)}{\partial x_l} \right\rangle = -\lim_{r\to 0} \partial_{r_k} \partial_{r_l} R_{ij}(\boldsymbol{r}) \,. \tag{3.7}$$

Since the local and instantaneous energy dissipation rate (cf. Eq. (3.11)) is defined in terms of the strain rate tensor $S_{ik} = (\partial u'_i(\boldsymbol{x},t)/\partial x_k + \partial u'_k(\boldsymbol{x},t)/\partial x_i)/2$, the mean energy dissipation rate can be directly related to contractions of the velocity gradient covariance tensor. Note that in a turbulent flow with zero-mean velocity, the strain rate tensor S_{ik} equals the fluctuation strain rate tensor s_{ik}.

The two-point velocity covariance tensor can be expressed in Fourier space through the spectral energy tensor [5]

$$\Phi_{ij}(\boldsymbol{\kappa}) = \frac{1}{(2\pi)^3} \iiint_{-\infty}^{+\infty} R_{ij}(\boldsymbol{r}) e^{-i\boldsymbol{\kappa}\cdot\boldsymbol{r}} \mathrm{d}\boldsymbol{r} \,, \tag{3.8}$$

where $\boldsymbol{\kappa}$ is the wave vector. For SHI turbulence, $\Phi_{ij}(\boldsymbol{\kappa})$ takes the form

$$\Phi_{ij}(\boldsymbol{\kappa}) = \frac{E(\kappa)}{4\pi\kappa^2} \left(\delta_{ij} - \frac{\kappa_i \kappa_j}{\kappa^2} \right) \tag{3.9}$$

where $E(\kappa)$ is the energy spectrum function.

Since access to the full energy spectrum function is not always available, one-dimensional spectra are of interest, too. The mean energy dissipation rate can be estimated from the inertial range scaling of the longitudinal one-dimensional spectrum (as shown in Eq. (3.17)), which can be calculated by both the energy spectrum function and the velocity covariance tensor [5]

$$E_{11}(\kappa_1) = \int_{\kappa_1}^{\infty} \frac{E(\kappa)}{\kappa} \left(1 - \frac{\kappa_1^2}{\kappa^2} \right) \mathrm{d}\kappa = \frac{1}{\pi} \int_{-\infty}^{\infty} R_{11}(\boldsymbol{e}_1 r_1) e^{-i\kappa_1 r_1} \mathrm{d}r_1 \,, \tag{3.10}$$

with the wavenumber κ_1 corresponding to the $\boldsymbol{e}_1$-direction and $R_{11}(0) = \langle u'^2 \rangle = \int_0^\infty E_{11}(\kappa_1) \mathrm{d}\kappa_1$.

This concludes the second-order statistics in terms of the velocity that we consider in the following to determine the mean energy dissipation rate.

3.2.3 Estimating the Energy Dissipation Rate

The energy dissipation rate can be derived from various statistical quantities. A non-exhaustive list of the most common methods applicable to single-point measurements are shown in Table 3.1. Details of selected methods considered in this study are presented in the following subsections. If not explicitly mentioned, the averages denoted with $\langle \cdot \rangle$ are defined globally.

range	Dissipation estimate (Eq.)	symbol	definition	assumption
dissipative sub-range	instantaneous (3.11)	ϵ_0	$2\nu\left(s_{ij}s_{ij}\right)$	
	(local) volume average (3.12)	$\langle\epsilon(\boldsymbol{x},t)\rangle_R$	$\frac{3}{4\pi R^3}\iiint_{\mathcal{V}(R)}\epsilon_0(\boldsymbol{x}+\boldsymbol{r},t)\mathrm{d}\boldsymbol{r}$	SHI
	(longitudinal) gradient (3.14)	ϵ_G	$15\nu\left\langle\left(\frac{\partial u_1'(\boldsymbol{x})}{\partial x_1}\right)^2\right\rangle$	SHI
	2nd-order SF (dissipation range) *	ϵ_{D2}	$15\nu D_{LL}(r)/r^2$	SHI, $r\lesssim\eta_K$
	zero-crossings *	ϵ_+	$15\pi^2\nu\langle u_1'^2\rangle N_L^2$	SHI
inertial sub-range	4/5 law * ((3.15), $n=3$)	ϵ_{I3}	$-5/4D_{LLL}(r)/r$	SHI, K41
	2nd-order SF (inertial range) ((3.15), $n=2$)	ϵ_{I2}	$\left(D_{LL}(r)/C_2\right)^{3/2}/r$	SHI, K41
	spectral (3.17)	ϵ_S	$\left(\frac{\kappa_1^{5/3}E_{11}(\kappa_1)}{18/55C_K}\right)^{3/2}$	SHI, K41
	cutoff filter *	ϵ_C	$\left(\frac{2}{3}\frac{2\langle u_C'^2\rangle}{18/55C_K\left(\kappa_{1,\mathrm{low}}^{-2/3}-\kappa_{1,\mathrm{up}}^{-2/3}\right)}\right)^{3/2}$	SHI, K41
energy injection scale	scaling argument (3.18)	ϵ_L	$C_\epsilon\sigma_{u_1'}^3/L_{11}$	SHI
	(global) mean (3.13)	$\langle\epsilon\rangle$	$\lim\limits_{R\to\infty}\langle\epsilon_0(\boldsymbol{x},t)\rangle_R$	SHI

Table 3.1 Various definitions of the energy dissipation rate from the dissipative and inertial sub-range to the energy injection range. Here, the definitions for various dissipation estimates are given in the space or wavenumber domain where ν is the viscosity, s_{ij} is the velocity fluctuation strain rate tensor, R is the radius of the averaging volume $\mathcal{V}(R)$ (window size for 1D data), $u_1'(\boldsymbol{x})$ is the longitudinal velocity fluctuation field along x_1, $D_{L\ldots}(r)$ is the nth-order longitudinal structure function for distance r, $\langle u_1'^2\rangle$ is the variance of $u_1'(\boldsymbol{x})$, $\sigma_{u_1'}$ is the standard deviation of $u_1'(\boldsymbol{x})$, N_L is the number of zero crossings of a velocity fluctuation signal per unit length, $C_2\approx 2$, $E_{11}(\kappa_1)$ is the one-dimensional energy spectrum with wavenumber κ_1, $C_K\approx 1.5$, $u_C'^2$ is the variance of a band-pass filtered signal for wavenumbers $k\in[k_{\mathrm{low}},k_{\mathrm{up}}]$, C_ϵ is the dissipation constant, L_{11} is the longitudinal integral scale, and η_K is the Kolmogorov length scale. Dissipation estimates indicated with * are not considered in detail in this work. The assumptions of stationarity (S), homogeneity (H), local isotropy (I) and Kolmogorov's second similarity hypothesis from 1941 (K41) are represented by their individual abbreviations. References are given in the corresponding sections in the main text.

Dissipative sub-range

Proceeding from the Navier-Stokes equations for an incompressible, Newtonian fluid, the instantaneous energy dissipation rate is given by [e.g. 5, 42]

$$\epsilon_0(\boldsymbol{x},t) = 2\nu\left(S_{ij}S_{ij}\right) . \tag{3.11}$$

The contribution of the fluctuating part to the energy dissipation is much larger than the contribution of the mean flow in the case of high-Re turbulent flows [5, 138]. Hence, the instantaneous energy dissipation rate can be defined in terms of the velocity fluctuations only [5] where, in Eq. (3.11) and Table 3.1, S_{ij} is replaced by the fluctuation strain rate tensor $s_{ij} = (\partial u_i'(\boldsymbol{x},t)/\partial x_j + \partial u_j'(\boldsymbol{x},t)/\partial x_i)/2$.

Averaged over a sphere with radius R and volume $\mathcal{V}(R)$, the (local) volume average of the instantaneous energy dissipation rate is [5]

$$\langle\epsilon_0(\boldsymbol{x},t)\rangle_R = \frac{3}{4\pi R^3}\iiint_{\mathcal{V}(R)}\epsilon_0(\boldsymbol{x}+\boldsymbol{r},t)\mathrm{d}\boldsymbol{r} . \tag{3.12}$$

The local volume average $\epsilon_R(\boldsymbol{x},t)$ converges to the global mean energy dissipation rate if R tends to infinity:

$$\langle\epsilon\rangle = \lim_{R\to\infty}\langle\epsilon_0(\boldsymbol{x},t)\rangle_R = -\nu\lim_{|\boldsymbol{r}|\to 0}\partial^2_{r_j}R_{ii}(\boldsymbol{r},t) , \tag{3.13}$$

where the right-hand-side follows from partial integration. In experiments, it is often not possible to measure $\epsilon_0(\boldsymbol{x},t)$. Under the assumption of statistically homogeneous and isotropic turbulence, the volume/time averaged energy dissipation rate are typically inferred from one-dimensional surrogates [136, 138, 140, 143, 163, 164, among others], such as:

$$\epsilon_G = -15\nu\lim_{|\boldsymbol{r}|\to 0}\partial^2_{r_1}R_{11}(\boldsymbol{r},t) = 15\nu\left\langle\left(\frac{\partial u_1'(\boldsymbol{x},t)}{\partial x_1}\right)^2\right\rangle = \frac{15\nu}{U^2}\left\langle\left(\frac{\partial u_1'(t)}{\partial t}\right)^2\right\rangle , \tag{3.14}$$

where the mapping between space and time domains is possible by applying the Taylor's hypothesis if $\sigma_{u_1'}/U \ll 1$ [131, 140]. The relationship shown in Eq. (3.14) is often called the "direct" method in the literature [131, 140, e.g.]. The deviation of ϵ_G from its global mean $\langle\epsilon\rangle$ depends quadratically on the turbulence intensity [131, 137, 162, 163].

Inertial sub-range: indirect estimate of energy dissipation rate

Kolmogorov's second similarity hypothesis from 1941 [43] provides another method for estimating the energy dissipation rate in the inertial range. Based on the inertial range scaling of the nth-order longitudinal structure function, the mean energy dissipation rate can be calculated by [5]

$$D_{L\ldots L}(r) = C_n(\epsilon_{In} r)^{\zeta_n} \Leftrightarrow \epsilon_{In} = \left(\frac{D_{L\ldots L}(r)}{C_n}\right)^{1/\zeta_n} \frac{1}{r}\,, \tag{3.15}$$

where C_n is a constant, e.g. $C_2 \approx 2$ [5], and $\zeta_n = n/3$ according to K41 by dimensional analysis. In practice, ϵ_{I2} (Table 3.1) is retrieved either by fitting a constant to the compensated longitudinal second-order structure function $D_{LL}(r)$, $n = 2$ in Eq. (3.15), or a power law ($\propto r^{2/3}$) to the inertial range of D_{LL}, Eq. (3.6), if the inertial range is pronounced over at least a decade. Accounting for intermittency, the scaling exponent of the nth-order structure function is modified to $\zeta_n = \frac{n}{3}[1 - \frac{1}{6}\mu(n-3)]$ where μ is the internal intermittency exponent [49]. The inertial range is bounded by the energy injection scale L at large scales and by the dissipation range at small scales. That is why the fit-range has to be chosen such that $\eta_K \ll r \ll L$. If the inertial range is not sufficiently pronounced, the extended self similarity can be used to extend the inertial range [165, 166]. Otherwise, ϵ_{I2} can also be approximated by the maximum of Eq. (3.15) (for $n = 2$) within the same range as before. This is possible because the maximum lies on the plateau in case of a perfect K41 inertial range scaling.

In the inertial range, the transverse second-order structure function $D_{NN}(r)$ is equal to $4D_{LL}(r)/3$ in a coordinate system where $\boldsymbol{r} = r\boldsymbol{e}_1$ is parallel to the longitudinal flow direction [5] highlighting the importance of the measurement direction.

Inertial sub-range: spectral method

According to K41 [43], the inertial subrange of the energy spectrum function scales as $E(\kappa) \propto \langle\epsilon\rangle^{2/3}\kappa^{-5/3}$ with the wavenumber κ by dimensional analysis. In isotropic turbulence, the energy spectrum function can be converted into a one-dimensional energy spectrum $E_{11}(\kappa_1)$ (Eq. (3.10)). The wavenumber space is not directly accessible from time-resolved point-like velocity measurements. Given the validity of Taylor's hypothesis, the one-dimensional energy spectrum $E_{11}(\kappa_1)$ transforms to the frequency domain with $F_{11}(f) = 2\pi E_{11}(\kappa_1)/U$ where $\kappa_1 = 2\pi f/U$ [e.g. 137, 167] yielding:

$$F_{11}(f) = 18/55 C_K \left(\frac{U}{2\pi}\epsilon_S\right)^{2/3} f^{-5/3}\,, \tag{3.16}$$

which yields

$$\epsilon_S = \frac{2\pi}{U}\left(\frac{f^{5/3}F_{11}(f)}{18/55 C_K}\right)^{3/2}\,, \tag{3.17}$$

with the one-dimensional Kolmogorov constant $C_K = 1.5$ [5, 168]. Applying Taylor's hypothesis to a flow with a randomly sweeping mean velocity causes the Kolmogorov constant to be systematically overestimated whereas the scaling of power-law spectra remains unaffected [158, 169]. Hence, Eq. (3.17) is still valid for a randomly sweeping mean velocity although ϵ_S is overestimated if C_K is not corrected for random sweeping.

F_{11} has the units of a power spectral density m^2/s and $\langle u_1'^2 \rangle = \int_0^\infty F_{11}(f)\mathrm{d}f$. Depending on the Fourier transform convention, the prefactor of C_K might vary [41, e.g.]. Under the assumption of Kolmogorov scaling in the inertial sub-range, this identity can be adopted to estimate the mean energy dissipation rate from low and moderate resolution velocity measurements of a finite averaging window [87, 140, 142, 170].

Energy injection scale

In equilibrium turbulence, the rate at which turbulent kinetic energy is transported across eddies of a given size is constant in the inertial range assuming high enough Reynolds numbers [e.g. 171]. By dimensional argument, this rate is proportional to $u^3(l)/l$, where $u(l)$ is the characteristic velocity scale of eddies of length l. Considering the integral scale L_{11} and its characteristic velocity scale $u(L_{11})$, namely the RMS velocity fluctuation $\sigma_{u_1'}$, the mean energy dissipation rate can be calculated by [143]

$$\epsilon_L = C_\epsilon \frac{\sigma_{u_1'}^3}{L_{11}} , \tag{3.18}$$

where C_ϵ is the dissipation constant and for time- and space-varying turbulence, it depends on both initial as well as boundary conditions and the large-scale structure of the flow [47, 145, 172, 173]. C_ϵ is found to be about 0.5 for shear turbulence [47, 174] and 1.0 [172, 175] (or 0.73 Sreenivasan [47]) for grid turbulence. In this work C_ϵ is assumed to be 0.5 which holds approximately in a variety of flows [54, 168, and references therein].

Usually, the longitudinal integral length scale L_{11} is defined as [5]

$$L_{11} = \lim_{r\to\infty} \int_0^r \mathrm{d}r' f(r') = \frac{\pi E_{11}(0)}{2\langle u_1'^2 \rangle} , \tag{3.19}$$

However, due to experimental limitations, r is often given by the first zero-crossing of $f(r)$ in both laboratory and *in situ* measurements [54, e.g.], or, alternatively, by the position where $f(r) = 1/e$ [176, 177]. Griffin et al. [178] carried out an integration for $r \to \infty$ performing an exponential fit in the vicinity of $f(r) = 1/e$. Notably, $E_{11}(0) = \int_0^\infty \mathrm{d}\kappa E(\kappa)/\kappa$ so that the estimation of L_{11} from the power spectrum is only recommended if $E(\kappa) = \frac{1}{2}\kappa^3 \frac{\mathrm{d}}{\mathrm{d}\kappa}\left(\frac{1}{\kappa}\frac{\mathrm{d}E_{11}(\kappa)}{\mathrm{d}\kappa}\right)$ [5] is accurately determined like in DNS. This approach not only requires a fully resolved velocity measurement but also a well converged $E_{11}(\kappa_1)$ as the conversion is highly sensitive to statistical scatter.

Ultimately, the choice of L_{11} strongly affects ϵ_L. In this work, we integrate $f(r)$ to the first zero-crossing because it does not depend on assumptions on the decay of $f(r)$ and the choice of the fit-range.

3.2.4 Simulations of homogeneous isotropic turbulence

In this study, the direct numerical simulations of statistically homogeneous isotropic turbulent flow with $74 \leq \mathrm{R}_\lambda \leq 321$ are used as the basis for evaluating the different methods for determining the dissipation rate, see Table 3.2. Thereby, the performance of the different methods to estimate the energy dissipation rate is not affected by violating fundamental assumptions, e.g., anisotropy or inhomogeneity. We assume that the velocity probe records idealized velocity time series neglecting the effect of transfer functions [e.g. 179, 180, regarding sonic anemometry] or noise [139, 146, 181].

The simulations are carried out with the parallelized solver TurTLE [115], which solves the Navier-Stokes equations on a periodic domain using a pseudo-spectral method with a third-order Runge-Kutta time stepping. Here we use a forcing scheme with a fixed energy injection rate on large scales. With this we reach a statistically stationary state of homogeneous isotropic turbulence within approximately two to three integral times.

To mimic an ensemble of single-point measurements, we introduced 1000 virtual, i.e. non-interacting probes into the flow, which move with a given constant speed in randomly-directed straight paths to record the local flow velocity. While the root mean square velocity fluctuation is determined by the Navier-Stokes simulation, we can control the mean flow speed through the speed of the virtual probe. The range of used constant speeds corresponds to turbulence intensities of 1-50%. Along the trajectories, we then sample the local three-dimensional velocity field (see Fig. 3.1) as well as the velocity gradient field, where we use spline-interpolation of order 5 to determine values in between grid points, see also [115, 182]. By projecting the velocity vector on the direction of the trajectory, $\boldsymbol{e}_1$, and the orthogonal directions, $\boldsymbol{e}_2$ and $\boldsymbol{e}_3$, we split the velocity field in longitudinal and transverse components, respectively. From the sampled velocity gradient tensor we compute the local instantaneous dissipation ϵ_0. The time step is limited either by the stability requirements of the flow solver or, for smaller turbulence intensities, by the required sampling frequency to capture the underlying flow. Here, we choose the time step such that the distance traveled by the probe within one step is around a tenth of the grid spacing, $\Delta t \approx 0.1\frac{\Delta x}{U}$. The grid spacing is chosen such that the highest wavenumber $k_{\max}$ satisfies $k_{\max}\eta \approx 3$.

Using Taylor's hypothesis, the longitudinal velocity time series correspond on average to $\sim 3000\eta_K$ (for more details see Table 3.2) so that second- and third-order moments of both longitudinal velocity fluctuations and increments are reasonably converged (see Fig. 3.12). To estimate ϵ_{I3}, ϵ_{I2} and ϵ_S, the longitudinal structure functions are evaluated for scales $20\eta_K \leq r \leq 500\eta_K$ or in frequency domain for $\frac{U}{500\eta_K} \leq f \leq \frac{U}{20\eta_K}$.

3.2.5 Variable Density Turbulence Tunnel

To evaluate the performance of different methods at Reynolds numbers applicable to atmospheric flows, we use the high-resolution hot-wire measurements of the longitudinal velocity components of the Variable Density Turbulence Tunnel [VDDT, 36]. The

case id	box size	R_λ	$\dot{E}$ [c.u.]	$k_{\max}\eta_K$	η_K [c.u.]	I	L_{11}/η_K	$\mathcal{L}/L_{11}$	N_p [#]
DNS 1.1	512	74	0.4	3	0.015	0.01	41.2	161	10000
DNS 1.2	512	74	0.4	3	0.015	0.05	41.4	160	10000
DNS 1.3	512	74	0.4	3	0.015	0.1	41.3	160	10000
DNS 1.4	512	74	0.4	3	0.015	0.24	41.3	21	10000
DNS 1.5	512	74	0.4	3	0.015	0.5	41.4	16	10000
DNS 2.0	1024	142	0.4	3	0.007	0.11	99.0	332.8	1000
DNS 2.1	1024	219	0.4	3	0.007	0.011	147.8	15.6	1000
DNS 2.2	1024	217	0.4	3	0.007	0.055	147.6	15.7	1000
DNS 2.3	1024	216	0.4	3	0.007	0.11	147.9	15.6	1000
DNS 2.4	1024	212	0.4	3	0.007	0.27	146.8	15.7	1000
DNS 2.5	1024	207	0.4	3	0.007	0.53	145.5	15.8	1000
DNS 3.1	2048	302	0.5	3	0.0034	0.011	260.9	13.6	1000
DNS 3.2	2048	299	0.5	3	0.0034	0.054	258.2	13.8	1000
DNS 3.3	2048	295	0.5	3	0.0034	0.11	254.8	14.0	1000
DNS 3.4	2048	314	0.5	3	0.0035	0.26	275.6	20.2	1000
DNS 3.5	2048	321	0.5	3	0.0035	0.53	282.9	14.7	1000

Table 3.2 Parameter overview for each DNS. R_λ is the Taylor scale Reynolds number, $\dot{E}$ the energy injection rate in code units (c.u.), $k_{\max}$ the largest resolved wavenumber, η_K the Kolmogorov length scale, $I = \sigma_{u_1'}/U$ is the turbulence intensity, L_{11} the longitudinal integral length scale derived from $E(\kappa)$, $\mathcal{L}$ is the average probe track distance and N_p the number of virtual probes. The turbulence intensity I is controlled by setting the probe mean velocity where $\sigma_{u_1'} \approx 1$ is the root mean square longitudinal velocity fluctuation.

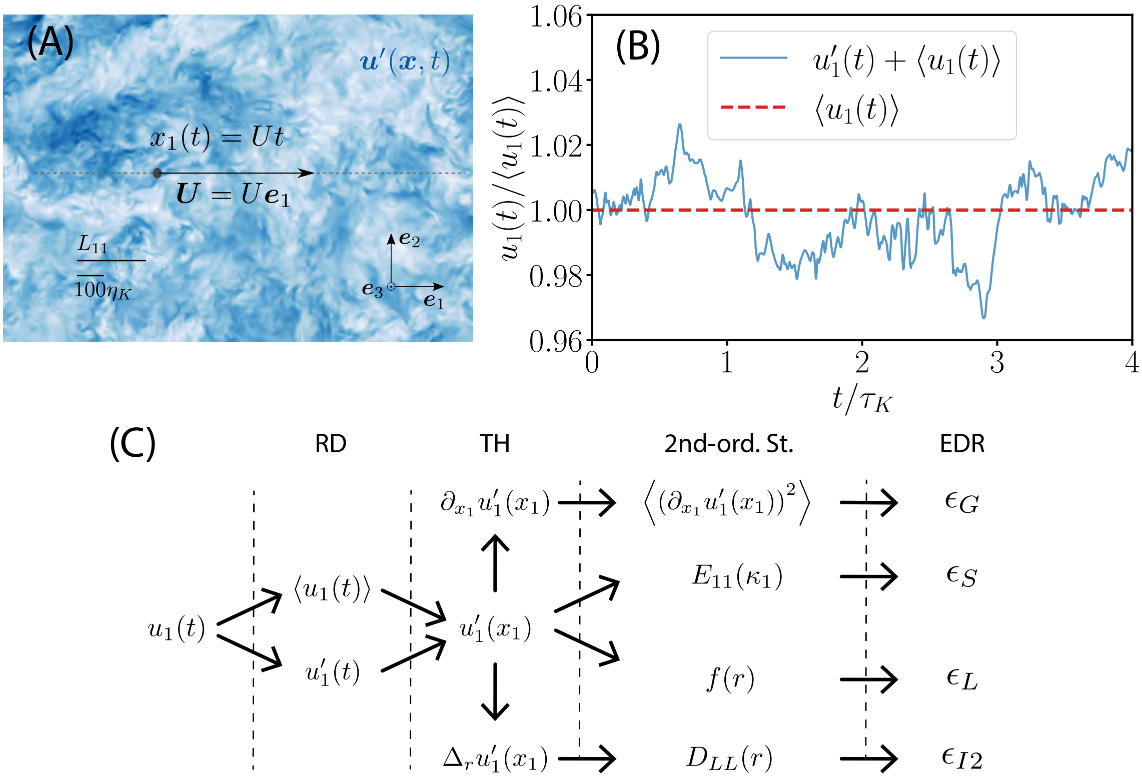
(A)
$\boldsymbol{u}'(\boldsymbol{x},t)$
$x_1(t) = Ut$
$\boldsymbol{U} = U\boldsymbol{e}_1$
L_{11}
$100\eta_K$
$\boldsymbol{e}_2$
$\boldsymbol{e}_3$
$\boldsymbol{e}_1$
(B)
$u_1'(t) + \langle u_1(t)\rangle$
$\langle u_1(t)\rangle$
$u_1(t)/\langle u_1(t)\rangle$
1.06
1.04
1.02
1.00
0.98
0.96
0
1
2
3
4
t/τ_K
(C)
RD
TH
2nd-ord. St.
EDR
$u_1(t)$
$\langle u_1(t)\rangle$
$u_1'(t)$
$u_1'(x_1)$
$\partial_{x_1} u_1'(x_1)$
$\Delta_r u_1'(x_1)$
$\left\langle (\partial_{x_1} u_1'(x_1))^2 \right\rangle$
$E_{11}(\kappa_1)$
$f(r)$
$D_{LL}(r)$
ϵ_G
ϵ_S
ϵ_L
ϵ_{I2}

Figure 3.1 From single-point velocity time records to the energy dissipation rate. (A) A virtual probe is sampling the three-dimensional velocity field of the DNS 3.1 (see Table 3.2) in time and space at a mean velocity U along its $\boldsymbol{e}_1$-direction corresponding to turbulence intensity of 1%. (B) *One*-dimensional velocity time series $u_1(t)$ (blue solid) with corresponding time average $U = \langle u_1(t)\rangle$ (Eq. (3.1), red dashed line) of the same DNS 3.1, where both $u_1(t)$ and U are re-scaled by U. (C) Visualization of the workflow from one-dimensional velocity time record $u_1(t)$ to the energy dissipation rate via different methods. First, $u_1(t)$ is decomposed in its mean and fluctuating part according to Reynolds decomposition (RD). Then, the velocity time series is converted into a one-dimensional velocity field invoking Taylor's hypothesis (TH). Subsequently, second-order statistics (2nd-ord. St.) of the longitudinal velocity fluctuations, its increments and first spatial derivative are inferred from which the energy dissipation rate is estimated with the help of different methods.

VDTT data used here is associated with R_λ between 1470 and 5864, which enables us to bridge the gap between DNS ($74 \leq \mathrm{R}_\lambda \leq 321$) and atmospheric $\mathrm{R}_\lambda \sim \mathcal{O}(10^3)$.

The VDTT is a recirculating wind tunnel where the working gas SF_6 is pressurized up to 15 bar. The VDTT has a horizontal length of 11.68 m and an inner diameter of 1.52 m where the rotation frequency of the fan sets the mean flow velocity ranging from 0.5 m/s to 5.5 m/s [36]. Long-range correlations of the turbulent flow determine its anisotropy. These long-range correlations are shaped with the help of an active grid consisting of 111 independently rotating winglets [155, 183]. The angular orientation of each winglet $\vartheta(t, y, z)$ can be individually adjusted in space and time by a control software depending on spatio-temporal grid-correlations [178]:

$$\vartheta(t, y, z) = \int K(t', y', z') A(t - t', y - y', z - z') \mathrm{d}t' \mathrm{d}y' \mathrm{d}z' \,, \tag{3.20}$$

where A is a three-dimensional random matrix of winglet angles and K is the correlation kernel. The turbulence in the experiments with $\mathrm{R}_\lambda \in \{4141, 5006, 5865\}$ was driven in an anisotropic way [183].

Longitudinal velocity fluctuations are temporally recorded with 30 μm to 60 μm long nanoscale thermal anemometry probes [NSTAP; 184, 185, among others] or a 450 μm long conventional hot-wire from Dantec [186] corresponding to a resolution of $< 3\eta_K$ and $< 5\eta_K$, respectively [155] at variable distances from the active grid ranging from $\approx 6{-}9\,\mathrm{m}$. The velocity measurements have been extensively characterized in terms of the mean flow profiles [183] as well as the decay of turbulent kinetic energy [147, 187] exposing velocity probability distribution functions (PDF) being flatter than Gaussian [183]. The inertial range scaling exponent ζ_2 of the longitudinal second-order structure function is in agreement with Kolmogorov's revised phenomenology from 1962 ($\zeta_2 = 0.693 \pm 0.003$ for $\mathrm{R}_\lambda > 2000$) for a large variety of wake generation schemes [188].

3.2.6 Quantification of systematic and random errors

Virtual probes record one-dimensional time records of DNS longitudinal velocity, from which the mean energy dissipation rate can be estimated by various methods and compared with the energy dissipation rate obtained directly from the DNS dissipation field. Generally, there are two different errors when estimating the mean energy dissipation rate, namely the systematic errors and random errors. The latter is related to the estimation variance of the mean energy dissipation rate, i.e. the statistical scatter of the $\langle\epsilon\rangle$-estimates around the true mean. The systematic error of the mean energy dissipation rate expresses itself in a non-vanishing ensemble average of the deviations from the ground-truth.

Systematic errors are an inherent feature of the methods used for estimating the dissipation rate, but are also affected by experimental limitations/imperfections such as averaging windows and finite turbulence intensity parameterized by R and I, respectively. One way to estimate these errors is to compare the estimated mean energy dissipation rate for a given averaging window R to the ground-truth of the DNS defined by the mean energy dissipation rate per virtual-probe track, i.e., $\langle \epsilon_0(\boldsymbol{x}, t) \rangle_R$. Another possibility would be to compare the estimates to the ensemble average of the mean energy dissipation rate from all virtual probes, i.e., $\langle \epsilon_0(\boldsymbol{x}, t) \rangle_R \rangle_N$. Either of these possibilities is valid and would be interesting to understand. However, our analysis shows that the second approach is associated with a slightly higher absolute value and a slightly higher standard deviation. For that reason, we have chosen the second approach to make a conservative assessment of the systematic errors, i.e., we compare the estimates of each method against $\langle \langle \epsilon_0(\boldsymbol{x}, t) \rangle_R \rangle_N$, by

$$\beta_i = \frac{\langle \epsilon_i \rangle_R}{\langle \langle \epsilon_0(\boldsymbol{x}, t) \rangle_R \rangle_N} - 1 \, , \tag{3.21}$$

where $i \in \{G, I3, I2, S, L\}$ and $\langle \epsilon_i \rangle_R$ is the estimate of the energy dissipation rate via method i under the experimental limitations/imperfection such as size of averaging window or finite turbulence intensity. To help distinguish between the different error terms in this manuscript, we refer to β as "reference-compared" systematic error.

In addition, the systematic error can be evaluated by comparing the estimates of the energy dissipation rate obtained by a method with imperfect data against the estimates obtained by the same method with optimal data. We denote these types of errors with δ and refer to them as "self-compared" errors. An experimental imperfection we considered here is the sensor misalignment, which is a non-zero angle of incidence θ between the longitudinal flow direction that sensor expect and U. To investigate the isolated effect of sensor misalignment, we consider a specific set of DNS with constant turbulence intensity ($I = 1\%$) and the entire track length for each virtual probe. The self-compared systematic error of each method due to misalignment is defined as

$$\delta_i(\theta) = \frac{\epsilon_i(\theta)}{\epsilon_i(0)} - 1 \, , \tag{3.22}$$

where $\epsilon_i(\theta)$ is the estimate of the energy dissipation rate via method $i \in \{G, I3, I2, S, L\}$ from data with misalignment θ and $\epsilon_i(0)$ is the estimated dissipation rate from the same method and flow conditions but with an aligned sensor, i.e. $\theta = 0$.

Estimates of the mean energy dissipation rate are susceptible not only to systematic errors, but also to random errors due to statistical uncertainty. For the averaging window, errors given by Eq. (3.21) would be the best indicator of systematic errors. However, random errors due to size of averaging window can also be significant. When the spatial averaging window R (or temporal averaging window τ) is finite, we capture the self-compared random error for each individual method by

$$\delta_i(R) = \sqrt{\left\langle \left(\frac{\langle \epsilon_i \rangle_R}{\langle \langle \epsilon_i \rangle_R \rangle_N} - 1 \right)^2 \right\rangle_N} \, , \tag{3.23}$$

where $\langle \epsilon_i \rangle_R$ is the local mean energy dissipation rate based on the averaging window

R normalised by its ensemble average, i.e. $\langle\langle\epsilon_i\rangle_R\rangle_N$. Eq. (3.23) indeed calculates the standard deviation of the normalized $\langle\epsilon_i\rangle_R$, which is used here as a proxy for the random error.

Symbol	Definition	Equation
β_i	reference-compared systematic error, i.e. relative to ground-truth reference $\langle\langle\epsilon_0(\boldsymbol{x},t)\rangle_R\rangle_N$	(3.21)
$\delta_i(\theta)$	self-compared (systematic) error of each method at a given misalignment angle θ, relative to the estimates provided by the same method but at $\theta = 0$	(3.22)
$\delta_i(R)$	self-compared (random) error due to finite R or τ	(3.23)

Table 3.3 Overview of investigated errors and their definitions. $i \in \{G, I3, I2, S, L\}$, where G stands for gradient method, $I3$ for 4/5 law, $I2$ for second-order structure function in the inertial range, S for the spectral method, and L for the scaling argument. The averaging window is denoted spatially by R and temporally by τ. The misalignment angle is represented by θ. The superscripts "sys" and "rnd" denote the systematic and random nature of the errors, respectively.

3.3 Results and Discussion

In the following, we first focus on the DNS data to calculate $\epsilon_G, \epsilon_{I3}, \epsilon_{I2}, \epsilon_S$, and ϵ_L from the entire longitudinal velocity time records of all virtual probes and compare these estimates against the ground-truth reference. Then, we systematically investigate the impact of turbulence intensity, (virtual) probe orientation, and averaging window size for all methods of interest. The influence of flow Reynolds number on the presented results are then discussed by taking into account the VDTT data together with the DNS data. Finally, we provide a proof of concept for a time-dependent dissipation rate calculation by comparing the dissipation time series measured by ϵ_G, ϵ_{I2}, and ϵ_L and its coarse-grained surrogate. In the following, we use the definitions of systematic and random errors as mentioned in Sec. 3.2.6.

3.3.1 Verification of the analytical methods and a first insight into their performance under ideal conditions

To verify the implementation of our methods, only data from cases with a low turbulence intensity of 0.01 and an averaging window covering the entire size of the probe track are used in this section. Furthermore, ϵ_{I2} and ϵ_{I3} are obtained by a fit according to Eq. (3.15) with $n = 2$ and $n = 3$, respectively, in the inertial range with $r \in [20\eta_K, 500\eta_K]$ for DNS 2.1 and 3.1. Analogously, ϵ_S is inferred from the inertial range fit, Eq. (3.17), in the range $f \in [U/(500\eta_K), U/(20\eta_K)]$. Due to the absence of an inertial range for low Taylor-scale Reynolds number (DNS 1.1 with $\mathrm{R}_\lambda = 74$, compare Fig. 3.16), the maximum of Eq. (3.15) is used to infer ϵ_{I2} and ϵ_{I3}.

The distribution of the mean energy dissipation rate estimated by $\epsilon_G, \epsilon_{I2}, \epsilon_{I3}, \epsilon_S$, and ϵ_L for each probe at $\mathrm{R}_\lambda = 302$ is shown in Fig. 3.2. Estimations for other R_λ are shown in supplementary Fig. 3.10. The ground-truth reference for the mean energy dissipation

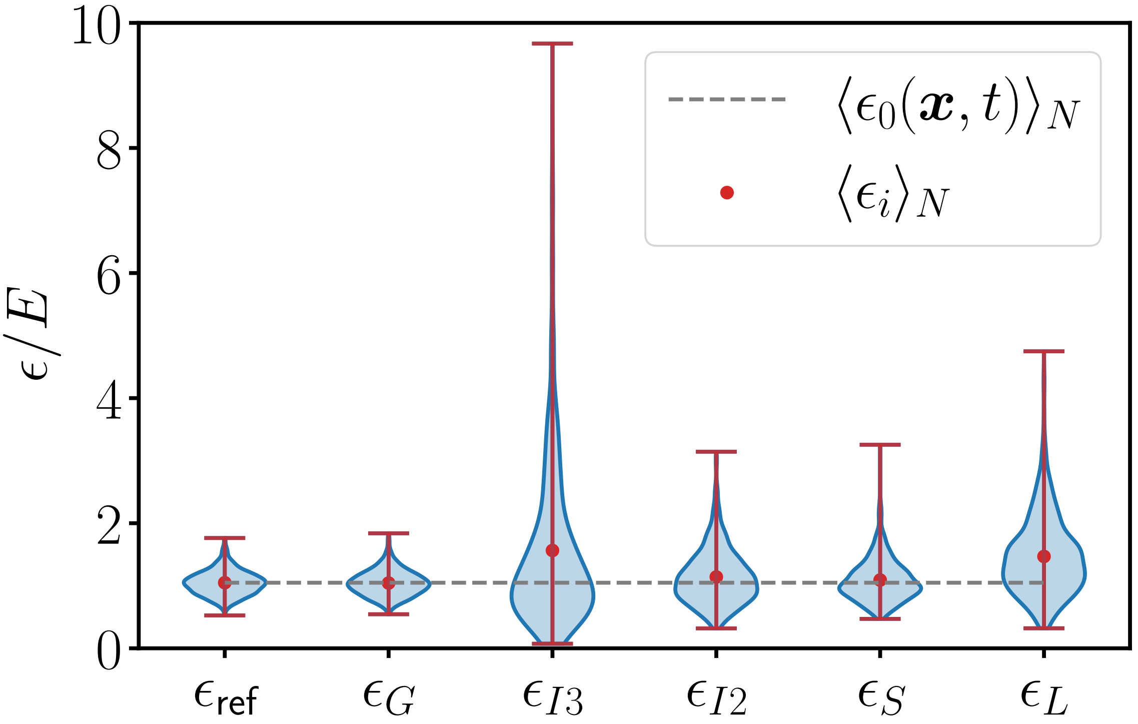

Figure 3.2 Validation of estimating the energy dissipation rate from $\epsilon_G, \epsilon_{I2}, \epsilon_{I3}, \epsilon_S$, and ϵ_L re-scaled by the energy injection rate $\dot{E}$. The data are taken from DNS 3.1 with 1000 probes, $\mathrm{R}_\lambda = 302$, $I = 1\%$, $\theta = 0°$ and maximal available averaging window ($R \approx 3550\eta_K$). The ensemble mean of each method $\langle\epsilon_i\rangle_N$ is denoted by red dots where the whiskers extend from the minimal to maximal estimate of ϵ_i where $i \in \{G, I3, I2, S, L\}$. The reference mean energy dissipation rate for each probe is given by ϵ_{ref}. The dashed line represents the re-scaled global mean energy dissipation rate of DNS 3.1 which is approximated by the ensemble average of the true mean energy dissipation rate along the trajectory of each virtual probe.

rate for each probe is given by $\epsilon_{\mathrm{ref}} = \langle\epsilon_0(\boldsymbol{x}, t)\rangle$ along the probe trajectory $\boldsymbol{x}$, which is the average of the instantaneous energy dissipation rate along the trajectory of each individual virtual probe (mean, median, standard deviation, range of β_{ref}: 0%, −0.7%, 18.6%, −50% . . . 68.2%) where $\beta_{\mathrm{ref}} = \langle\epsilon_0(\boldsymbol{x}, t)\rangle/\langle\langle\epsilon_0(\boldsymbol{x}, t)\rangle\rangle_N - 1$. The best performing method is the gradient method ϵ_G (mean, median, standard deviation, range of β_G: −0.5%, 1.7%, 19.3%, −48.1% . . . 75.4%). The range of β_G, i.e. −49.8% . . . 68.2%., is also very close to the range of β_{ref}. The method with highest error is ϵ_{I3} (mean, median, standard deviation, range of β_{I3}: 49.2%, 10.1%, 59.6%, −93.1% . . . 822.2%). The superior performance of ϵ_G compared to others is mainly due to the fact that it relies on second-order dissipative statistics that can be captured with fast statistical convergence within a short sampling interval. Hence, the distribution of ϵ_G and ϵ_{ref} are similar. ϵ_{I3}, on the other hand, relies on third-order moments of the velocity increments of inertial scales associated with slower statistical convergence compared to ϵ_G. Hence, longer velocity records under stationary conditions are needed. For this reason, the third-order structure function is not considered further in this study, as one of the main objectives of this study is to evaluate different methods suitable for extracting the time-dependent energy dissipation rate.

Fig. 3.2 also shows that the estimates of the energy dissipation rate provided by $D_{LL}(r)$ and $E_{11}(\kappa_1)$ are close to each other, which can be explained by the fact that they are both second-order quantities (in real and Fourier space, respectively) connected by $f(r)$. Furthermore, ϵ_{I2} tends to overestimate the energy dissipation rate as the mean is 8.8% higher than $\langle\epsilon(\boldsymbol{x},t)\rangle_N$ (median $\beta_{I2} \sim 3.1\%$, standard deviation 41.7%, $-69.6\% < \beta_{I2} < 199.8\%$). ϵ_S exhibits a similar overestimation (mean $\beta_S \sim 4.1\%$, median $\beta_S \sim -2.0\%$, standard deviation 32.1%, $-55.2\% < \beta_S < 210.4\%$), though to a lesser extent. However, ϵ_S depends much stronger on properly setting the fit-range than ϵ_{I2} (supplementary Fig. 3.11). The spectral method ϵ_S can differ by a factor of 2 from ϵ_{I2} depending on the high-frequency limit. This factor of 2 is in accordance with a comparison of ϵ_{I2} and ϵ_S by a linear fit resulting in a slope close to 0.5 [154]. In the DNS, the power spectrum is subject to strong statistical uncertainty at high frequencies without ensemble-averaging the spectra of each virtual probe or longer DNS runtimes. As the high-frequency limit of the inertial range of the spectrum is hardly distinguishable from its dissipation range, the choice of the fit-range range for ϵ_S is related to the fit-range of the longitudinal second-order structure function by $f \in [U/(500\eta_K), U/(20\eta_K)]$ as mentioned above. Wacławczyk et al. [153] found that the estimation of the energy dissipation rate from the power spectral density is generally robust at small wavenumbers whereas the second-order structure function performs better at larger wavenumbers. With our choice of the fit-range $r \in [20\eta_K, 500\eta_K]$, we confirm that ϵ_{I2} is already reliable at the lower end of the inertial range where dissipative effects are negligible.

At last, ϵ_L overestimates $\langle\epsilon(\boldsymbol{x},t)\rangle_N$ by 40% on average (median $\beta_L \sim 31.5\%$, $-69.5\% < \beta_L < 352.9\%$). This systematic overestimation might be due to the difficulty in determining L_{11} as different methods for estimating the integral length L_{11} can contribute to the systematic bias of ϵ_L. As mentioned above, we infer the longitudinal integral length from fitting $f(r)$ to the first zero crossing which yields, at least in the DNS of this work, a systematic underestimation, as illustrated in Fig. 3.12. Figure 3.12 and 3.13 suggest that the scatter of ϵ_L is affected by the scatter of both $\sigma_{u_1'}$ and L_{11}. However, the accuracy of the dissipation constant C_ϵ, which is a function of large-scale forcing and initial conditions [47, 145, 172, 173], can potentially cause larger mean deviations of ϵ_L from $\langle\epsilon(\boldsymbol{x},t)\rangle_N$. Advantageously, the large-scale estimate ϵ_L is applicable to low-resolution measurements and only weakly biased with respect to the ground-truth of DNS 1.1 where the variance is better converged (see Table 3.4 and Fig. 3.10).

To compare to the results obtained from DNS 3.1, the bias of each method for DNS 1.1 and 2.1 is presented in Table 3.4 (more details can also be found in the supplementary Fig. 3.10). Both DNS 1.1 and 2.1 with $\mathrm{R}_\lambda = 74$ and $\mathrm{R}_\lambda = 210$, respectively, show that ϵ_G reproduces the global reference $\langle\epsilon(\boldsymbol{x},t)\rangle_N$ closely ($\langle\beta_G\rangle_N < 1\%$) as in DNS 3.1. In contrast, ϵ_{I3} is associated with the largest overestimates $\langle\epsilon(\boldsymbol{x},t)\rangle_N$ for any R_λ. Both ϵ_{I2} and ϵ_S show comparably small deviations from $\langle\epsilon(\boldsymbol{x},t)\rangle_N$. The mean

DNS	$\langle\beta_G\rangle_N$	$\langle\beta_{I3}\rangle_N$	$\langle\beta_{I2}\rangle_N$	$\langle\beta_S\rangle_N$	$\langle\beta_L\rangle_N$
1.1	-0.003 ± 0.001	0.132 ± 0.005	-0.047 ± 0.002	0.011 ± 0.002	-0.044 ± 0.003
2.1	-0.002 ± 0.006	0.506 ± 0.038	-0.011 ± 0.014	0.074 ± 0.010	0.313 ± 0.017
3.1	-0.005 ± 0.006	0.492 ± 0.039	0.088 ± 0.013	0.041 ± 0.010	0.400 ± 0.020

Table 3.4 The systematic error of each method β_i relative to the global mean energy dissipation rate, Eq. (3.21), of each DNS where $i \in \{G, I3, I2, S, L\}$. The error is given by the standard error which is defined as the standard deviation divided by the square root of the number of samples. In both DNS 2.1 and 3.1, ϵ_{I2} and ϵ_{I3} were obtained by fitting Eq. (3.15) for $n = 2$ and $n = 3$, respectively, in the range $r \in [20\eta_K, 500\eta_K]$. This fit-range is also used for calculating ϵ_S and it was converted into frequency domain by $f = U/r$, where U is the mean velocity. In the case of DNS 1.1, the maximum of Eq. (3.15) was used to infer ϵ_{I2} due to the absence of a pronounced inertial range. We used the maximum available window size R in all cases, fixed turbulence intensity $I = 1\%$ and considered perfect alignment, i.e. $\theta = 0°$.

relative deviation of ϵ_S due to the change in fit-range is much larger than the mean values of Table 3.4. This is why the fit-range was chosen to be constant for DNS 2.1 ($r \in [20\eta_K, 500\eta_K]$ and $f \in [U/(500\eta_K), U/(20\eta_K)]$) like in DNS 3.1 in order to prevent for additional influences due to varying fit-ranges. Within these boundaries of the fit-range for $\langle D_{LL}(r)\rangle_N$, the scaling exponent varied by approx. ±30%. It is found that the systematic errors of ϵ_{I2} and ϵ_S are smaller and comparable to those of the gradient method when a fitting range is used for each dataset in which the scaling of the structure function is close to the expected scaling, e.g. fit-range of $r \in [50\eta_K, 100\eta_K]$ for DNS 2.1.

While ϵ_L is in close agreement with $\langle\epsilon(\boldsymbol{x}, t)\rangle_N$ for DNS 1.1 ($\mathrm{R}_\lambda = 74$), it strongly deviates for DNS 2.1 and 3.1, as elaborated above. In this context, we suggest that large deviations for ϵ_L and ϵ_{I3} are due to statistical uncertainties as DNS 2.1 and 3.1 are shorter in terms of the integral length scale L_{11} than DNS 1.1 (Table 3.2, Fig. and 3.12). However, although the box size of all DNS (see Table 3.2) is on the order of 6 integral length scales, the ensemble of all probes represent a velocity record with a total length of $\mathcal{O}(10^5)$ integral length scales for DNS 1.1 so that the statistics are well converged (see Fig. 3.12A and 3.12B, for instance). Considering the reasonable agreements we found between the mean energy dissipation rate estimated by different methods for DNS 1.1 (Table 3.4) and the global value, we can verify the correct implementation of the different methods studied here within the limits of the different methods and statistical convergence.

3.3.2 Validity of Taylor's hypothesis and impact of random sweeping effects

A finite turbulence intensity causes the time to space conversion of velocity statistics to be inaccurate and, hence, affects the energy dissipation rate. In the case of high turbulence intensity ($I \gtrsim 0.5$), the eddy turnover time is on the same order as the advection time. As a result, the local directionality of the flow is significantly varying in time and space, which hinders the applicability of the Taylor's hypothesis. Here, we quantify the impact of random sweeping on the accuracy of determining the mean energy dissipation rate. Therefore, we set the mean speed of the virtual probes in each DNS so that the turbulence intensity, and in consequence the random sweeping, is a controlled parameter.

Fig. 3.3 shows the systematic errors β_i for ϵ_G, ϵ_{I2}, ϵ_S, and ϵ_L at different turbulence intensities for DNS 3.1-5. For each virtual probe taken into account in Fig. 3.3, we used the entire time series so that the size of the averaging window is maximal. While each method has a different systematic error and scatter, Fig. 3.3 indicates that the mean relative deviation of each estimate from $\langle\epsilon(\mathbf{x},t)\rangle$ increases with turbulence intensity. This is particularly strong for the gradient method. For $I = 1\%$ and $I = 10\%$, the gradient method has the lowest scatter in terms of the standard deviation σ_{β_G} (19.3% and 27.3%) and the lowest systematic error in terms of the $\langle\beta_G\rangle_N$ (-0.5% and 6.1%), respectively. At higher turbulence intensities, ϵ_{I2} is the least affected method with $\sigma_{\beta_{I2}} = 37.2\%$ and $\langle\beta_{I2}\rangle_N = 6.5\%$ for $I = 25\%$ as well as $\langle\beta_{I2}\rangle_N = 24.5\%$ and $\sigma_{\beta_{I2}} = 56.9\%$ for $I = 50\%$. At the highest turbulence intensities, both ϵ_L and ϵ_S are associated with lower mean β than that of ϵ_G.

The fraction of track samples that can lead to a deviation of larger than 100% increases from 0% to $\sim$ 60% for ϵ_G as the turbulence intensity increases from 1% to 50%. We hypothesize that these deviations of the mean are the result of random sweeping effects, which limit the applicability of Taylor's hypothesis. In frequency space, Taylor's hypothesis establishes a one-to-one mapping between the frequency and the streamwise wavenumber, i.e. $\omega = \kappa_1 U$. As the turbulence intensity grows, a randomly sweeping mean velocity smears out this correspondence between frequencies and wavenumbers.

To quantify the impact of random sweeping on estimates of ϵ, we first consider the influence of random sweeping on the gradient method. For the gradient method, Lumley [162] and Wyngaard and Clifford [137] have shown that in isotropic turbulence random sweeping leads to an overestimation of the volume-averaged mean energy dissipation rate by a factor of $1 + 5I^2$, i.e. $\epsilon_G = \epsilon_0[1 + 5\,I^2]$. To illustrate this result, we consider a model wavenumber-frequency spectrum, which is based on the same modeling assumptions used in Wyngaard and Clifford [137]. It enables us to conduct a systematic assessment of the interplay between Taylor's hypothesis and the random sweeping effects. The model wavenumber-frequency spectrum tensor $\Phi_{ij}(\boldsymbol{\kappa},\omega)$ can be derived from an elementary linear random advection model [158, 169], which in case of SHI turbulence can be expressed in terms of the energy tensor $\Phi_{ij}(\boldsymbol{\kappa})$:

$$\Phi_{ij}(\boldsymbol{\kappa},\omega) = \frac{\Phi_{ij}(\boldsymbol{\kappa})}{\sqrt{2\pi\kappa^2 I^2 U^2}} \exp\left(-\frac{(\omega/U - \kappa_1)^2}{2\kappa^2 I^2}\right) . \tag{3.24}$$

Within the model, the wavenumber-frequency spectrum $\Phi_{ij}(\boldsymbol{\kappa},\omega)$ consists of the energy spectrum tensor in wavenumber space $\Phi_{ij}(\boldsymbol{\kappa})$ multiplied by a Gaussian frequency distribution. $\Phi_{ij}(\boldsymbol{\kappa},\omega)$ has a mean value proportional to the mean velocity and a

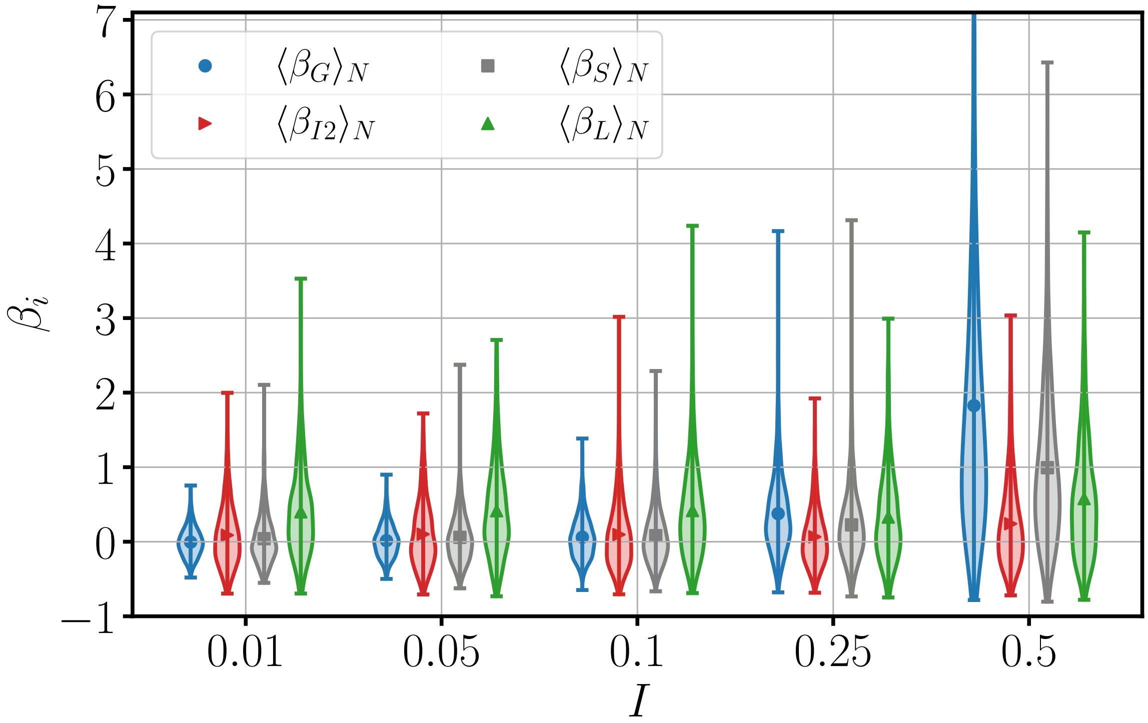

Figure 3.3 Systematic error β_i, Eq. (3.21), as a function of turbulence intensity $I \in \{0.01, 0.05, 0.1, 0.25, 0.5\}$ for ϵ_G (●), ϵ_{I2} (▶), ϵ_S (■), and ϵ_L (▲). The energy dissipation rates are estimated from each longitudinal velocity time series of DNS 3.1-5 with ideal alignment ($\theta = 0°$) where the maximal available window size was used. The fit-range for the inertial range of the power spectral density is chosen to be within $U/(500\eta_K) \leq f \leq U/(20\eta_K)$ where η_K is the Kolmogorov length scale, and, equivalently in space domain, $20\eta_K \leq r \leq 500\eta_K$ for the longitudinal second-order structure function. The upper limit of the y-axis is chosen to be 7.1 for improving the plot visibility (there are some outliers of ϵ_G for $I = 50\%$).

variance proportional to the RMS velocity fluctuations. When the RMS velocity fluctuations tend to zero at fixed mean velocity, i.e. in the limit of vanishing turbulence intensity, the frequency distribution tends to a delta function, re-establishing the one-to-one correspondence between the frequency and the wavenumber in the direction of the mean flow. To establish the connection to the different methods using longitudinal components and Taylor's hypothesis, we consider the $i = j = 1$ component of Eq. (3.24). One obtains the estimate for the longitudinal wavenumber spectrum based on Taylor's hypothesis which includes effect of random sweeping by first integrating over $\boldsymbol{\kappa}$. This leads to the frequency spectrum $\tilde{E}_{11}(\omega)$, which corresponds to the one obtained from temporal single-point measurements of the longitudinal velocity component:

$$E_{11}(\kappa_1)d\kappa_1 = \frac{1}{U}\tilde{E}_{11}(\omega)d\omega = \frac{2}{U}\left[\int \Phi_{11}(\boldsymbol{\kappa'}, \omega)d\boldsymbol{\kappa'}\right] d\omega\,. \tag{3.25}$$

Secondly, one applies Taylor's hypothesis, corresponding to a substitution $\omega = \kappa_1 U$, where the prefactor $1/U$ cancels due to the Jacobian $\left|\frac{d\omega}{d\kappa_1}\right|$. In order to numerically asses the impact of a finite turbulence intensity, we first assume a model wavenumber spectrum [5, Eq. 6.246 ff.]:

$$E(\kappa) = C_K \langle \epsilon \rangle^{2/3} \kappa^{-5/3} \left(\frac{\kappa L}{[(\kappa L)^2 + c_L]^{1/2}} \right)^{5/3+p_0} \exp(-\beta \kappa \eta_K) \,, \qquad (3.26)$$

where L is the energy injection scale and $c_L = 6.78$, $p_0 = 2$ and $\beta = 1$ are positive constants. Based on this model wavenumber spectrum, Fig. 3.4 shows the overestimation of the spectrum (pre-multiplied by κ_1^2) in the inertial range and in the dissipative range by evaluating Eq. (3.25) for different turbulence intensities. Here, the overestimation is most pronounced in the dissipative range.

Finally, this enables us to evaluate the influence of random sweeping on the gradient method since it is closely related to the wavenumber spectrum. Expressed in wavenumber space, the relation, Eq. (3.14), takes the form:

$$\epsilon_G = 15\nu \int \kappa_1^2 E_{11}(\kappa_1) d\kappa_1 = \epsilon_0 [1 + 5I^2] \qquad (3.27)$$

which recovers the result by [162] and [137]. Due to the κ_1^2-weighting, the mean dissipation rate is highly sensitive to the viscous cutoff of the energy spectrum, which is overestimated by random sweeping effects, see Fig. 3.4. As a consequence, deviations of the estimated dissipation rate are growing rapidly with turbulence intensity. In the right panel of Fig. 3.4, we compare the effect of random sweeping on the gradient method obtained through Eqs. (3.24), (3.25) and (3.27) with a model spectrum, the one computed by Lumley [162], and the observed deviations by measurements of the virtual probes in a DNS flow, here shown are the DNS 3.1-5. In fact, the estimate from [162] can explain the magnitude of deviations observed by the virtual probes in case of ϵ_G up to $I = 25\%$. The strong deviation of β_G at $I = 50\%$ is likely due to the sensitivity of the gradients on the space-to-time conversion via Taylor's hypothesis. At high turbulence intensities the relative error of estimating the mean velocity increases. Therefore, individual spatial increments are both under- and overestimated. As the dissipation is quadratic in the gradients, overestimated gradients are over-weighted. This deviations do not appear in evaluating (3.27) as there the mean velocity is a parameter we choose.

Now let us consider the two inertial subrange methods. Here, as one can see in Fig. 3.3 and 3.4, the increase of the mean relative deviation, β, is less pronounced. In the inertial subrange random sweeping causes an overestimation of the spectrum of merely several percent while the inertial range scaling is preserved as shown in Wilczek, Xu, and Narita [158]. As both the second-order structure function and the spectral method are based on the inertial subrange of the energy spectrum, the effect of a randomly sweeping mean velocity is expected to be small on ϵ_{I2} and ϵ_S. Here, the overestimation of the spectrum can be used to express the relative systematic deviation of both ϵ_{I2} and ϵ_S for different turbulence intensities analytically:

$$\beta_{I2} = \beta_S = (C_T(I))^{3/2} - 1 \quad \text{with} \quad C_T(I) = \frac{5}{6}\int_0^\infty \mathrm{d}y \left[\operatorname{erf}\left(\frac{y+1}{\sqrt{2}I}\right) - \operatorname{erf}\left(\frac{y-1}{\sqrt{2}I}\right)\right] y^{2/3}\,, \tag{3.28}$$

where $C_T(I)$ quantifies the spectral overestimation as function of mean wind and fluctuations defined as in [158]. In Fig. 3.4B we compare the observed deviations from the DNS to Eq. (3.28). This shows that Eq. (3.28) underestimates β_{I2} for $I \in \{0.01, 0.05, 0.1\}$ (i.e. DNS 3.1, 3.2 and 3.3). The underestimation is most likely due to additional random errors associated with finite averaging window lengths. It is obvious from Table 3.2 that DNS 3.3 has statistically the shortest probe tracks $\sim 3440\eta_K$ (DNS 3.1: $\sim 3550\eta_K$, DNS 3.2: $\sim 3560\eta_K$). Nonetheless, β_{I2} matches the prediction of Eq. (3.28) for $I \in \{0.25, 0.5\}$ where the corresponding probe tracks statistically amount to $\sim 5570\eta_K$ and $\sim 4260\eta_K$, respectively. The effect of the averaging window size on ϵ_{I2} is explored in Sec. 3.3.4. We conclude that Eq. (3.28) can be used to estimate the error introduced by random sweeping of ϵ_{I2}.

At turbulence intensities larger than 15%, β_S is smaller than Lumley's prediction for the gradient method, i.e. $5\,I^2$. $\tilde{\beta}_S(I)$ underestimates the relative error of the spectral method β_S. This may be due to the strong dependence of ϵ_S on the U-based fitting range, i.e., $f \in [U/(500\eta_K), U/(20\eta_K)]$, which can differ significantly between virtual probes at high turbulence intensities. Further work is needed to assess the dependence of the spectral method on the choice of the fit-range for finite turbulence intensities.

3.3.3 Probe Orientation

In this section, we assess the influence of probe misalignment with respect to the mean flow direction on estimating the energy dissipation rate at the energy injection scale, the inertial range and the dissipation range. We assume the angle θ between the (virtual) anemometer and the global mean wind direction $\frac{\boldsymbol{U}}{|\boldsymbol{U}|}$ to be constant throughout the sampling trajectory. In general, the rotation matrix around an arbitrary rotation axis $\hat{\boldsymbol{n}}$ with $n_i n_i = 1$ is given by $\boldsymbol{\mathcal{R}}^{\hat{\boldsymbol{n}}}_{ij}(\theta) = (1-\cos\theta)n_i n_j + \cos\theta\delta_{ij} + \sin\theta\epsilon_{ijk}n_k$, where ϵ_{ijk} is the Levi-Cevita tensor and δ_{ij} the Kronecker delta. At first, we consider the covariance tensor $R_{ij}(\boldsymbol{r'})$ as the integral length scale, the second-order structure function tensor as well as the velocity gradient covariance tensor depend on $R_{ij}(\boldsymbol{r'})$ (Eqs. (3.3), (3.5) and (3.7), respectively). In the sensor frame of reference, the covariance tensor is given by

$$R_{ij}(\boldsymbol{r'}) = u'^2\left(g(r')\delta_{ij} + [f(r') - g(r')]\,\frac{r'_i r'_j}{r'^2}\right)\,, \tag{3.29}$$

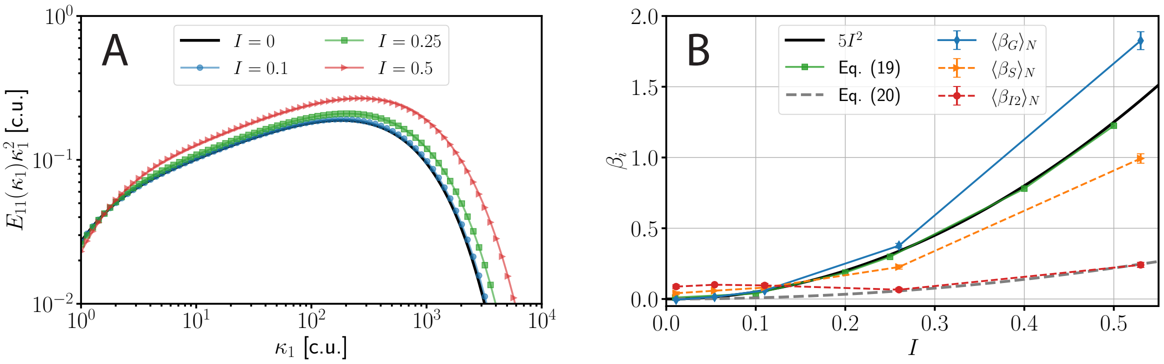

Figure 3.4 The effects of random sweeping on the energy dissipation, Eq. (3.25), assuming a model spectrum. (A) Premultiplied energy spectrum with random sweeping effects for turbulence intensities $I \in \{0.1, 0.25, 0.5\}$ where the original energy spectrum corresponds to $I = 0$. (B) Systematic over-prediction illustrated by the relative error β_i, Eq. (3.21), at different turbulence intensities. The systematic over-prediction by [162] (solid black) matches with the numerically obtained systematic error β_G for the gradient method relative to the ground-truth reference $\langle\epsilon\rangle$ by using the model spectrum (Eq. (3.27), green squares). Both reasonably estimate the data obtained from DNS 3.1-5 (blue diamonds). Also, we show the systematic over-prediction of inertial subrange methods (β_S: orange triangles, and β_{I2}: red circles, both from Eq. (3.21)) compared to the analytically derived error obtained by a Gaussian random sweeping model ($\beta_{I2,S}$, Eq. (3.28), grey dashed).

where $r'_i = \boldsymbol{\mathcal{R}}^{\hat{\boldsymbol{n}}}_{ij}(\theta) r_j$ and $r' = r$. As only the longitudinal component in the sensor frame of reference is measured, Eq. (3.29) reads for $i = j = 1$ and $\boldsymbol{r} = r\boldsymbol{e}_1$

$$\begin{aligned} R_{11}(\boldsymbol{r'}) &= \langle u'^2\rangle \left(g(r) + [f(r) - g(r)] \frac{\boldsymbol{\mathcal{R}}^{\hat{\boldsymbol{n}}}_{1l}(\theta) r_l \boldsymbol{\mathcal{R}}^{\hat{\boldsymbol{n}}}_{1k}(\theta) r_k}{r^2} \right) && (3.30) \\ &= \langle u'^2\rangle \left(g(r) + [f(r) - g(r)] \left(\cos^2\theta + n_1^4 (1 - \cos\theta)^2 + 2 n_1^2 (1 - \cos\theta)\cos\theta\right) \right) . && (3.31) \end{aligned}$$

For further simplification, we assume without loss of generality that the mean wind changes direction only in the horizontal plane. With this we can set $\hat{\boldsymbol{n}} = 1\boldsymbol{e}_3$, which yields for $\boldsymbol{r'} = r'\boldsymbol{e}'_1$

$$R_{11}(r'\boldsymbol{e}'_1)/\langle u'^2\rangle = f(r') = \langle u'^2\rangle \left(g(r) + [f(r) - g(r)] \cos^2\theta \right) , \tag{3.32}$$

which we interpret as the measured autocorrelation function. Then, the measured longitudinal integral length scale, Eq. (3.19), amounts to

$$L'_{11}(\theta) = \int_0^\infty \mathrm{d}r' f(r') = \int_0^\infty \mathrm{d}r \cos\theta (\cos^2\theta f(r) + (1 - \cos^2\theta) g(r)) = \frac{1}{2} L_{11} \cos\theta \left(1 + \cos^2\theta \right) , \tag{3.33}$$

where the integration of $f(r)$ and $g(r)$ is carried out in the last step, see Eq. (3.19), while considering the fact that $L_{22} = L_{11}/2$ for isotropic turbulence [5]. As it can be seen from Eq. (3.33), ϵ_L also depends on θ. Then, the analytically derived error for ϵ_L due to misalignment of the sensor and the longitudinal wind direction is given by

$$\delta_L(\theta) = \frac{\epsilon_L(\theta)}{\epsilon_L(0)} - 1 = \frac{2}{\cos\theta(1+\cos^2\theta)} - 1\,, \tag{3.34}$$

where $\epsilon_L(\theta)$ represents the energy dissipation that is derived given an angle of incidence θ and $\epsilon_L(0)$ is the reference value for perfect alignment of the mean flow direction and the probe, i.e. when $\theta = 0$.

An analogous argument also holds for the second-order structure function tensor, Eq. (3.5):

$$D_{11}(r') = D_{NN}(r) + [D_{LL}(r) - D_{NN}(r)]\cos^2\theta = D_{LL}(r)\left(\frac{4-\cos^2\theta}{3}\right)\,, \tag{3.35}$$

where the transverse second-order structure function $D_{NN}(r) = D_{22}(r) = D_{33}(r)$ is expressed as $D_{NN}(r) = 4D_{LL}(r)/3 = 4C_2(r\epsilon)^{2/3}/3$ in SHI turbulence [5]. Hence, the analytically derived error $\delta_L(\theta)$ as a function of θ is

$$\delta_{I2}(\theta) = \frac{\epsilon_{I2}(\theta)}{\epsilon_{I2}(0)} - 1 = \left(\frac{4-\cos^2\theta}{3}\right)^{3/2}\frac{1}{\cos\theta} - 1\,, \tag{3.36}$$

where $\epsilon_{I2}(\theta)$ represents the energy dissipation that is derived given an angle of incidence θ and $\epsilon_{I2}(0)$ is the reference value for perfect alignment of the mean flow direction and the probe.

The misalignment error for the gradient method can be estimated analytically starting from the longitudinal component of the velocity gradient covariance tensor R_{1111} — it can be also expressed in terms of the velocity covariance tensor Eq. (3.7). Following similar arguments as above and starting from Eq. (3.7), assuming $\boldsymbol{r} = r\boldsymbol{e}_1$ and applying the rotation about an axis $\hat{\boldsymbol{n}}$ with $n_i n_i = 1$, we obtain

$$R_{1111}(0) = -\lim_{r'\to 0}\partial_{r'}\partial_{r'}R_{11}(r'\boldsymbol{e}_1') = -\frac{u'^2}{\cos^2\theta}\lim_{r\to 0}\partial_r^2\left[g(r) + [f(r)-g(r)]\frac{r^2\cos^2\theta}{r^2}\right]\,, \tag{3.37}$$

where $\partial_{r'} = \partial_r/\cos\theta$ due to the rotation. Using $\partial_r^2 g(r) = 2\partial_r^2 f(r) + \frac{r}{2}\partial_r^3 f(r)$ [5], the velocity gradient covariance tensor reduces to

$$R_{1111}(0) = -\frac{u'^2}{\cos^2\theta}\lim_{r\to 0}(2-\cos^2\theta)\partial_r^2 f(r) + (1-\cos^2\theta)\frac{r}{2}\partial_r^3 f(r) \tag{3.38}$$

$$= \left\langle\left(\frac{\partial u}{\partial x_1}\right)^2\right\rangle\frac{2-\cos^2\theta}{\cos^2\theta}\,, \tag{3.39}$$

where $-u'^2 \lim_{r\to 0} \partial_r^2 f(r) = \langle (\partial u/\partial x_1)^2 \rangle$ [5] is used for the last step. With the assumption that $r \ll \eta_K$ and Eq. (3.13), the analytically derived error of ϵ_G as a function of θ can be calculated to

$$\delta_G(\theta) = \frac{\epsilon_G(\theta)}{\epsilon_G(0)} - 1 = 2\left(\frac{1}{\cos^2\theta} - 1\right) , \tag{3.40}$$

where $\epsilon_G(\theta)$ represents the energy dissipation that is derived given an angle of incidence θ and $\epsilon_G(0)$ is the reference value for perfect alignment of the mean flow direction and the probe.

To compare the analytical expressions to DNS results, the sensing orientation of the virtual probes is rotated around the $\boldsymbol{e}_3$-axis in the coordinate system of each the virtual probe by an angle θ relative to their direction of motion, i.e. the $\boldsymbol{e}_1$-axis. Then, $\epsilon_L(\theta)$, $\epsilon_{I2}(\theta)$, and $\epsilon_G(\theta)$ are inferred from the new longitudinal velocity component. The ensemble averaged relative errors of the estimated energy dissipation rates $\delta(\theta)$ due to misalignment is shown as a function of θ in Fig. 3.5 in the range of ±50° both for DNS and the analytically derived Eqs. (3.40), (3.34), and (3.36). In general, the ensemble averaged systematic errors follow the analytically derived errors reliably in terms of the limits of accuracy for all R_λ at turbulence intensity $I = 1\%$. The longitudinal second-order structure function is the best performing method with a systematic error $\langle \delta_{I2} \rangle_N$ of lower than 20% for $\theta \in [-25°, 25°]$, which increase to 100% at $\theta = \pm 50°$. $\langle \delta_L \rangle_N$ is similarly effected by misalignment but slightly larger than $\langle \delta_{I2} \rangle_N$. Despite its fast statistical convergence, the ϵ_G is the most vulnerable method by misalignment compared to the other two methods.

In experiments where the sensor can be aligned to the mean wind direction within $\theta \in [-10°, 10°]$ over the entire record time, $\delta_i(\theta)$ is expected to be small. Further work is needed to evaluate the impact of a time dependent misalignment angle $\theta(t)$. We suppose that keeping the angle of attack θ fixed over the entire averaging window, here the entire time record of each probe, potentially leads to overestimation of $\delta_i(\theta)$ with θ being a function of time in practice.

3.3.4 Systematic and random errors due to finite averaging window size R

In various experimental conditions, the maximal size of the averaging window is constrained. If one wants to measure the mean energy dissipation rate of on individual cloud, as an example, the averaging window is bounded by the cloud edges. But also generally, the flow can be statistically non-stationary, e.g. due to rapidly changing ambient conditions in the atmospheric boundary layer. This is why it is necessary to know to which accuracy the mean energy dissipation rate can be determined given a specific window size R. In this section, we tackle this question by evaluating the longitudinal velocity time records of DNS and wind tunnel for specific window sizes R — at least under ideal conditions of SHI turbulence.

Here our goal is to investigate how the accuracy of estimating the global mean

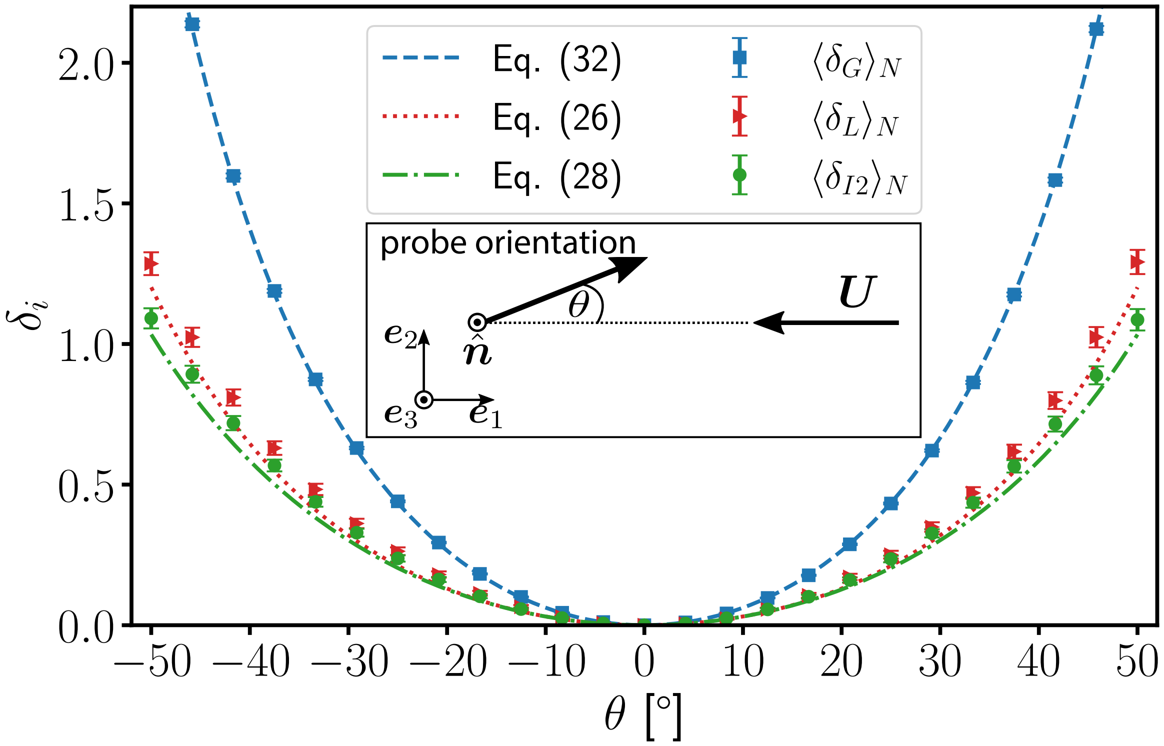

Figure 3.5 Influence of misalignment between probe orientation and the mean flow direction $\boldsymbol{U}$ in terms of the average error of the energy dissipation rate $\delta_i(\theta)$ as a function of the angle of attack θ. The energy dissipation rates are derived from DNS 3.1 with a turbulence intensity of 1%, $\mathrm{R}_\lambda = 293$ and maximally available window size. The error bars are given by the standard error of the mean. The analytically derived errors $\delta_G(\theta)$, $\delta_L(\theta)$, and $\delta_L(\theta)$ are given by Eqs. (3.40), (3.34), and (3.36), respectively. The ordinate is limited from 0 to 2.2 to guarantee a better visibility for $\delta_L(\theta)$ and $\delta_{I2}(\theta)$. The inset visualizes the misalignment angle θ between the probe orientation and the mean flow direction $\boldsymbol{U}$. The rotation axis is denoted by $\hat{\boldsymbol{n}}$. As mentioned above, the mean flow direction $\boldsymbol{U}$ is considered as the longitudinal direction of the flow.

energy dissipation rate depends on the averaging window size by investigating the associated systematic and random errors individually. To do this, we select an averaging window of size R from the beginning of each track of virtual probes for case DNS 3.1. In this way, we obtain 1 subrecord for each virtual probe, which amounts to a total of 1000 subrecords for each averaging window R. From each of these subrecords a mean value of ϵ_0 (i.e. $\langle\epsilon_0(\boldsymbol{x},t)\rangle_R$)), $\langle\epsilon_G\rangle_R$, $\langle\epsilon_L\rangle_R$ and $\langle\epsilon_{I2}\rangle_R$ are then evaluated. The smallest R considered for these analyses is $501\eta_K$, which is limited by the upper bound of the fitting range $r \in [20\eta_K, 500\eta_K]$ for estimating ϵ_{I2}. The largest window size considered in this section is $3000\eta_K$, which is limited by the total length of the virtual-probe track (Table 3.2).

Before comparing estimates of the energy dispersion rate using different methods, let us first compare the locally averaged energy dispersion rate $\langle\epsilon_0(\boldsymbol{x},t)\rangle_R$) with the instantaneous energy dispersion rate, which is shown in Fig. 3.6A. All averaging window sizes create PDFs with similar shape, but significantly different from the shape of the instantaneous field. The larger the volume over which the dissipation field is averaged, the more the PDF($\langle\epsilon_0(\boldsymbol{x},t)\rangle_R$) converges to a peak at the global mean energy dissipation rate normalised by $\dot{E}$, i.e. $\langle\epsilon_0(\boldsymbol{x},t)\rangle/\dot{E} \approx 1.0$.

We can further explore the influence of averaging window R for each method by examining the distribution of systematic errors, i.e., β_i, as shown in Fig. 3.6B-D. First main point to note is the fact that all methods at small R tend to peak at a dissipation rate lower than the global. Hence, the mean energy dissipation rate is most likely underestimated. All PDF($\beta_i(R)$) become narrower and the mean relative errors $\beta_i(R)$ converge to 0 as the R increases. The second main point to consider is the statistical uncertainty, causing a random error in estimating the local mean energy dissipation rate $\langle\epsilon_0(\boldsymbol{x},t)\rangle_R$. As it can be seen in Fig. 3.6B-D, the width of the distribution is wide with asymmetric long tails, especially for β_{I2} and β_L. This is an indication that high random errors are to be expected in the estimation of the mean energy distribution rate.

We now focus on random errors associated with ϵ_G, ϵ_L and ϵ_{I2} analytically. We denote $\langle\epsilon_G\rangle_R$, $\langle\epsilon_L\rangle_R$ and $\langle\epsilon_{I2}\rangle_R$ the energy dissipation rates that are estimated for a longitudinal velocity time record for a window of size R. For the calculation of random errors caused by the choice of the size of the averaging window, we consider DNS 1.3, 2.3, and 3.3, as well as wind tunnel experiments that all have a comparable turbulence intensity of $I \approx 10\%$.

Both the second-order structure function, Eq. (3.6), and the scaling argument, Eq. (3.18), depend on the variance $\langle u_1'^2\rangle$ of the longitudinal velocity time record. ϵ_G is also related to $\langle u_1'^2\rangle$ through Eqs. (3.14) and (3.3). The variance $\langle u_1'^2\rangle$ itself is subject to both systematic and random errors in case of a finite averaging window $R < \infty$. Assuming an ergodic, hence, a stationary velocity-fluctuation time-record with a vanishing mean, the systematic error in estimating the variance over an averaging

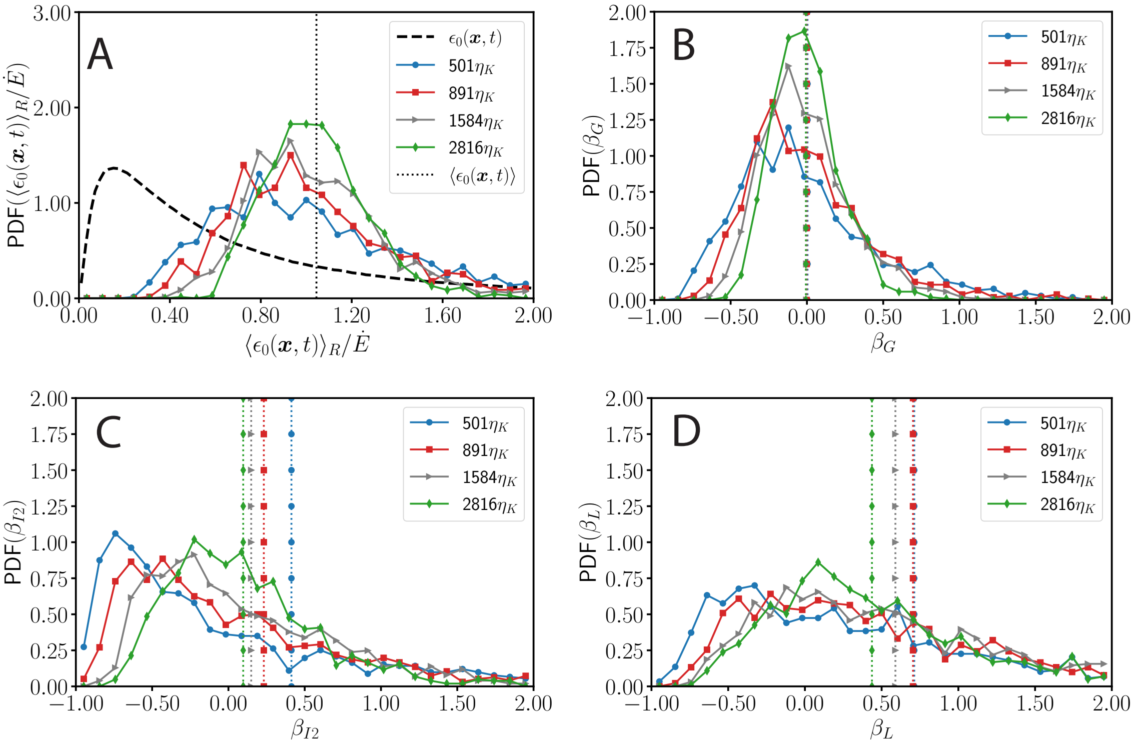

Figure 3.6 The effect of the averaging window size R (A) on the distribution of $\langle\epsilon_0(\boldsymbol{x},t)\rangle_R/\dot{E}$; and on the accuracy of estimates obtained via (B) $\langle\epsilon_G\rangle_R$, (C) $\langle\epsilon_{I2}\rangle_R$, and (D) $\langle\epsilon_L\rangle_R$ in terms of the systematic errors β_G, β_{I2}, and β_L, respectively, from the ground-truth reference $\langle\epsilon_0(\boldsymbol{x},t)\rangle_R$ as given by Eq. (3.21). The velocity time records of the longitudinal component are taken from DNS 3.1 ($R_\lambda = 302$, $I = 1\%$, $\theta = 0°$). In (A), the distribution of the instantaneous dissipation rate $\epsilon_0(\boldsymbol{x},t)/\dot{E}$ sampled by all virtual probes is shown by the dashed line, and the global average energy dissipation rate normalized by $\dot{E}$ is shown by the dotted vertical line. The other PDFs in A are from the local average of the energy dissipation rate obtained from a window of size R at the beginning of each virtual probe, i.e. 1000 averaged values for a given R. In (B), (C) and (D) the vertical dotted lines correspond to ensemble averages of the systematic errors β_i. The ensemble average of β_G slightly decreases from 0.4% for $R = 501\eta_K$ to -0.7% for $R = 2815\eta_K$ where the standard deviation of β_G decreases from 50% to 22%. The ensemble average of β_{I2} decreases from 41% to 10% and the standard deviation from 185% to 5%. β_L exhibits stronger deviations (mean β_L of $\sim 44\%$ and standard deviation $\sim 67\%$ for $R = 2816\eta_K$).

window of size R is given by [following 56, while applying Taylor's hypothesis]

$$\Delta_{\langle u_1'^2\rangle} = \left\langle \frac{\langle u_1'^2\rangle_R}{\langle u_1'^2\rangle} - 1 \right\rangle_N \approx -2\frac{L_{11}}{R}\,, \tag{3.41}$$

where $\langle u_1'^2\rangle_R$ is the estimated variance based on the (finite) averaging window R, $\langle u_1'^2\rangle$ is the true variance and it is assumed $R \gg L_{11}$. The always negative error predicted by equation (3.41) indicates that for finite averaging window sizes, the variance $\langle u_1'^2\rangle$ is always statistically underestimated, which agrees with Figure 3.12A. Eq. (3.41) furthermore indicates that the systematic error of the variance estimates can be neglected for *sufficiently* long averaging windows $R \gg L_{11}$.

The variance estimates are also subject to statistical uncertainty, which is also known as the random error of variance estimation [56]. Assuming that $u_1'(t)$, which has a zero mean, can be modeled by a stationary Gaussian process and that its autocorrelation function is sufficiently well represented by an exponential, the random error of estimating the variance can be expressed as [following 56, while applying Taylor's hypothesis]

$$e_{\text{rand}} = \sqrt{\left\langle \left(\frac{\langle u_1'^2\rangle_R - \left\langle \langle u_1'^2\rangle_R \right\rangle_N}{\langle u_1'^2\rangle} \right)^2 \right\rangle_N} \approx \sqrt{\left\langle \left(\frac{\langle u_1'^2\rangle_R}{\left\langle \langle u_1'^2\rangle_R \right\rangle_N} - 1 \right)^2 \right\rangle_N} \approx \sqrt{\frac{2L_{11}}{R}}\,, \tag{3.42}$$

where it is assumed $R \gg L_{11}$ such that the systematic error can be neglected and, hence, $\langle\langle u_1'^2\rangle_R\rangle_N \approx \langle u_1'^2\rangle$. Here $\langle\langle u_1'^2\rangle_R\rangle_N$ is the ensemble average of the variance estimates $\langle u_1'^2\rangle_R$ for an averaging window R. It can be seen that e_{rand} is larger than the systematic error, (3.41), when $R > L_{11}$.

Consequently, the estimation of the mean energy dissipation rate by the scaling argument, Eq. (3.18), is affected by the (absolute) random error of the variance estimation given by the product of e_{rand} and $\left\langle \langle u_1'^2\rangle_R \right\rangle_N$. Invoking the Gaussian error propagation, the analytically derived error reads

$$\delta_L(R) = \frac{1}{\langle \epsilon_L\rangle_R} \frac{\partial \langle \epsilon_L\rangle_R}{\partial \langle u_1'^2\rangle_R} \underbrace{\underbrace{e_{\text{rand}}}_{\text{rel. rnd. err. of } \langle u_1'^2\rangle_R} \quad \left\langle \langle u_1'^2\rangle_R \right\rangle_N}_{\text{abs. rnd. err. of } \langle u_1'^2\rangle_R} = \frac{3}{2}\sqrt{\frac{2L_{11}}{R}}\,. \tag{3.43}$$

$\delta_L(R)$ is a relative error, hence the prefactor $1/\langle \epsilon_L\rangle_R$. Notably, $\delta_L(R)$ scales as $R^{-1/2}$.

Similarly, the longitudinal second-order structure function is also affected by the estimation variance of the variance,

$$e_{D_{LL}} = \sqrt{\left\langle \left(\frac{D_{LL}(r;R)}{\langle D_{LL}(r;R)\rangle_N} - 1 \right)^2 \right\rangle_N} = \sqrt{\left\langle \left(\frac{2\langle u_1'^2\rangle_R (1-f(r))}{2\,\langle\langle u_1'^2\rangle_R\rangle_N (1-f(r))} - 1 \right)^2 \right\rangle_N} \approx \sqrt{\frac{2L_{11}}{R}}\,, \tag{3.44}$$

where $D_{LL}(r;R)$ is the longitudinal second-order structure function evaluated over an averaging window of size R and under the assumption that the longitudinal autocorrelation function $f(r)$ is well converged over the range of the averaging window.

Thus, the uncertainty of estimating the variance propagates to $\langle\epsilon_{I2}\rangle_R$ relying on $D_{LL}(r;R)$ (Eq. (3.15) for $n=2$). The random error $\delta_{I2}(R)$ can be analytically inferred from the random error of the second-order structure function $\sigma_{D_{LL}}$ by Gaussian error propagation yielding

$$\delta_{I2}(R) = \frac{1}{\langle\epsilon_{I2}\rangle_R}\frac{\partial\langle\epsilon_{I2}\rangle_R}{\partial D_{LL}} e_{D_{LL}} \langle D_{LL}(r;R)\rangle_N = \frac{3}{2}\sqrt{\frac{2L_{11}}{R}}\,, \tag{3.45}$$

which shows that $\delta_{I2}(R)$ scales as $R^{-1/2}$ similar to $\delta_L(R)$. Considering Eqs. (3.14) and (3.3), the gradient method can also be expressed as a function of the variance $\langle u_1'^2\rangle$. Hence, Gaussian error propagation yields:

$$\delta_G(R) = \frac{1}{\langle\epsilon_G\rangle_R}\frac{\partial\langle\epsilon_G\rangle_R}{\partial\langle u_1'^2\rangle_R} e_{\mathrm{rand}} \left\langle \langle u_1'^2\rangle_R \right\rangle_N = -15\nu\frac{1}{\langle\epsilon_G\rangle_R}\lim_{|r|\to 0}\partial_r^2 f(r) e_{\mathrm{rand}} \left\langle \langle u_1'^2\rangle_R \right\rangle_N = \sqrt{\frac{2L_{11}}{R}}\,, \tag{3.46}$$

assuming $R \gg L_{11}$ such that the systematic error is negligible such that $\langle\langle u_1'^2\rangle_R\rangle_N \approx \langle u_1'^2\rangle$.

Equations (3.43), (3.45), and (3.46) are expressed as a function of R and L_{11}, which do not reveal the dependency of random errors on the Reynolds number. In addition, this expression relies on large scales that depend on the scale of the energy input, which makes it difficult to fairly compare the errors between different flows as it is not a universal feature. Therefore, we want to link the averaging window to the Kolmogorov length scale η_K, which only depends on the viscosity and the mean energy dissipation rate. We can rewrite these equations in terms of η_K, R and R_λ as follows:

$$\delta_{I2}(R) = \delta_L(R) = \frac{3}{2}\sqrt{\frac{2L_{11}}{R}} = \frac{3}{2}\sqrt{2\frac{\eta_K}{R}\frac{L_{11}}{L}\left(\frac{3}{20}\mathrm{R}_\lambda^2\right)^{3/4}} \approx \frac{3}{2}\sqrt{\frac{\eta_K}{R}\left(\frac{3}{20}\mathrm{R}_\lambda^2\right)^{3/4}} \tag{3.47}$$

$$\delta_G(R) = \sqrt{\frac{2L_{11}}{R}} \approx \sqrt{\frac{\eta_K}{R}\left(\frac{3}{20}\mathrm{R}_\lambda^2\right)^{3/4}} \tag{3.48}$$

where we have invoked $L_{11}/L \sim 1/2$, which is valid at sufficiently high R_λ and used the relationship $L/\eta_K = \left(\frac{3}{20}\mathrm{R}_\lambda^2\right)^{3/4}$ [5]. Following the intuition, the longer the averaging window, the smaller the random error of each method.

Furthermore, Eqs. (3.47) and (3.48) provide a mean to choose a suitable averaging window size to achieve a given random error threshold a. Let R_a be the averaging window of size R such that $\delta_i(R) < a$. Then, the required averaging window R_a for ϵ_{I2} and ϵ_L is

$$R_a/\eta_K = \frac{9}{4}\left(\frac{3}{20}\mathrm{R}_\lambda^2\right)^{3/4}\frac{1}{a^2}\,, \tag{3.49}$$

where the required averaging window size R_a scales with $\mathrm{R}_\lambda^{3/2}$. Similarly, the required averaging window for ϵ_G is

$$R_a/\eta_K = \left(\frac{3}{20}\mathrm{R}_\lambda^2\right)^{3/4}\frac{1}{a^2}\,. \tag{3.50}$$

For example, for the random errors of ϵ_{I2} and ϵ_L to be less than 10% at $\mathrm{R}_\lambda = 1000$, the averaging window should be $R \sim 2 \times 10^6 \eta_K \sim 2 \times 10^4 L_{11}$, while for ϵ_G the required averaging window is $R \sim 8 \times 10^5 \eta_K \sim 10^4 L_{11}$.

Figure 3.7 shows the empirical random errors $\delta_G(R)$ (Fig. 3.7A) and $\delta_{I2}(R)$ (Fig. 3.7B) as a function of the averaging window size for various R_λ based on VDTT data (for ϵ_L see supplementary Fig. 3.14). To do this, we select an averaging window of size R, where $1000\eta_K < R < \mathcal{O}(10^6\eta_K)$, from the beginning of each 30 s time-segment from the VDTT longitudinal velocities are recorded (a total of 47 to 597 time-segments depending on R_λ).

The scaling of $\delta_G(R)$ and $\delta_{I2}(R)$ is well predicted for $R \gtrsim 10L_{11}$ as expected from Eqs. (3.46) and (3.45) and the assumptions we made to derive them. However, for smaller R a statistical convergence of ϵ_G, ϵ_{I2} or ϵ_L against the mean energy dissipation rate cannot be expected, in particular when $R/L_{11} < 1$.

Furthermore, it is evident from Fig. 3.7 that the random errors do not fully collapse on each other for different Reynolds numbers and at a given R/L_{11}. Moving horizontally on a line of constant random error, e.g., the dashed line of 50% error, the required window size increases with R_λ, as shown in the insets of Figs. 3.7A and B. Predictions of Eqs. (3.49) and (3.50) are also shown in these plots via solid/blue lines.

For both ϵ_G and ϵ_{I2}, the theoretical expectation for R_a tends to overestimate the actual averaging window size at which a random error of 50% is achieved. This overestimation is expected as the theoretical expectation for R_a, Eqs. (3.49) and (3.50), are derived assuming that large-scale quantities such as $f(r)$ and L_{11} are fully converged. However, ϵ_G is technically relying on small scales. ϵ_G depends on velocity fluctuation gradients, which are numerically obtained by central differences. Hence, each increment in the velocity record contributes to the average in the gradient method, Eq. (3.14). In the case of ϵ_{I2}, the number of possible increments reduces for larger separations for a finite averaging window. By definition, the exact computation of L_{11} requires even a fully converged $f(r)$ for all r.

However, VDTT experiments with $\mathrm{R}_\lambda > 3000$) underestimate the prediction of Eq. (3.41) by about a factor of 2. This is particularly clear for ϵ_L shown in Fig. 3.14. This

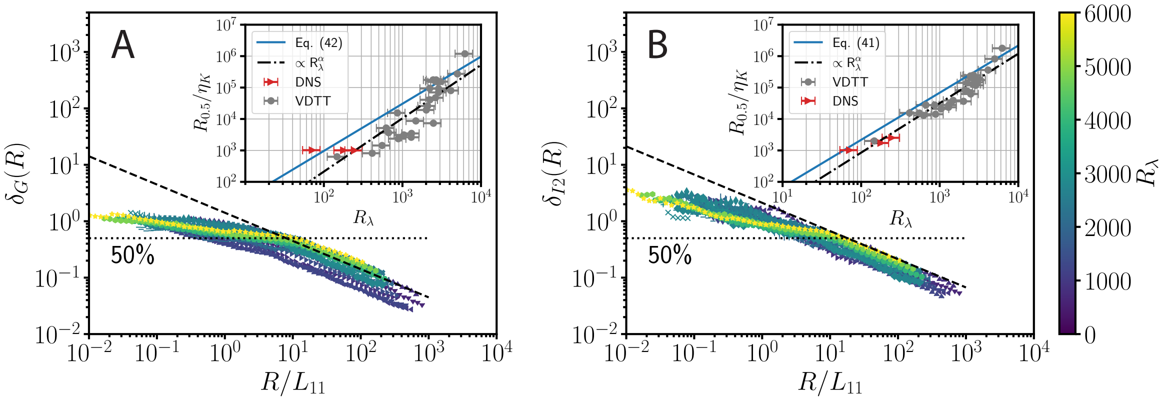

Figure 3.7 Random errors $\delta_G(R)$ (A) and $\delta_{I2}(R)$ (B) as a function of re-scaled averaging window size R/L_{11} obtained from VDTT data at various R_λ shown by the colorbar. The analytical results for $\delta_G(R)$ (A, Eq. (3.46)) and $\delta_{I2}(R)$ (B, Eq. (3.45)) are shown by the dashed black lines. The dotted black line annotated with "50%" in each subplot corresponds to 50% error-threshold. The insets show the sizes of the averaging windows in terms of η_K when $\delta_{G,I2}(R) \leq 0.5$ as a function of Taylor microscale Reynolds number R_λ. The inset plots include data from both DNS (red triangles) and the VDTT (grey circles). DNS data used for the inset plots are from cases 1.3, 2.3 and 3.3 with $I = 10\%$ and $\theta = 0°$. The solid, blue lines show the prediction of the required averaging window according to Eq. (3.50) (A-inset) and Eq. (3.49) (B-inset). The black dash-dotted line in inset plots is a fit to the data: $\log R/\eta_K = \frac{3}{4}\log\frac{3}{20} - 2\log a_{\text{fit}} + \alpha \log R_\lambda$ yielding $\alpha = 1.70 \pm 0.18$ and $a_{\text{fit}} = 1.67 \pm 0.64$ (A-inset); $\log R/\eta_K = \log\frac{9}{4}\frac{3}{20}^{3/4} - 2\log a_{\text{fit}} + \alpha \log R_\lambda$ yielding $\alpha = 1.57 \pm 0.09$ and $a_{\text{fit}} = 0.95 \pm 0.32$. (B-inset)

deviation at high R_λ can be explained, at least in part, by the strong assumptions made for the derivation of the random errors, i.e., the equations (3.45), (3.43), and (3.46). In particular, for experiments with high Re in VDTT, the assumption of Gaussian velocity fluctuations with zero skewness is questionable, as shown in Fig. 3.15. Lenschow, Mann, and Kristensen [56] has already established that the size of the averaging window for a skewed Gaussian process [see Eq. (19) in 56] must be twice as large as for a Gaussian process with vanishing skewness. However, further work is needed to investigate these deviations and improve the theoretical prediction.

3.3.5 Estimating the transient energy dissipation rate

As it has been shown in previous Figs. 3.6 and 3.7, both systematic and random error decrease with the size of the averaging window. For a correct estimate of the magnitude, it is therefore advantageous to choose the averaging window as large as possible, but this has the price that the transient trend smaller than the selected window size cannot be reproduced. In addition, it is also important to know to what extent the estimated trend correlates with the actual trend. Given a certain averaging window size R, here we empirically evaluate if trends in the coarse-grained time-series are physical or rather statistical. In other words, we ask the question if local estimates of the mean energy dissipation rate follow the ground-truth reference $\langle\epsilon_0(\boldsymbol{x},t)\rangle_R$ or not. Respecting the intermittent nature of turbulence and energy dissipation, the standard deviation of $\langle\epsilon_0(\boldsymbol{x},t)\rangle_R$ is a first proxy for the variability of the trend in $\langle\epsilon_0(\boldsymbol{x},t)\rangle_R$. Hence, detecting the true trend requires that β_i and $\delta_i(R)$ are smaller than the standard deviation of $\langle\epsilon_0(\boldsymbol{x},t)\rangle_R$.

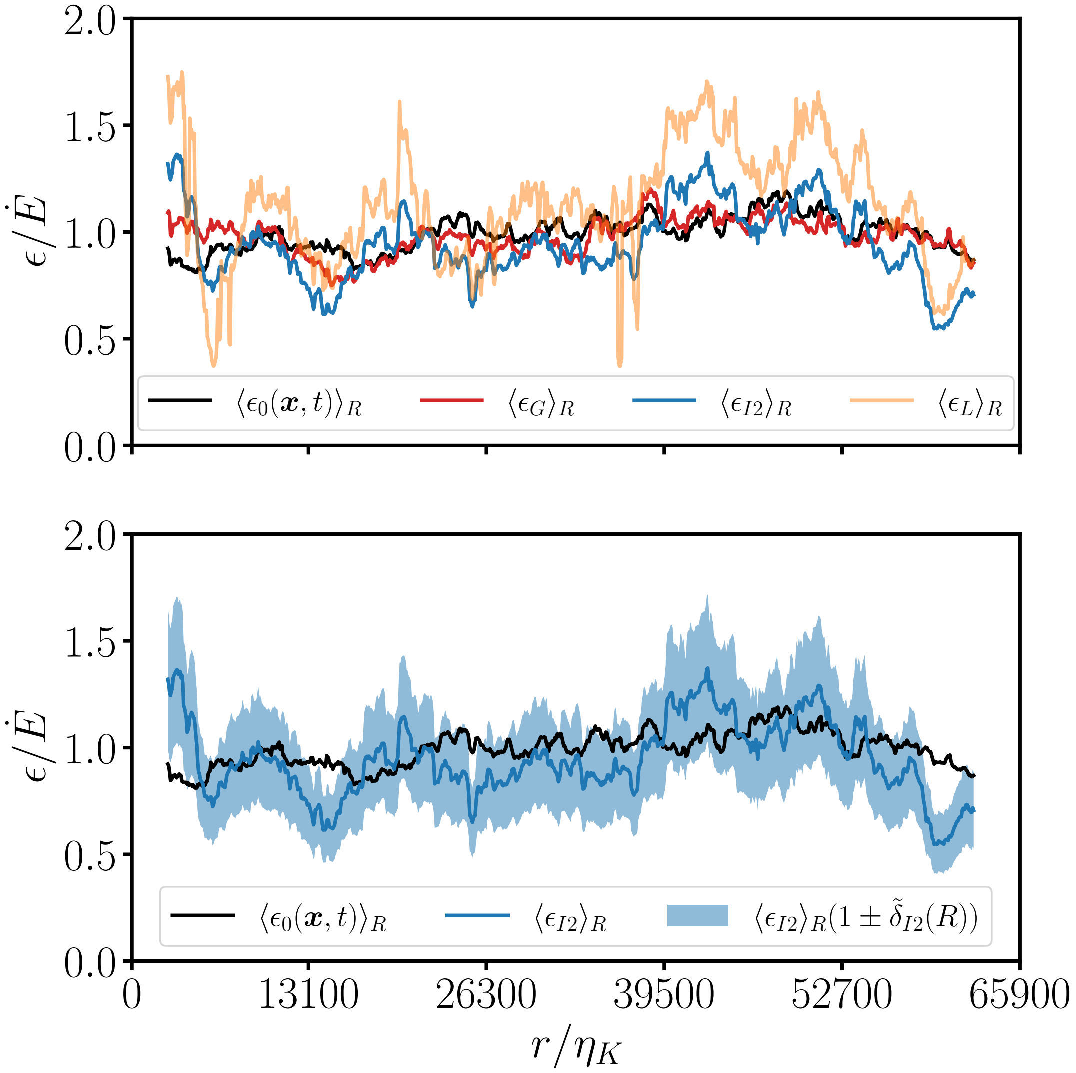

Figure 3.8 (Upper plot) Proof of concept for estimating the coarse-grained energy dissipation rate $\langle\epsilon_0(\boldsymbol{x},t)\rangle_R$ re-scaled by the energy injection rate $\dot{E}$ via the one-dimensional surrogates $\langle\epsilon_G\rangle_R$, $\langle\epsilon_{I2}\rangle_R$, and $\langle\epsilon_L\rangle_R$ for $\mathrm{R}_\lambda = 142$, $R/\eta_K \approx 5500$, $\theta = 0°$ and a turbulence intensity $I = 10\%$ (DNS 2.0). All estimates are re-scaled by the energy injection rate $\dot{E}$, too. We narrowed the fit-range to $20\eta_K \leq r \leq 200\eta_K$ ensuring optimal fit results. (Lower plot) Comparison between $\langle\epsilon_{I2}\rangle_R/\dot{E}$ with estimated random error according to Eq. (3.45) for the averaging window R and $\langle\epsilon_0(\boldsymbol{x},t)\rangle_R$.

It can be already concluded from Figs. 3.2, 3.7, 3.10 and 3.14 that ϵ_G is the most promising candidate to capture the true trend. However, to fully answer the above questions, we need to conduct more in-depth analysis. The upper plot in Fig. 3.8 shows the re-scaled and coarse-grained dissipation field $\langle\epsilon_0(\boldsymbol{x},t)\rangle_R$ for a sliding window of size $R \approx 5500\eta_K$ and a turbulence intensity $I = 10\%$ obtained from track of one virtual probe for case DNS 2.0 ("probe 0"). Consistent with results shown earlier, $\langle\epsilon_G\rangle_R$ follows $\langle\epsilon_0(\boldsymbol{x},t)\rangle_R$ best in comparison with $\langle\epsilon_{I2}\rangle_R$ and $\langle\epsilon_L\rangle_R$. Both $\langle\epsilon_{I2}\rangle_R$ and $\langle\epsilon_L\rangle_R$ are associated with substantial scatter, although $\langle\epsilon_{I2}\rangle_R$ has smaller deviations from the ground-truth overall. Other probe tracks sample different portions of the flow which is why a quantitative conclusion is not possible from one single probe. A more comprehensive evaluation of which method is able to capture the true trend is conducted below.

The lower plot in Fig. 3.8 shows $\langle\epsilon_{I2}\rangle_R$ together with the random error of ϵ_{I2} as defined by Eq. (3.45). Despite the strong scatter, the ground-truth reference is nearly always within the errorbar of ϵ_{I2} with some exceptions, e.g. $r/\eta_K < 5000$ or $r/\eta_K \approx 44000$. It can also be seen that $\langle\epsilon_{I2}\rangle_R$ is, if at all, only weakly correlated with the ground-truth reference $\langle\epsilon_0(\boldsymbol{x},t)\rangle_R$ for a window size of $R/\eta_K \approx 5500$. This shows that it is extremely difficult, if at all possible, to track the true trend with low-resolution time records, which prevents the use of the gradient method.

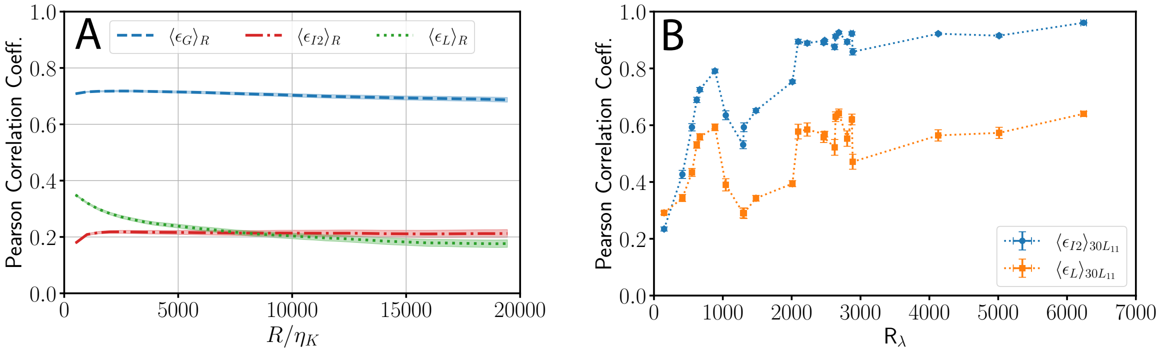

Figure 3.9 A: Dependence of the Pearson correlation coefficient between $\langle\epsilon_i\rangle_R$ and $\langle\epsilon_0(\boldsymbol{x},t)\rangle_R$ as a function of the re-scaled averaging window R/η_K where $i \in \{G, I2, L\}$. Time records of the longitudinal velocity by all virtual probes and $\langle\epsilon_0(\boldsymbol{x},t)\rangle_R$ are taken from DNS 2.0 with $\mathrm{R}_\lambda = 142$, turbulence intensity $I = 10\%$ and perfect alignment ($\theta = 0°$). The shaded region is given by the standard error. B: Dependence of the Pearson correlation coefficient between $\langle\epsilon_{I2,L}\rangle_R$ and $\langle\epsilon_G\rangle_R$ as a function R_λ for a fixed re-scaled averaging window $R = 30L_{11}$. The error bars of the ensemble averaged coefficients are given by the standard error.

To assess this correlation more quantitatively, we evaluate Pearson's correlation coefficient between the ground-truth reference $\langle\epsilon_0(\boldsymbol{x},t)\rangle_R$ and ϵ_G, ϵ_{I2} as well as ϵ_L, respectively, as a function of the re-scaled averaging window size R/η_K for all virtual probes of case DNS 2.0. As an example, Pearsons correlation coefficient between $\epsilon_0(\boldsymbol{x},t)\rangle_R$ and ϵ_{I2} is 0.33 in Fig. 3.8 (upper plot). Figure 3.9A shows the ensemble averages of Pearson's correlation coefficient together with the standard error (shaded area). While $\langle\epsilon_G\rangle_R$ has a pronounced correlation with the ground-truth reference $\langle\epsilon_0(\boldsymbol{x},t)\rangle_R$, both $\langle\epsilon_{I2}\rangle_R$ and $\langle\epsilon_L\rangle_R$ are only very weakly correlated with $\langle\epsilon_G\rangle_R$.

The effect of R_λ on Pearson's Correlation coefficient is shown in Fig. 3.9B also for the VDTT experiments at various R_λ. Here, we compare ϵ_{I2} and ϵ_L to ϵ_G in the absence of ground-truth. To ensure a negligible systematic error, we chose a fixed averaging window of $R = 30L_{11}$ for each R_λ. Figure 3.9B shows that the correlation for ϵ_{I2} is always higher than that of ϵ_L except for very low R_λ. There is a non-monotonic behavior in the correlation coefficients in Fig. 3.9B that seems to be related to the skewness values shown in Fig. 3.15. Nonetheless, there is a clear increase in correlation coefficients with R_λ. Firstly, the random error of $\delta_{I2}(R)$ ranges from 20% to 40% at $R = 30L_{11}$. Secondly, the kurtosis of the instantaneous energy dissipation field scales with $\mathrm{R}_\lambda^{3/2}$ [5, 49] which is why the variability in the instantaneous energy dissipation field increases with R_λ. Hence, at small $\mathrm{R}_\lambda^{3/2}$ and $R = 30L_{11}$, $\langle\epsilon_{I2}\rangle_{30L_{11}}$ scatters only randomly around the global mean energy dissipation rate (with a 3% standard deviation of $\langle\epsilon_G\rangle_{30L_{11}}$), which is why the correlation coefficient is low. In contrast, at large R_λ and $R = 30L_{11}$, the locally averaged mean energy dissipation rate $\langle\epsilon_G\rangle_{30L_{11}}$ fluctuates stronger ($\approx$ 30% standard deviation of $\langle\epsilon_G\rangle_{30L_{11}}$) where $\delta_{I2}(R)$ is already comparable.

3.4 Summary

We have presented an extensive review on the analysis procedure for estimating the energy dissipation rate from single-point one-dimensional velocity time records along with an overview of the their advantages and disadvantages (see Table 3.1). The main methods considered in this study are the gradient method ϵ_G, the 2nd-order SF (inertial range) method ϵ_{I2}, the spectral method ϵ_S, and the scaling argument ϵ_L. We have provided a systematic assessment of the accuracy of inferring the energy dissipation rate from such one-dimensional velocity time series as a function of turbulence intensity, probe orientation with respect to the longitudinal direction, and the effect of a finite averaging window size. We used DNS data with Reynolds numbers in the range $74 \leq \mathrm{R}_\lambda \leq 321$ as well as experimental data from high-resolution one-dimensional wind tunnel measurements with Reynolds numbers in the range $147 \leq \mathrm{R}_\lambda \leq 5864$ to evaluate the performance of different methods against robust benchmark values. The results presented in this study help to assess the accuracy of the energy dissipation rate estimates as a function of several parameters, such as finite turbulence intensity, misalignment between sensor and longitudinal flow direction, and finite size of the averaging window. The main results are:

- Each method could reproduce the ground-truth reference $\langle\epsilon(\boldsymbol{x},t)\rangle$ to within less than 10 % for well converged statistics and at low turbulence intensity. The most accurate method is the gradient method (ϵ_G) and the least accurate method is the one based on the 4/5 law (ϵ_{I3}) (see Figure 3.2). The "reference-compared" systematic error tend to be overestimated due to the global choice of the fit-range, e.g. lower systematic errors for ϵ_{I2} can be obtained by choosing a fit-range for each DNA dataset that is in a range where the scaling of the structure function is closest to the expected scaling.

- In the case of finite turbulence intensities, ϵ_G, ϵ_S and ϵ_{I2} systematically overestimate the ground-truth energy dissipation rate. The gradient method (ϵ_G) is most affected by a finite turbulence intensity I whereas ϵ_{I2} is the least affected (see Figs. 3.3 and 3.4B). The overestimation can be captured by a random advection model (Fig. 3.4). Regarding the small-scale estimate ϵ_G, the random advection model is in close agreement with the error formula provided by Lumley [162] ($\beta_G \propto 5I^2$).
- Considering the probe orientation, the gradient method (ϵ_G) is most affected by misalignment between the probe orientation and the longitudinal flow direction whereas ϵ_{I2} is the least affected (Figure 3.5) (compare Eqs. (3.40), (3.34), and (3.36)).
- We provide scaling arguments $\delta_i(R)$ to estimate the required averaging window size optimized for a desired random error threshold for ϵ_G, Eq. (3.50), ϵ_{I2}, Eq. (3.49), and ϵ_L, Eq. (3.49). With this, we can estimate a coarse-grained energy dissipation rate to within a predicted uncertainty as shown in Fig. 3.8. Systematic errors β_i are smaller than random errors $\delta_i(R)$ for $R > 2L_{11}$.
- The random error of the gradient method $\delta_G(R)$ converges at least 4-5 times faster than ϵ_{I2} (compare Eqs. (3.49) and (3.50)).
- Only ϵ_G reliably estimates the transient energy dissipation rate $\langle\epsilon\rangle_R$ although it is most vulnerable to experimental imperfections/limitations.

Appendix 3.A Nomenclature

Symbol	Definition	Equation	Dimensions
A	large-scale anisotropy parameter	$3\langle u_1'^2\rangle/(2k)$	
C_K	Kolmogorov constant related to $E(\kappa)$	1.5	
C_ϵ	dissipation constant	0.5	
$D_{ij}(\boldsymbol{r})$	second-order velocity structure function tensor	(3.5)	L^2T^{-2}
$E(\kappa)$	energy spectrum function	$\iiint_{-\infty}^{\infty} \frac{1}{2}\Phi_{ii}(\boldsymbol{\kappa})\delta(\lvert\boldsymbol{\kappa}\rvert-\kappa)\mathrm{d}\boldsymbol{\kappa}$	L^3T^{-2}
$E_{11}(\kappa_1)$	one-dimensional energy spectrum	(3.10)	L^3T^{-2}
$F_{11}(f)$	power spectral density of longitudinal velocity	$\frac{\Delta t}{N}\mathcal{F}(u_1(t))\mathcal{F}^*(u_1(t))$	L^2T^{-1}
$\mathcal{F}(x)$	(discrete) Fourier transform	$\sum_{j=0}^{N-1} x(t_j)\exp(-2\pi i t_j/\Delta t)$	
I	turbulence intensity	$\sigma_{u_1'}/U$	
L	length scale characteristic of large eddies, e.g. energy injection scale	$k^{3/2}/\epsilon$	L
L_{11}	longitudinal integral length scale of the turbulent flow	(3.19)	L
$R_{ij}(\boldsymbol{r})$	velocity (two-point, one-time velocity auto-) covariance tensor	(3.3)	L^2T^{-2}
$R_{ijkl}(\boldsymbol{r})$	velocity gradient covariance tensor	(3.7)	T^{-2}
Re	Reynolds number	$\frac{UL}{\nu}$	
R_λ	Taylor-scale Reynolds number	$\sqrt{\frac{15\sigma_{u_1}^4}{\nu\langle\epsilon\rangle}}$	
Re_L	turbulence Reynolds number	$\frac{k^{1/2}L}{\nu}$	
S_{ij}	strain rate tensor	$(\frac{\partial u_i(\boldsymbol{x},t)}{\partial x_j}+\frac{\partial u_j(\boldsymbol{x},t)}{\partial x_i})/2$	T^{-1}
T	longitudinal integral time scale of the turbulent flow	$\int_0^\infty f(\tau)\mathrm{d}\tau$	T
$\boldsymbol{U}$, U_τ	global-mean velocity vector of the flow and the local-mean of the longitudinal velocity component for averaging window of duration τ relative to the virtual probe	(3.1)	LT^{-1}
a_{fit}	fit parameter related to Eq. (3.49)		
$\dot{E}$	energy injection rate of the DNS		L^2/T^{-3}
f	frequency		T^{-1}
$f(r)$	longitudinal velocity auto-correlation [coefficient] function	$R_{11}(r)/R_{11}(0)$	
$g(r)$	transverse velocity auto-correlation [coefficient] function	$f(r)+r\partial_r f(r)/2$	
k	turbulent kinetic energy	$(u_1'^2+u_2'^2+u_3'^2)/2$	L^2T^{-2}
$\boldsymbol{r}$, r	distance vector (or rather radial coordinate) and its absolute value		L
s_{ij}	[velocity] fluctuation strain rate tensor	$(\frac{\partial u_i'(\boldsymbol{x},t)}{\partial x_j}+\frac{\partial u_j'(\boldsymbol{x},t)}{\partial x_i})/2$	T^{-1}
t	time		T
$\boldsymbol{u}$	(Eulerian) velocity vector of the flow	$u_1\boldsymbol{e}_1+u_2\boldsymbol{e}_2+u_3\boldsymbol{e}_3$	LT^{-1}
$\boldsymbol{u}'$	velocity fluctuation vector of the flow	$\boldsymbol{u}-\boldsymbol{U}$	LT^{-1}
$\langle u_1'^2\rangle$	variance of longitudinal velocity fluctuations	$\int_0^\infty E_{11}(\kappa_1)\mathrm{d}\kappa_1$	L^2T^{-2}
$\boldsymbol{x}$	position vector	$x_1\boldsymbol{e}_1+x_2\boldsymbol{e}_2+x_3\boldsymbol{e}_3$	L
$\Phi_{ij}(\boldsymbol{\kappa})$	energy tensor (velocity spectrum tensor)	(3.8)	L^5T^{-2}
α	fit parameter related to Eq. (3.49)		
δ_{ij}	Kronecker delta		
Δt	time increment	$\min\{t_{j+1}-tj\}$	T
ϵ	energy dissipation rate		L^2T^{-3}
$\epsilon_0(\boldsymbol{x},t)$	instantaneous energy dissipation rate	(3.11)	L^2T^{-3}
ϵ_R	locally volume averaged energy dissipation rate	(3.12)	L^2T^{-3}
$\langle\epsilon\rangle$	global-mean energy dissipation rate (rate of dissipation of turbulent kinetic energy)	(3.13)	L^2T^{-3}
ϵ_{ijk}	Levi-Cevita tensor		
ζ_n	nth-order structure function exponent	$\frac{\mathrm{d}\log D_{L\ldots}(r)}{\mathrm{d}\log r}$	
η_K	Kolmogorov length scale	$(\nu^3/\langle\epsilon\rangle)^{1/4}$	L
θ	angle of incidence between probe orientation and longitudinal flow direction		°
$\boldsymbol{\kappa}$	wave vector		L
λ	longitudinal Taylor (micro-)scale	$\sqrt{\frac{30\nu u_1'^2}{\langle\epsilon\rangle}}$	L
ν	kinematic viscosity		L^2T^{-1}
σ_x	standard deviation of quantity x		
$\sigma_{u_1'}$	root mean square of longitudinal velocity fluctuations		LT^{-1}
ω	angular frequency	$2\pi f$	T
$\langle\ldots\rangle_N$	ensemble average		
$\langle\ldots\rangle_R$	volume average [line average for 1D signal]		

Table 3.5 Nomenclature for the turbulent flow. If our naming convention differs from the terminology in [5], we add the convention of Pope in parentheses. Our annotations are marked by brackets. Equations are either directly given or referenced from definitions below.

Symbol	Definition
1, 2, 3	indices of vectors and tensors
C	cutoff
D	dissipation range
G	gradient
$I2$	inertial range of second-order structure function
$I3$	inertial range of third-order structure function
L	longitudinal
N	ensemble (e.g. $\langle\cdot\rangle_N$ for ensemble average)
$N\ldots$	transverse (e.g. NN for transverse second-order structure function)
R	averaging window size in space
S	inertial range of the power spectral density
p	probe
ref	(ground-truth) reference
τ	averaging window size in time

Table 3.6 Nomenclature for the subscripts.

Appendix 3.B Supplementary Figures

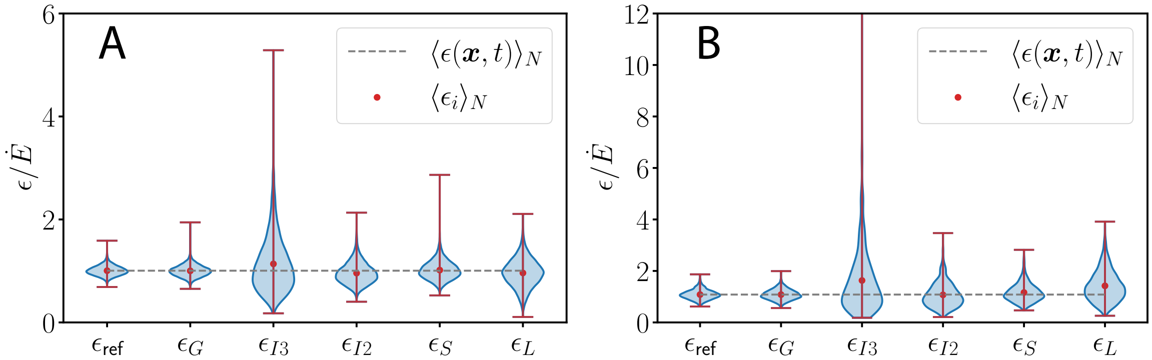

Figure 3.10 Validation of estimating the energy dissipation rate from $\epsilon_G, \epsilon_{I2}, \epsilon_{I3}, \epsilon_S$, and ϵ_L. All estimates are re-scaled by the energy injection rate $\dot{E}$. The data is taken from DNS 1.1 (A) and 2.1 (B), turbulence intensity $I = 1\%$. The ensemble mean of each method $\langle \epsilon_i \rangle_N$ is denoted by red dots where the whiskers extend from the minimal to maximal estimate of ϵ_i where $i \in \{G, I3, I2, S, L\}$. As the inertial range of DNS 1.1 ($I = 1\%$, $\theta = 0°$ and maximal available averaging window) is not well pronounced due to the low $\mathrm{R}_\lambda \sim 74$, we used the maximum of Eq. (3.15) in order to retrieve $\epsilon_{I2,3}$. The dashed line represents the global mean energy dissipation rate of DNS 1.1 and 2.1 ($\mathrm{R}_\lambda = 219$, $I = 1\%$, $\theta = 0°$ and maximal available averaging window), respectively, which is approximated by the ensemble average of the true mean energy dissipation rate along the trajectory of each virtual probe. ϵ_{ref} is the reference distribution of ground-truth global mean energy dissipation field originating from the dissipation field along the trajectory of each virtual probe.

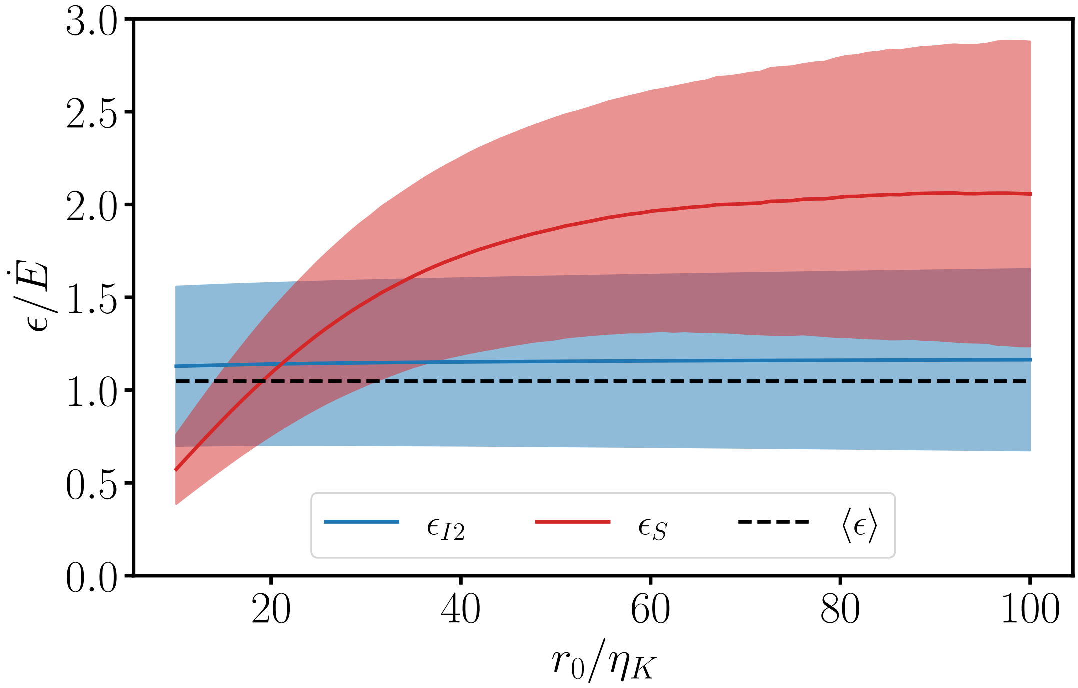

Figure 3.11 Estimates of the mean energy dissipation rate as a function of the fit-range for ϵ_{I2} and ϵ_S for DNS 3.1 (1000 probes, $R_\lambda = 302$, $I = 1\%$, $\theta = 0°$ and maximal available averaging window) re-scaled by the energy injection rate $\dot{E}$. The solid line represents the ensemble average whereas the shaded region is given by the standard deviation. $r_0 \in [10\eta_K, 100\eta_K]$ is the lower boundary of the fit-range for ϵ_{I2} where the upper boundary is fixed at $r_1 = 500\eta_K$. For ϵ_S, the fit-range is given by $f \in [U/r_1, U/r_0]$. The dashed line denotes the global mean energy dissipation rate.

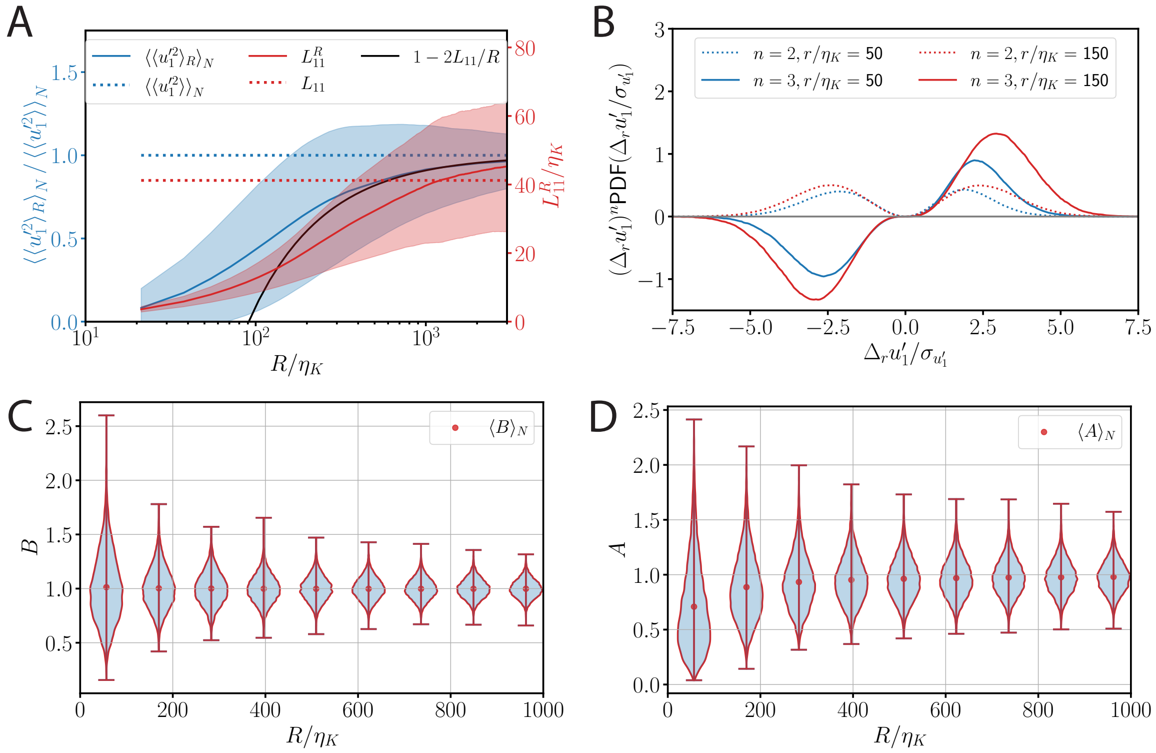

Figure 3.12 Convergence of higher-order statistical quantities and longitudinal integral length scale as well as small and large-scale anisotropy obtained from all virtual probes of DNS 1.1 ($R_\lambda = 74$, $I = 1\%$, $\theta = 0°$). (A) The variance of the longitudinal velocity fluctuations $\langle u_1'^2\rangle$ and the longitudinal integral length scale L_{11}^R as a function of averaging window size R normalized by the Kolmogorov length scale η_K. $\langle u_1'^2\rangle$ is re-scaled by the ensemble averaged variance of the longitudinal velocity fluctuations. For large R, $\langle\langle u_1'^2\rangle_R\rangle_N$ converges to $\langle u_1'^2\rangle \approx \langle\langle u_1'^2\rangle\rangle_N$ (blue-dotted line) and the systematic error of the variance (solid-black line), Eq. (3.41), decays to 0. L_{11}^R is the longitudinal integral length scale obtained from averaging windows of size R. For large R, L_{11}^R should converge to L_{11} (red-dotted line) which is not fully achieved in this range of R. (B) Premultiplied PDFs of second and third-order velocity increments over distances $r = 50\eta_K$ and $r = 150\eta_K$. The tails of the pre-multiplied PDFs have decayed to zero for large (and re-scaled) increments $\Delta_r u_1'/\sigma_{u_1'}$ so that they can globally considered to be converged. (C) Small-scale anisotropy based on the ratio of longitudinal gradients to the instantaneous energy dissipation $B = \epsilon_G/\langle\epsilon_0(\boldsymbol{x}, t)\rangle$. In isotropic turbulence, $B = 1$ on average. (D) Large-scale anistropy parameter $A = 3\langle u_1'^2\rangle/(2k)$ as a function of averaging window R where k is the turbulent kinetic energy and $\langle u_1'^2\rangle$ the variance of the longitudinal velocity fluctuations. In isotropic turbulence, $A = 1$ on average.

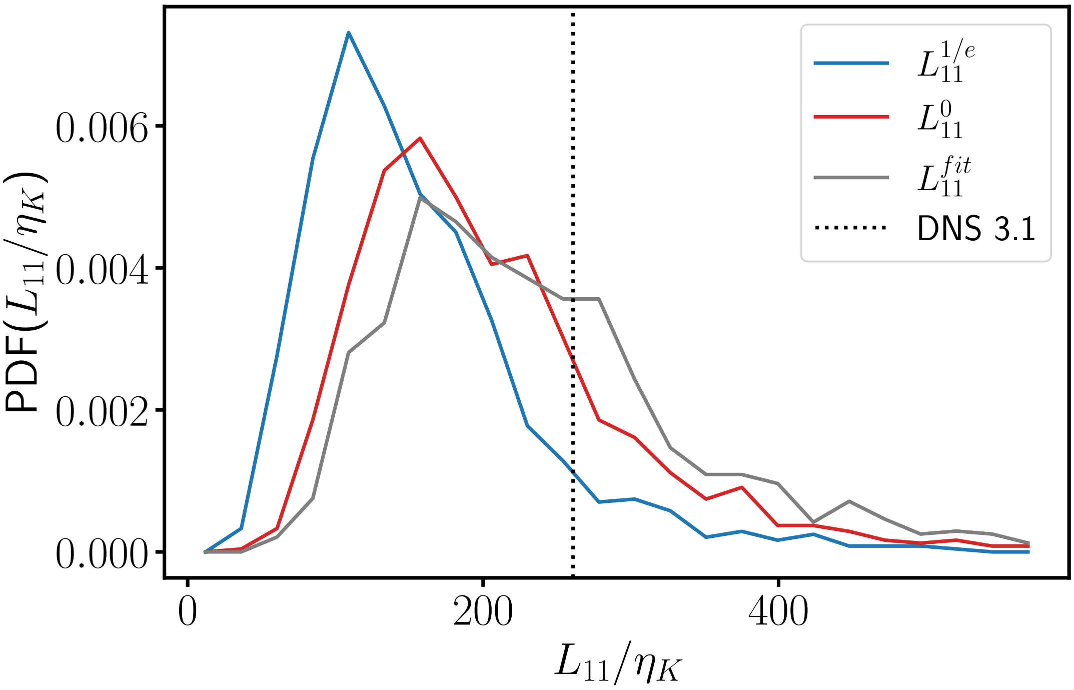

Figure 3.13 Different estimated of the integral length from DNS 3.1 withR$_\lambda = 302$, $I = 1\%$, $\theta = 0°$ and maximal available averaging window). L_{11}^{0} is inferred from integrating $f(r)$ to its first zero whereas $L_{11}^{1/e}$ refers to the integration of $f(r) > 1/e$. L_{11}^{fit} extends $f(r)$ with an exponential tail where the integration is performed up to infinity. The black dotted line is the reference from DNS 3.1 obtained by Eq. (3.19). All estimates are re-scaled by η_K.

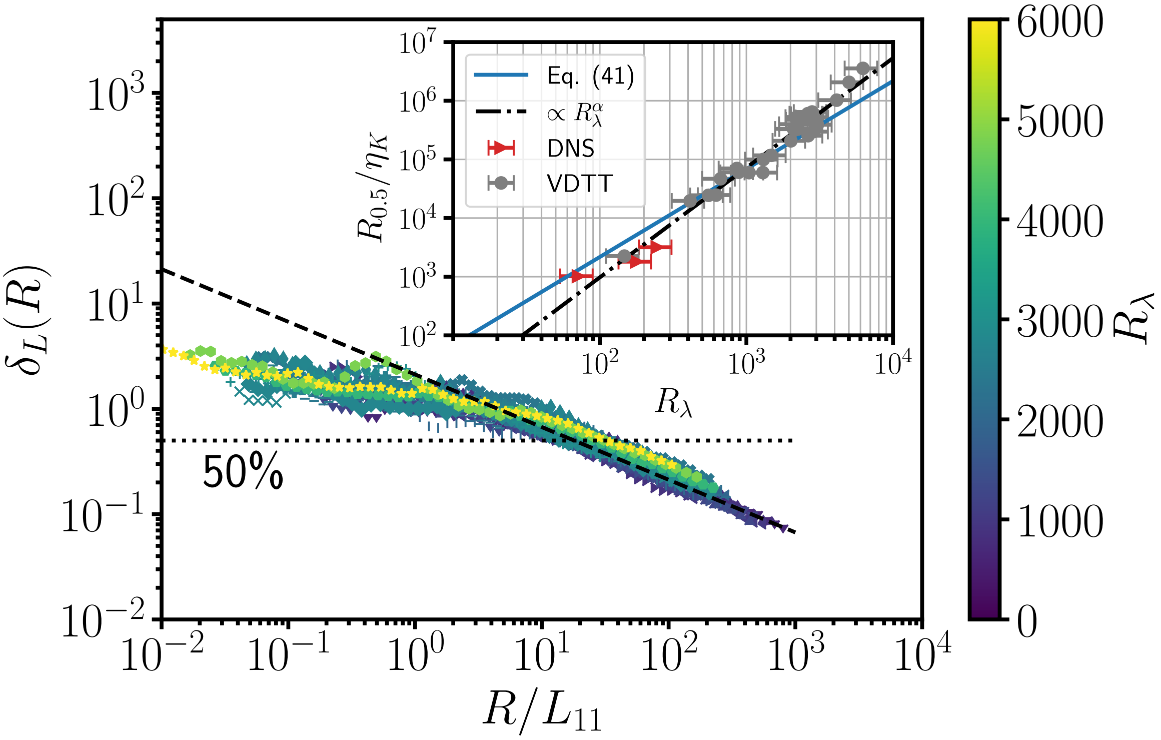

Figure 3.14 Convergence of energy dissipation rate estimates for ϵ_L. The empirical random error $\delta_L(R)$ is plotted as a function of re-scaled averaging window size R/L_{11} from VDTT experiments at various R_λ. The analytical result for the random error (Eq. (3.43)) is shown by the dashed black line. (Inset) The insets show the length of the averaging window in terms of η_K where $\hat{\delta}_L^R$ is less than 50% as a function of Taylor microscale Reynolds number R_λ. The inset plot shows data from DNS 1.3, 2.3 and 3.3 (red triangles) and the VDTT (grey circle). The three red dots mark the experiments with the highest R_λ where the isotropy of the grid forcing in the VDTT is not guaranteed anymore. The solid, blue line shows Eq. 3.49 resolved for $R_{0.5}/\eta_K$. The double logarithmic fit ($\log R/\eta_K = \frac{3}{4}\log\frac{9}{4}\frac{3}{20} - 2\log a_{\mathrm{fit}} + \alpha\log \mathrm{R}_\lambda$) is performed for the scaling argument resulting in $\alpha = 1.87 \pm 0.06$ and $a_{\mathrm{fit}} = 1.75 \pm 0.22$ (black dash-dotted line) .

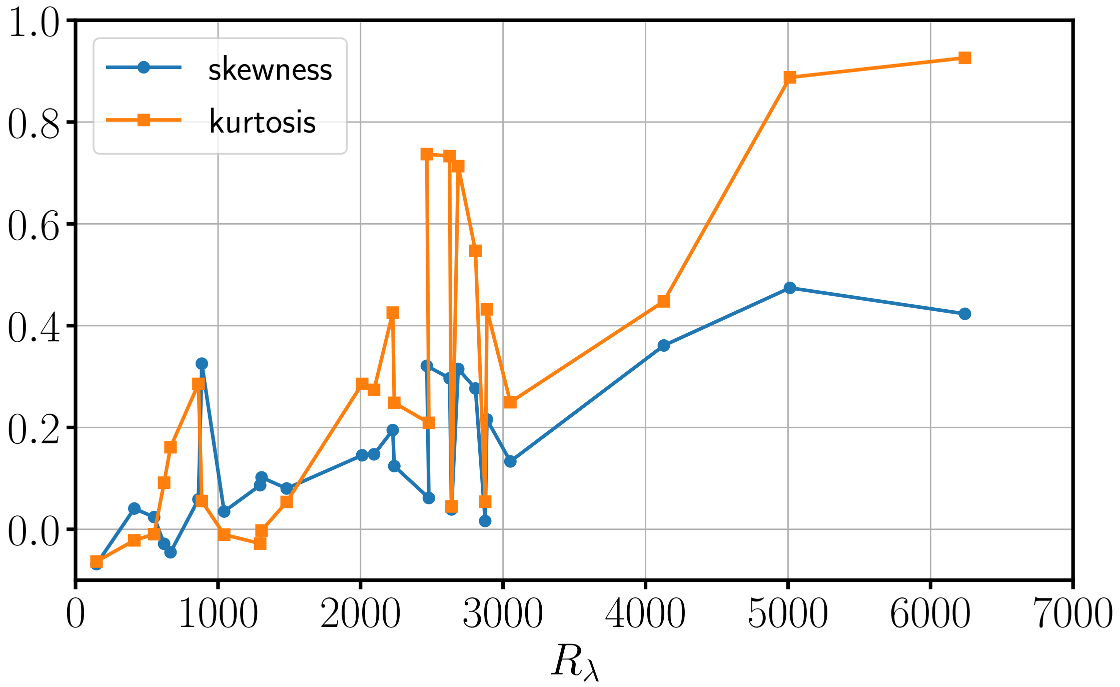

Figure 3.15 Skewness and kurtosis of all VDTT experiments as a function of R_λ. The skewness vanishes for normally distributed velocity time records. Similarly, the kurtosis equals 0 for normally distributed velocity time records, according to Fisher's convention.

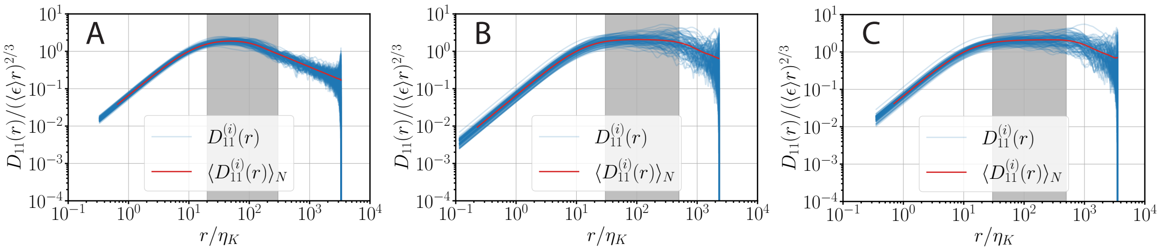

Figure 3.16 Longitudinal second-order structure functions for DNS 1.1 (A), DNS 2.1 (B), and DNS 3.1 (C). The grey shaded region represents the fit-range (Eq. (3.15)) for each DNS. The individual longitudinal second-order structure functions are calculated from the velocity time records along the $\boldsymbol{e}_1$-direction of each virtual probe (blue lines). The ensemble averaged longitudinal second-order structure functions are shown in red.

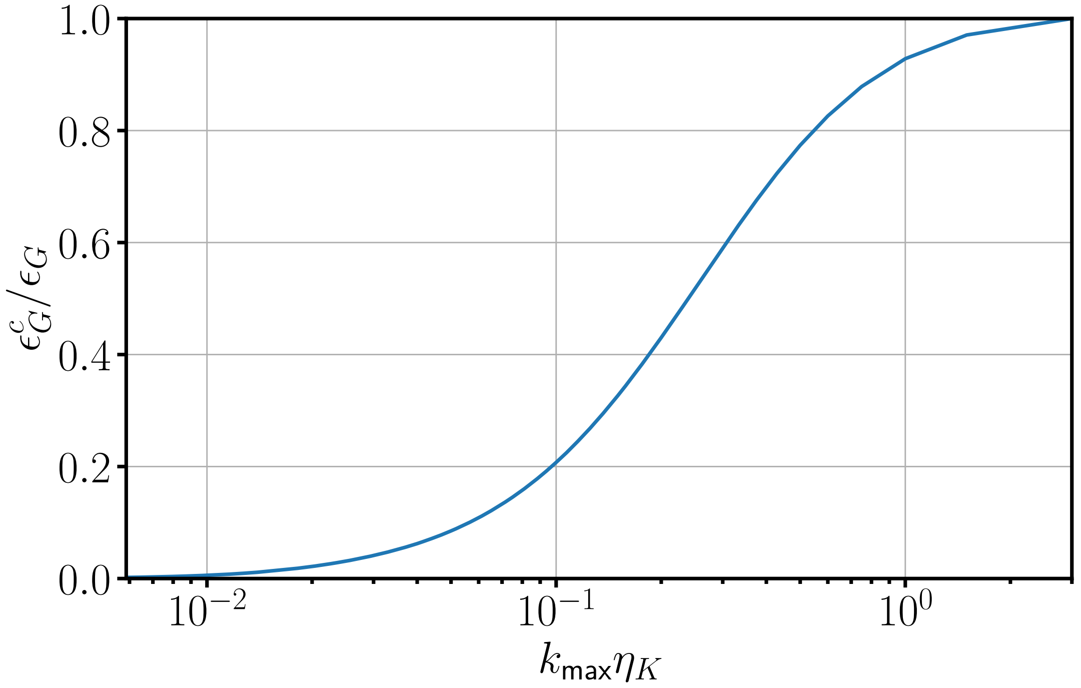

Figure 3.17 Resolution effect on ϵ_G. ϵ_G^c refers to the coarse-grained velocity time record. Coarse-graining is realized by taking only every nth value of the fully resolved velocity time record where $n \in [1, 512]$, thereby controlling the resolution $k_{\max}\eta_K$. Velocity data are taken from DNS 2.0 ($\mathrm{R}_\lambda = 142$, $R \approx 32000\eta_K$, $I = 10\%$, $\theta = 0°$).

Chapter 4

Atmospheric Turbulence and Cloud Microphysics in the Trade-wind region

In this chapter, I report on atmospheric turbulence characteristics both in cloud-free and cloudy air in the trade wind region. Therefore, I consider time-records of the longitudinal velocity unless otherwise stated. Furthermore, I describe cloud microphysics of trade-wind cumulus clouds sampled by cloud droplet probes as mentioned in Chapter 2. The droplet number concentration n, Eq. (1.66), is obtained using time-records of the longitudinal velocity by the PSS8 pitot tube and cloud droplet probes to count the cloud droplets per time.

If not mentioned otherwise, both atmospheric turbulence characteristics and cloud microphysics are derived from relative wind speed measurements, which are in the longitudinal, i.e. streamwise, direction of the flow in a first approximation. Hence, these longitudinal velocity time-records are neither transformed to the Earth frame-of-reference nor corrected for platform motion. For that reason, the vertical eddy covariance measurements are not meaningful and will not be part of this thesis. However, I will show that corrections are not required in a certain range of scales for characterizing atmospheric turbulence if relevant modes of the platform motion are filtered. If not mentioned otherwise, a 4th order Butterworth filter is used to retrieve low-pass filtered velocity time-series with `scipy.signal.filtfilt`.

Reasonable platform motion correction requires i.a. three-dimensional filtered orientation and angular velocity time series. Regarding the large-scale motion and assuming that the mean wind speed $U \sim 10\,\mathrm{m/s}$ and $u' \lesssim 1\,\mathrm{m/s}$, the platform rotates about up to 10° in time periods of several seconds. This amounts to rotation rates of up to $10\,^\circ/\mathrm{s}$. To temporally resolve platform motions occurring on smaller scales (compare power spectral density of the roll rate in Sec. 2.4.2), high temporally resolved measurements at $> 10\,\mathrm{Hz}$ with sub-degree accuracy ($< 0.1^\circ$) are needed in order to capture platform angular velocity accurately. The SBG Ellipse-N is nominally capable of sub-degree accuracy and temporal resolution of up to 200 Hz. Unfortunately, the yaw angle measurements are polluted by a drift on the order of $360\,^\circ/\mathrm{h}$, which is nearly impossible to correct. It is possible that this deficiency is caused by ground loops in the MPCK both instrument boxes (MPCK+ and mini-MPCK). Another possible explanation is the setting of the acquisition frequency of 200 Hz, which might stretch the capabilities of the SBG in conditions of mediocre GNSS reception. In the future, SBG will be operated at 20 Hz only and ground loops have been identified and avoided in revised iterations of both instrument boxes.

In this chapter, I first report on atmospheric turbulence measurements at constant altitude to illustrate and justify the analysis procedure (Sec. 4.1). Then, I provide estimates of atmospheric turbulence characteristics within the marine boundary layer as a function of altitude as well as diurnal cycle and assess the anisotropy of the atmospheric flow (Sec. 4.2 and Sec. 4.3). Subsequently, I give an overview of cloud microphysical measurements during the EUREC^{4}A field campaign and a hint at cloud droplet spatial clustering in a precipitating cloud (Sec. 4.4). At last, the effect of filtering is evaluated in Sec. 4.B.

Eberhard Bodenschatz, Gholamhossein Bagheri, Freja Nordsiek, Philipp Höhne, Oliver Schlenczek, Torben Neumann and me developed and built the MPCK+. Eberhard Bodenschatz, Gholamhossein Bagheri, Freja Nordsiek,Oliver Schlenczek, Antonio Ibañez Landeta and me developed and built the mini-MPCK. During EUREC^{4}A , Eberhard Bodenschatz, Gholamhossein Bagheri, Freja Nordsiek, Antonio Ibañez Landeta, Oliver Schlenczek, Marcel Meyer, Andreas Kopp, Johannes Güttler, Kashwan Hall and I acquired the data. Eberhard Bodenschatz, Gholamhossein Bagheri, Freja Nordsiek,Oliver Schlenczek and I organized the data. I performed the data analysis.

4.1 Atmospheric Turbulence Measurements at Constant Altitude

Turbulence measurements in the atmosphere are challenging because of, i.a., changing synoptic conditions, diurnal cycle and topographic effects. Even in marine environments, the mean wind direction varies in time and in space. Considering Flight 12 on M161 aboard RV Meteor during EUREC^{4}A field campaign, I prove the concept of characterizing atmospheric turbulence with the Max Planck Cloudkites including the choice of the averaging window T in a non-stationary flow. Thereby, I focus on the simplest instrument box, the micro-MPCK, which behaves like a weather vane as argued in Sec. 2.D. Hence, the influence of platform alignment motions is negligible in a first approximation. In consequence, neither filtering nor corrections for platform motion are applied in this section. As Flight 12 serves to acquire long time series at nominally constant altitude, the altitude profile is also simple and suited for optimizing statistical convergence. In this section, I first provide an overview of M161 Flight 12. After that, I demonstrate statistical convergence in atmospheric turbulence and find the best size for the averaging window. At last, I present bulk turbulence characteristics for M161 Flight 12. The energy dissipation rate estimates in the sub-cloud layer will be considered in more detail in Sec. 4.2.

4.1.1 Overview of M161 Flight 12

During M161 Flight 12, the micro-MPCK was launched on February 15 2020 at 18:48 UTC and landed on February 16 2020 at 12:25 UTC which amounts to approx. 17 flight hours. Thus, Flight 12 on M161 is one of the longest continuous flights during the EUREC^{4}A field campaign. As shown by the barometric altitude time-record $z_{\mathrm{PSS8}}(t)$ of the micro-MPCK in Fig. 4.1A, the micro-MPCK was probing the atmospheric boundary layer in a narrow altitude range between 80 m to 120 m above MSL where the altitude fluctuates approximately by $\sigma_{z_{\mathrm{PSS8}}} \approx 6\,\mathrm{m}$. Together with the total flight time, this flight strategy gives the possibility to illustrate statistical convergence in the context of atmospheric measurements across the diurnal cycle.

The effect of the diurnal cycle on the air temperature is shown by the air temperature time-record in Fig. 4.1B. The diurnal cycle is strongly connected to radiative heating by the sun. Close to Barbados, the sunset is at approx. 18:00 AST (UTC - 4) and sunrise at approximately 06:30 AST. The decrease in air temperature (Fig. 4.1B) starts at 02:00 UTC and lags 4 h behind the sunset. This time delay is attributed to the huge heat capacity of the ocean heating the boundary layer after sunset. The decrease in air temperature by 0.5 K lasts $\sim 4\,\mathrm{h}$ (from 02:00 to 06:00 UTC) while the increase after sunrise takes only 1 h. Hence, the diurnal cycle causes air temperature changes on time scales $\sim 1\,\mathrm{h}$. As mentioned below, this time scale seems to be critical for the assumption of a stationary turbulent flow.

In addition to atmospheric state parameters, such as static pressure p_s and air temperature T, the micro-MPCK measured the relative wind in terms of the longitudinal velocity $u_1(t)$ as a function of time (Fig. 4.1C). Visually, $u_1(t)$ is prone to large-scale variations on time scales $\gtrsim 1\,\mathrm{h}$, which might be related to the RV Meteor velocity with respect to ground. As mentioned above, reasonable correction for platform motion is not possible but also not necessarily required for the keel-strapped micro-MPCK. Under the assumption of statistically stationary turbulence, a vertical mean velocity profile can be estimated in order to check at which altitude the micro-MPCK leaves the wake of RV Meteor. The height-averaged longitudinal velocity $\langle u_1(t)\rangle_z$ over vertical increments of 5 m as a function of altitude above MSL is shown in Fig. 4.1D. $\langle u_1(t)\rangle_z$ saturated for altitudes higher than $\sim 40\,\mathrm{m}$ indicating that the micro-MPCK is out of the wake of RV Meteor and possibly the atmospheric surface layer.

4.1.2 Statistical Convergence in atmospheric turbulence

Characterizing a stationary turbulent flow requires statistical convergence of at least the mean and variance estimates. As mentioned in Sec. 1.2.6, I define $\langle u_1'^2\rangle_\tau$ to be converged if the systematic error, Eq. (1.63), is much smaller than the random error $\sqrt{2\langle u_1'^2\rangle^2 T_{11}/\tau}$ being defined in [56] for $\tau \gg T_{11}$. Both systematic and random errors decrease monotonically with τ. Thus, it is favorable to choose the maximally available averaging window τ. To illustrate the effect of the averaging window τ, $u_1(t)$ is assumed to be stationary in time. Later, this assumption will be checked as well.

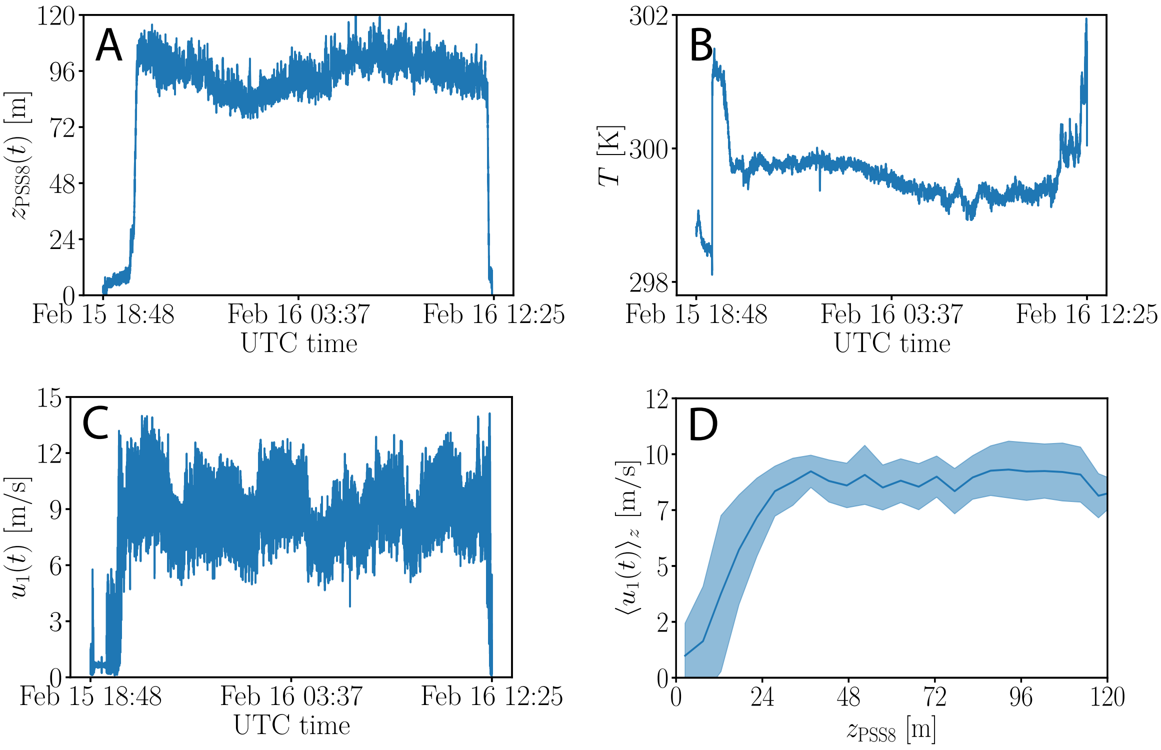

Figure 4.1 Overview of M161 Flight 12 on RV Meteor over night from February 15 2020 to February 16 2020 during EUREC^{4}A field campaign. Barometric altitude time-record $z_{\mathrm{PSS8}}(t)$ of the micro-MPCK flown at approximately constant altitude above MSL (A). Time-records of air temperature T (B) and relative wind speed $u_1(t)$ (C) are shown for the entire flight. D: The mean wind speed averaged over altitude increments of 5 m saturates for altitudes higher than ≈ 40 m above MSL.

At first, I investigate the dependence of variance estimates from the longitudinal velocity time record $\langle u_1'^2\rangle_\tau$ on the temporal averaging window size τ. Therefore, $\langle u_1'^2\rangle_\tau$ is evaluated for each τ for the entire time series following the procedure in [56] where each averaging window τ corresponds to one realization of the flow. Then, $\langle\langle u_1'^2\rangle_\tau\rangle_N$ is the ensemble average of $\langle u_1'^2\rangle_\tau$ as shown in Fig. 4.2A. The shaded region is given by the standard error of the mean in order to capture statistical scatter. The large deviation between $\langle\langle u_1'^2\rangle_\tau\rangle_N$ and the predicted variance estimate, Eq. (1.61) with $\tau \lesssim 5T_{11}$ ($T_{11} = 46\,\mathrm{s}$), is expected. In the range of $40T_{11} \leq \tau \leq 70T_{11}$, $\langle\langle u_1'^2\rangle_\tau\rangle_N$ overlaps with the predicted variance estimate, Eq. (1.61) with $\tau = 65T_{11}$, within the standard error. In Fig. 4.2A, $\tau = 50T_{11}$ is in the center of the overlap region between the empirical and theoretical curve. For $\tau > 80T_{11}$, $\langle\langle u_1'^2\rangle_\tau\rangle_N$ deviates strongly from the predicted variance estimate, Eq. (1.61), suggesting non-stationarity. This is in accordance with the time scale over which the air temperature changes (M161 Flight 12: ~ 1 h due to diurnal cycle, Fig. 4.1B). Hence, $\tau \sim 1$ h poses an upper limit on reasonable averaging windows although it has to be emphasized that this is a time *scale*, which itself is influenced by environmental conditions unlike in laboratory experiments or simulations.

To focus on time scales below 1 h, i.e. the time scale of non-stationarity, the longitudinal velocity time record is divided into segments of $3600\,\mathrm{s} \approx 78T_{11}$ where the ensemble consists of S segments. In each segment, $\langle\langle u_1'^2\rangle_\tau\rangle_N$ is evaluated similar to the previous procedure. Consequently, $\langle\langle\langle u_1'^2\rangle_\tau\rangle_N\rangle_S$ is the ensemble average of $\langle\langle u_1'^2\rangle_T\rangle_N$ over all segments S. Then, the predicted variance estimate, Eq. (1.61) with $\tau = 65T_{11}$, is within the standard error of $\langle\langle\langle u_1'^2\rangle_\tau\rangle_N\rangle_S$ in the range $10T_{11} \leq \tau \leq 78T_{11}$ (Fig. 4.2B). In Fig. 4.2A, $\tau = 39T_{11}$ is at the beginning of the overlap region while $\tau = 50T_{11}$ is in the center of the overlap region between the empirical and theoretical curve, as mentioned before. For $\tau = 1800\,\mathrm{s} \approx 39T_{11}$, $\langle\langle\langle u_1'^2\rangle_\tau\rangle_N\rangle_S$ is underestimated by ≈ 5% compared to $\langle u_1'^2\rangle_{65T_{11}}$. Using $\sqrt{2\langle u_1'^2\rangle^2 T_{11}/\tau}$ for the random error of the variance estimate [56], the random error of $\langle u_1'^2\rangle_\tau$ is 18% which is significantly larger than the systematic error of the variance estimate. Hence, $\langle u_1'^2\rangle_\tau$ is reasonably converged for $\tau = 1800\,\mathrm{s}$ in the limit of accuracy. To resolve turbulence characteristics in time, I choose the averaging window $\tau = 39T_{11}$, which is the shortest reasonable averaging window possible.

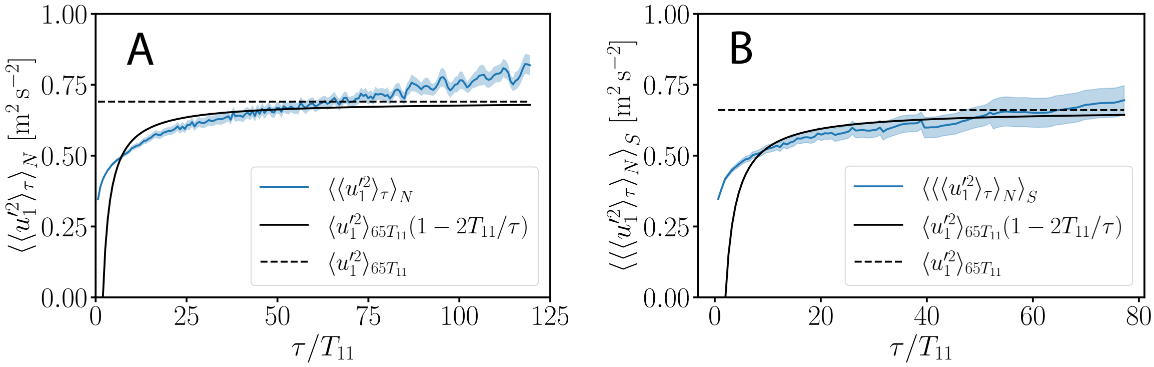

Figure 4.2 Variance estimates of longitudinal velocity time record $\langle u_1'^2\rangle_\tau$ as a function of the temporal averaging window size τ re-scaled by the integral time scale $T_{11} = 46\,\mathrm{s}$. $\langle\langle u_1'^2\rangle_\tau\rangle_N$ represents the ensemble average based on the averaging window τ. The shaded blue region is given by the standard error of the mean. The systematic underestimation of the variance estimate is shown by the solid black line and given by Eqs. (1.63) and (1.61). A: $u_1'(t)$ is assumed to be stationary. $\tau = 39T_{11}$ is at the beginning of the overlap region while $\tau = 50T_{11}$ is in the center of the overlap region between the empirical and theoretical curve. B: Taking into account the non-stationarity, the longitudinal velocity time record is divided into segments of $S = 3600\,\mathrm{s}$. In each segment, $\langle\langle u_1'^2\rangle_\tau\rangle_N$ is evaluated for each τ. $\langle\langle\langle u_1'^2\rangle_\tau\rangle_N\rangle_S$ is the average of $\langle\langle u_1'^2\rangle_T\rangle_N$ over all segments S. The black dashed line illustrates $\langle u_1'^2\rangle_{65T_{11}}$, i.e. the variance estimate based on an averaging window of $65T_{11}$. The theoretical expectation, Eq. 1.63, is within the standard error of the variance estimate with an averaging window $\tau = 39T_{11}$ denoted by $\langle u_1'^2(t)\rangle_{39T_{11}}$. In the following, the shortest reasonable averaging window is chosen to $\tau = 39T_{11}$ in order to resolve turbulence characteristics in time.

However, atmospheric flows are generally non-stationary due to, i.a., the diurnal cycle. Above, we assumed $u_1(t)$ to be a statistically stationary time-record of the longitudinal velocity. According to [5], a time series of a random process is statistically stationary if all statistics are independent of a shift in time. Here, a less strict criterion has to be applied because the mean velocity of the flow is not accurately known due to time-dependent platform motions as a result of ship motions. Therefore, I regard $u_1(t)$ as *statistically stationary* if changes of $\langle u_1'^2(t)\rangle_\tau$ under time shifts of the averaging window τ are smaller than the random error of the variance estimate $\sqrt{2\langle u_1'^2\rangle^2 T_{11}/\tau}$ [56]. In the following, I will refer to $\langle u_1'^2\rangle_{65T_{11}}$ as the reference for estimating errors because $\tau = 65T_{11}$ is significantly shorter than $\tau = 78T_{11}$ and still agrees with the prediction, Eq. (1.61), as shown in Fig. 4.2A. In doing so, the random error $\langle u_1'^2\rangle_\tau$ is 18% for $\tau = 1800\,\mathrm{s}$ and 32% for $\tau = 600\,\mathrm{s}$. The systematic errors are 4% and 15%, respectively, in comparison to $\langle u_1'^2\rangle_{65T_{11}}$.

Figure 4.3 shows $\langle u_1'^2(t)\rangle_\tau$ as a function of time indicating that $\langle u_1'^2(t)\rangle_\tau$ fluctuates significantly. This might hint at the fact that the stationarity assumption is not fulfilled globally. As an example, $\langle u_1'^2(t)\rangle_\tau$ drops by 60% on February 16 2020 at 04:30 UTC (dotted line in Fig. 4.3), which is larger than the random error of the variance estimate $\sqrt{2\langle u_1'^2\rangle^2 T_{11}/\tau}$ for both $\tau = 600\,\mathrm{s}$ and $\tau = 1800\,\mathrm{s}$. However, there are local time intervals (e.g. February 15 2020 at 23:45 UTC to February 16 2020 at 01:25 UTC, the gray shaded region in Fig. 4.3) over which $u_1(t)$ appears to be approximately statistically stationary. In that time interval, $\langle u_1'^2(t)\rangle_{1800\,\mathrm{s}}$ is constant within 12%, which is smaller than the random error of $\approx$ 18%. Furthermore, $\langle u_1'^2(t)\rangle_\tau$ fluctuates about 17% for $\tau = 600\,\mathrm{s}$, which is lower than the random error, too. Remarkably, $\langle u_1'^2(t)\rangle_{600\,\mathrm{s}}$ tends to be lower than $\langle u_1'^2(t)\rangle_{1800\,\mathrm{s}}$, which is due to the underestimated variance as illustrated in Fig. 4.2. To summarize, the choice of an averaging window $\tau = 1800\,\mathrm{s}$ compromises between statistical convergence and still being temporally shorter than characteristic time scales of non-stationarities of $\sim 1\,\mathrm{h}$. This is further consistent with Risius et al. [54] and Stull [40] as mentioned in Sec. 1.2.6.

4.1.3 Bulk Turbulence Characteristics of M161 Flight 12

A major goal of this section is to prove the capability of the Max Planck Cloud Observatory to characterize atmospheric turbulence based on one-dimensional velocity time-records along the trajectory of the micro-MPCK within the limits of (statistical) accuracy. The configuration of the micro-MPCK can be considered as the experimental equivalent of the idealized weather vane which is why the micro-MPCK bridges the gap between simulation and *in-situ* measurement. Advantageously, it has been shown in Sec. 2.4.4 that basic turbulence characteristics such as the energy dissipation rate are only slightly affected by the alignment motions of a weather vane. For that reason, one can assume that turbulence statistics obtained from measurements with the micro-MPCK do not necessarily require corrections of these alignment motions or filtering. After describing the bulk turbulence characteristics of M161 Flight 12, this assumption will be discussed by comparing it to VDTT experiments.

In this thesis, turbulence is characterized in terms of the mean energy dissipation rate. To cope with non-stationarity, the estimation of the mean energy dissipation rate is based on an averaging window $\tau = 1800\,\mathrm{s}$ (Sec. 4.1.2). It has been shown

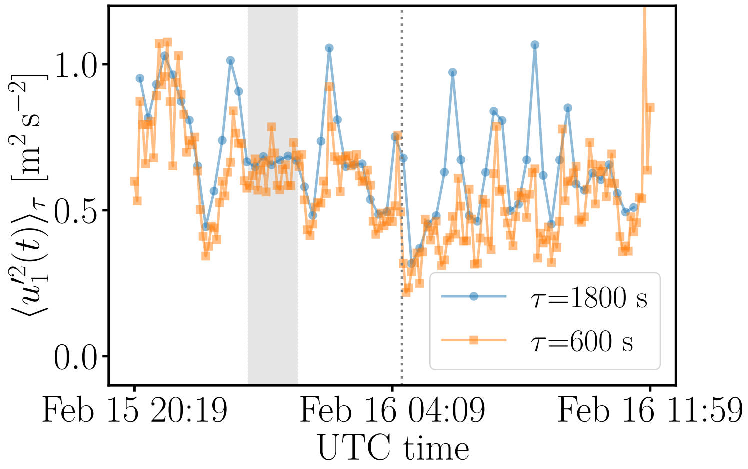

Figure 4.3 The variance of longitudinal velocity fluctuations $\langle u_1'^2(t)\rangle_\tau$ based on an averaging window τ as a function of UTC time. Two averaging windows $\tau = 1800\,\mathrm{s}$ and $\tau = 600\,\mathrm{s}$ are chosen to visualize the effect of time shifting the averaging window. If the change in $\langle u_1'^2(t)\rangle_\tau$ is *smaller* than the random error $\sqrt{2\langle u_1'^2\rangle^2 T_{11}/\tau}$ for a specific time interval, the flow can be regarded as stationary for this time window (e.g. grey region). The dotted line indicates 04:30 UTC.

in Chapter 3 that the most reliable estimate of the energy dissipation rate is ϵ_{I2} for airborne measurements in the atmosphere as it is least affected by misalignment as well as finite turbulence intensity I and as it converges reasonably fast. Estimating the mean energy dissipation rate by ϵ_{I2} requires mapping the longitudinal velocity time-record onto one-dimensional spatial lags, which invokes Taylor's hypothesis (Sec. 3.2.1). As the mean turbulence intensity for M161 Flight 12 is $I = 9\%$ ($I_{\max} = 12\%$), Taylor's hypothesis can be safely applied. Hence, the energy dissipation rate can be obtained following the procedure as illustrated in Fig. 3.1. The resulting estimates for ϵ_{I2} and turbulence quantities relying on ϵ_{I2} are presented by histograms in bulk ignoring the diurnal cycle or other changes in synoptic conditions.

ϵ_{I2} is obtained by fitting the second-order longitudinal structure function $D_{LL}(r)$ in the inertial range. Fig. 4.4A shows the second-order longitudinal structure functions $D_{LL}^\tau(r)$ estimated for each averaging window τ (blue lines). Under the assumption of stationarity, $\langle D_{LL}^\tau(r)\rangle_N$ is obtained by ensemble-averaging $D_{LL}^\tau(r)$ (red line). $\langle D_{LL}^\tau(r)\rangle_N$ reveals a pronounced inertial range with a $r^{2/3+1/36}$-scaling as predicted by K62 (gray dashed line). This is supported by the local scaling exponent $\zeta_2(r)$ being defined by [188]:

$$\zeta_2(r) = \frac{\mathrm{d}\log D_{LL}(r)}{\mathrm{d}\log r}\,. \tag{4.1}$$

The fit region $r \in [2\,\mathrm{m}, 20\,\mathrm{m}]$ is visually identified based on Fig. 4.4A and shaded in gray. The best fitting range for $\langle D_{LL}^{\tau}(r)\rangle_N$ would be $r \in [2\,\mathrm{m}, 6\,\mathrm{m}]$ although $\zeta_2(r)$ scatters strongly for individual $D_{LL}^{\tau}(r)$ in that range. The longer fit range is chosen to reduce the influence of that scatter on ϵ_{I2}. However, as $\zeta_2(r) = 0.71$ on average (standard deviation of 0.09) for $2\,\mathrm{m} \leq r \leq 20\,\mathrm{m}$, it is acceptable to use ϵ_{I2} invoking $r^{2/3}$-scaling according to K41. The resulting estimates of ϵ_{I2} obtained from each $D_{LL}^{\tau}(r)$ are cumulatively shown by the histogram of the energy dissipation rate estimates ϵ_{I2} (Fig. 4.4B). The most frequent mean energy dissipation rate during M161 Flight 12 is $\epsilon_{I2} \approx 8\,\mathrm{mW/kg}$. This value is in accordance with energy dissipation rate estimates in mountainous terrain where a range between $10^{-4} - 10^{-2}\mathrm{W/kg}$ is observed [54]. More precisely, Fig. 4.4B shows a double peak. In the first half of M161 Flight 12, the time-resolved ϵ_{I2} ($\tau = 1800\,\mathrm{s}$) strongly fluctuates by a factor of 2 while ϵ_{I2} is more uniform in the second half of M161 Flight 12. The strong fluctuations in the first half might be due to the advection of more turbulent patches. However, the presence of the double peak lacks detailed understanding. For completeness, the averaging window is chosen in time to be $\tau = 1800\,\mathrm{s}$, which is converted into the spatial averaging window $R = \langle u_1(t)\rangle_\tau \tau$ as shown in Fig. 4.4D. The most frequent spatial averaging window R is 17 km.

The estimate of the mean energy dissipation rate ϵ_{I2} serves as a basis for estimating the Kolmogorov length scale η_K, Eq. (1.12), the longitudinal Taylor micro-scale λ_f, Eq. (1.34), the integral length scale L_{11}, Eq. (1.29), and the Taylor-scale Reynolds number R_λ, Eq. (1.38). The corresponding histograms are shown in Fig. 4.5A-D. Starting with η_K, the most frequent Kolmogorov length scale is $\eta_K = 0.75\,\mathrm{mm}$. Moreover, λ_f is most frequently 0.16 m whereas the most likely integral length scale L_{11} is 21 m. Using the relation for the transverse Taylor micro-scale $\lambda_g = \sqrt{10}\eta_K^{2/3} L^{1/3}$ [5], one can estimate the energy injection scale from η_K and λ_g: $L = \left(\frac{\lambda_g}{\sqrt{10}\eta_K^{2/3}}\right)^3 \approx 81\,\mathrm{m}$ with $\eta_K = 0.75\,\mathrm{mm}$ and $\lambda_g = 0.11\,\mathrm{m}$. In homogeneous isotropic turbulence with $L_{11} = L/2$ at high R_λ, the integral scale is $\approx 40\,\mathrm{m}$ which is close to the average integral scale of $\langle L_{11}\rangle_N \approx 38\,\mathrm{m}$ but twice as large as the most frequent L_{11} in Fig. 4.5C. As the most likely R_λ is ≈ 4300 and $\langle \mathrm{R}_\lambda\rangle_N \approx 5100$ (4.5D), the assumption on high R_λ is valid. Despite this discrepancy and taking into account that the integral scale is *estimated* by a scaling argument, the estimated length scale across the entire range of turbulent scales are consistent.

To evaluate the accuracy of the Taylor-scale Reynolds number and the turbulence length scales, the accuracy of ϵ_{I2} is critical. As mentioned before, the accuracy of ϵ_{I2} can be captured by the systematic and random error based on the averaging window R and integral length scale L_{11}. The random error is estimated by Eq. (3.45). The relative systematic error $\delta_{I2}^{\mathrm{sys}}(R)$ can be derived similarly to $\delta_{I2}(R)$ (Sec. 3.3.4):

$$\delta_{I2}^{\mathrm{sys}}(R) = \left(1 - 2\frac{L_{11}}{R}\right)^{3/2} - 1\,, \tag{4.2}$$

where the histograms of $\delta_{I2}^{\mathrm{sys}}(R)$ and $\delta_{I2}(R)$ are shown in Fig. 4.6. The systematic error $\delta_{I2}^{\mathrm{sys}}(R)$ is <2% and can be neglected in the following. The most frequent random error

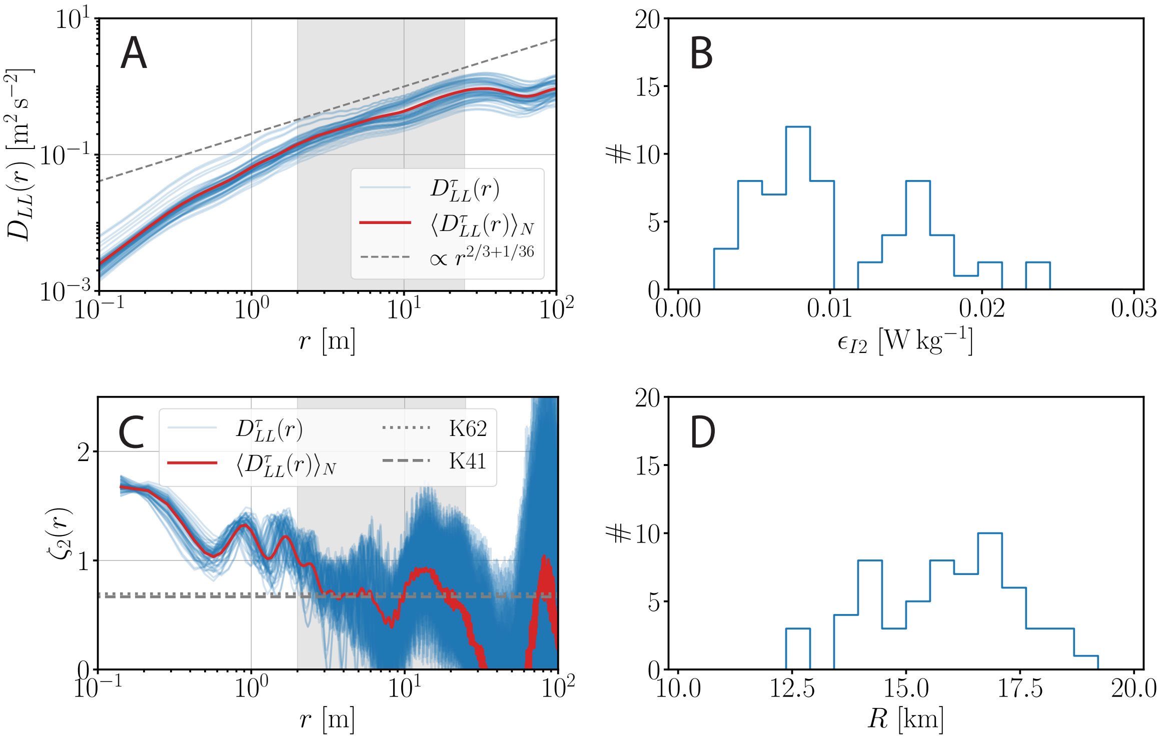

Figure 4.4 Energy dissipation rate estimate ϵ_{I2} for M161 Flight 12 derived from second-order longitudinal structure functions. A: The second-order longitudinal structure function $D^{\tau}_{LL}(r)$ is estimated for each averaging windows τ (blue lines). Under the assumption of stationarity, the ensemble average $\langle D^{\tau}_{LL}(r)\rangle_N$ is shown by the red line. The expected K62 scaling in the inertial range is indicated by the gray dashed line. The fit region is visually identified and shaded in gray. B: Histogram of the energy dissipation rate estimate ϵ_{I2} obtained from each $D^{\tau}_{LL}(r)$. The fit range corresponds to the gray-shaded region in (A) or (C). C: Local scaling exponent $\zeta_2(r)$ of $D^{\tau}_{LL}(r)$ (blue lines) according to Eq. (4.1) and $\langle D^{\tau}_{LL}(r)\rangle_N$ (red line). The expected scaling exponents in the inertial range are drawn for K41 (gray dashed line) and K62 (gray dotted line). The fit region is gray-shaded. D: The averaging window is chosen in time $\tau = 1800\,\mathrm{s}$ converting to the spatial averaging window $R = \langle u_1(t)\rangle_\tau \tau$, which is shown in the histogram.

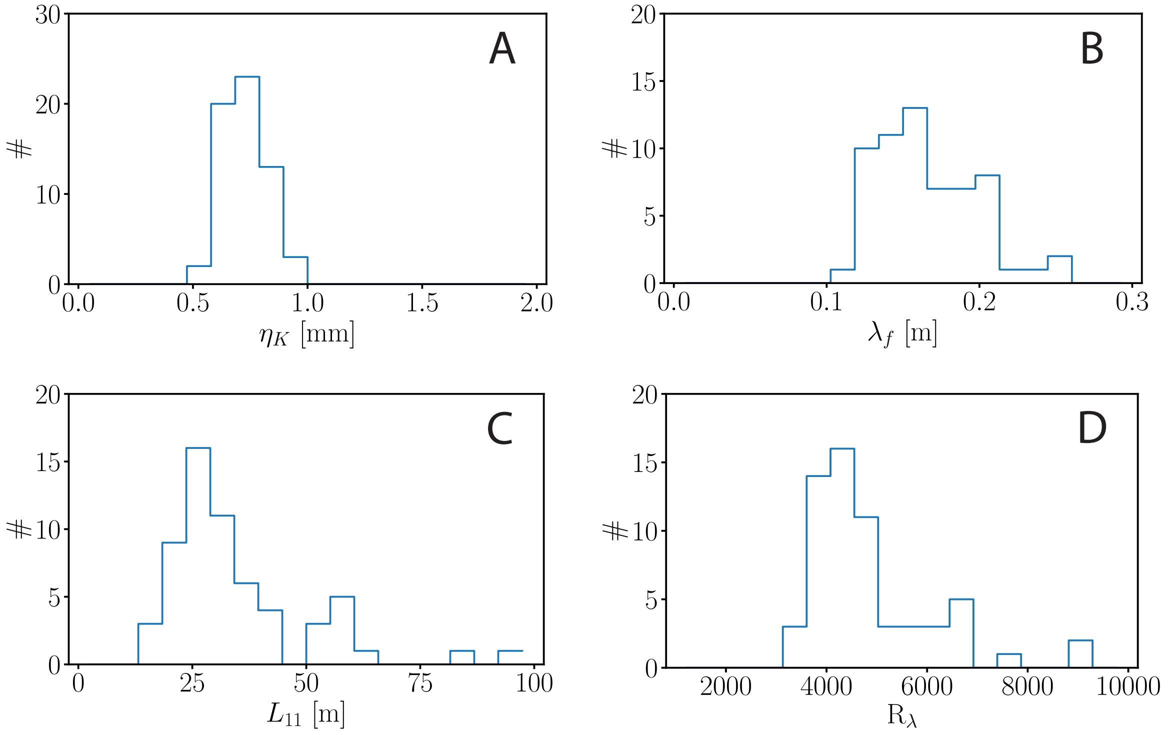

Figure 4.5 Bulk turbulence characteristics of M161 Flight 12 for averaging window of $\tau = 1800\,\mathrm{s}$. Histograms are shown for the Kolmogorov length scale η_K (A), the longitudinal Taylor micro-scale λ_f (B), the integral length scale L_{11} (C) and the Taylor micro-scale Reynolds number R_λ (D). Histograms in B, C and D are limited up to 20 counts (#) for better visibility.

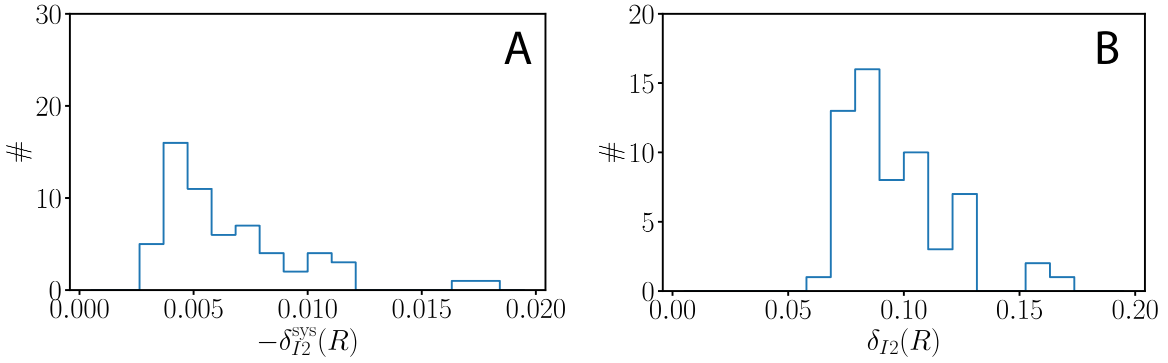

Figure 4.6 Histograms of the systematic error $\delta_{I2}^{\mathrm{sys}}(R)$ (A) and the random error $\delta_{I2}(R)$ (B) of the energy dissipation rate estimate ϵ_{I2} for M161 Flight 12. $R = U\tau$ is the spatial averaging window with $\tau = 1800\,\mathrm{s}$. Both errors are estimated from L_{11} and $\langle u_1'^2 \rangle_R$ based on the same R and, hence, have to be regarded rather as statistical estimates.

is $\delta_{I2}(R) = 8\%$ based on the estimated R and L_{11}.

While the plausibility of the length scale has been demonstrated above, the significance of the R_λ-estimate is assessed in the following. Estimating R_λ by $\mathrm{R}_\lambda \equiv u'\lambda_g/\nu$ and choosing $u' = \sqrt{\langle u_1'^2 \rangle_{65T_{11}}} = 0.81\,\mathrm{m/s}$, $\nu = 1.552 \times 10^{-5}\,\mathrm{m^2/s}$ and $\lambda_g = 0.12\,\mathrm{m}$, one obtains $\mathrm{R}_\lambda \approx 6300$. This is 15% higher than $\langle \mathrm{R}_\lambda \rangle_N \approx 5100$ (Fig. 4.5A) which has been derived from ϵ_{I2} and L_{11}. The expected error $e(\mathrm{R}_\lambda)$ due to the random error in ϵ_{I2} can be calculated by Gaussian error propagation and by the chain rule to

$$\begin{aligned} e(\mathrm{R}_\lambda) &= \left| \frac{\partial \mathrm{R}_\lambda}{\partial \epsilon_{I2}} \delta_{I2}(R) \epsilon_{I2} \right| = \left| \left(\frac{\mathrm{R}_\lambda}{6\epsilon_{I2}} - \frac{2}{3} \frac{R_\lambda}{\epsilon_{I2}} \right) \delta_{I2}(R) \epsilon_{I2} \right| \\ &= \frac{1}{2} \mathrm{R}_\lambda \delta_{I2}(R) \equiv \left| \frac{\partial \left(\frac{u'\lambda_g(\epsilon_{I2})}{\nu} \right)}{\partial \epsilon_{I2}} \delta_{I2}(R) \right| \end{aligned} \tag{4.3}$$

with

$$\frac{\partial}{\partial \epsilon_{I2}} L^{2/3} = -\frac{2}{3} \frac{1}{\epsilon_{I2}} L^{2/3}\,, \tag{4.4}$$

Equation (4.3) yields $e(\mathrm{R}_\lambda = 5100) \approx 200$ and $e(\mathrm{R}_\lambda = 6300) \approx 250$ assuming that the random error is 10% (compare the most frequent value in Fig. 4.6B). Using the maximum value of $\delta_{I2}(R)$ observed during M161 Flight 12 ($\delta_{I2}(R) \approx 15\%$), $e(\mathrm{R}_\lambda = 5100) \approx 380$ and $e(\mathrm{R}_\lambda = 6300) \approx 470$. These values suggest that the uncertainty in R_λ cannot be fully captured by the random error of ϵ_{I2}. Presumably, it is further affected by the uncertainty in L_{11} of about 50% as illustrated by the deviation between the most frequent and mean value of L_{11}. Notably, $\delta_{I2}(R)$ is proportional to $L_{11}^{3/2}$. Thus, $\delta_{I2}(R)$ potentially changes by a factor significantly larger than 1. However, R_λ is less amplified by ν in Eq. (1.38) which scales only as $\nu^{-1/2}$ in contrast to $\mathrm{R}_\lambda \equiv u'\lambda_g/\nu$. A similar range in R_λ has been observed in the surface layer in mountainous terrain with a most likely $\mathrm{R}_\lambda \approx 3000$ and maximal $\mathrm{R}_\lambda \sim 10^4$ [54].

At last, these measurements are compared to VDTT experiments [188]. The first point to note is that the PSS8 cannot resolve the dissipative scales in flows with $\eta_K \sim 1\,\mathrm{mm}$. In addition, due to recovering the PSS8 velocity time measurement and the filtering in the frequency domain at 12 Hz (see Sec. 2.A), the local scaling exponent should not be trusted for scales below $\sim 1\,\mathrm{m}$. The strong oscillation at those scales might be also due to platform motion. Despite minor oscillations of $\zeta_2(r)$ around 2/3, the agreement of $\zeta_2(r)$ derived from $\langle D_{LL}^{\tau}(r) \rangle_N$ for $r \in [2\,\mathrm{m}, 6\,\mathrm{m}]$ in the inertial range with the K62-prediction is remarkable. Assuming the energy injection scale to be $L \sim 80\,\mathrm{m}$ as estimated above, $r/L \sim 10^{-2}$ in the range $2\,\mathrm{m} \leq r \leq 6\,\mathrm{m}$. In the decade from $10^{-2} \leq r/L \leq 10^{-1}$, $\zeta_2(r)$ shows a comparable plateau in the VDTT experiments with $\mathrm{R}_\lambda > 1000$, which is in accordance with the observed R_λ for M161 Flight 12. For $r > 20\,\mathrm{m}$, a uniform scaling according to K41 or K62 is not expected anymore as $r \sim L$. Large scales at $r > 20\,\mathrm{m}$ take longer to converge due to the complex nature of atmospheric flows and are not expected to exhibit the same scaling behavior due to the non-universality of turbulence at scales comparable to or larger than L_{11}. Furthermore, the agreement of $\zeta_2(r)$ in the inertial range with Kolmogorov's prediction at least in the range $r \in [2\,\mathrm{m}, 6\,\mathrm{m}]$ suggests that the micro-MPCK measures statistically isotropic turbulence. Hence, the flow distortion of the helikite is supposedly small in that range. To summarize, the micro-MPCK is able to characterize turbulence in terms of the mean energy dissipation rate, length scales and Taylor micro-scale Reynolds number. The same holds for all other configurations that are keel-mounted. Tether-mounted instruments measure a flow that is less distorted by the helikite but the dynamics of platform motion are more complex, too.

4.2 Atmospheric Turbulence Characteristics of the Marine Boundary Layer

In this section, turbulence characteristics of the trade-wind sub-cloud layer are presented. After determining the height of the boundary layer depth, atmospheric stability is described in terms of the Richardson number. Subsequently, bulk turbulence characteristics are presented and the assumption on local isotropy validated.

4.2.1 Top of stably stratified Boundary Layers

Airborne measurements with the MPCKs are performed at various altitudes. To compare these measurements, the altitudes have to be re-scaled by, e.g., the top of the boundary layer (TBL). There are various definitions for the TBL relating to the cloud base, the lifting condensation level or a capping inversion of a scalar. Here, we will determine the TBL in terms of the virtual potential temperature θ_v, which is approximately constant with altitude in the mixed layer due to turbulence-induced mixing and warm-air entrainment from above [110, 189], hence

$$\frac{\partial \theta_v}{\partial z} = 0\,. \tag{4.5}$$

The layer above the mixed layer is usually called the free atmosphere or troposphere. As the free atmosphere is warmer than the mixed layer, θ_v increases at the top of the mixed layer [189], hence

$$\frac{\partial \theta_v}{\partial z} > 0\,. \tag{4.6}$$

This increase in θ_v is known as a capping inversion. Thus, the top of the boundary layer can be determined based on (i) the mixed layer and (ii) the capping inversion.

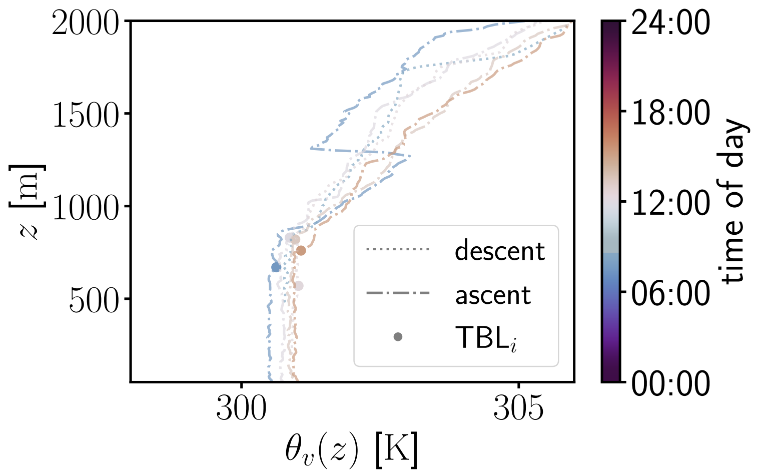

Figure 4.7 Vertical profiles of the virtual potential temperature $\theta_v(z)$ recorded by radiosondes during EUREC^{4}A field campaign. During M161 Flight 10, three radiosondes [88] were launched on RV Meteor (cf. Sec. 2.4.3) where ascents are visualized by dash-dotted lines and descents by dotted lines. The top of the boundary layer (TBL) is shown by the circle where only the estimate TBL$_i$ is shown. Each vertical profile is colored in order to visualize the diurnal cycle where the colorbar denotes the Atlantic Standard Time (AST) of the day (HH:MM AST). AST corresponds to UTC - 4h.

Here, similar to [190], the top of the boundary layer is estimated from (i) by

$$\mathrm{TBL}_i = \min_z \left(|\theta_v(z) - \langle \theta_v \rangle_{ML}| > \delta_{\theta_v} \right) \ , \tag{4.7}$$

$$\delta_{\theta_v} = \max \left(\max \left(|\theta_v(z) - \langle \theta_v \rangle_{ML}| \right), 0.2\,\mathrm{K} \right) \ , \tag{4.8}$$

where $\langle \theta_v \rangle_{ML}$ is the average of θ_v in the mixed layer (ML) over the altitude range 100 m to 400 m and 0.1 K is the absolute accuracy of the temperature. If TBL$_i$ < 500 m, TBL$_i$ is set to 500 m because the cloud base was higher than 500 m above MSL according to remote sensing data[1]. Exemplarily, the estimate TBL$_i$ is shown in Fig. 4.7 derived from three radio soundings [88] during M161 Flight 10. During EUREC^{4}A , radio sondes were launched from RV Meteor and RV Maria S. Merian to profile the atmosphere for measuring , e.g., air temperature, air pressure and relative humidity [88]. In contrast to radio soundings (compare Sec. 2.4.3), the MPCK measurements did not always reach altitudes above the inversion which is why θ_v is retrieved via Eq. (1.53) from radio soundings [88]. The accuracy of TBL$_i$ is $\sim$ 100 m, which is comparable to the variability of the cloud base as observed by radar reflectivity [191]. As radio soundings correspond to one-dimensional samples along the flight trajectory, individual datasets are potentially prone to large statistical scatter.

Moreover, motivated by simplified θ_v-profiles above the inversion [40, 189], the top of the boundary layer can also be estimated from (ii) by linearly extrapolating the θ_v-profile and looking for the interception with $\langle\theta_v\rangle_{ML}$. Then, the top of the boundary layer can be estimated by

---

[1] Personal communication with Heike Kalesse-Los

$$\mathrm{TBL}_{ii} = \min_z \left(\left| \frac{\partial\theta_v}{\partial z} z + \theta_v^0 - \langle\theta_v\rangle_{ML} \right| < 0.1\,\mathrm{K} \right) , \tag{4.9}$$

where the slope $\frac{\partial\theta_v}{\partial z}$ and the interception θ_v^0 are obtained by a linear fit above the inversion, i.e. z ranging from 900 m to 1900 m. Both approaches assume a simplified profile of θ_v, where TBL_i tends to underestimate TBL. Moreover, the accuracy TBL_{ii} depends a lot on the sharpness of the inversion and the depth of the entrainment zone above the mixed layer. Therefore, TBL results from averaging TBL_i and TBL_{ii} in this work.

4.2.2 Stability of the Boundary Layer

One important goal of this thesis is to characterize atmospheric turbulence in the marine boundary layer over the full diurnal cycle. Turbulence is suppressed in stably stratified boundary layers, though [40]. Therefore, it is further interesting to investigate the stability of the boundary layer over the diurnal cycle, too, and to assess the strength of turbulence. The Richardson number Ri is a dimensionless parameter that captures the strength of static stability compared to shear-generated turbulence [41].

According to Eq. (1.55), the Richardson number depends on the vertical gradient of horizontal wind components $u_{1,2}$. Assuming that the MPCK instruments are aligned with the stream-wise direction and that $u_{2,3} \ll u_1$, it is sufficient to consider the u_1 component in the platform frame of reference. Hence, the gradient Richardson number can be approximated for an averaging window τ by

$$\mathrm{Ri} = \frac{g}{\langle\theta_v\rangle_\tau} \frac{\frac{\partial\theta_v}{\partial z}}{\left(\frac{\partial u_1}{\partial z}\right)^2} , \tag{4.10}$$

where $g = 9.81\,\mathrm{m/s^2}$ is the gravitation constant and $\langle\theta_v\rangle_\tau$ is the time average of θ_v for an averaging window τ. The vertical gradients of θ_v and u_1 are obtained by a linear fit against the altitude z. Furthermore, the platform speed with respect to ground is subtracted from the wind speed measurement in the platform frame of reference under the assumption that the streamwise wind direction and the platform velocity are always parallel. However, as the research vessels were not moving with constant speed with respect to ground, a correction is necessary to capture the denominator of Eq. (4.10) correctly. Moreover, the time-record of u_1 is low-pass filtered at 1/30Hz to suppress high-frequency platform motion. The author will usually estimate Ri by Eq. (4.10) unless otherwise stated. In the following, Richardson numbers with absolute values larger than ~ 10 are unphysical (Sec. 1.2.5) and hence discarded.

During EUREC^{4}A , the MPCK instruments recorded the virtual potential temperature θ_v and wind velocity along the flight trajectory, hence at varying altitudes.

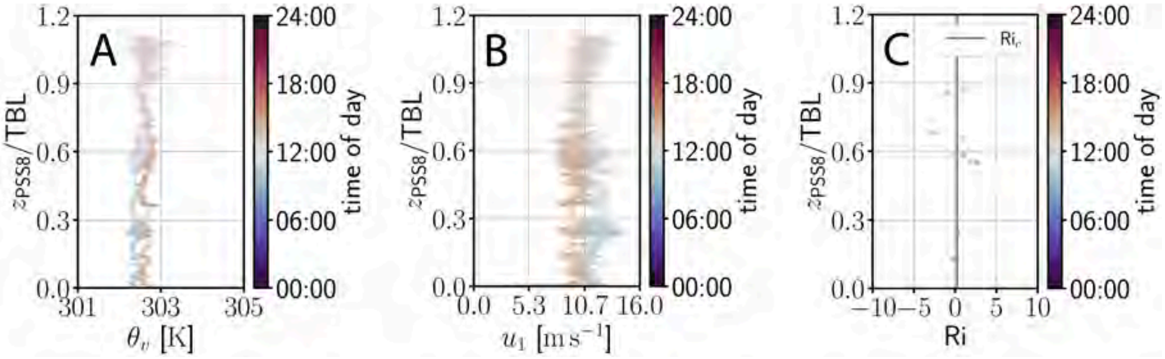

Figure 4.8 Profiles of the virtual potential temperature θ_v (A), the longitudinal wind speed u_1 (B) recorded by the mini-MPCK and the Richardson number Ri (C), Eq. (4.10), for Flight 10 on RV Meteor (M161). The averaging window is $\tau = 1800\,\mathrm{s}$. $Ri_c = 0.25$ is the critical Richardson number below which the flow is fully turbulent. The barometric altitude z_{PSS8} is obtained from the PSS8 and re-scaled by the top of the boundary layer (TBL). The color code corresponds to the local time of the day (AST). The entire time series of M161 Flight 10 is shown in Fig. 2.7A.

Exemplary profiles acquired during M161 Flight 10 are shown in Fig. 4.8 where the color code corresponds to the time of the day in AST (UTC - 4) and where the altitude time series of M161 Flight 10 is shown in Fig. 2.7A. The color code also reveals if the mini-MPCK ascended or descended. For example in Fig. 4.8A, the color of θ_v changes from grayish ($\sim$ 12:00 AST) at $z_{\mathrm{PSS8}}/\mathrm{TBL} \gtrsim 1$ to light orange ($\sim$ 15:00 AST) at $z_{\mathrm{PSS8}}/\mathrm{TBL} = 0$ which corresponds to a descent. The top of the boundary layer (TBL) is obtained from radio soundings as described in Sec. 4.2.1, which were conducted simultaneously with research flights of the MPCK+ or the mini-MPCK. Considering the mini-MPCK, θ_v is calculated from time-records of the static pressure by the PSS8 and the corrected air temperature and specific humidity by the sonic (Sec. 2.B). As shown in Figs. 4.8A and B, the daytime variability of both θ_v and u_1, also recorded by the sonic, is small during noon as the earlier ascent and later descent nearly overlap. Vertically, θ_v is roughly constant during the ascent whereas θ_v decreases with altitude for $0.6 < z_{\mathrm{PSS8}}/\mathrm{TBL} < 1$ during the descent resulting in a locally negative vertical gradient of θ_v (Fig. 4.8A). Still during the descent, θ_v increases with altitude for $0.4 < z_{\mathrm{PSS8}}/\mathrm{TBL} < 0.6$ hinting at a stable layer. Regarding horizontal wind speed, u_1 changes with altitude by $2\,\mathrm{m/s}$ to $4\,\mathrm{m/s}$ (Figs. 4.8B), hence vertical shear is observed. From Eq. (4.10) and vertical profiles of u_1 and θ_v, the Richardson number can be estimated. As expected, Ri is negative $0.6 < z_{\mathrm{PSS8}}/\mathrm{TBL} < 1$ and positive for $0.4 < z_{\mathrm{PSS8}}/\mathrm{TBL} < 0.6$ (Fig. 4.8C). Despite that the estimation of Ri is crude, Ri<1 suggests the presence of turbulence. It should be noted that the Ri is estimated from one-dimensional measurements which is why individual points might be influenced by thermals.

To study atmospheric stability more systematically and over the full diurnal cycle, Ri is calculated for all flights (except for Flight 1, 4 and 6 due to an unphysical velocity time record) on M161 aboard RV Meteor as shown in Fig. 4.9A and B. The

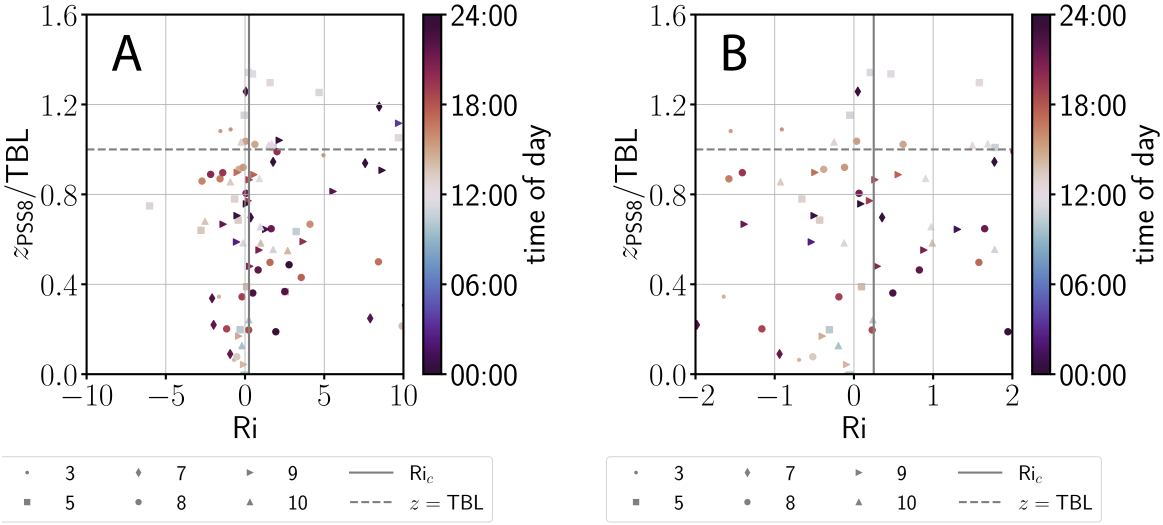

Figure 4.9 Richardson number Ri as function of barometric altitude z_{PSS8} for flights 3, 5, 7, 8, 9 and 10 on M161 aboard RV Meteor. $Ri_c = 0.25$ is the critical Richardson number (solid gray line) below which the flow is fully turbulent. The barometric altitude z_{PSS8} is obtained from the PSS8 and re-scaled by the top of the boundary layer (TBL) as shown by the gray dashed line.

lowest portion of the boundary layer ($z_{\mathrm{PSS8}}/\mathrm{TBL} < 0.4$) is mostly unstable as $Ri < 0$ except for some outliers. In the middle ($0.4 < z_{\mathrm{PSS8}}/\mathrm{TBL} < 0.6$), it is still turbulent as $0 < Ri < 1$ (Fig. 4.9B). Statically, the altitude range $0.4 < z_{\mathrm{PSS8}}/\mathrm{TBL} < 0.6$ is neutral to stable as $\partial\theta_v/\partial z \gtrsim 0$. Within the limit of accuracy, this is in agreement with $\partial\theta_v/\partial z = 0$ in a well-mixed layer. In the case of $0.7 < z_{\mathrm{PSS8}}/\mathrm{TBL} < 1$, the boundary layer tends to be unstable again especially at times around 18:00 (sunset) as shown in Fig. 4.9A for M161 Flight 8 and 9. The static instability results from $\partial\theta_v/\partial z < 0$ (compare Figs. 4.33B and C). Given that $\mathrm{Ri} > 0$ at lower altitudes ($0.4 < z_{\mathrm{PSS8}}/\mathrm{TBL} < 0.6$) but at similar times after sunset, it is unlikely that the whole boundary layer is statically unstable. Possibly, this might be due to entrainment of warmer air parcels from the free atmosphere. However, this suggestion cannot be checked without analyzing vertical fluxes, e.g. of heat and moisture. Above the top of the boundary layer, the flow is stably stratified in most cases as expected. Flight 3 (small dots) shows some local instability above TBL. This is also obvious from the profile of θ_v with locally $\partial\theta_v/\partial z = 0$ (Fig. 4.33A). In total, the boundary layer is considered to be turbulent over the diurnal cycle and the full range as often $Ri \lesssim 1$ (Fig. 4.9B) despite that $\mathrm{Ri} \sim 10$ in some cases.

4.2.3 Turbulence Characteristics in the Trade-wind Boundary Layer

According to the previous Sec. 4.2.2, it is expected that the boundary layer is turbulent across the entire diurnal cycle and across its vertical extent. As mentioned in Sec. 3.1, the mean energy dissipation rate is a central turbulence characteristic. The purpose of this section is to estimate the most relevant features of a turbulent flow in terms of the mean energy dissipation rate obtained from one-dimensional time-records of the longitudinal velocity.

The general procedure for estimating the mean energy dissipation rate is illustrated in Fig. 3.1 where, similar to Sec. 4.1.3, ϵ_{I2} and an averaging window of $\tau = 1800\,\mathrm{s}$ is used to estimate the mean energy dissipation rate. This procedure is based on the assumption of locally isotropic turbulence and the applicability of Taylor's hypothesis, which is generally fulfilled as the turbulence is 7% on average with a standard deviation of 4%. The isotropy of the turbulent flow is assessed in Sec. 4.3. Additionally, it should be noted that all flights with unphysical velocity signals are ignored, i.e. M161 Flight 1, 4 and 6. Furthermore, due to platform motion, the longitudinal velocity time-records are high-pass filtered with $f_c = 0.5\,\mathrm{Hz}$ where the effect is assessed in Sec. 4.B. In this section, error bars are given by Eq. (3.45) for $\langle\epsilon_{I2}\rangle_\tau$ and by the re-scaled standard deviation of z during the averaging window τ. As the flight altitude of the helikite is not exactly constant, the error (uncertainty) of the re-scaled barometric altitude $z_{\mathrm{PSS8}}/\mathrm{TBL}$ is captured by the standard deviation. Here, $\langle\epsilon_{I2}\rangle_\tau$-values with an altitude uncertainty larger than 50 m are discarded. We concentrate on measurements of the mini-MPCK during M161 (RV Meteor) because the profiling of the boundary layer is dedicated to studying its turbulent structure. On MSM89, cloud measurements were prioritized which is why these flights are analyzed in more detail later (Sec. 4.4). A summary of the bulk turbulence features during MSM89 is delivered in Fig. 4.35 and Table 4.8. The averaged relative random errors e in Tables 4.1 and 4.8 are given by Eqs. (3.45), (1.61), (3.42), (4.3) and (4.14) for $\langle\epsilon_{I2}\rangle_\tau$, U, $\sigma_{u_1'}$, R_λ, and L_{11}, respectively. The averaged relative random errors e for η_K and λ_f are given by:

$$e(\eta_K) = \left|\frac{\partial\eta_K}{\partial\langle\epsilon_{I2}\rangle_\tau}\delta_{I2}(R)\langle\epsilon_{I2}\rangle_\tau\right| = \frac{\eta_K}{4\langle\epsilon_{I2}\rangle_\tau}\delta_{I2}(R)\langle\epsilon_{I2}\rangle_\tau = \frac{\eta_K}{4}\delta_{I2}(R)\,, \tag{4.11}$$

$$e(\lambda_f) = \left|\frac{\partial\lambda_f}{\partial\langle\epsilon_{I2}\rangle_\tau}\delta_{I2}(R)\langle\epsilon_{I2}\rangle_\tau\right| = \frac{\lambda_f}{2\langle\epsilon_{I2}\rangle_\tau}\delta_{I2}(R)\langle\epsilon_{I2}\rangle_\tau = \frac{\lambda_f}{2}\delta_{I2}(R)\,, \tag{4.12}$$

$$\tag{4.13}$$

invoking Gaussian error propagation with respect to the relative random error in $\langle\epsilon_{I2}\rangle_\tau$.

To assess the daily variability of the mean energy dissipation rate, an overview of the mean energy dissipation rate estimates $\langle\epsilon_{I2}\rangle_\tau$ is shown as a function of re-scaled barometric altitude $z_{\mathrm{PSS8}}/\mathrm{TBL}$ in Fig. 4.10 under the assumption of a stationary flow for that period (time scale of days to weeks). The order of magnitude of $\langle\epsilon_{I2}\rangle_\tau$ ranges from $1 \times 10^{-5}\,\mathrm{W/kg}$ to $1 \times 10^{-3}\,\mathrm{W/kg}$, which possibly contradicts the assumption of global stationarity on a weekly scale. To test this hypothesis, mean scaling exponents ζ_2 of $D^\tau_{LL}(r)$ within the fit range are classified by their deviation from the K62-prediction where a deviation of 0.1 is accepted. Thus, ζ_2 is in agreement with K62 if $|\zeta_2 - 2/3 + 1/36| < 0.1$ (group 1) corresponding to the highly opaque $\langle\epsilon_{I2}\rangle_\tau$ -values in Fig. 4.10. Otherwise, $|\zeta_2 - 2/3 + 1/36| \geq 0.1$ and ζ_2 is not in agreement with

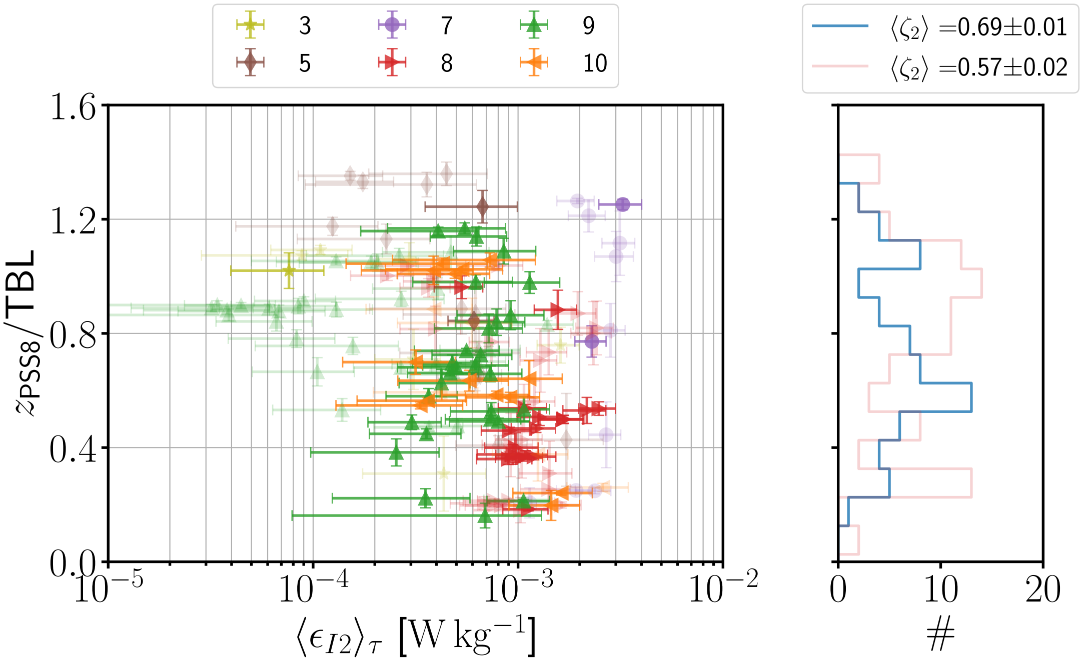

Figure 4.10 Overview of mean energy dissipation rate estimates $\langle\epsilon_{I2}\rangle_\tau$ obtained from one-dimensional time-records of the longitudinal velocity during EUREC^{4}A with the mini-MPCK on M161 (RV Meteor) as a function of the re-scaled barometric altitude z_{PSS8}. TBL is the abbreviation for top of the boundary layer and the averaging window $\tau = 30\,\mathrm{min}$. Error bars are given by Eq. (3.45) for $\langle\epsilon_{I2}\rangle_\tau$ and by the re-scaled standard deviation of z_{PSS8} during the averaging window τ. Highly opaque $\langle\epsilon_{I2}\rangle_\tau$ -values are obtained from longitudinal second-order structure functions $D^\tau_{LL}(r)$ with a mean scaling exponent ζ_2, which satisfies $|\zeta_2 - 2/3 + 1/36| < 0.1$ (in agreement with K62) in the fit range. In contrast, weakly opaque $\langle\epsilon_{I2}\rangle_\tau$-values stem from $D^\tau_{LL}(r)$ with $|\zeta_2 - 2/3 + 1/36| \geq 0.1$. Furthermore, $\langle\epsilon_{I2}\rangle_\tau$ is highly opaque only if the standard deviation of the altitude is lower than 50 m. The right panel shows the number counts of $\langle\epsilon_{I2}\rangle_\tau$ -values agreeing with K62 in blue and the number counts of $\langle\epsilon_{I2}\rangle_\tau$-values disagreeing with K62 in (weakly opaque) red. The ensemble average of each ζ_2-group is denoted by $\langle\zeta_2\rangle$.

K62 (group 2) where $\langle \epsilon_{I2} \rangle_\tau$-value are weakly opaque in Fig. 4.10. Thus, if the inertial range is well pronounced and if the mean scaling exponent is in accordance with K62, ϵ_{I2} is considered to be a valid method to estimate the mean energy dissipation rate. Focusing on time periods where ζ_2 is in agreement with K62, $\langle \epsilon_{I2} \rangle_\tau$ ranges only from 4×10^{-4} W/kg to 2×10^{-3} W/kg except for only a few significant outliers. Hence, the mean energy dissipation rate is fairly constant on a daily to weekly time scale which is investigated in more detail below. Furthermore, the right panel of Fig. 4.10 shows the number counts of averaging windows τ during which the ensemble-averaged mean scaling exponent $\langle \zeta_2 \rangle = 0.69 \pm 0.01$ is agreeing with K62 in blue. The agreement between K62 and $\langle \zeta_2 \rangle$ is remarkable. Likewise, the number counts of averaging windows τ during which the ensemble-averaged mean scaling exponent $\langle \zeta_2 \rangle = 0.57 \pm 0.02$ disagrees with K62 is shown in (weakly opaque) red. Hence, the ensemble-averaged mean scaling exponent is systematically lower than predicted by K62. In the following, only those time periods are considered during which $|\zeta_2 - 2/3 + 1/36| < 0.1$ and the altitude uncertainty below 50 m.

Even though the mean energy dissipation rate did not reveal a trend on a daily to weekly time scale, the atmosphere changes on hourly time scales. As an example, the air temperature changes at time scales below one hour (Sec. 4.1.1). Likewise, a signature of that time scale is found in the cloud fraction time-evolution over the diurnal cycle increasing after sunset [192, 193]. The dynamics of shallow cumuli are coupled to heat and moisture fluxes, hence to convection [68]. In general, atmospheric turbulence is driven by wind shear from the surface and buoyancy driven convection. As convection, hence the energy injection, varies on hourly time scales, it is expected that the mean energy dissipation rate varies over the diurnal cycle, too. Overall, the profile of $\langle \epsilon_{I2} \rangle_\tau$ does not reveal a significant trend with the local time of the day in Fig. 4.11A. Nevertheless, considering Flight 9 on M161, $\langle \epsilon_{I2} \rangle_\tau$ slightly increases from ≈ February 05 2020 19:00 AST to February 06 2022 00:00 AST but also with altitude. Hence, it is not unambiguously that the increase is purely due to the effects of the diurnal cycle. However, the vertical profile of θ_v has a negative slope for that time frame (February 05 2020 19:00 AST to February 06 2022 00:00 AST) during M161 Flight 9, as shown in Fig. 4.33C, suggesting an unstable stratification which is critical for convection. Therefore the increase in $\langle \epsilon_{I2} \rangle_\tau$ is most likely related to the diurnal cycle. Similarly, the variance $\langle u_1'^2 \rangle_\tau$ shows an increase with time for the same time frame (Fig. 4.11B). Both L_{11}, Eq. (1.29), and R_λ, Eq. (1.38), are derived from $\langle \epsilon_{I2} \rangle_\tau$ and $\langle u_1'^2 \rangle_\tau$ and, therefore, reveal a similar behavior (Figs. 4.11C and D). The error bars for $\langle u_1'^2 \rangle_\tau$ and R_λ are given by Eqs. (3.42) and (4.3), respectively. The error of L_{11} due to $\delta_{I2}(R)$, the random error of $\langle \epsilon_{I2} \rangle_\tau$, reads:

$$e(L_{11}) = \left| \frac{\partial L_{11}}{\partial \langle \epsilon_{I2} \rangle_\tau} \delta_{I2}(R) \langle \epsilon_{I2} \rangle_\tau \right| = \frac{L_{11}}{\langle \epsilon_{I2} \rangle_\tau} \delta_{I2}(R) \langle \epsilon_{I2} \rangle_\tau = L_{11} \delta_{I2}(R) \,. \tag{4.14}$$

Considering the error bars being derived from the random error $\delta_{I2}(R)$, $\langle \epsilon_{I2} \rangle_\tau$, $\langle u_1'^2 \rangle_\tau$, L_{11} and R_λ only, if at all, weakly depend on altitude. A general trend with altitude is not significant although, for L_{11} and R_λ, it seems that two branches

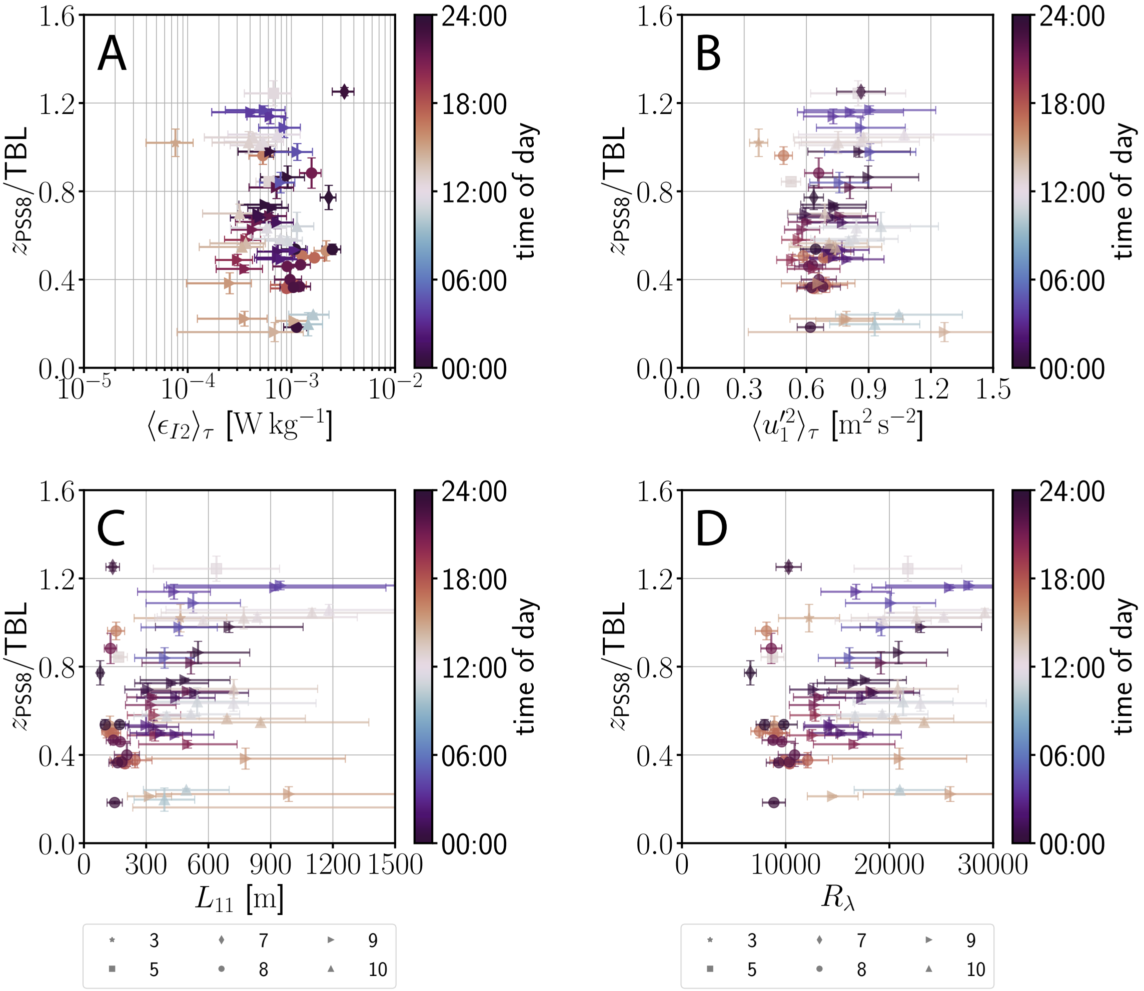

Figure 4.11 Influence of the diurnal cycle on bulk turbulence. The color code corresponds to the local time of the day (UTC - 4h). TBL is the abbreviation for top of the boundary layer and the averaging window $\tau = 1800\,\mathrm{s}$. The error bars for z are given by the standard deviation of z during the averaging window τ. A: The mean energy dissipation rate estimates $\langle\epsilon_{I2}\rangle_\tau$ are obtained from one-dimensional time-records of the longitudinal velocity during EUREC^{4}A with the mini-MPCK on M161 (RV Meteor). The error bars are given by Eq. (3.45) for $\langle\epsilon_{I2}\rangle_\tau$. B: The variance of velocity fluctuations $\langle u_1'^2\rangle_\tau$ is based on unfiltered u_1'. Error bars are only considered for the barometric altitude. C: The longitudinal integral length scale L_{11} is estimated by Eq. (1.29). Error bars are obtained via Eq. (4.14). D: The Taylor micro-scale Reynolds number R$_\lambda$ is obtained by Eq. (1.38). Error bars are obtained via Eq. (4.3).

emerge (Figs. 4.11C and D) where the left branch is constant with altitude in the limit of accuracy. The left branch is mostly populated by M161 Flight 8 where the boundary layer was stably stratified (Fig. 4.33B) but with vertical shear of the wind speed (Fig. 4.33D). This is confirmed by the Richardson numbers which are mostly positive for $z_{\mathrm{PSS8}}/\mathrm{TBL} < 1$ (Fig. 4.9). The right branch consists predominantly of M161 Flight 9 and is possibly related to larger convective structures with slightly negative Richardson numbers for $z_{\mathrm{PSS8}}/\mathrm{TBL} < 1$ (Fig. 4.9)). A more profound analysis, including vertical fluxes in the Earth frame of reference, is required for supporting this hypothesis. Ignoring the effect of the diurnal cycle, it is possible to summarize bulk turbulence properties in terms of PDFs in Fig. 4.13 and in terms of statistical quantities in Table 4.1. The above considerations explain the presence of multiple peaks in the PDFs of L_{11} and R_λ (Fig. 4.13).

The PDFs of the systematic and random errors $\delta_{I2}^{\mathrm{sys}}(R)$ and $\delta_{I2}(R)$, respectively, is shown in Fig. 4.12. As both errors are inferred in retrospect from, i.a., the estimated L_{11}, the scatter is expected. Therefore, both $\delta_{I2}^{\mathrm{sys}}(R)$ and $\delta_{I2}(R)$ should be interpreted as rough estimates on the accuracy of $\langle\epsilon_{I2}\rangle_\tau$ where the systematic error is only half as large as the random error on average. The random error $\delta_{I2}(R)$ is the largest compared to $\delta_{I2}^{\mathrm{sys}}(R)$, the systematic error $\delta_{I2}(\theta)$ due to misalignment and due to finite turbulence intensity $\beta_{I2}(I)$ (compare Fig. 4.34).

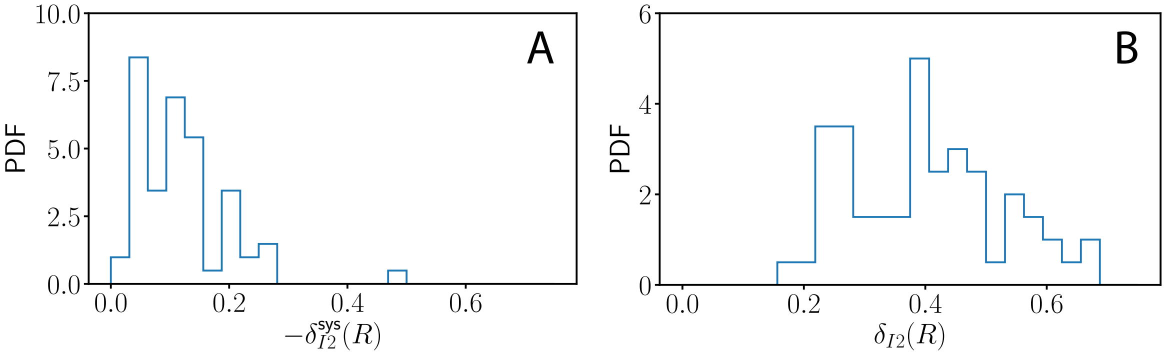

Figure 4.12 PDFs of the systematic error $\delta_{I2}^{\mathrm{sys}}(R)$ (A) and the random error $\delta_{I2}(R)$ (B) of the energy dissipation rate estimate $\langle\epsilon_{I2}\rangle_\tau$ during EUREC^{4}A on M161 aboard RV Meteor. $R = U\tau$ is the spatial averaging window with $\tau = 1800\,\mathrm{s}$. Both errors are estimated from L_{11} and $\langle u_1'^2\rangle_R$ based on the same R and, hence, have to be regarded rather as statistical estimates.

The turbulence features are calculated based on the mean energy dissipation rate, which is obtained from a filtered time-record of the longitudinal velocity with a cutoff frequency $f_c = 0.5\,\mathrm{Hz}$. As shown in Sec. 4.B, both the energy dissipation rate $\langle\epsilon_{I2}\rangle_\tau$ as well as the variance $\langle u_1'^2\rangle_\tau$ decrease with f_c (e.g. Fig. 4.32B). Hence, L_{11} is underestimated if $\langle u_1'^2\rangle_\tau$ is evaluated from the filtered time-record of the longitudinal velocity. In contrast, L_{11} obtained from the unfiltered $\langle u_1'^2\rangle_\tau$ should be rather interpreted as an estimation of the upper bound on L_{11}. Similarly, it is expected that R_λ, Eq. (1.38), is overestimated. Assuming that $\sigma_{u_1'} = \sqrt{\langle u_1'^2\rangle_\tau}$ from unfiltered $u_1(t)$ might be $\sim 30\%$

too high and the estimate of the mean energy dissipation rate $\sim 30\%$ too low results in an overestimation of L_{11} by a factor of 3 and of R_λ by 2. As an example, a biased estimate $L_{11} \sim 500\,\mathrm{m}$ would amount to $L_{11}^c \approx 160\,\mathrm{m}$ and $\mathrm{R}_\lambda \sim 20000$ would amount to $\mathrm{R}_\lambda^c \approx 10000$ where c denotes "correct".

	unit	mean	median	std	e [%]
U	m/s	12.29	12.22	1.02	1.68
$\sigma_{u_1'}$	m/s	0.74	0.73	0.14	-
$\langle \epsilon_{I2} \rangle_\tau$	mW/kg	0.88	0.73	0.57	40.84
η_K	mm	1.50	1.48	0.25	10.21
λ_f	m	0.59	0.60	0.17	20.42
L_{11}	m	462	411	333	40.84
R_λ		16057	16336	6178	20.42

Table 4.1 Bulk turbulence features obtained from mini-MPCK time-records of the longitudinal velocity component $u_1(t)$ on M161 (RV Meteor) during EUREC^{4}A . $U = \langle u_1(t) \rangle_\tau$ is the mean velocity obtained from $u_1(t)$ for the averaging window τ, $\sigma_{u_1'}$ the RMS fluctuation of $u_1(t)$, $\langle \epsilon_{I2} \rangle_\tau$ the estimate of the mean energy dissipation rate according to Eq. (3.15) with $n = 2$, η_K the Kolmogorov length scale, λ_f the longitudinal Taylor micro-scale, L_{11} the integral length scale and R_λ the Taylor micro-scale Reynolds number. For each turbulence feature, the mean, median, standard deviation (std) and relative random error e in % are given. e is obtained by Eqs. (3.45), (1.61), (4.3), (4.14), (4.11) and (4.12) for $\langle \epsilon_{I2} \rangle_\tau$, U, R_λ, L_{11}, η_K and λ_f, respectively. The averaging window is $\tau = 1800\,\mathrm{s}$. $u_1(t)$ is not corrected for platform motion.

4.3 Reynolds stress Anisotropy

The estimation of the mean energy dissipation rate according to Kolmogorov's second similarity hypothesis is based on the assumption of statistically (and locally) isotropic turbulence. At least in the fit range ($r \in [2\,\mathrm{m}, 6\,\mathrm{m}]$), the mean scaling exponents of $D_{LL}(r)$ are close to Kolmogorov's prediction of $\zeta_2 \approx 0.69$ in the inertial range for isotropic turbulence. Although this agreement between observed and predicted scaling exponents hints at isotropic turbulence in the inertial range, Kolmogorov's prediction of $\zeta_2 \approx 0.69$ relies on the assumption of local isotropic turbulence conditioned on the local energy dissipation rate in the first place [49]. Hence, an independent measure of anisotropy is needed for confirming the inertial range isotropy, which would justify the estimation of the mean energy dissipation rate as described above.

4.3.1 Graphical Representation of Reynolds stresses

For sufficiently high R_λ turbulent flows, Kolmogorov's phenomenology from 1941 hypothesizes a range of scales $r \ll L$ where the turbulence is statistically isotropic where L scales with the energy injection scale. This hypothesis implies that statistics

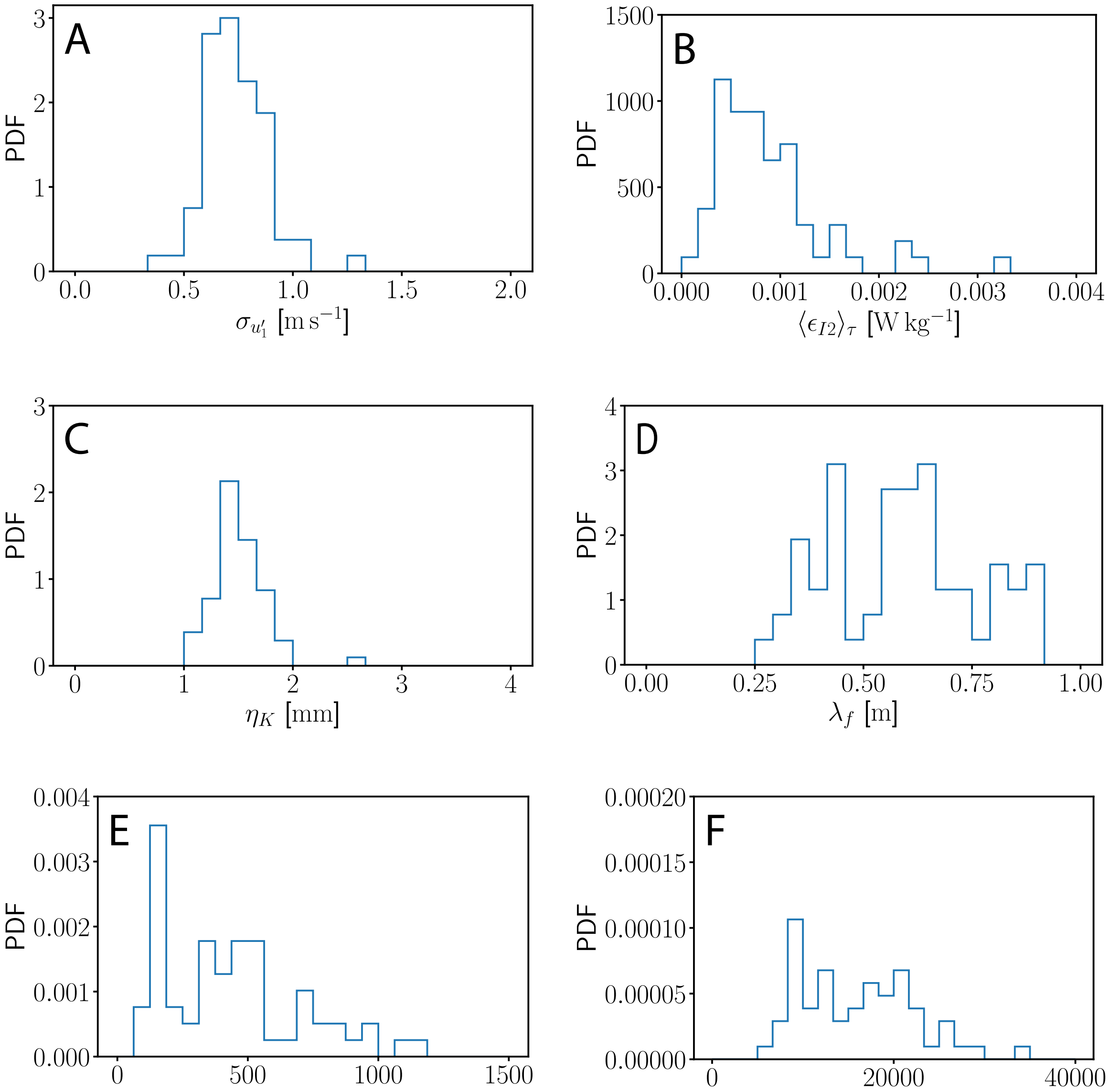

Figure 4.13 Turbulence features during EUREC^{4}A on M161 aboard RV Meteor. PDFs are shown for the longitudinal RMS velocity fluctuation $\sigma_{u'_1}$ based on unfiltered u'_1 (A), the mean energy dissipation rate estimate $\langle\epsilon_{I2}\rangle_\tau$ (B), the Kolmogorov length scale η_K (C), the longitudinal Taylor micro-scale λ_f (D), the longitudinal integral length scale L_{11} (E) and the Taylor micro-scale Reynolds number R$_\lambda$ (F).

State of turbulence (shape of Reynolds stress ellipsoid)	Invariants	eigenvalues of b_{ij}
Isotropic (sphere)	$\eta = \xi = 0$	$\lambda_1 = \lambda_2 = \lambda_3 = 0$
2C axisymmetric (disk)	$\eta = 1/6$, $\xi = -1/6$	$\lambda_1 = \lambda_2 = 1/6$
1C (line)	$\eta = 1/3$, $\xi = 1/3$	$\lambda_1 = 2/3$, $\lambda_2 = \lambda_3 = -1/3$
axisymmetric (prolate spheroid)	$\eta = \xi$	$-1/3 \leq \lambda_1 = \lambda_2 \leq 0$
axisymmetric (oblate spheroid)	$\eta = -\xi$	$0 \leq \lambda_1 = \lambda_2 \leq 1/6$
2C (ellipse)	$\eta = \left(1/27 + 2\xi^3\right)^{1/2}$	$\lambda_1 + \lambda_2 = 1/3$

Table 4.2 Special states of the Reynolds stress tensor described by the invariants ξ and η as well as by eigenvalues λ_i of b_{ij}."2C" is the abbreviation for two-component and "1C" for one-component. Table is based from [5].

of scales $r \ll L$ are independent of large scales and universal even if the large scales L are anisotropic. As an example, a first model with a linear return to isotropy for decaying homogeneous anisotropic turbulence is proposed in terms of the normalized anisotropy tensor b_{ij}, Eq. (1.11), [194]. However, the return-to-isotropy has also been experimentally studied in three types of homogeneous anisotropic grid turbulence revealing a non-linear return-to-isotropy [195]. As six components of b_{ij} are required to characterize the anisotropy, a more convenient approach is the so-called "Lumley triangle" characterizing the anisotropy graphically [5, 196]. This approach is based on the fact that $b_{ii} = 0$ which is why the anisotropy can be described by two independent invariants of b_{ij} only [5]. The invariants are obtained from b_{ij} in the principle axis given by

$$\tilde{b}_{ij} = \begin{pmatrix} \lambda_1 & 0 & 0 \\ 0 & \lambda_2 & 0 \\ 0 & 0 & -(\lambda_1 + \lambda_2) \end{pmatrix} ,$$

where $\lambda_{1,2} \geq 0$ are the eigenvalues of b_{ij}. Then, the two independent invariants η and ξ can be obtained from the principle invariants $\mathbf{II}_b$ and $\mathbf{III}_b$[5]:

$$6\eta^2 = -2\mathbf{II}_b = b_{ii}^2 = b_{ij}b_{ji} = 2(\lambda_1^2 + \lambda_1\lambda_2 + \lambda_2^2)\,, \tag{4.15}$$

$$6\xi^3 = 3\mathbf{III}_b = b_{ii}^3 = b_{ij}b_{jk}b_{ki} = -3\lambda_1\lambda_2(\lambda_1 + \lambda_2)\,. \tag{4.16}$$

Hence, every Reynolds stress tensor corresponds to a point in the ξ - η plane. Special states of turbulence enclose a region in the ξ - η plane, which is known as the "Lumley triangle". These states are listed in Table 4.2. Only the points within the Lumley triangle (as shown in Fig. 4.14) belong to *realizable* Reynolds stresses. Otherwise, if the eigenvalues are complex or negative, the Reynolds stresses are *non-realizable*, and the (ξ, eta)-pair lies outside the Lumley triangle. The interested reader is referred to [5] for more details.

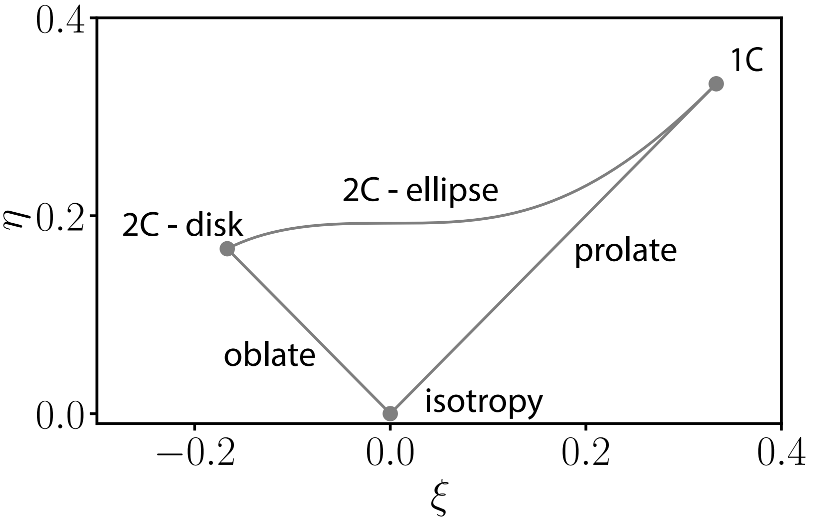

Figure 4.14 Graphical representation of special turbulence states in terms of the Lumley triangle in the $\eta - \xi$ plane. Figure based on [195].

4.3.2 Anisotropy in high-R$_\lambda$ flows

Here, the graphical representation of Reynolds stresses by the Lumley triangle is used to confirm the inertial range isotropy of the turbulent flow. Thereby, the assumptions of Kolmogorov's phenomenology are justified independently, which, in retrospect, allows for the estimation of the mean energy dissipation rate as described above.

The Reynolds stresses are obtained from time-records of the three-dimensional wind vector in the platform frame of reference with the help of the sonic of the mini-MPCK. Here, the invariants are calculated from Eqs. (4.15) and (4.16) based on:

$$\xi = \sqrt[3]{-\frac{1}{2}\lambda_1\lambda_2(\lambda_1+\lambda_2)}\,, \tag{4.17}$$

$$\eta = \sqrt{\frac{1}{3}(\lambda_1^2+\lambda_1\lambda_2+\lambda_2^2)}\,. \tag{4.18}$$

In the following, "invariants" refers to ξ, Eq. (4.17), and η, Eq. (4.18).

The invariants are shown in Fig. 4.15 for each mini-MPCK flight during the EUREC^{4}A field campaign in the marine boundary layer as well as for snapshots taken in DNS of homogeneous isotropic turbulence (gray stars). In Fig. 4.15A, the turbulence in the platform frame of reference appears to be statistically anisotropic for both tether-mounted (circles) and spare-mounted (upright triangles) flights without high-pass filtering the data. However, as the mini-MPCK is prone to platform motions, filtering is needed (Sec. 2.4.2, cutoff frequency of $f_c = 0.5\,\mathrm{Hz}$). The invariants obtained from high-pass filtered wind vector time-records ($f_c = 0.5\,\mathrm{Hz}$) are shown in Fig. 4.15B. First point to note is that the flow appears to be more isotropic on scales $l \lesssim U/f_c = 20\,\mathrm{m}$ (with $U \sim 10\,\mathrm{m/s}$ and $f_c = 0.5\,\mathrm{Hz}$) than globally for each flight. Moreover, invariants

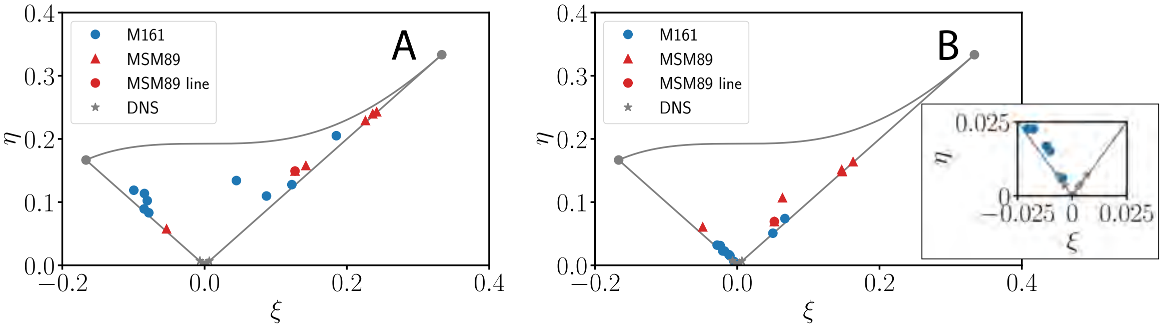

Figure 4.15 Lumley triangle in terms of the invariants ξ, Eq. (4.17), and η, Eq. (4.18), obtained from EUREC^{4}A field measurements for each mini-MPCK flight and from DNS of homogeneous isotropic turbulence. The velocity wind vector is measured *in situ* as a function of time by the mini-MPCK with the help of the sonic during EUREC^{4}A field campaign. Invariants obtained from measurements on M161 aboard RV Meteor are shown in blue, on MSM89 aboard RV Maria S. Merian in red and from single snapshots of DNS 3.1 – 3.5 of homogeneous isotropic turbulence, Table 3.2, by gray stars. Circles denote flights with a tether-mounted mini-MPCK with a separation of at least 50 m to the helikite ("M161" and "MSM89 line"). Upright triangles represent flights where the mini-MPCK is mounted to the main spare on MSM89 ("MSM89"). Gray circles and gray lines represent special states of turbulence according to Table 4.2. A: Time-records of the wind vector are not filtered. B: Time-records of the wind vector are filtered at $f_c = 0.5\,\mathrm{Hz}$. The inset shows a zoom close to the origin.

obtained from flights in the tether-mounted configuration appear to be more isotropic than flights in the spare-mounted configuration. Some of the invariants obtained from filtered time-records of the three-dimensional wind vector during M161 are even close to DNS as demonstrated in the inset of Fig. 4.15B. Hence, in the platform frame of reference, the turbulence appears to be globally isotropic on scales $l \lesssim 20\,\mathrm{m}$. This is in agreement with the ensemble-averaged scaling exponent, e.g. $\langle\zeta_2\rangle = 0.74 \pm 0.06$ for M161 Flight 10, overlapping with the K62-prediction. Already, it can be concluded that the estimation of the mean energy dissipation rate according to Kolmogorov's phenomenology is justified for scales $l \lesssim 20\,\mathrm{m}$.

To evaluate how well the isotropy assumption of Kolmogorov's phenomenology is fulfilled for shorter averaging windows, the Lumley triangle has been also visualized for finite averaging windows of $\tau = 30\,\mathrm{min}$. In contrast to bulk anisotropy in Fig. 4.15, invariants obtained from mini-MPCK wind vector time-records for averaging windows of 30 min are compared to each virtual probe in DNS 3.3 as shown in Fig. 4.16A. On the one hand, reducing the averaging window enhances the statistical scatter as argued, e.g., in Sec. 4.1.2. On the other hand, sampling a three-dimensional turbulent flow along a one-dimensional trajectory might affect the invariants, too. Presumably, the combination of finite averaging windows and one-dimensional sampling causes the scatter of the invariants in the regime $0 \leq \eta \leq 0.15$ and $-0.15 \leq \xi \leq 0.2$ for both DNS 3.3 and mini-MPCK. Hence, there is no significant difference between invariants obtained from virtual probes sampling DNS of homogeneous isotropic turbulence along

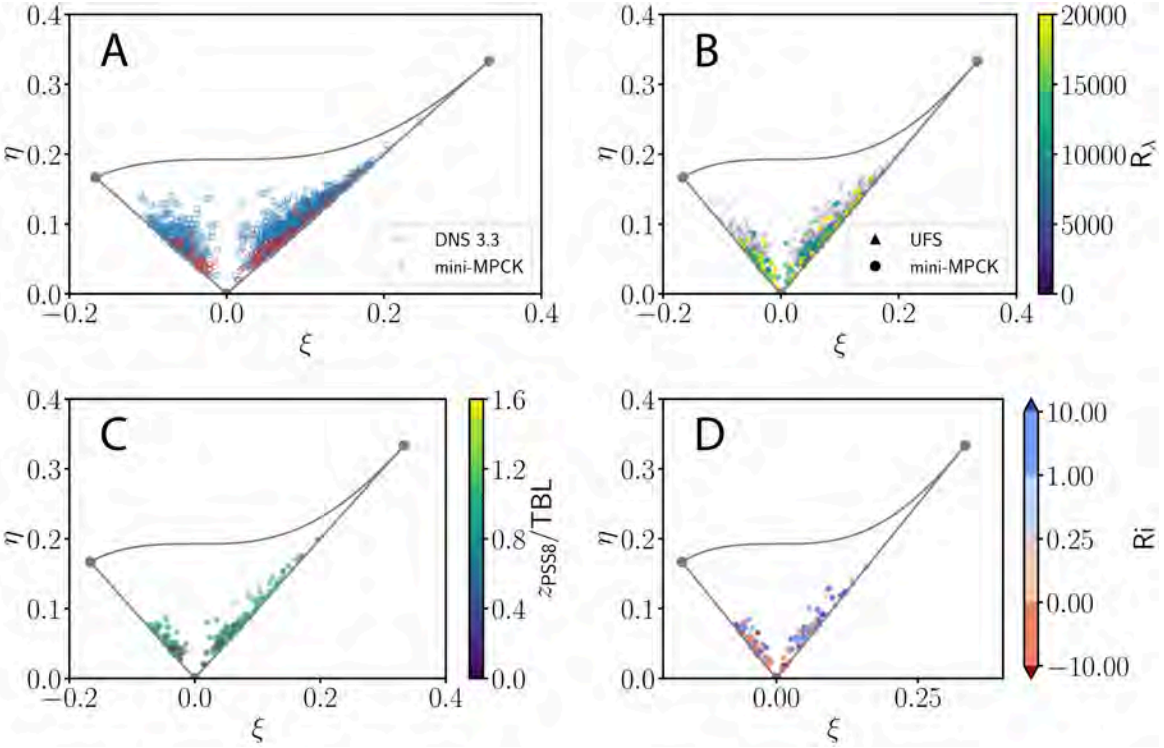

Figure 4.16 Lumley triangle for individual averaging windows $\tau = 30\,\text{min}$ obtained from tether-mounted mini-MPCK time-records of the wind vector. A: Invariants obtained from measurements with the mini-MPCK for averaging windows τ are compared to each virtual probe of DNS 3.3 (Table 3.2). B: Invariants from airborne measurements with the mini-MPCK are compared to ground-based measurements in mountainous terrain (personal communication with Steffen Risius) where each point is colored by R_λ. C: Invariants obtained from the mini-MPCK wind vector measurements are shown as a function of barometric altitude z_{PSS8} above MSL re-scaled by the top of the boundary layer (TBL). D: In order to characterize the effect of static stability on the invariants, they are colored as a function of the Richardson number Ri.

a one-dimensional trajectory and mini-MPCK measurements.

Furthermore, invariants from airborne measurements in the marine boundary layer with the mini-MPCK are compared to ground-based measurements in mountainous terrain on Mt. Zugspitze [54, 197] as shown in Fig. 4.16B. The invariants obtained from ground-based measurements (upright triangles) tend to be more anisotropic than the invariants obtained from filtered airborne measurements in the marine boundary layer. On the one hand, this might be an effect of R_λ which is higher by at least a factor of 2 for measurements in the marine boundary layer compared to ground-based measurements in mountainous terrain. On the other hand, UFS measurements are conducted within the surface layer in the presence of shear [54]. Another possible cause for this deviation is the filtering in the case of mini-MPCK measurements.

In contrast to UFS measurements in the surface layer, the mini-MPCK sampled the boundary layer in the well-mixed region and in the cloud layer as shown in Fig. 4.16C.

The invariants obtained by the mini-MPCK tend to isotropy in the well-mixed region of the marine boundary layer, i.e. where the virtual potential temperature is constant with height [40] as fulfilled for $0.1 \leq z_{\mathrm{PSS8}}/\mathrm{TBL} \leq 0.8$, while the flow appears to be comparable to ground-based measurements for $0.8 \leq z_{\mathrm{PSS8}}/\mathrm{TBL}$. Taking into account the inaccuracy of $\sim 100\,\mathrm{m}$ in determining the depth of the boundary layer (TBL), the regime $0.8 \lesssim z_{\mathrm{PSS8}}/\mathrm{TBL}$ is close to an inversion which imposes a large-scale anisotropy on the flow. The influence of decreasing line tension on the invariants remains undetermined because of the absence of a tensiometer on RV Meteor.

At last, anisotropy is investigated with respect to static stability being captured by the Richardson number Ri, Eq. (4.10). Here, the invariants are determined for the same averaging windows with $\tau = 30\,\mathrm{min}$ as Ri. As the flow is considered to be statically stable for $\mathrm{Ri} > 1$, it is expected that the flow tends to be more anisotropic than for $\mathrm{Ri} < 1$ where the flow is expected to be fully turbulent, which can be confirmed as shown in Fig. 4.16D. To summarize, the isotropy assumption of Kolmogorov's phenomenology can be considered as being fulfilled for scales $l \sim 20\,\mathrm{m}$ and in the platform frame of reference as there is no significant difference to velocity measurements of virtual probes in DNS of homogeneous isotropic turbulence. Thus, the estimation of the mean energy dissipation rate based on averaging windows with $\tau = 30\,\mathrm{min}$ is justified.

4.4 *In-situ* Measurements of Trade-wind Cumuli

Up to now, the atmosphere has been treated like a single-phase flow consisting of moist air, i.e. a combination of dry air and water vapor. In practice, atmospheric flows rather consist of multiple phases. As the air temperature never fell below 0 K over the period of the Cloudkite measurements, one can assume that the atmosphere is a particle-laden flow with moist air and liquid water droplets. From here on, liquid water droplets are called "cloud droplets" (or cloud particles in general). This section aims at providing an overview of cloud measurements, characterizing cloud turbulence, describing cloud droplet statistics and giving a first inside in a precipitating cloud. Cloud droplet measurements are based on FCDP and CDP-2 measurements, i.e. time-series of cloud droplet size histograms at 2 Hz and particle-by-particle (PbP) time series with a temporal resolution of 1 µs. PIV and holography measurements by the MPCK+ are not considered in the scope of this section. The protocol for checking the validity of measurements is explained in Sec. 4.A and is applied to obtain the subsequent results.

During the EUREC^{4}A field campaign, both the MPCK+ (FCDP) and mini-MPCK (CDP2) sampled cloud-free air as well as marine trade-wind cumuli at different evolution stages and at various mesoscale cloud patterns, e.g. so-called flowers as discussed in Sec. 4.4.3 [198]. The cloud droplet probes (abbreviated with CDP in the following), i.e. FCDP and CDP2, count and size cloud droplets. Clouds, and even different regions within a cloud, can be characterized in the first approach by the cloud droplet number concentration n, which is obtained according to Eq (1.66).

Overall, the cloud droplet number concentration n obtained from cloud particle

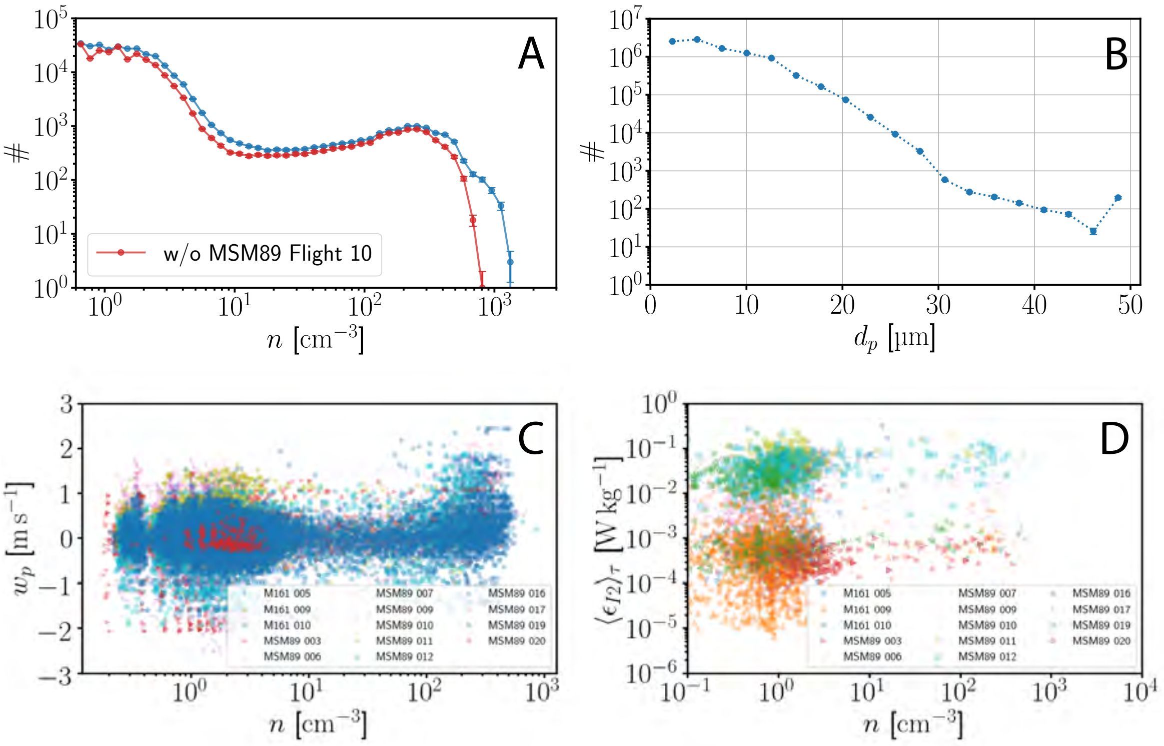

Figure 4.17 Overview of droplet measurements during the EUREC^{4}A field campaign with the MPCK+ and the two mini-MPCKs aboard RV Maria S. Merian and RV Meteor. A: The histogram of droplet number concentration n is obtained from the FCDP and CDP-2 measurements. The number concentration n is determined via Eq. (1.66) from all cloud droplets measured by the CDP-2 and FCDP with $d_p \leq 50\,\mu\mathrm{m}$ where the CDP detects cloud droplets with a diameter down to $2\,\mu\mathrm{m}$ and the FCDP down to $1.25\,\mu\mathrm{m}$. The relative wind speed is acquired by a pitot tube (PSS8). The blue curve shows the histogram of n obtained from all considered flights and the red curve shows the histogram of all flights except for MSM 89 Flight 10 ("w/o MSM89 Flight 10"). B: The histogram of droplet diameters d_p is obtained from FCDP and CDP-2 measurements. In A and B, # is the number count of occurrences per bin and the errorbars are given by the square root of the number counts within each bin under the assumption of Poisson distributed counting statistics. C: The platform vertical velocity w_p is acquired by the SBG and plotted against n. D: The energy dissipation rate estimate $\langle\epsilon_{I2}\rangle_\tau$ is obtained from PSS8 relative wind speed measurements for an averaging window of $\tau = 60\,\mathrm{s}$ and plotted against n.

size histogram records at 2 Hz spans 3 orders of magnitude (from $\mathcal{O}(n) \sim 1/\text{cm}^3$ to $\sim \mathcal{O}(n) \sim 1 \times 10^3/\text{cm}^3$) as shown in Fig. 4.17A. At low number concentrations $n \sim 1/\text{cm}^3$, the histogram of n reveals a plateau but the number counts per n-bin (denoted by #) decay by two orders of magnitude for n ranging from $2/\text{cm}^3$ to $10/\text{cm}^3$. At higher $n > 10/\text{cm}^3$, # grows from 400 to 1200 where the local maximum is at $n = 250/\text{cm}^3$. This local peak is identified with the most likely number concentration in trade-wind cumuli that were sampled by the MPCK+ and mini-MPCK. Based on the decay of the n-histogram for $n > 1/\text{cm}^3$ and the local maximum of n at $n = 250/\text{cm}^3$, a reasonable range of cloud droplet number concentrations for cloud-free air is chosen as $n \leq 10/\text{cm}^3$, which corresponds to 95% of the total CDP measurement time. In the following, $n > 10/\text{cm}^3$ is considered to be cloudy air (5% of the total CDP measurement time, up to 7.3% depending on altitude [38]). Aircraft-borne measurements during EUREC^{4}A determine the cloud fraction at the cloud base to on average 3.5 % [10]. The error bars in Fig. 4.17A (and other histograms in the following) are given by the standard deviation of a Poisson distribution $\sqrt{\#}$ under the assumption that occurrences per n-bin are independent of the last occurrence.

As mentioned in Sec. 4.A, time periods of unphysical velocity measurements or cloud droplet measurements close to sea surface have been discarded. Furthermore, the maximum number concentration was lower than $1000/\text{cm}^3$ for all flights but MSM89 Flight 10 (maximum $n \approx 1300/\text{cm}^3$). Therefore, histograms of the number concentration are shown for all flights and all flights except for MSM89 Flight 10 in Fig. 4.17A. Both the altitude as well as wind speed measurement were physical for MSM89 Flight 10. The CDP recorded exceptionally high number counts, which were about one order of magnitude higher in comparison to all other flights. Further research is needed to understand the anomaly.

One limitation of the CDP2 is that it records only particle inter-arrival times (and their diameters) for the first 256 particles per sampling interval of $\approx 0.5\,\text{s}$ [25]. However, the modest n combined with the low relative wind speed encountered with the helikites results in a mean fraction of missed PbP-data of 0.25 (median 0.15, minimum 0.003 and maximal 0.79) which is much less than > 0.94 in case of aircraft measurements with a relative wind speed of $\approx 90\,\text{m/s}$ [25]. For completeness, it should be added that the CDP2 includes all (valid) particles in the histogram data at 2 Hz.

The CDPs not only counted but also sized cloud particles in terms of the cloud particle diameter d_p. Cloud droplets with a diameter $d_p \leq 7\,\mu\text{m}$ are most frequent among the measured cloud droplet (55%) whereas 39% attributed to the size range 7 µm to 15 µm (Fig. 4.17B). Only 5.9% of the measured cloud droplets have a diameter within 15 µm to 23 µm and only 0.1% of the measured cloud droplets are larger than 23 µm in diameter. It should be noted that the FCDP accumulates also larger particles in the last droplet diameter bin so that the last bin in Fig. 4.17B appears to be enhanced due to rain. As explained in more detail below, cloud droplets with a diameter below 7 µm are not only encountered in clouds but also often in cloud-free air. Larger droplets with diameters up to 20 µm are predominantly present exclusively in cloudy air, i.e. at high n. This is expected because cloud droplets grow in a super-saturated environment where the time evolution of the super-saturation field depends on the vertical velocity [107, and references therein]. Likewise, as most cloud condensation nuclei (CCN) are activated in a supersaturated environment [58], high number concentrations of cloud droplets, i.e. activated CCN, are related to regions of vertical updrafts (Fig. 4.17C). Here, the vertical updrafts are captured by the vertical platform velocity w_p that corresponds to the low-pass filtered vertical flow velocity on scales similar to the size of the helikite ($\mathcal{O}(10\,\mathrm{m})$). In cloud-free air, there is, if at all, only a weak correlation between n and w_p (Fig. 4.17C). In dilute cloudy air, i.e. n ranging from $10/\mathrm{cm}^3$ to $100/\mathrm{cm}^3$, significantly negative values of w_p are observed where negative vertical velocity is associated to downdrafts. These downdrafts are potentially related to a subsiding shell of cold air at the cloud edge (medium n) and are caused by evaporative cooling at the cloud top. In consequence, the buoyancy within the subsiding shell should be negative. Furthermore, the energy dissipation rate ($\langle \epsilon_{I2} \rangle_\tau$ with $\tau = 60\,\mathrm{s}$) tends to be higher for higher n for all flights. The turbulence within trade-wind cumuli is considered in more detail in Sec. 4.4.1.

Radiative properties of clouds, warm rain initiation and the stage of cloud evolution are related to the droplet size distribution, which is a function of time and space [e.g. 23]. The particle size distribution is, i.a., affected by turbulent processes such as mixing and collision-coalescence [e.g. 4, 23, 80, and references therein]. Despite that the histogram of the number concentration n gives a valuable overview, it lacks information on the dependence of the number concentration n on both cloud droplet size d_p and altitude. Taking into account cloud droplet sizes, a cumulative cloud droplet number density $\tilde{n}$ conditioned on a cloud droplet diameter range can be defined as:

$$\tilde{n} = \sum_{j=k}^{l} n(d_p^j)\,, \tag{4.19}$$

where the droplet size range is considered for diameter bins between d_p^k and d_p^l. Hence, if $\tilde{n}/n = 0$ ($n \neq 0/\mathrm{cm}^3$), no particles are within the considered droplet size range. In contrast, all particles are within the droplet size range if $\tilde{n}/n = 1$. Figure 4.18 shows a distribution of the relative cumulative number concentration $\tilde{n}/n$ against the number concentration n where both quantities have been binned. Counting the number of occurrences (#) per bin (n - $\tilde{n}/n$ -

bin) provides an overview of which droplet size range contibutes most to the total cloud droplet population. Furthermore, as the cloud base is not constant in time and space, altitude measurements have to be re-scaled by the cloud base in order to compare all flights with CDP records. Here, the top of the boundary layer (TBL) is used to estimate the cloud base where the procedure is explained in Sec. 4.2.1. As the cloud base varies up to 100 m in altitude, which is similar to the accuracy of determining TBL, generous altitude regimes have to be chosen. As TBL ranges from 600 m to 900 m above mean sea level (MSL), altitude ranges are (i) $0.8 < z_{\mathrm{PSS8}}/\mathrm{TBL} < 1.2$ ("low"), (ii) $1.2 < z_{\mathrm{PSS8}}/\mathrm{TBL} < 1.6$ ("medium") and (iii) $z_{\mathrm{PSS8}}/\mathrm{TBL} > 1.6$ ("high") where z_{PSS8} is the barometric altitude obtained from the static pressure of the PSS8 pitot tube. In

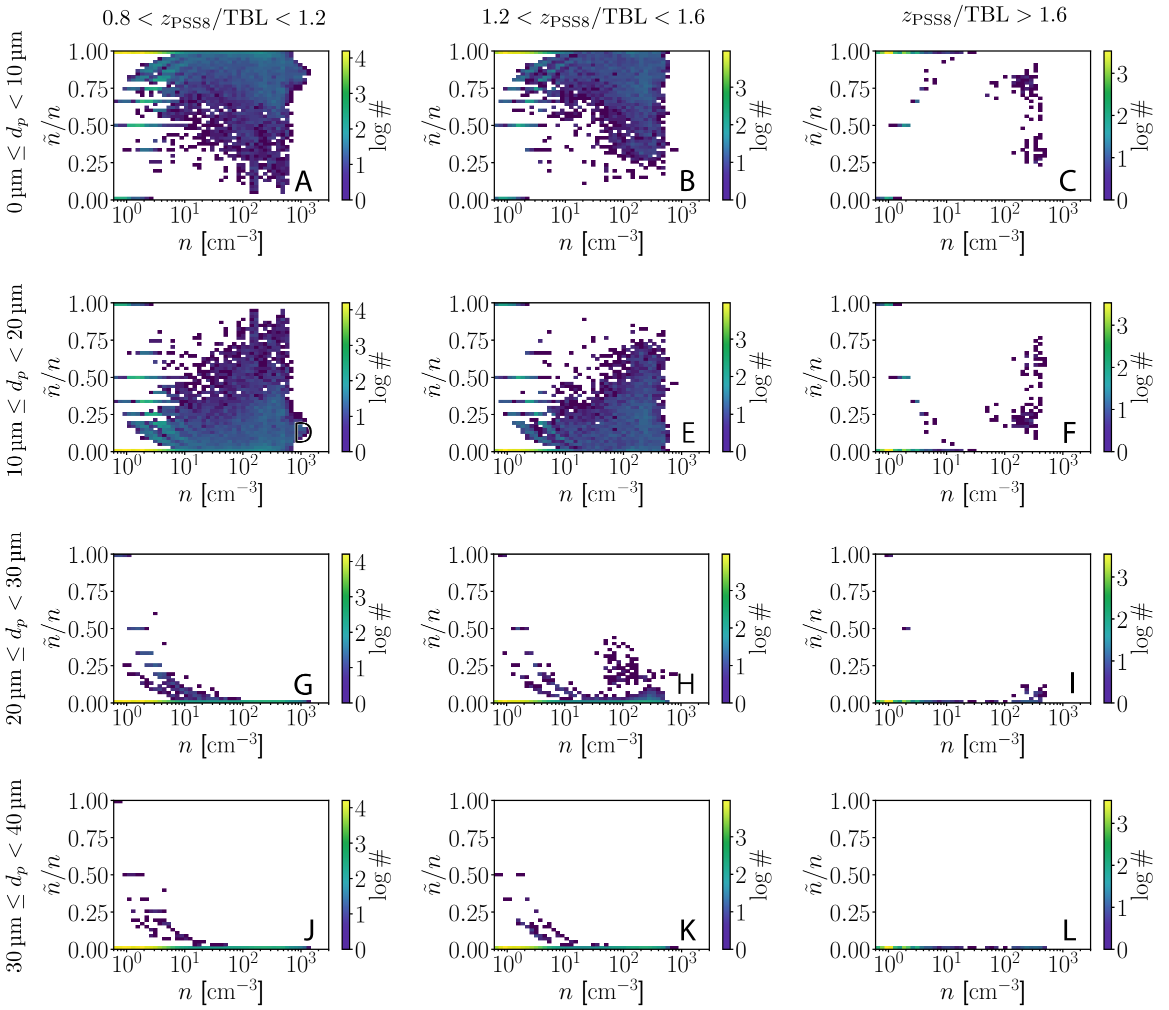

Figure 4.18 Cumulative cloud droplet number density $\tilde{n}$ within a range of droplet sizes as a function of total number density n. $\tilde{n}/n$ is the fractional contribution of cloud droplets within a size range to the total population n. The colorbar is given by the logarithm of number of occurrences per bin (#). Each panel corresponds to an altitude range above MSL (z_{PSS8}), which is re-scale by TBL, and a range of droplet sizes d_p.

doing so, the percentage of measurements in clouds ($n > 10/\mathrm{cm}^3$) is 3.6% at low, 3.5% at medium and 0.2% at high altitudes. Considering dense clouds, i.e. $n > 100/\mathrm{cm}^3$, the measurement time percentage is 2.1% at low, 2.3% at medium and 0.2% at high altitude.

For most sampled clouds between $0.8 < z_{\mathrm{PSS8}}/\mathrm{TBL} < 1.2$ consisted of cloud droplets with $0\,\mu\mathrm{m} < d_p < 10\,\mu\mathrm{m}$ (Fig. 4.18A) whereas only a smaller fraction of the droplet population had diameters $10\,\mu\mathrm{m} < d_p < 20\,\mu\mathrm{m}$ (Fig. 4.18D). The large percentage of cloud droplets with $0\,\mu\mathrm{m} < d_p < 10\,\mu\mathrm{m}$ ($\sim 75\%$) can be attributed to droplet activation at the cloud base and subsequent condensational growth up to $d_p \sim 10\,\mu\mathrm{m}$ in $\sim 10\,\mathrm{s}$ assuming 1% super-saturation [21].

Depending on the exact altitude of the cloud base and CDP measurement altitude, it is possible that the CDP measurement is taken 100 m above the cloud base. Assuming a vertical velocity of $\sim 1\,\mathrm{m/s}$, an air parcel needs $\sim 100\,\mathrm{s}$ for an ascent of 100 m. Further assuming a supersaturation of $\sim 1\%$, it is possible that cloud droplets grow up to $d_p \lesssim 20\,\mu\mathrm{m}$ [21, 107]. In the medium altitude range $1.2 < z_{\mathrm{PSS8}}/\mathrm{TBL} < 1.6$, most clouds exhibit similar $\tilde{n}$ although cloud droplets in the diameter range $10\,\mu\mathrm{m} < d_p < 20\,\mu\mathrm{m}$ are more frequent at $n \gtrsim 100/\mathrm{cm}^3$. As the growth rate due to condensation $\propto 1/d_p$ [21], it is expected that cloud droplets are, on average, larger at medium altitude range compared to the low altitude range at cloud base.

Considering the diameter range $20\,\mu\mathrm{m} < d_p < 30\,\mu\mathrm{m}$ (Fig. 4.18G, H, and I), firstly one branch appears at low altitude for cloud-free air ($n \leq 10/\mathrm{cm}^3$). Secondly, another branch emerges in cloudy air ($n > 10/\mathrm{cm}^3$) at medium altitude (Fig. 4.18H), which only weakly ($< 10\%$) contributes to the total droplet population in most cases. In the range $10/\mathrm{cm}^3 < n < 100/\mathrm{cm}^3$, i.e. diluted cloud air such as cloud edge or cloud top, cloud particles with $20\,\mu\mathrm{m} < d_p < 30\,\mu\mathrm{m}$ can contribute up to 75% of the population. At high altitudes, the droplet population still comprises droplets with $20\,\mu\mathrm{m} < d_p < 30\,\mu\mathrm{m}$ in a few cases. To summarize, droplets with $d_p > 20\,\mu\mathrm{m}$ are most frequently encountered near the cloud top and when the number density is moderate, say $n \lesssim 300/\mathrm{cm}^3$. High droplet number concentrations ($n > 500/\mathrm{cm}^3$) are usually associated with a narrow droplet size distribution with mean diameters below 10 µm. This observation is consistent with previous measurements [199].

According to previous consideration on condensational growth, the CDPs only rarely measured droplets with $d_p > 30\,\mu\mathrm{m}$ in low altitude region $0.8 < z_{\mathrm{PSS8}}/\mathrm{TBL} < 1.2$ (Fig. 4.18J). These large droplets are most frequently encountered at $z_{\mathrm{PSS8}}/\mathrm{TBL} > 1.2$(Fig. 4.18K and L). In cloudy, but dilute air, i.e. $10/\mathrm{cm}^3 < n < 100/\mathrm{cm}^3$, they amount to less than 10% of the population. These droplet sizes are the best candidates for inertial effects. Large droplets will be considered in more detail in the case of a rain event in Sec. 4.4.3. Notably, at high altitude range $z_{\mathrm{PSS8}}/\mathrm{TBL} > 1.6$, only a few droplets were observed (Fig. 4.18C, F, I and L). On the one hand, this altitude range is sampled the least by the mini-MPCK and MPCK+. On the other hand, shallow marine cumuli are only a couple of hundred meters deep so this range might be already above the top of shallow cumuli.

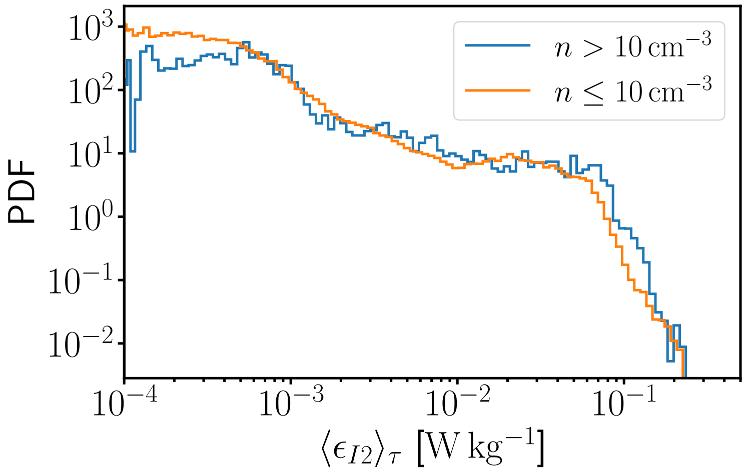

Figure 4.19 PDF of the estimated mean energy dissipation rate in cloudy air ($n > 10/\mathrm{cm}^3$) and in cloud-free air ($n \leq 10/\mathrm{cm}^3$). The mean energy dissipation rate is estimated by $\langle \epsilon_{I2} \rangle_\tau$, Eq. (3.15) with $n = 2$, for averaging windows of $\tau = 60\,\mathrm{s}$.

4.4.1 Turbulence Characteristics of Trade-wind Cumuli

In section 4.2.3, bulk turbulence features of both the sub-cloud and cloud layer have been estimated. However, turbulence in clouds is generated by buoyancy and shear, which is coupled to phase changes [e.g. 4, and references therein]. The energy dissipation is enhanced near the cloud top and the cloud edges [127, 140], which affects cloud droplet - turbulence interactions. To investigate cloud droplet - turbulence interactions within clouds in terms of the Stokes number or the non-dimensional settling velocity (both depend on ϵ), it is, therefore, necessary to condition the turbulence analysis on cloud events. As mentioned in Sec. 4.4, the condition $n \leq 10/\mathrm{cm}^3$ is well suited for cloud-free air. In the following, global statistics of turbulence characteristics are presented irrespective of the cloud evolution stage.

The (local) mean energy dissipation rate $\langle \epsilon \rangle_\tau$ is obtained from averaging windows $\tau = 60\,\mathrm{s}$ compromising between the horizontal extent of the cloud and convergence of $\langle \epsilon \rangle_\tau$. The PDF of the estimated local mean energy dissipation rates is shown in Fig. 4.19. At $\langle \epsilon_{I2} \rangle_\tau \gtrsim 1 \times 10^{-4}\,\mathrm{W/kg}$, the likelihood of measuring cloud-free air is 4 times higher than cloudy air while cloudy events are as probable as cloud-free events for $\langle \epsilon_{I2} \rangle_\tau \sim 1 \times 10^{-3}\,\mathrm{W/kg}$. This regime could be related to a dissolving stage of the cloud life cycle. To validate this hypothesis, though, further parameters such as buoyancy or vertical velocity in the Earth frame of reference would have to be invoked. Large $\langle \epsilon_{I2} \rangle_\tau \gtrsim 1 \times 10^{-1}\,\mathrm{W/kg}$ are found to be 4 times more likely in cloudy air. It should be noted that from here on, turbulence characteristics in clouds are compared to cloud-free air based on the same averaging window ($\tau = 60\,\mathrm{s}$) because $\langle \epsilon \rangle_\tau$ or $\langle u_1'^2 \rangle_\tau$ themselves are a function of τ.

Due to the short averaging window $\tau = 60\,\mathrm{s}$, the relative random error of $\langle \epsilon_{I2} \rangle_\tau$, Eq. (3.45), is on average $\approx 90\%$ resulting in a large uncertainty for other turbulence features large as well. The estimate of the random error is based on the median integral length scale, which is estimated from all research flights with the MPCK+ and mini-MPCK during EUREC^{4}A based on $\tau = 1800\,\mathrm{s}$. However, Eq. (3.45) is derived under the assumption of stationarity. As individual clouds evolve in time, estimating the relative random error of $\langle \epsilon_{I2} \rangle_\tau$ via Eq. (3.45) is not straightforward. As all scaling exponents of $D_{LL}(r)$ within the fit range are accepted, the scaling criterion is redundant. Instead, the error of $\langle \epsilon_{I2} \rangle_\tau$ is now estimated by the deviation of the maximum of Eq. (3.15) ($n = 2$) and the corresponding fit. In the case of a well-pronounced K41-scaling range, Eq. (3.15) ($n = 2$) reveals a plateau extended over the fit range. In that case, the maximum is close to the fit by definition.

The resulting estimates of various turbulence features in trade-wind cumuli and cloud-free air are summarized in Tables 4.3 and 4.4. On average and based on the condition $n > 10/\mathrm{cm}^3$, the local mean energy dissipation rate is found to be twice as large in trade-wind cumuli as outside clouds. The RMS velocity fluctuations $\sigma_{u_1'}$ are 15% higher in clouds than in ambient air. Accordingly, it is expected that characteristic length scales outside clouds are larger than in clouds, which is the case as shown by L_{11}, λ_f and η_K. The smaller length scales are plausible because the turbulence in clouds is driven locally, e.g. within the shear region formed between the updraft in the cloud core and the subsiding shell around the cloud [79]. The subsiding shell is divided in an outer and inner shell, which are 10 m in order of magnitude thick depending on the cloud evolution stage [79]. Hence, the Taylor-scale Reynolds number R_λ is on average smaller in clouds than outside clouds. However, these average considerations are bound to large standard deviations. Considering the integral scale L_{11} in clouds, the standard deviation is 109 m. Thus, a significant fraction of cloud events has an integral scale of $\mathcal{O}(L_{11}) \sim 100\,\mathrm{m}$. During EUREC^{4}A , the typical depth of shallow cumuli is $\lesssim 500\,\mathrm{m}$, which is visually determined from radar reflectivity data [191]. The energy injection scale can be obtained from the largest convective role, which is given by the cloud depth, i.e. $\lesssim 500\,\mathrm{m}$, and imposes an upper bound to the integral scale. Integral scale estimates, which are larger than 500 m are considered outliers.

At last, it should be noted that the mean wind speed is below 10 m/s. This implies a spatial resolution of CDP measurements at 2 Hz of less than 5 m. A spatial resolution of 5 m is not sufficient to resolve mixing processes where cloud microphysical quantities change on length scales ~40 cm to 60 cm [25]. To study fine-scale processes of that length scale or smaller, PbP data with a time resolution of $1 \times 10^{-6}\,\mathrm{s}$ (spatial resolution of $1 \times 10^{-5}\,\mathrm{m}$) would have to be invoked.

4.4.2 Statistics of Cloud Droplets in Trade-wind Cumuli

In the atmosphere, typical cloud droplets with diameters up to 25 µm, as observed at EUREC^{4}A , are generally two orders of magnitude smaller than the Kolmogorov length scale of the turbulent flow in which they are embedded. Besides the gravitational force, the dynamics of cloud droplets is coupled predominantly to the dissipative scales of the flow being captured by the cloud particle Stokes number St [e.g. 4]. The relative

	unit	mean	median	std
U	m/s	7.83	7.02	2.61
$\sigma_{u'_1}$	m/s	0.66	0.65	0.25
$\langle\epsilon_{I2}\rangle_\tau$	mW/kg	31.45	20.85	35.87
η_K	mm	0.94	0.70	0.54
λ_f	m	0.20	0.11	0.17
L_{11}	m	62	12	109
R_λ		4302	2714	4109

Table 4.3 Cloud turbulence features obtained from time-records of the longitudinal velocity component $u_1(t)$ on both MSM89 (RV Maria S. Merian) and M161 (RV Meteor) during EUREC^{4}A by both the MPCK+ and mini-MPCK. $U = \langle u_1(t)\rangle_{30L_{11}\tau}$ is the mean velocity obtained from $u_1(t)$ for the averaging window τ, $\sigma_{u'_1}$ the RMS fluctuation of $u_1(t)$, $\langle\epsilon_{I2}\rangle_\tau$ the estimate of the mean energy dissipation rate according to Eq. (3.15) with $n = 2$, η_K the Kolmogorov length scale, λ_f the longitudinal Taylor micro-scale, L_{11} the integral length scale and R_λ the Taylor micro-scale Reynolds number. For each turbulence feature, the mean, median and standard deviation (std) are given. The averaging window is $\tau = 60\,\mathrm{s}$. $u_1(t)$ is not corrected for platform motion. The MPCK+ and mini-MPCK are considered to be inside clouds if the cloud droplet number density $n > 10/\mathrm{cm}^3$.

	unit	mean	median	std
U	m/s	9.06	9.04	2.80
$\sigma_{u'_1}$	m/s	0.55	0.55	0.24
$\langle\epsilon_{I2}\rangle_\tau$	mW/kg	16.51	1.51	25.49
η_K	mm	1.34	1.31	0.78
λ_f	m	0.33	0.26	0.27
L_{11}	m	120	37	160
R_λ		5726	3514	4761

Table 4.4 Bulk turbulence features obtained from time-records of the longitudinal velocity component $u_1(t)$ both on MSM 89 (RV Maria S. Merian) and M161 (RV Meteor) during EUREC^{4}A in cloud-free air ($n \leq 10/\mathrm{cm}^3$). $U = \langle u_1(t)\rangle_\tau$ is the mean velocity obtained from $u_1(t)$ for the averaging window τ, $\sigma_{u'_1}$ the RMS fluctuation of $u_1(t)$, $\langle\epsilon_{I2}\rangle_\tau$ the estimate of the mean energy dissipation rate according to Eq. (3.15) with $n = 2$, η_K the Kolmogorov length scale, λ_f the longitudinal Taylor micro-scale, L_{11} the integral length scale and R_λ the Taylor micro-scale Reynolds number. For each turbulence feature, the mean, median and standard deviation (std) are given. The averaging window is $\tau = 60\,\mathrm{s}$. $u_1(t)$ is not corrected for platform motion.

impact of gravity to turbulence is captured by the non-dimensional settling velocity Sv [e.g. 23, and references therein]. Both parameters identify potential cloud droplet growth due to collision-coalescence and gravitational collection, which are important to the initiation of rain in warm clouds [4, 23]. In the following, the parameter space of cloud droplets is characterized in terms of St and Sv, which both depend on the cloud droplet diameter and the energy dissipation rate.

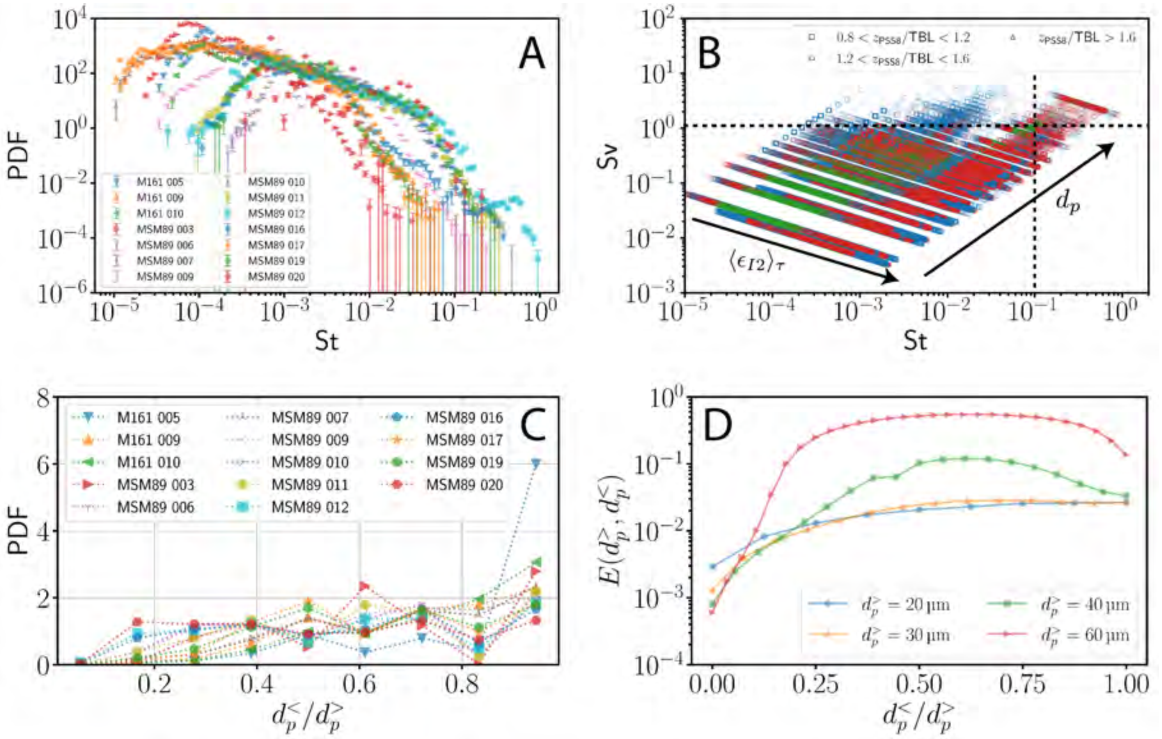

Figure 4.20 Cloud droplet statistics in trade-wind cumuli based on measurements of MPCK+ and mini-MPCK during EUREC^{4}A . A: The PDF of the Stokes number St is shown for all flights based on the PbP-records acquired by FCDP and CDP-2. B: Non-dimensional settling velocity parameter Sv as a function of cloud droplet Stokes number St for various altitude ranges. The altitude is re-scaled by TBL (z_{PSS8}/TBL). Arrows visualize the dependence on the mean energy dissipation rate estimate $\langle \epsilon_{I2} \rangle_\tau$ and the droplet diameter d_p. C: PDF of droplet size ratio of two subsequent droplets where $d_p^>$ is the larger droplet and $d_p^<$ the smaller droplet. D: Collision efficiency E according to [64]. $\tau = 60\,\mathrm{s}$ is the averaging window.

The Stokes number, Eq. (1.70), is obtained from PbP data under the assumption of a constant kinematic viscosity of air $\nu = 1.5571 \times 10^{-5}\,\mathrm{m}^2/\mathrm{s}$ and a constant density of liquid water $\rho_{\mathrm{H_2O}} = 997\,\mathrm{kg/m}^3$. The energy dissipation rate is estimated by $\langle \epsilon_{I2} \rangle_\tau$ with $\tau = 60\,\mathrm{s}$. To calculate St, PbP-time stamps are matched with the time of $\langle \epsilon_{I2} \rangle_\tau$, which is implicitly assumed to be constant over the averaging window. The resulting PDF of St obtained from PbP cloud droplet diameters during EUREC^{4}A is shown in Fig. 4.20A. The vast majority of the encountered cloud droplets have a Stokes number St < 0.01 (86% on average, maximally 99.99%) where droplet inertia can be neglected. Inertial effects such as the sling effect just become significant for St $\gtrsim 0.1$ [28, 61]. The fraction of cloud droplets with $\mathrm{St} > 0.1$ is 0.1% for all flights and 0.56% for MSM89 Flight 12 where the MPCK+ sampled precipitating clouds. This flight is investigated in more detail in Sec. 4.4.3.

Despite that, the vast majority of cloud droplets behave most likely as tracer particles ($\mathrm{St} < 0.01$). The terminal velocity of a droplet is $\propto d_p^2$ in still air [4] so that gravitational settling could dominate cloud droplet motion. Furthermore, previous considerations have shown an altitude dependence of the droplet size PDF and the presence of particles larger than 20 µm (Sec. 4.4). Therefore, it is necessary to condition the Sv-St parameter space on altitude, i.e. vertical distance to cloud base, as shown in Fig. 4.20B. Considering the regime $\mathrm{Sv} > 1$ and $\mathrm{St} < 0.1$, gravitational settling is an important process compared to droplet inertia in shallow cumulus clouds particularly in the low altitude range $0.8 < z_{\mathrm{PSS8}}/\mathrm{TBL} < 1.2$. This regime is associated with a moderate $\langle \epsilon_{I2} \rangle_\tau$ (on average 2×10^{-3} W/kg), $L_{11} \approx 177$ m and an average cloud droplet diameter of 17 µm. In the regime $\mathrm{Sv} < 1$ and $\mathrm{St} < 0.1$, neither gravitational settling nor droplet inertia plays a significant role. This regime is the “tracer” regime and is related to $\langle \epsilon_{I2} \rangle_\tau$ (on average 4×10^{-2} W/kg) and small particle diameters (average $d_p \approx 7$ µm). This regime is occupied by all altitude ranges and associated with an average integral scale of $L_{11} \approx 45$ m. A significant fraction of cloud droplets in the medium altitude regime $1.2 < z_{\mathrm{PSS8}}/\mathrm{TBL} < 1.6$ is dominated by droplet inertia, i.e. $\mathrm{Sv} < 1$ and $\mathrm{St} > 0.1$. Cloud droplets are attributed to this regime with an average diameter of 15 µm and in turbulent regions with $\langle \epsilon_{I2} \rangle_\tau$ being 8×10^{-2} W/kg on average. Furthermore, the Taylor-scale Reynolds number is $\mathrm{R}_\lambda \sim 1660$ hinting at strong local fluctuations of the energy dissipation rate due to intermittency. This is supported by an average measured integral length scale L_{11} of only 5 m.

The regime where rain is initiated presumably the most efficiently is for $\mathrm{Sv} > 1$ and $\mathrm{St} > 0.1$ with $\langle \epsilon_{I2} \rangle_\tau$ being 6×10^{-2} W/kg ($\mathrm{R}_\lambda \approx 2330$, $L_{11} \approx 10$ m and $d_p \approx 16$ µm on average). Due to finite droplet inertia ($0.1 < \mathrm{St} < 1$), cloud droplets mostly occupy regions of low vorticity in the turbulent flow while, simultaneously, they tend to settle [4, 20]. As they mostly pass through strain-dominated regions of the flow [4, 20], it is expected that the relative velocities between cloud droplets differ. It can be concluded that gravitational collection is combined with collision-coalescence. If $\mathrm{Sv} \gg 1$, the gravitational collection dominates over collision-coalescence. Most of the cloud droplets in that Sv-St range ($\mathrm{Sv} > 1$ and $\mathrm{St} > 0.1$) are sampled at $1.2 < z_{\mathrm{PSS8}}/\mathrm{TBL} < 1.6$, which might be due to the flight strategy. Further analysis is required to validate the explanation above where holography and PIV data promise valuable insight. Furthermore, the gap between $\mathrm{Sv} \gtrsim 1$ and $\mathcal{O}(\mathrm{St}) \sim 0.01$ is remarkable. It can be suggested that cumuli with a sufficient depth to reach the medium altitude regime exhibit higher energy dissipation rates. To validate or falsify this hypothesis, measurements of cloud top altitudes of the sampled clouds have to be taken into account. Turbulent characteristics should be subsequently conditioned on the cloud top altitude and should reveal bimodal behavior.

The efficiency of collision-coalescence depends on the sizes of colliding droplets [64, 200]. Despite that the CDPs cannot resolve collision events, they deliver cloud droplet sizes of two successive cloud droplets. Ignoring the turbulent flow and thermodynamics of the background, two neighboring droplets can be considered as best candidates for a collision. To estimate the efficiency of these potential collisions, the size ratio of two successive droplets is calculated. $d_p^>$ is the larger droplet and $d_p^<$ the smaller so the values lie within 0 and 1. The PDF of $d_p^</d_p^>$ is shown in Fig. 4.20C. The first point to note is that ratios of 0.1 and smaller are very rare. This can be explained by the fast condensational growth of cloud droplets up to a few microns and the fact that cloud droplets larger than 20 µm are rare (e.g. Fig. 4.17B). Despite variability among the flights, droplet size ratios between 0.2 and 0.8 are nearly equally likely. The largest range is observed for a size ratio of 0.6. In case of MSM89 Flight 12 , a local minimum at size ratio about 0.5 emerges. The size ratio increases again at 0.6 and 0.7. As an example, a size ratio of 0.6 to 0.7 corresponds to neighboring droplets of 20 µm and 30 µm in diameter. In the case of MSM89 Flight 12 where the droplet size ratio is higher for 0.6 and 0.7 compared to 0.5 and 0.9. As illustrated in Fig. 4.20D, the collision efficiency $E(d_p^>, d_p^<)$ is optimal in the range 0.5 to 0.75 [64]. The observed size ratios during the rain event in MSM89 Flight 12 (cf. Sec. 4.4.3), therefore, are in the optimal range.

Most cloud processes, among which is collision-coalescence, are related to the spatial distribution of cloud droplets [23]. The spatial distribution of cloud droplets in trade-wind cumuli is investigated as a function of the inter-particle distance Δr. The inter-particle distance is obtained from the PbP-inter-arrival time and low-pass filtered relative wind speed (cutoff frequency at 0.05 Hz due to platform motion). The counting statistics is conditioned on cloudy air, i.e. $n > 10/\text{cm}^3$. The PDFs of inter-particle distances irrespective of their size are shown in Fig. 4.21A where Δr is re-scaled by the Kolmogorov length scale for global comparison. Up to $\Delta r \sim 1\eta_K$, the error bars are large due to counting statistics. however, MSM89 Flight 3 and 12 as well as M161 Flight 5 exhibit different behavior than the other flights. In the case of Flight 5, the enhanced probability of $\Delta r < 1\eta_K$, is due to high particle counts at low altitude in the lowest size bin (and does not appear in Figs. 4.21B-D anymore). The CDP2 does not provide chemical information about the recorded particles. I suppose that it measured sea spray or large aerosols which is why this flight is not further considered. However, during MSM89 Flight 12, $\Delta r < \eta_K$ is more likely than $\Delta r > \eta_K$ which hints at spatial clustering. In this context, it would be interesting to evaluate statistics on inter-particle distances from 3D positions in order to avoid the projection issues of the one-dimensional quantity Δr. Between $1\eta_K - 10\eta_K$, the PDF is nearly constant. On these scales, the distribution of particles in space appears to be random.

However, the probability of finding two particles separated by $10\eta_K$ to $100\eta_K$ (i.e. 0.6 cm to 6 cm) is 3 to 4 orders of magnitude smaller than droplets separated by Δr between $1 - 10\ \eta_K$. In other words, shorter inter-particle distances of $\Delta r \sim 1\eta_K - 10\eta_K$ are more likely than $\Delta r \sim 10\eta_K - 100\eta_K$. This suggests that scales comparable to $10\eta_K - 100\eta_K$ are less populated, i.e. devoid of cloud droplets. These regions, that are not occupied by cloud droplets, are also known as “cloud voids” and have been experimentally measured on Mt. Zugspitze. Cloud voids on Mt. Zugspitze have an average size of 70 η_K [39], which is in agreement with the Δr-measurements in trade-wind cumuli. However, this drop can also be associated with merging different cloud regions in the PDF. The number density in the cloud core is higher than at the cloud edge, where entrainment and mixing processes occur. Thus, it is possible that the two plateaus are related to the cloud core and cloud edge. This would imply that cloud droplets, neglecting their size, are nearly randomly distributed. Conditioning the PDF of Δr to cloud core with $n > 100/\mathrm{cm}^3$, the PDF also deviates from Poisson behavior for $\Delta r > 60\eta_K$ (Fig. 4.22). Therefore, the spatial distribution of cloud droplets is only close to being random for scales $\Delta r < 60\eta_K$.

Furthermore, the inter-particle distances depend on the droplet size range. The inter-particle distances increase with increasing d_p-threshold (Fig. 4.21B-D) where the minimum distance is several η_K in the case of $d_p > 15\,\mu\mathrm{m}$. Considering cloud droplets larger than 15 µm, PDFs of MSM89 Flights 11, 12 and 18 exhibit power-law-like behavior. In [25], this is attributed to dynamic processes such as entrainment.

To summarize, the Sv-St parameter space spans four orders of magnitude for both parameters. Hence, diverse dynamics of cloud droplets embedded in a turbulent flow are expected. For a rain event, the droplet size ratio has a local maximum at ≈ 0.6 where the collision efficiency is optimal. The droplet spatial distribution suggests cloud voids but more detailed analysis, ideally paired with an analysis of 3D droplet positions, is needed.

4.4.3 Cloud Droplet Statistics in Precipitating Cloud

Up to now, cloud droplet statistics were investigated for trade-wind cumuli in general where the statistics comprised, i.a., different cloud evolution stages or mesoscale cloud patterns. In this section, one rain event (MSM89 Flight 12) is picked to characterize turbulence and cloud droplet statistics in a rainy cloud. The general cloud pattern during MSM89 Flight 12 was “flower”, which is a cloud pattern with a typical size of 20 km to 200 km lacking a unique shape and being well separated from each other [198] as shown in Fig. 4.23. The MPCK+ sampled clouds of the flower in the orange square of Fig. 4.23 where the radar reflectivity proves that the clouds are precipitating from 19:00:00 AST on (Fig. 4.24, [191]). The following analysis is a first step towards unraveling the role of turbulence in the onset of precipitation in so-called warm clouds, i.e. clouds consisting of liquid water droplets only.

The total time series of the cloud droplet number concentration MSM89 Flight 12 is shown in Fig. 4.25A where the grey period highlights the time period of the rain event being considered in the following. From here on, we consider the gray-shaded region with a time frame from 19:06:00 AST to 19:13:00 AST, if mentioned otherwise. During that time period, the CDP sampled in total 114754 droplets (113114 PbP-droplets) where 659 droplets have a diameter larger than 20 µm and 266 droplets with $d_p > 40\,\mu\mathrm{m}$. The number concentration for that time period (shaded region) is on average $108/\mathrm{cm}^3$ with a peak concentration of $319/\mathrm{cm}^3$ (median $n = 94/\mathrm{cm}^3$ and std $n = 103/\mathrm{cm}^3$).

The inset of Fig. 4.25A shows the MPCK+ barometric altitude z_{PSS8} as a function of AST time varying by 75 m. The helikite responds to a low-pass filtered vertical velocity

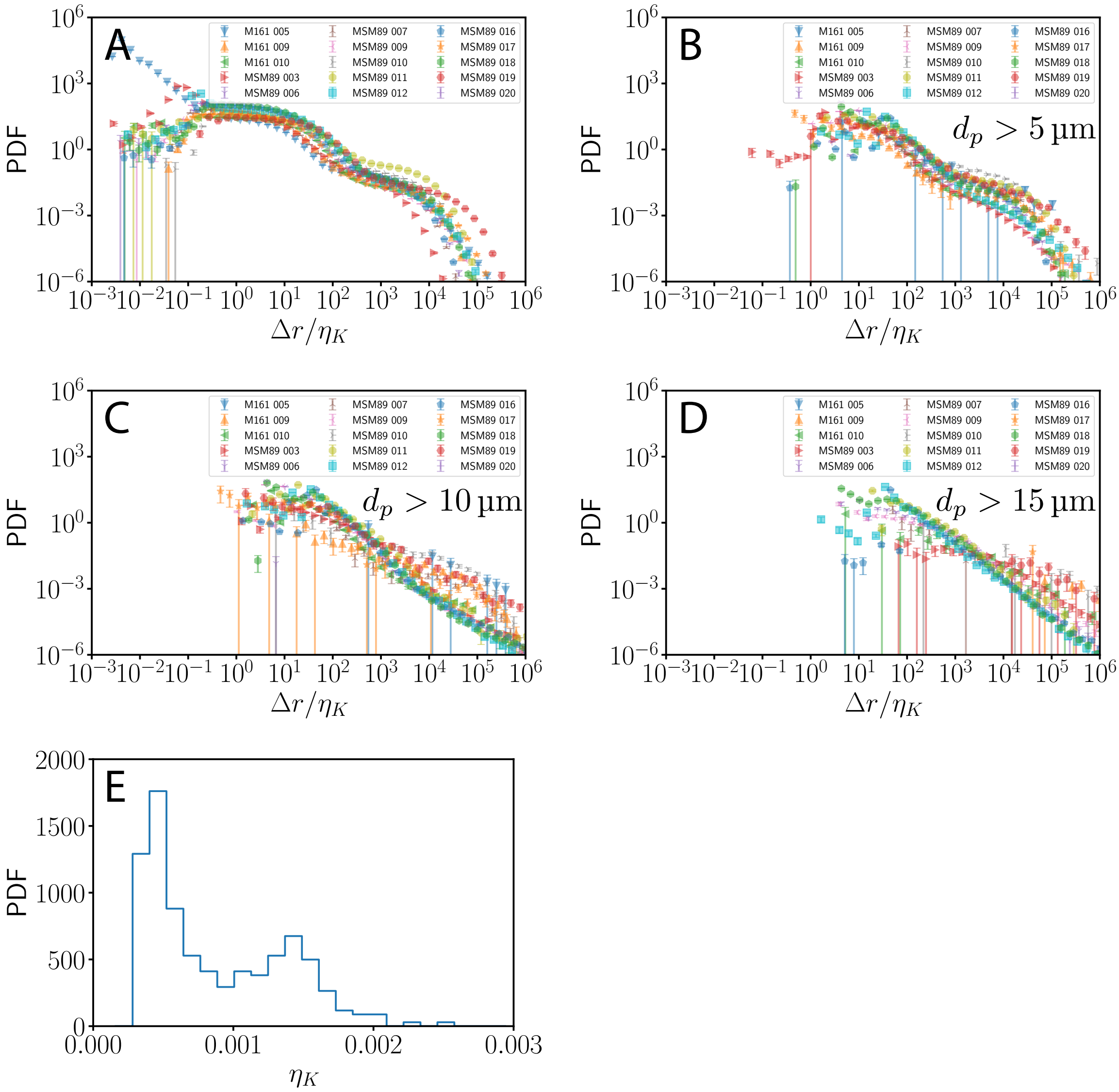

Figure 4.21 Probability density functions (PDF) of inter-particle distance (Δr) re-scaled by the Kolmogorov length scale η_K. A: The $\Delta r/\eta_K$-PDF is calculated for all cloud droplets. B-D: The $\Delta r/\eta_K$-PDFs are calculated for all cloud droplets with a diameter $d_p > 5\,\mu m$, $d_p > 10\,\mu m$ and $d_p > 15\,\mu m$. η_K is the average Kolmogorov length scale obtained from all averaging windows with a cloud droplet number concentration $n > 10/cm^3$. In each averaging window, η_K is obtained by Eq. (1.12) where the mean energy dissipation rate ϵ is estimated by $\langle \epsilon_{I2} \rangle_\tau$ and the averaging window $\tau = 60\,s$. E: Probability distribution function of η_K in cloudy air, where the η_K estimates are not averaged over each flight.

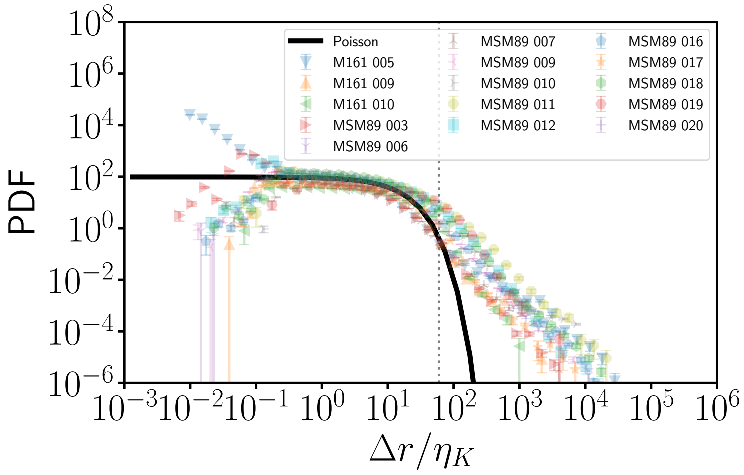

Figure 4.22 PDF of inter-particle distances Δr re-scaled by the Kolmogorov length scale η_K for cloud core regions defined by $n > 100/\text{cm}^3$. η_K is the average Kolmogorov length scale obtained from all averaging windows with a cloud droplet number concentration $n > 10/\text{cm}^3$. In each averaging window, η_K is obtained by Eq. (1.12) where the mean energy dissipation rate ϵ is estimated by $\langle \epsilon_{I2} \rangle_\tau$ and the averaging window $\tau = 60\,\text{s}$. The average PDF of all flights is fitted by a Poisson-distribution ("Poisson"). The dotted line is marks at $\Delta r = 60\eta_K$.

of the atmospheric flow filtering on spatial scales characteristic to helikite dimensions. As long as the winch is idle and the mean wind speed is constant, the helikite moves vertically if the large-scale vertical velocity of the flow changes. Consequently, the low number counts of cloud droplets at approximately 19:09:00 AST (Fig. 4.25B) is coincidental with a large-scale downdraft. Furthermore, the inset also shows the time evolution of the local mean energy dissipation rate $\langle \epsilon_{I2} \rangle_\tau$ estimates based on an averaging window of $\tau = 60\,\text{s}$. The local mean energy dissipation rate varies by nearly one order of magnitude with high values $\sim 0.1\,\text{W/kg}$ in the period between the red dashed lines. These comparably high values of $\langle \epsilon_{I2} \rangle_\tau$ coincide with significantly larger cloud droplet diameters (Fig. 4.25A and B). Note that the error bars are given by the difference between the maximum of the compensated structure function and the inertial range fit as explained in Sec. 4.4.1. The estimates of the local mean energy dissipation rate $\langle \epsilon_{I2} \rangle_\tau$ are obtained as explained in Sec. 4.A.

Besides the comparably high number counts of cloud droplets with $d_p > 20\,\mu\text{m}$ in the red bounded time frame (total number of cloud droplets is 10477, among which 349 droplets with $d_p > 20\,\mu\text{m}$ and 100 droplets with $d_p > 40\,\mu\text{m}$), $N(d_p)$ reveals a nearly permanent first peak at low $d_p \approx 3\,\mu\text{m}$ and second peak close to $d_p \approx 12\,\mu\text{m}$ (Fig. 4.25B). The first peak is most likely associated with CCN activation within the cloud but further investigation is beyond the scope of this thesis. The second peak at $d_p \approx 12\,\mu\text{m}$ is associated with cloud droplets that grew by condensation. The second peak extends up to $d_p \approx 16\,\mu\text{m}$ and the number of cloud droplets decays sharply for $d_p > 22\,\mu\text{m}$ even within the bounded region. Assuming statistically homogeneous and

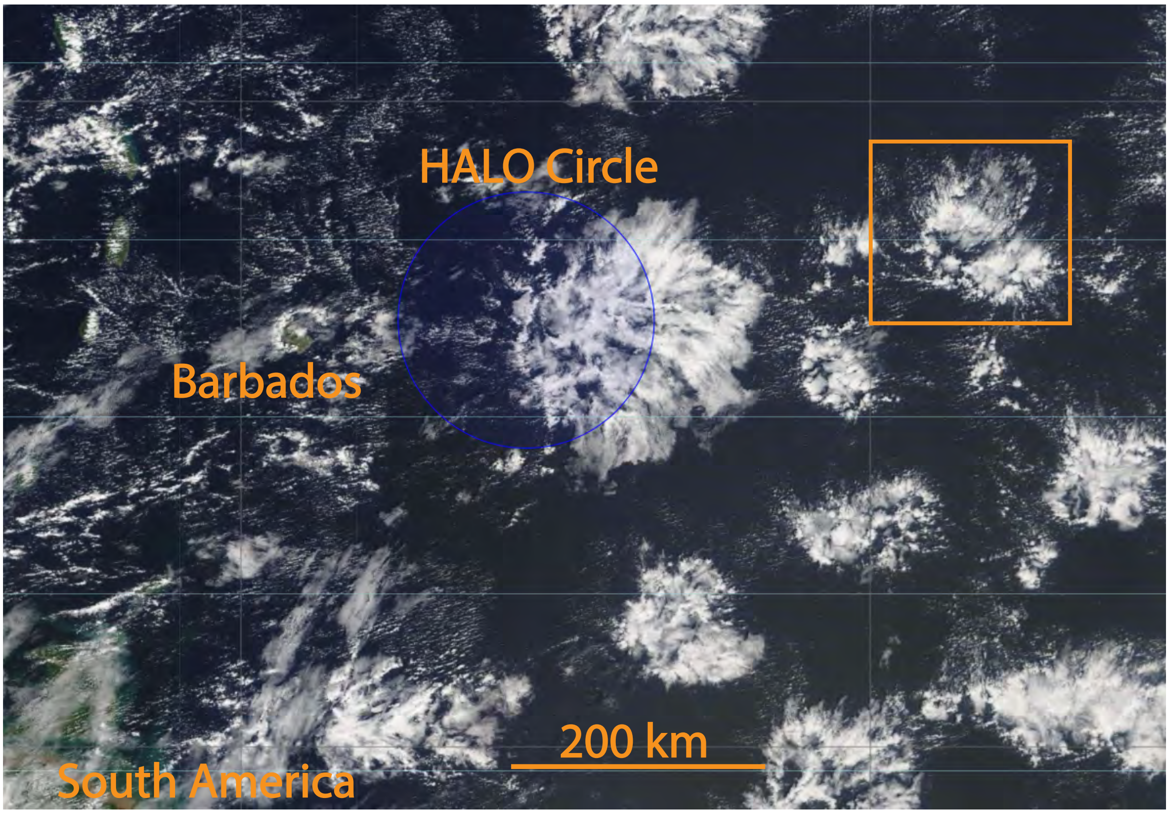

Figure 4.23 Satellite image of MODIS Terra satellite with cloud reflectivity from the overpass on February 12 2020 at 14:32 AST. The mesoscale cloud pattern upstream of Barbados is "flower". The MPCK+ on RV Maria S. Merian (MSM89 Flight 12) was close to the HALO Circle ($\sim$ 200 km in diameter [38]) on February 12 2020 at 19:00:00 AST. Taking into account the North-Easterly wind direction and the mean wind speed ($\approx$ 5 m/s), the MPCK+ sampled the flower in the red square. Source: https://observations.ipsl.fr/aeris/eurec4a/Leaflet/index.html. Taken on 2023-01-10.

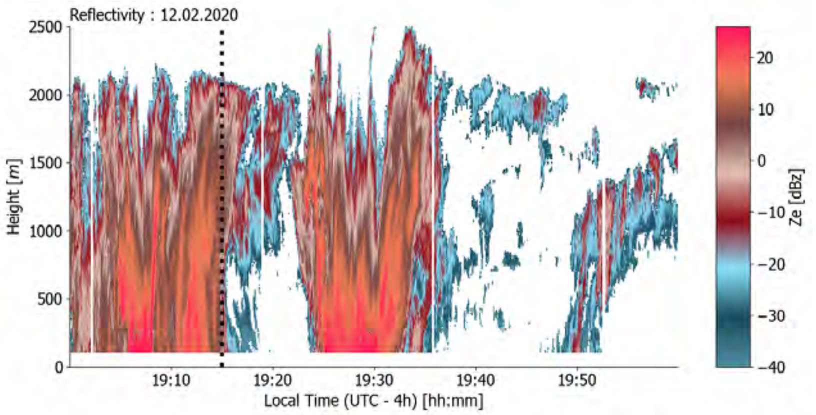

Figure 4.24 Radar reflectivity from W-band radar on February 12 2020 from 19:00 AST to 20:00 AST as a function of height, i.e. altitude above MSL, aboard RV Maria S. Merian [191]. Flying at an altitude of $\approx 900\,\mathrm{m}$ above MSL at a mean wind speed of $U \approx 5\,\mathrm{m/s}$, the MPCK+ is about 3 min downstream of RV Maria S. Merian. Source: https://atmos.meteo.uni-koeln.de/~cacquist/eurec4a/dataBrowser4.html. Taken on 2023-01-10.

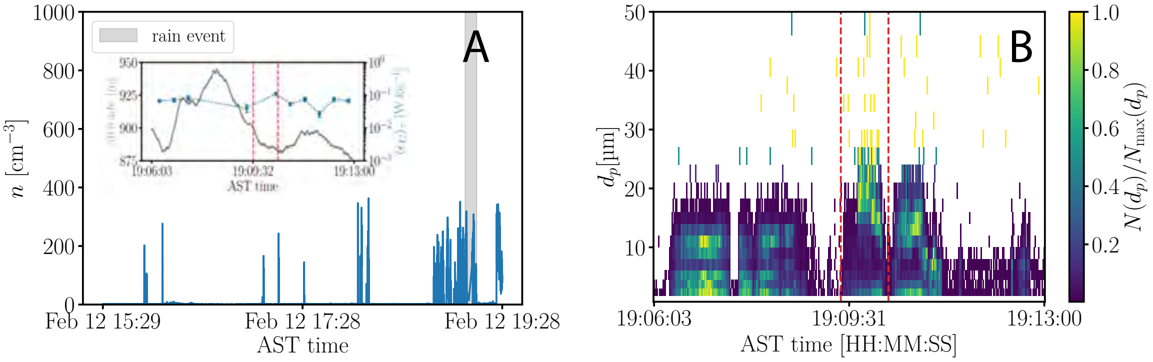

Figure 4.25 A: Cloud droplet number concentration as a function of time for MSM89 Flight 12. The time frame from 19:06:00 AST to 19:13:00 AST is shaded in gray. The inset shows the barometric altitude z_{PSS8} as a function of AST time as well as the local mean energy dissipation rate $\langle \epsilon_{I2} \rangle_\tau$, Eq. (3.15) with $n = 2$ and $\tau = 60\,\mathrm{s}$. The error bars are given by the difference between maximum and fit of Eq. (3.15) with $n = 2$ in the fit range. B: Histogram of cloud droplet diameters $N(d_p)$ as a function of time. The histogram is re-scaled by the maximum number count over the time period (19:06:00 AST to 19:13:00 AST) within a cloud droplet diameter bin $N_{\max}(d_p)$. The red dashed lines bound a time period where the histogram of cloud droplet diameters are significantly larger than before and after.

stationary conditions over the time frame of interest (19:06:00 AST to 19:13:00 AST), purely condensational growth of cloud droplets activated at the cloud base should lead to a single peak, here at $d_p \approx 12\,\mu\mathrm{m}$. Therefore, the origin of droplet diameters $d_p > 22\,\mu\mathrm{m}$ cannot be simply explained by condensational growth only. In the following, the effect of collision-coalescence is therefore assessed in more detail.

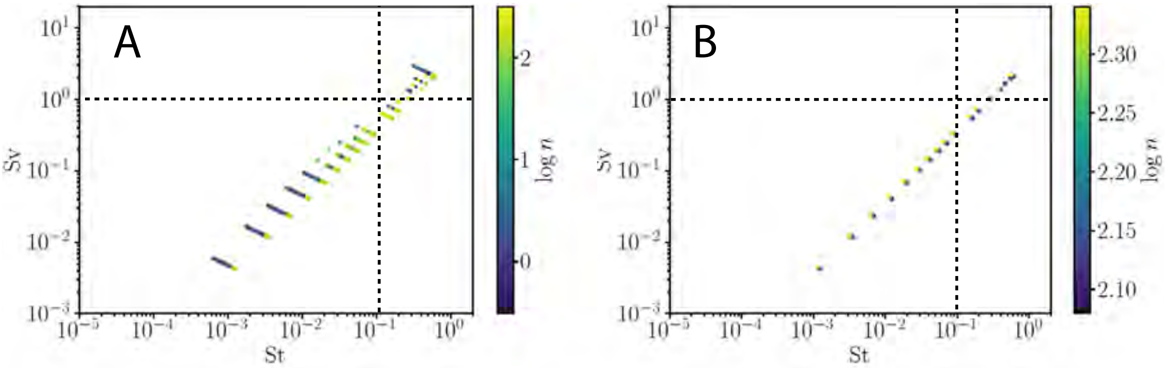

Figure 4.26 Non-dimensional settling velocity parameter and cloud droplet Stokes number on MSM 89 Flight 12. A: The Sv-St parameter space is obtained from all cloud droplets in the PbP-record from 19:06:00 AST to 19:13:00 AST. B: The Sv-St parameter space is shown only for PbP-records between 19:09:23 AST and 19:10:34 AST, i.e. the time frame bounded by the dashed red lines in Fig. 4.25. Each Sv-St point is colored in terms of the number concentration n.

To evaluate the possibility of collision-coalescence, individual cloud droplets must fulfill either $\mathrm{Sv} > 1$ or $\mathrm{St} > 0.1$ or both. Droplets attributed to this parameter space are the best candidates to become a so-called “collector”-droplets resulting in drizzle or rain. According to Eqs. (1.70) and (1.71), both Sv and St increase with d_p^2, which is why high St and Sv are expected for large droplets. During the rain event on MSM89, most cloud droplets with $\mathrm{Sv} > 1$ pertain to $\mathrm{St} > 0.1$ as shown in Fig. 4.26A. In the time frame of 19:09:23 AST and 19:10:34 AST with an enhanced fraction of droplets $> 20\,\mu\mathrm{m}$ in diameter, even all droplets with $\mathrm{Sv} > 1$ pertain to $\mathrm{St} > 0.1$. These cloud droplets are inertial and settle due to gravity. In a downdraft, this implies mean accelerations larger than gravitational acceleration. Moderate $\mathrm{Sv} \gtrsim 1$ combined with $\mathrm{St} > 0.1$ can lead further to preferentially settling through strain-dominated regions of the turbulent flow [4]. Most droplets with $\mathrm{St} < 0.1$ behave like tracers with $\mathrm{Sv} < 1$ and can thus be considered as background. For completeness, each Sv-St point in Fig. 4.26 is colored in terms of the number concentration n where n is inferred from the histogram data at 2 Hz. As St and Sv are calculated based on PbP-records of the cloud droplet diameter, the histogram time is interpolated to the PbP-time where n is assumed to be constant for each time interval of 0.5 s.

Considering precipitating clouds and assuming that collision coalescence plays a significant role in the initiation of rain in warm clouds, the collision efficiency is anticipated to be near the optimum. As mentioned in Sec. 4.4.2, the collision efficiency depends on the droplet size ratio $d_p^{<}/d_p^{>}$, which is shown for both the entire rain event

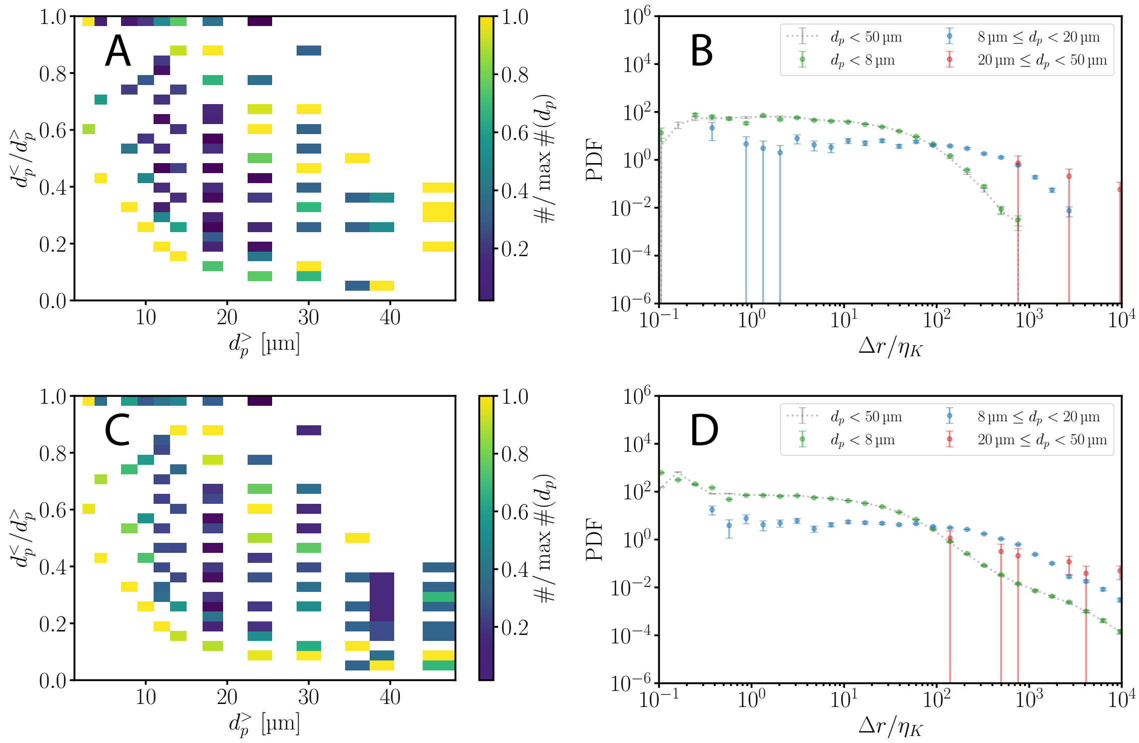

Figure 4.27 Normalized histogram of droplet size ratio $d_p^</d_p^>$ as a function of the $d_p^>$ and PDF of inter-particle distance Δr for the rain event. $d_p^>$ is the larger and $d_p^<$ the smaller droplet. # is the number count per $d_p^</d_p^> - d_p^>$ bin. Δr is re-scaled by the Kolmogorov length scale η_K. A: The droplet size ratio $d_p^</d_p^>$ is inferred from PbP-records of the cloud droplet diameter for the total time period (19:06:00 AST to 19:13:00 AST). B: The $\Delta r/\eta_K$ -PDF of total time period (19:06:00 AST to 19:13:00 AST) is shown for all droplets (gray dotted line) and for various diameter ranges. C: The droplet size ratio $d_p^</d_p^>$ is inferred from PbP-records of the cloud droplet diameter for 19:09:23 AST and 19:10:34 AST only. D: The $\Delta r/\eta_K$-PDF of total time period (19:09:23 AST to 19:10:34 AST) is shown for all droplets (gray dotted line) and for various diameter ranges. The $\Delta r/\eta_K$-range is limited to the range of 1×10^{-1} to 1×10^{4} for better visibility. Error bars are derived under the assumption of Poissonian counting statistics.

(Fig. 4.27A) and for a single cloud with larger droplet diameters (Fig. 4.27C). For better contrast, the droplet size ratio is normalized by the maximal number count per size bin ($\max \#(d_p)$). Smaller droplets generate a wide range from ~ 0.2 to 1 at $d_p^> \lesssim 15\,\mu\text{m}$. This is because of the double peak in droplet sizes as shown in Fig. 4.25B. The wide spread of $d_p^</d_p^>$ suggests that different stages of condensational cloud droplet growth are spatially mixed. Furthermore, taking into account the small collision efficiency for small droplets (Fig. 4.20D), a ratio of 0.7 does not necessarily hint at collision. Larger droplets with diameters $d_p > 23\,\mu\text{m}$ seem to be in proximity with smaller droplets as $d_p^</d_p^> \approx 1$ only happens for smaller droplets. Therefore, a droplet size ratio $d_p^</d_p^> \approx 1$ can only be due to condensational growth in statistically stationary and homogeneous conditions. This is further supported by the PDF of inter-particle distances for the diameter range $20\,\mu\text{m} \leq d_p < 50\,\mu\text{m}$ (Figs. 4.27B and D). The minimum distance of droplets in the diameter range $20\,\mu\text{m} \leq d_p < 50\,\mu\text{m}$ is found to be beyond $100\eta_K$ (Tables 4.5 and 4.6). For droplets larger than $30\,\mu\text{m}$ and smaller than $40\,\mu\text{m}$, the most frequent size ratio is 0.4 and 0.7. Assuming that these droplets are a result of collisions of $20\,\mu\text{m}$-droplets, 7 collisions are needed for a $20\,\mu\text{m}$ to grow to a droplet with $d_p = 40\,\mu\text{m}$. The likelihood for collisions is largest in regions of high number concentration as the inter-particle distances are likely to be smaller than in regions of low number concentration such as the cloud edge (Fig. 4.28). Considering droplet growth by condensation, the time for a $40\,\mu\text{m}$-droplet to grow in a constantly super-saturated environment of 1% is $\sim 300\,\text{s}$ [21]. As the bulk of cloud droplets seems to be bound to diameters smaller than $20\,\mu\text{m}$, it can be concluded that this is the limit of condensational growth in that rain event. Therefore, it is very likely that larger droplets are due to collision-coalescence.

To summarize, the case study of the rain event hints at a significant impact of collision-coalescence to rain initiation in warm clouds. Both gravitational collections as well as sling events can be expected considering the Sv-St parameter space. It would be interesting to complement these conclusions with measurements of super-saturation (fluctuations) in the future. The effect of charge is not considered in the scope of this thesis although it might affect the spatial distribution of cloud droplets on distances $\ll \eta_K$ as suggested by Fig. 4.28.

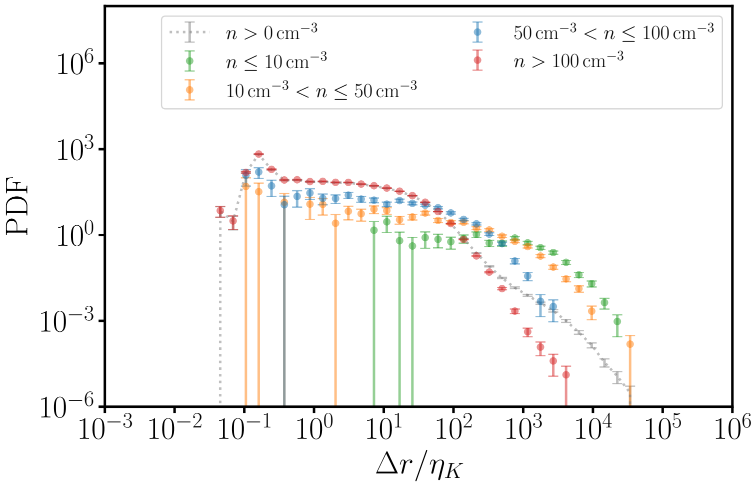

Figure 4.28 PDF of re-scaled inter-particle distance Δr conditioned on the cloud droplet concentration n. The $\Delta r/\eta_K$ -PDF of total time period 19:06:00 AST to 19:13:00 AST is shown for all droplets (gray dotted line) and for various ranges of the number concentration n. The number concentration is inferred from time intervals of 0.1 s based on PbP-records of inter-arrival time.

	unit	mean	median	std
U	m/s	5.44	5.46	0.17
$\sigma_{u_1'}$	m/s	0.69	0.68	0.06
$\langle\epsilon_{I2}\rangle_\tau$	mW/kg	69.87	69.53	12.42
η_K	mm	0.48	0.47	0.02
λ_f	m	0.06	0.05	0.01
L_{11}	m	4	3	1
R_λ		1458	1338	294

Table 4.5 Cloud turbulence features obtained from time-records of the longitudinal velocity component $u_1(t)$ for 19:06:00 AST to 19:13:00 AST in MSM89 Flight 12. $U = \langle u_1(t)\rangle_\tau$ is the mean velocity obtained from $u_1(t)$ for the averaging window τ, $\sigma_{u_1'}$ the RMS fluctuation of $u_1(t)$, $\langle\epsilon_{I2}\rangle_\tau$ the estimate of the mean energy dissipation rate according to Eq. (3.15) with $n = 2$, η_K the Kolmogorov length scale, λ_f the longitudinal Taylor micro-scale, L_{11} the integral length scale and R_λ the Taylor micro-scale Reynolds number. For each turbulence feature, the mean, median and standard deviation (std) are given. The averaging window is $\tau = 60\,\mathrm{s}$. $u_1(t)$ is not corrected for platform motion.

	unit	mean	median	std
U	m/s	5.32	5.31	0.07
$\sigma_{u'_1}$	m/s	0.73	0.73	0.01
$\langle \epsilon_{I2} \rangle_\tau$	mW/kg	98.52	100.22	8.08
η_K	mm	0.44	0.43	0.01
λ_f	m	0.05	0.05	0.00
L_{11}	m	3	3	1
R_λ		1370	1354	134

Table 4.6 Cloud turbulence features obtained from time-records of the longitudinal velocity component $u_1(t)$ for 19:09:23 AST to 19:10:34 AST in MSM89 Flight 12. $U = \langle u_1(t) \rangle_{30L_{11}} \tau$ is the mean velocity obtained from $u_1(t)$ for the averaging window τ, $\sigma_{u'_1}$ the RMS fluctuation of $u_1(t)$, $\langle \epsilon_{I2} \rangle_\tau$ the estimate of the mean energy dissipation rate according to Eq. (3.15) with $n = 2$, η_K the Kolmogorov length scale, λ_f the longitudinal Taylor micro-scale, L_{11} the integral length scale and R_λ the Taylor micro-scale Reynolds number. For each turbulence feature, the mean, median and standard deviation (std) are given. The averaging window is $\tau = 60\,\mathrm{s}$. $u_1(t)$ is not corrected for platform motion

Appendix 4.A Protocol for Validity Flag

To investigate cloud microphysics of individual clouds, it is desirable to estimate a mean energy dissipation rate per cloud. This requires that the averaging window is short enough, hence the choice of the averaging window $\tau = 60\,\mathrm{s}$. In the case of such short averaging windows, it is possible that second-order statistics such as the variance $\langle u_1'^2 \rangle$ are not fully converged (cf. Sec. 4.1.2). In addition, the pitot tube measures the relative wind speed inaccurately at low wind speeds ($U < 3\,\mathrm{m/s}$) or it might be clocked by cloud droplets, which both potentially causes wind measurement errors (compare gray shaded regions in Fig. 4.29A and Fig. 4.29B). Hence, it is necessary to detect unphysical turbulence parameters resulting from such erroneous velocity measurements.

As an example, integral length scales larger than the boundary layer depth, i.e. the scale of the largest convective roles, are unphysical. Therefore, the integral length scale is required to be smaller than the boundary layer depth, i.e. $L_{11} < 800\,\mathrm{m}$. Furthermore, a quality flag for ϵ_{I2} is related to the mean scaling exponent $\langle \zeta_2 \rangle$ in the inertial range of the longitudinal second-order structure function according to [96] where $0.3 < \langle \zeta_2 \rangle < 0.9$. Moreover, if the inertial range of the longitudinal second-order structure function, Eq. (3.15) with $n = 2$, is well pronounced, the maximum of the compensated structure function $\langle \epsilon_{I2}^{\mathrm{max}} \rangle_\tau$ is close to the plateau, e.g. $\left| \frac{\langle \epsilon_{I2}^{\mathrm{max}} \rangle_\tau}{\langle \epsilon_{I2} \rangle_\tau} - 1 \right| < 0.3$ where $\langle \epsilon_{I2} \rangle_\tau$ is defined by Eq. (3.15) with $n = 2$ and $\langle \epsilon_{I2}^{\mathrm{max}} \rangle_\tau$ by the maximum of Eq. (3.15) with $n = 2$. As the estimate $\langle \epsilon_{I2} \rangle_\tau$ invokes Taylor's hypothesis, the turbulence intensity has to be smaller than 25%. In this work, the criteria for characterizing turbulence are:

- $U > 3\,\mathrm{m/s}$
- $L_{11}^{>} < 800\,\mathrm{m}$
- $0.3 < \langle \zeta_2 \rangle < 0.9$
- $\left| \frac{\langle \epsilon_{I2}^{\mathrm{max}} \rangle_\tau}{\langle \epsilon_{I2} \rangle_\tau} - 1 \right| < 0.3$
- $\sigma_{u_1'}/U < 0.25$

where $L_{11}^{>}$ is the upper limit of the integral length scale. These criteria are applied in order to characterize turbulence based on averaging windows of $\tau = 60\,\mathrm{s}$ as outlined in Sec. 4.4.1. All averaging windows τ, which do not fulfill all requirements, are considered as outliers and are discarded. Decreasing the upper limit of the integral scale from $L_{11}^{>} \approx 1000$ to $L_{11}^{>} \approx 100$ decreases the fraction of *valid* averaging windows τ from 62% to 46% as shown in Fig. 4.30A. Furthermore, the upper limit of physical integral scales with $L_{11}^{>} \approx 800$ lies within a region where the Taylor-scale Reynolds number R_λ does not change. Hence, this choice is considered to be reasonable.

Errors in the longitudinal velocity measurements not only affect various estimates of turbulence characteristics but also the cloud droplet number concentration. Unphysical time-records of the longitudinal velocity time-record have been discarded for MPCK+ or mini-MPCK research flights EUREC^{4}A field campaign have been discarded based on visual check of the longitudinal velocity time series. However, short time intervals

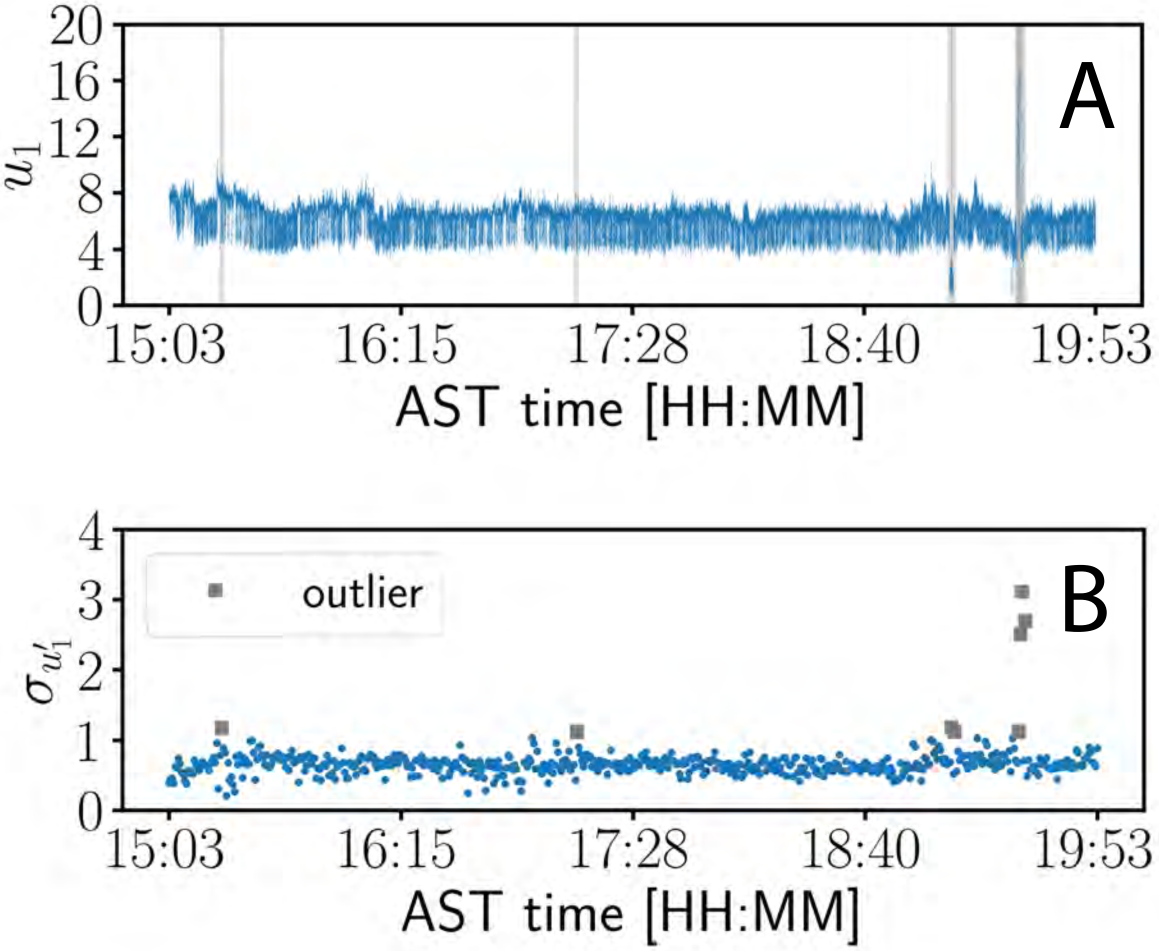

Figure 4.29 Outlier detection of the longitudinal velocity time-record. A: Time-record of the relative longitudinal velocity measurement u_1 of MSM89 Flight 12 as a function of AST time. Gray regions are identified as erroneous. B: RMS fluctuations of u_1 as a function of AST time for an averaging window $\tau = 60\,\mathrm{s}$. Outlier averaging windows are indicated by gray squares.

not directly visible so that an additional outlier detection has to be performed. So doing, based on the averaging window $\tau = 60\,\mathrm{s}$, the $\sigma_{u_1'}$-signal is median filtered with a kernel size of 30. Based on the transient median of $\sigma_{u_1'}$, a standard deviation σ is calculated from the $60\,\mathrm{s}$-$\sigma_{u_1'}$-signal. In a stationary signal, the variation would only rarely exceed the 3σ. Hence, an outlier is detected if $\sigma_{u_1'}$ of a single averaging window exceeds 3σ, which is then neglected. This process is iterated 100 times. Then, the remaining $60\,\mathrm{s}$-$\sigma_{u_1'}$ estimates are considered to be physical. This yields a quality flag for the longitudinal velocity time record as shown in Fig. 4.29A and B that is subsequently used to infer the cloud droplet number concentration.

However, there are still unphysical cloud droplet number concentrations in some localized events, where the absolute cloud droplet number counts per time are significantly higher compared to other clouds of the same flight. This concerns M161 Flight

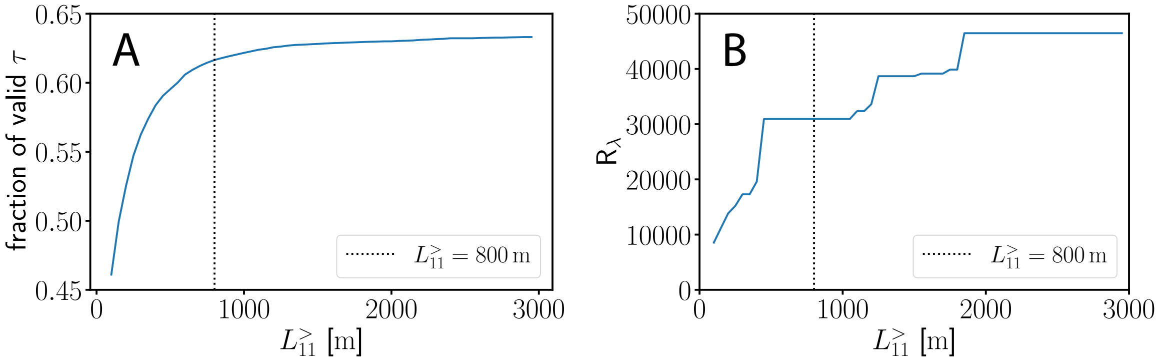

Figure 4.30 Impact of outlier filtering on valid fraction of averaging windows τ (A) and on the maximum R_λ estimate (B) as a function of the upper limit of the longitudinal integral length scale $L_{11}^{>}$.

005 when the mini-MPCK is still on RV Meteor. Moreover, an unphysical wind speed measurement is not detected by the algorithm explained above for on specific time interval during MSM89 Flight 12. Both time periods are neglected manually. Further checks are needed in case of MSM89 Flight 10 to verify high cloud droplet number counts per time but the velocity measurement is physical and the MPCK+ was far away from the ship. This is why, this flight is not discarded in the scope of this work.

Appendix 4.B Effect of Filtering

The Max Planck Cloudkites record the velocity in the platform frame of reference. Similar to wind velocity measurements on aircraft, the measured wind vector has to be transformed to the Earth frame of reference. This procedure is known for wind velocity measurements, e.g. on aircraft [201] or tethered balloons [98]. However, the helikite motions are driven by the turbulent flow across a wide range of scales (Sec. 2.4.2), which has been observed also by Egerer et al. deploying a helium-filled balloon [96]. Further corrections with respect to misalignment can be applied to the wind velocity data in the Earth frame of reference, by assuming $\langle u_3' \rangle_\tau = 0$ [202]. Corrections for platform motion require that the measurements of orientation, rotation rates and acceleration are not drifting, noisy and synchronized in time with wind measurement data. In principle, the SBG Ellipse-N is able to provide such a data set. However, due to non-ideal configuration, mediocre GNSS reception and signal noise, it is likely that these corrections will not succeed on EUREC^{4}A data. That is why a cutoff frequency $f_c = 0.5\,\mathrm{Hz}$ is chosen in order to suppress the influence of platform motion on the turbulence analysis. Here, I want to discuss the effect of filtering on the RMS velocity $\sigma_{u_1'}$ and the energy dissipation rate ϵ_{I2}.

The effect of filtering is illustrated by three different cases: (I) the uniformly moving virtual probes in DNS (Fig. 4.31A and B), (II) the keel-strapped micro-MPCK (Fig. 4.31C and D) and (III) the tether-mounted mini-MPCK on M161 Flight 10 (Fig. 4.31E and F). In case (I), DNS 3.3 is chosen due to the highest R_λ and a turbulence intensity of $I = 10\%$, which is close to atmospheric observations. Furthermore, uniformly moving probes in DNS 3.3 (Table 3.2) are taken because "weather vane"-like probes measure a similar mean energy dissipation rate for $I = 10\%$. However, the range of cutoff frequency is smaller compared to cases (II) and (III) because of the smaller separation of large and small scales as a consequence of R_λ being only ~ 300. In all cases, the energy dissipation rate is estimated by ϵ_{I2} with a constant fit range across the entire range of applied cutoff frequencies (case (I): $r \in [20\eta_K, 200\eta_K]$, case (II): $r \in [2\,\mathrm{m}, 4\,\mathrm{m}]$, case (III): $r \in [2\,\mathrm{m}, 4\,\mathrm{m}]$).

All three cases show a strong dependency of both $\sigma_{u_1'}$ and ϵ_{I2} on the cutoff frequency as shown in Fig. 4.31 where $\sigma_{u_1'}(f_c)$ and $\epsilon_{I2}(f_c)$ are given relative to the case with the lowest $f_c \gtrsim 0$ and referred to as "0". Both $\sigma_{u_1'}$ and ϵ_{I2} are ensemble averages over all virtual probes in case (I) and over all averaging windows $\rangle_\tau = 1800\,\mathrm{s}$ in case (II) and (III). Starting with case (I), both $\sigma_{u_1'}(f_c)$ and $\epsilon_{I2}(f_c)$ decay with f_c only indicating a plateau for small f_c. Considering cases (II) and (III), $\sigma_{u_1'}$ decreases moderately for $f_c < 0.1\,\mathrm{Hz}$ and decays much faster between $0.1\,\mathrm{Hz} < f_c < 0.2\,\mathrm{Hz}$ as shown in Figs. 4.31C and E. In contrast, ϵ_{I2} shows a longer plateau in Figs. 4.31D and F, where ϵ_{I2} only minimally changes up to $f_c \sim 0.1\,\mathrm{Hz}$. Assuming that L_{11} $100\,\mathrm{m}$ and U $10\,\mathrm{m/s}$ in the atmosphere, $f_c \sim 0.1\,\mathrm{Hz}$ corresponds to a cutoff length scale $l_c \sim L_{11}$. Hence, cutoff frequencies corresponding to length scales larger than L_{11} are only slightly affected by filtering. This is supported by derivatives $\mathrm{d}\epsilon_{I2}/\mathrm{d}f_c \approx 0$ (red lines in Figs. 4.31B, D, and F).

However, $f_c = 0.5\,\mathrm{Hz}$ corresponds to a length scale $l_c \sim 20\,\mathrm{m}$ with L_{11} $100\,\mathrm{m}$ and U $10\,\mathrm{m/s}$ in the atmospheric boundary layer. In contrast to the plateau region in Figs. 4.31D and F, ϵ_{I2} decays between $0.1\,\mathrm{Hz} < f_c \lesssim 0.5\,\mathrm{Hz}$ and the rate of change $\mathrm{d}\epsilon_{I2}/\mathrm{d}f_c$ is non-zero. This suggests that $f_c = 0.5\,\mathrm{Hz}$ is in a regime that strongly varies with f_c, which is unfavorable. At $f_c = 0.5\,\mathrm{Hz}$, the underestimation of $\epsilon_{I2}(f_c)$ is 40% in case (II) compared to $\epsilon_{I2}(0)$. In cases (II) and (III), $\sigma_{u_1'}(f_c)$ is underestimated by 70 - 80% in comparison to $\sigma_{u_1'}(0)$. However, taking into account that the references $\sigma_{u_1'}(0)$ and $\epsilon_{I2}(0)$ are also affected by platform motions for cases (II) and (III), the relative comparison is not ideal.

To compare case (I) with cases (II) and (III), the cutoff frequency of $f_c = 0.5\,\mathrm{Hz}$ in (II) and (III) has to be re-scaled. In code units (c.u.) of DNS where $L_{11} \approx 1$ c.u., f_c is 50 c.u. At $f_c = 50$ c.u., ϵ_{I2} nearly vanishes. As mentioned above, the separation of scales in DNS 3.3 is much lower than in the atmosphere which makes it impossible to relate f_c of cases (II) and (III) to η_K of DNS. Therefore, case (I) cannot be invoked to justify or to falsify the choice of f_c. Case (I) rather supports the dependence of $\sigma_{u_1'}$ and ϵ_{I2} on f_c in general.

A complementary approach for investigating the effect of filtering involves the fact that the mean energy dissipation rate $\langle\epsilon\rangle$ can be obtained by integrating a pre-multiplied energy spectrum $E(\kappa)$ [5]

$$\langle\epsilon\rangle = 2\nu \lim_{\kappa_c \to 0} \int_{\kappa_c}^{\infty} \mathrm{d}\kappa \kappa^2 E(\kappa)\,, \tag{4.20}$$

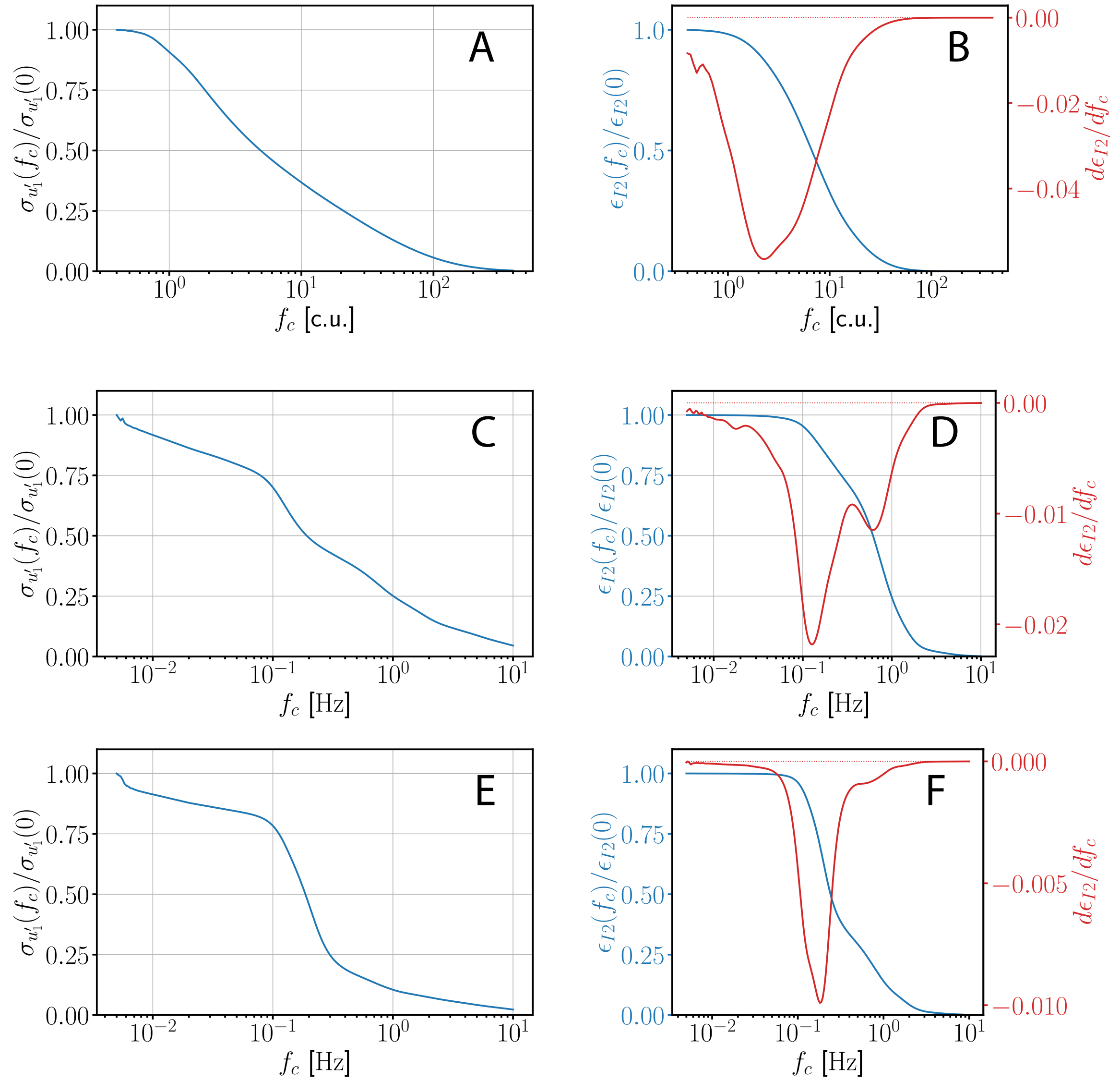

Figure 4.31 Effect of filtering on the RMS velocity fluctuations $\sigma_{u_1'}$ and the energy dissipation rate ϵ_{I2} as a function of the cutoff frequency f_c. (A, B) Virtual probes sample DNS of homogeneous isotropic turbulence at random directions but constant speed for a turbulence intensity of $\approx 10\%$ and $\mathrm{R}_\lambda \approx 295$. Hence, the dynamics of virtual probes are statistically uncorrelated with the flow. (C, D) The micro-MPCK is mounted directly to the keel of the $34\,\mathrm{m}^3$ helikite. This configuration is similar to a weather vane. $D_{LL}(r)$ is fitted for $r \in [2\,\mathrm{m}, 6\,\mathrm{m}]$. (E, F) The mini-MPCK is always attached to the main tether of a $75\,\mathrm{m}^3$ helikite. The helikite behaves like a weather vane driving the platform motion of the tether-mounted mini-MPCK. $D_{LL}(r)$ is fitted for $r \in [2\,\mathrm{m}, 6\,\mathrm{m}]$.

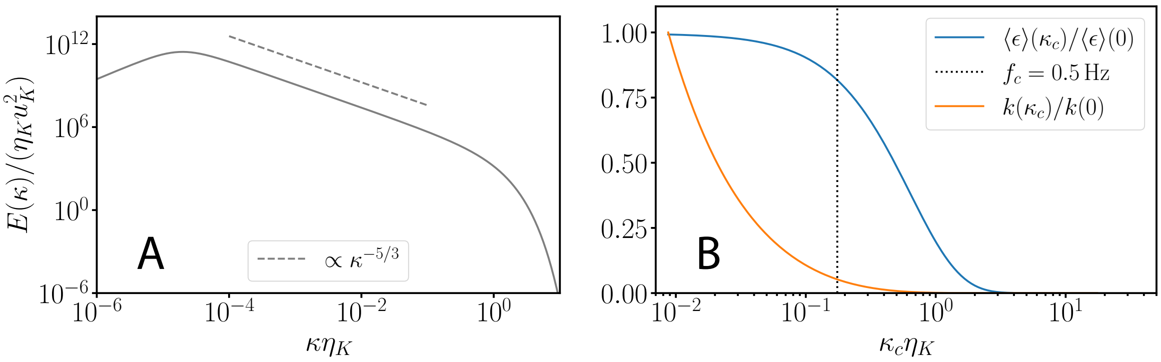

Figure 4.32 The effect of filtering using a model spectrum. A: The model spectrum, Eq. (4.22), follows with $C_K = 1.5$, $p_0 = 2$, $c_L = 6.78$, $\beta = 2.1$, $L \sim 200\,\mathrm{m}$, $\langle\epsilon\rangle \sim 0.001\,\mathrm{W/kg}$, $U \sim 10\,\mathrm{m/s}$ and $\nu = 1.552 \times 10^{-5}\,\mathrm{m^2/s}$. B: The effect of filtering on $\langle\epsilon\rangle$ is modeled by introducing a finite integration boundary in Eq. (4.20). The dashed line corresponds to $f_c = 0.5\,\mathrm{Hz}$ with $\kappa_c = 2\pi U/f_c$.

where ν is the kinematic viscosity, $\kappa = 2\pi/l$, l a length scale, $\kappa_c = 2\pi U/f_c$ and f_c a cutoff frequency. Similarly, the turbulent kinetic energy k can be obtained by [5]

$$k = \lim_{\kappa_c \to 0} \int_{\kappa_c}^{\infty} \mathrm{d}\kappa E(\kappa)\,. \tag{4.21}$$

In homogeneous isotropic turbulence, $k = 3/2\langle u_1'^2\rangle = 3/2\sigma_{u_1'}^2$. A model spectrum of homogeneous isotropic turbulence with an exponential decay [203] is defined in [5, Eq. 6.246 ff.]:

$$E(\kappa) = C_K \langle\epsilon\rangle^{2/3} \kappa^{-5/3} \left(\frac{\kappa L}{[(\kappa L)^2 + c_L]^{1/2}} \right)^{5/3 + p_0} \exp(-\beta\kappa\eta_K)\,, \tag{4.22}$$

where $C_K = 1.5$ the Kolmogorov constant, $p_0 = 2$ and $c_L = 6.78$ and $\beta = 2.1$ are positive constants. Here, $L \sim 200\,\mathrm{m}$ is the energy injection scale, $\langle\epsilon\rangle \sim 0.001\,\mathrm{W/kg}$, $U \sim 10\,\mathrm{m/s}$ and $\nu = 1.552 \times 10^{-5}\,\mathrm{m^2/s}$. This set of parameters corresponds to $\mathrm{R}_\lambda = \left(\frac{20}{3}\right)^{1/2} \left(\frac{L}{\eta_K}\right)^{4/3} \approx 7100$. The non-dimensional model spectrum is shown in Fig. 4.32A. The influence of filtering on the estimation of $\langle\epsilon\rangle$ can be modeled by integrating Eq. (4.20) for various κ_c, i.e. neglecting the limit $\kappa_c \to 0$. Similarly to case (I) - (III), $\langle\epsilon\rangle(\kappa_c)$ decays with κ_c as shown in Fig. 4.32B. $\langle\epsilon\rangle(2\pi U/f_c)$ with $f_c = 0.5\,\mathrm{Hz}$ is underestimated by $\sim 20\%$. As $\sigma_{u_1'} = \sqrt{\langle u_1'^2\rangle} = \sqrt{2k/3}$ is dominated by large scales, the effect of $\sigma_{u_1'}$ is larger. Regarding the model spectrum in Fig. 4.32, $k(2\pi U/f_c)$ is underestimated by 95% which corresponds to underestimating $\sigma_{u_1'}(2\pi U/f_c)$ by about 78% in case of homogeneous isotropic turbulence at $f_c = 0.5\,\mathrm{Hz}$.

To summarize, the effect of filtering on ϵ_{I2} is most likely between 20% and 40% whereas the effect on $\sigma_{u_1'}$ is about 80% at large R_λ. Note that $\mathrm{R}_\lambda \propto \left(\frac{L}{\eta_K}\right)^{4/3}$ implying that the separation of scales grows with R_λ. As k is mostly stored in large scale and

$\langle\epsilon\rangle$ mostly stored in small scales, k decays much faster with κ_c as shown in Fig. 4.32B. As R_λ is very high in the atmosphere, small R_λ are not further discussed and the interested reader is referred to [5].

Appendix 4.C Supplementary Tables

Research Cruise	Flight	fit range [m]	f_c [Hz]	f_{filt} [Hz]
M161	1	(2 , 6)	0.5	10.0
	10	(2 , 6)	0.5	10.0
	3	(0.7 , 2.5)	0.5	10.0
	4	(0.7 , 2.5)	0.5	10.0
	5	(2 , 5)	0.5	10.0
	6	(2 , 6)	0.5	10.0
	7	(2 , 6)	0.5	10.0
	8	(2 , 6)	0.5	10.0
	9	(2 , 6)	0.5	10.0
	12	(2.0 , 20.0)	0.5	10.0
MSM89	10	(1 , 5)	None	10.0
	7	(2 , 5)	0.5	10.0
	13	(2 , 5)	0.5	10.0
	15	(2 , 5)	0.5	10.0
	17	(2 , 5)	0.5	10.0
	19	(2 , 5)	None	10.0
	2	(2 , 5)	None	10.0
	5	(2 , 5)	None	10.0
	6	(0.8 , 3)	0.5	10.0
	8	(0.7 , 2.5)	0.5	10.0
	11	(0.7 , 2.5)	0.5	10.0
	12	(0.7 , 2.5)	0.5	10.0
	14	(2 , 5)	0.5	10.0
	16	(2 , 5)	0.5	10.0
	18	(0.7 , 2.0)	0.5	10.0
	9	(0.7 , 2.5)	0.5	10.0
	20	(0.7 , 2.5)	0.5	10.0
	3	(0.7 , 2.5)	0.5	10.0

Table 4.7 Energy dissipation rate analysis parameters. Regarding EUREC^{4}A , all energy dissipation rates have been estimated via $epsilon_{I2}$ based on one-dimensional time-records of the wind speed acquired by the PSS8 pitot tube.

	unit	mean	median	std	e [%]
U	m/s	6.16	5.57	1.68	1.27
$\sigma_{u_1'}$	m/s	0.69	0.71	0.16	-
$\langle \epsilon_{I2} \rangle_\tau$	mW/kg	19.61	13.45	20.52	16.89
η_K	mm	0.87	0.72	0.41	4.22
λ_f	m	0.20	0.13	0.28	8.45
L_{11}	m	134	19	1042	16.89
R_λ		4853	3492	9652	8.45

Table 4.8 Bulk turbulence features obtained from time-records of the longitudinal velocity component $u_1(t)$ on MSM89 (RV Maria S. Merian) during EUREC^{4}A by both the MPCK+ and mini-MPCK. $U = \langle u_1(t) \rangle_{30L_{11}} \tau$ is the mean velocity obtained from $u_1(t)$ for the averaging window τ, $\sigma_{u_1'}$ the RMS fluctuation of $u_1(t)$, $\langle \epsilon_{I2} \rangle_\tau$ the estimate of the mean energy dissipation rate according to Eq. (3.15) with $n = 2$, η_K the Kolmogorov length scale, λ_f the longitudinal Taylor micro-scale, L_{11} the integral length scale and R_λ the Taylor micro-scale Reynolds number. For each turbulence feature, the mean, median, standard deviation (std) and relative random error e in % are given. e is obtained by Eqs. (3.45), (1.61), (4.3), (4.14) (4.11) and (4.12) for $\langle \epsilon_{I2} \rangle_\tau$, U, R_λ, L_{11}, η_K and λ_f respectively. The averaging window is $\tau = 1800\,\mathrm{s}$. $u_1(t)$ is not corrected for platform motion.

Appendix 4.D Supplementary Figures

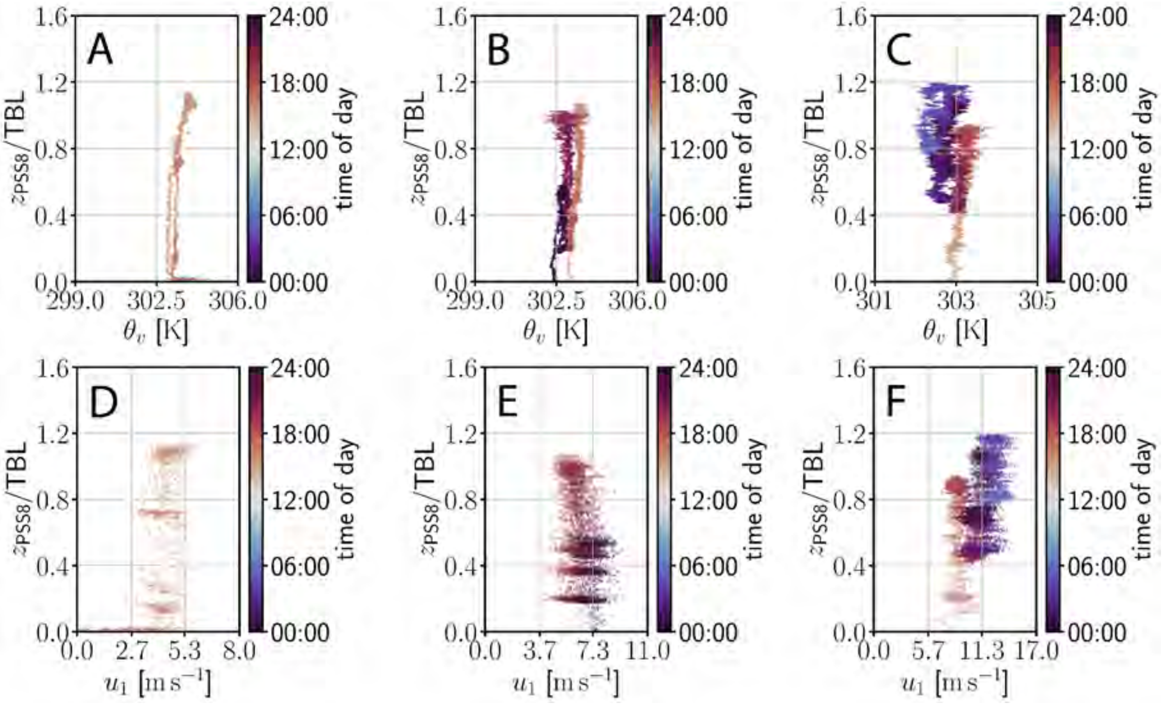

Figure 4.33 Vertical profiles of the virtual potential temperature θ_v and the longitudinal velocity u_1 recorded on M161 Flight 3 (A, C) Flight 8 (B, D) and Flight 9 (C, F). TBL represents Top of the Boundary layer. Color code visualized the local time of the day (ATS) corresponding to UTC - 4. The barometric altitude is acquired by the PSS8.

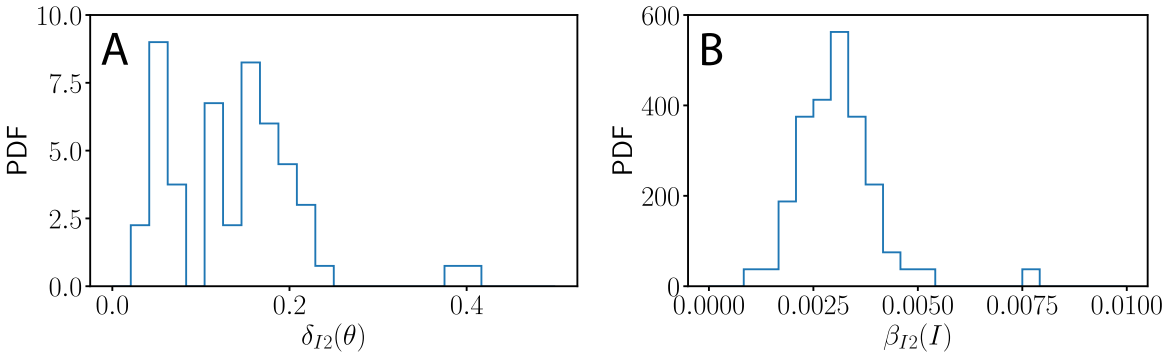

Figure 4.34 PDFs of the systematic errors $\delta_{I2}(\theta)$, Eq. (3.36), due to misalignment (A) and $\beta_{I2}(I)$, Eq. (3.28),due to finite turbulence intensity (B) of the energy dissipation rate estimate $\langle\epsilon_{I2}\rangle_\tau$ during EUREC^{4}A on M161 aboard RV Meteor. θ is the average angle of misalignment and I the turbulence intensity. Both errors are estimated from averaging windows with $\tau = 1800\,\mathrm{s}$.

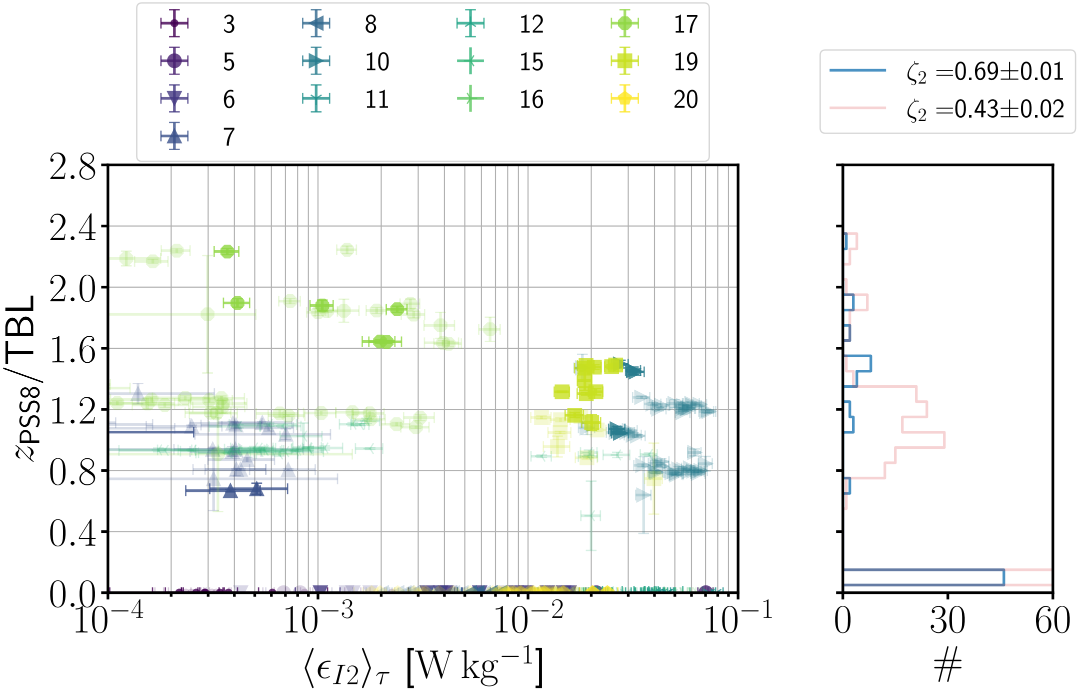

Figure 4.35 Overview of mean energy dissipation rate estimates $\langle\epsilon_{I2}\rangle_\tau$ obtained from one-dimensional time-records of the longitudinal velocity during EUREC^{4}A on MSM89 (RV Maria S. Merian) as a function of the re-scaled barometric altitude z_{PSS8}. TBL is the abbreviation for top of the boundary layer and the averaging window $\tau = 30\,\mathrm{min}$. Error bars are given by Eq. (3.45) for $\langle\epsilon_{I2}\rangle_\tau$ and by the re-scaled standard deviation of z during the averaging window τ. Highly opaque $\langle\epsilon_{I2}\rangle_\tau$ -values are obtained from longitudinal second-order structure functions $D_{LL}^\tau(r)$ with a mean scaling exponent ζ_2, which satisfies $|\zeta_2 - 2/3 + 1/36| < 0.1$ (in agreement with K62) in the fit range. In contrast, weakly opaque $\langle\epsilon_{I2}\rangle_\tau$-values stem from $D_{LL}^\tau(r)$ with $|\zeta_2 - 2/3 + 1/36| \geq 0.1$. Furthermore, $\langle\epsilon_{I2}\rangle_\tau$ is highly opaque only if the standard deviation of the altitude is lower than 50 m. The right panel shows the number counts of $\langle\epsilon_{I2}\rangle_\tau$ -values agreeing with K62 in blue and the number counts of $\langle\epsilon_{I2}\rangle_\tau$-values disagreeing with K62 in (weakly opaque) red. The ensemble average of each ζ_2-group is denoted by $\langle\zeta_2\rangle$.

Chapter 5

Discussion and Outlook

In this section, an overall discussion, outlook and summary are presented. Both the experimental approach and individual results are mostly discussed in the previous Chapters 2, 3 and 4. Therefore, more general aspects are considered in the following.

5.1 Discussion

5.1.1 Turbulence Measurements in the Trade-wind Boundary Layer

In this thesis, turbulence characteristics are inferred from one-dimensional velocity time-records in the atmosphere being probed by balloon-borne instruments, the MPCK+ and the mini-MPCK. Concerning the performance of balloon-borne measurements with the mini-MPCK, the interested reader is referred to Sec. 2.5. Similarly, the accuracy of different methods of estimating the mean energy dissipation rate was discussed in Sec. 3.3. Here, I concentrate on the discussion of turbulence characteristics and anisotropy of the lower atmosphere.

Turbulence Characterization by Balloon-borne Measurements

The velocity is measured relative to the airborne instrument. Based on the one-dimensional measurements of relative velocity in time, turbulence characteristics are estimated from the local and global mean energy dissipation rate estimate and the corresponding variance estimates. In case the instrument is attached to the helikite, it is prone to platform motion affecting the relative velocity measurement. Modeling the helikite as a weather vane, it has been shown that the effect of platform motion can be neglected for both the variance and energy dissipation rate for turbulence intensities up to 25%. During the EUREC^{4}A field campaign, the turbulence intensity was 7% on average with a standard deviation of 4% based on relative velocity measurements. Hence, the effect of platform motion is considered to be negligible if the instrument is mounted at the helikite. Otherwise, if the instrument is attached to the line, it not only adjusts to the mean wind direction (which it is supposed to do) but also exhibits pendulum-like motions. Without corrections for platform motion, these pendulum motions have to be filtered out because they affect inertial range statistics expressing themselves in anomalous inertial range scaling of the longitudinal second-order structure function. Presumably, they also result in overestimating the variance. It has been argued that variance estimates based on filtered velocity records systematically underestimate the true variance $\langle u_1'^2 \rangle$ most likely by up to 40%. However, balloon-borne measurements tend to overestimate $\langle u_1'^2 \rangle$ by approximately 30% [114], which might compensate partially for the variance underestimation associated with filtering. This impacts also the systematic bias in R_λ and L_{11}, which is thus likely to be overestimated in Sec. 4.2.3.

Atmospheric *in-situ* measurements in time are accompanied by finite averaging windows. As mentioned before, the variance estimate and energy dissipation rate estimate depend on the choice of the averaging window. In steady flows, longer averaging yields better statistical convergence (cf. Chapter 3). As an example, wind tunnel measurements are conducted for time periods of $\sim 10^7$ integral time scales and more [147, 204]. In the atmospheric boundary layer, the diurnal cycle poses an upper limit on a reasonable averaging window. Assuming a large-eddy turnover time of $\sim 600\,\mathrm{s}$ (boundary layer depth $\sim 600\,\mathrm{m}$ and vertical velocity scale $\sim 1\,\mathrm{m/s}$), an averaging window of $\tau = 1800\,\mathrm{s}$ corresponds to 3 large eddy turnover times. Assuming that the energy injection scale is about 1/6 of the large-eddy scale [5] and assuming homogeneous isotropic turbulence with $L_{11}/L \sim UT_{11}\ UT \approx 1/2$ (T is the energy injection time scale and U a velocity scale), the averaging window of $\tau = 1800\,\mathrm{s}$ corresponds to 36 integral time scales. In contrast to wind tunnel measurements, it is hence expected that the statistical uncertainty does not vanish. As an example, the relative random error of the mean energy dissipation rate is about 40% and the systematic error is about 10% for mini-MPCK measurements on RV Meteor.

Both the random and the systematic error of the mean energy dissipation rate propagate to other turbulence features such as the Taylor-scale Reynolds number R_λ, Eq. (1.38). Ignoring the inaccuracy in the integral length scale estimate according to Eq. 1.29, the relative random error of R_λ is approximately 20%. In the context of the Taylor-scale Reynolds number R_λ, it should be pointed out that, advantageously, the amplification due to the low value of kinematic viscosity is reduced in Eq. (1.38) compared to Eqs. (1.37). However, Eq. (1.38) depends on the choice of a “large eddy” length scale. Choosing the energy injection scale $L \approx 2L_{11}$ results in $2^{2/3} \approx 1.58$ higher R_λ. Similarly, using the longitudinal Taylor-micro scale λ_f instead of the transverse Taylor micro-scale λ_g causes a systematic deviation by a factor of $\sqrt{2}$. Furthermore, L_{11} depends on the averaging window τ in consequence of the τ-dependent variance $\langle u_1'^2 \rangle_\tau$ and energy dissipation rate estimate. Hence, R_λ depends also on τ (cf. Tables 4.1, 4.8 and 4.4). As the systematic underestimation of $\langle u_1'^2 \rangle_\tau$ is monotonically increasing with τ, Eq. (1.63), the same trend is expected for L_{11} and R_λ. *In-situ* measurements in mountainous terrain on Mt. Zugspitze report $\mathrm{R}_\lambda \sim 3000$ [54] whereas tower-based R_λ-measurements in the atmospheric surface layer of Brookhaven National Laboratory

(USA) ranges from 1×10^4 to 2×10^4 [205]. It should be noted that the averaging window of this work ($\tau = 1800\,\mathrm{s}$) is shorter than the averaging window chosen in the tower-based measurement ($\tau \geq 2000\,\mathrm{s}$) [205]. Considering the loose definition of R_λ, which potentially causes a discrepancy of $\sim 50\%$, the PDFs of $\mathrm{R}_\lambda \sim$ as presented in Figs. 4.5 and 4.13 are plausible.

To systematically assess turbulence in trade-wind cumuli, the analysis is conditioned on the cloud droplet number concentration n. Due to the low cloud fraction, i.e. the fraction of time where $n > 10/\mathrm{cm}^3$, an averaging window of $\tau = 1800\,\mathrm{s}$ is too large. Therefore, the averaging window size was reduced to $\tau = 60\,\mathrm{s}$ resulting in higher relative random errors ($\approx 90\%$). However, these estimates are based on assumptions of a stationary flow, which is questionable at least in growing and dissolving clouds. Thus, one has to be careful with estimating the relative random error via δ_{I2} although the estimated random error of 90% hints at large statistical uncertainty. One possibility to mediate the non-stationarity of evolving clouds is to evaluate the buoyancy and vertical velocity of the cloud. As an example, growing clouds are positively buoyant in the cloud core with rising air motions [79]. Since this is beyond the scope of this thesis, the error in estimating the local mean energy dissipation rate has been chosen to be the deviation of the maximum of Eq. (3.15) ($n = 2$) and the corresponding fit. On average, the deviation amounts to 22% for the bulk and 21% in clouds with $n > 10/\mathrm{cm}^3$. Based on that deviation and recalling that the energy dissipation rate is on average twice as high inside clouds as in cloud-free air, the difference can be considered significant. As mentioned before, random errors of R_λ, L_{11}, λ_f and η_K are inferred via Gaussian error propagation and are given by Eqs. (4.3), (4.14), (4.11) and (4.12), respectively. Each of these equations is proportional to the relative random error $\delta_{I2}(R)$ with a pre-factor ≤ 1. In relative terms (e.g. $e(\eta_K)/\eta_K$), this implies that the relative errors are equal to or less than $\delta_{I2}(R)$. Using the deviation of the maximum of Eq. (3.15) ($n = 2$) and the corresponding fit ($\approx 22\%$) as a measure for the random error, the relative random error for each of these quantities is less than 22%. Considering the mean values of Tables 4.3 and 4.4, the relative deviation is larger indicating significant differences between cloud turbulence and bulk.

Similar energy dissipation rates $\sim 1 \times 10^{-2}\,\mathrm{W/kg}$ have been measured in a previous field experiment (RICO, aircraft-borne) as well [127]. During CARRIBA, higher energy dissipation rates inside trade-wind cumuli up to $\sim 1 \times 10^{-1}\,\mathrm{W/kg}$ near the cloud top have been measured by a helicopter-borne instrument [8]. Hence, local mean energy dissipation rates in clouds inferred from balloon-borne one-dimensional velocity measurements in time during EUREC^{4}A are consistent with previous energy dissipation rate measurements.

The Richardson number

The stability of the atmospheric boundary layer is captured by the Richardson number Ri, which is an important non-dimensional parameter to analyze entrainment in an inversion layer [52]. Such an inversion layer is observed in the trade-wind boundary layer above a mixed layer (Sec. 4.2.1). In the re-scaled altitude range $0.8 \leq z_{\mathrm{PSS8}}/\mathrm{TBL} \leq 1.2$, a large variability of Ri is observed. Especially in the late afternoon until sunset at 18:00 AST, Ri is often negative suggesting unstable stratification and turbulence (Fig. 4.9A). During noon and night, significantly positive values up to $\mathrm{Ri} \sim 10$ are observed hinting at stable stratification. Presumably, the high variability in Ri is coupled to large-scale motions of the free atmosphere, which are referred to as mesoscale motions [9, 190]. In the middle of the mixed layer $z_{\mathrm{PSS8}}/\mathrm{TBL} \approx 0.5$ and taking into account the difficulties in estimating Ri as outlined below, values of $0 \leq \mathrm{Ri} < 1$ indicate either a well-mixed layer or a stable stratification. Based on the impression gained from six research flights, it is unlikely to encounter an entirely unstably stratified sub-cloud layer. How far this affects the cloud fraction, which is important for the Earth's radiation budget and this climate warming [9], remains an open question.

The Ri-values reported in this thesis originate from one-dimensional measurements and hence refer to localized events. To calculate the vertical gradient of the mean velocity, the platform speed with respect to ground is simply subtracted from the mean relative wind speed under the assumption of perfect alignment of the mini-MPCK and the mean wind direction. According to Sec. 2.4.2, the angles of attack and sideslip are non-zero (Fig. 2.9) revealing that the perfect-alignment assumption is not generally fulfilled. In most cases, the misalignment is approximately 20° causing an error of 7% in the mean wind speed and is therefore neglected in the context of Ri (24% for M161 Flight 5). Furthermore, Ri depends on the virtual potential temperature θ_v, Eq. (1.53), which is a function of the specific humidity. As the specific humidity is obtained from the relative humidity measurement, insufficient ventilation due to the front nose of the mini-MCPK might cause a larger response time of the humidity sensor. To quantify this error, adequate control experiments in the laboratory would be necessary. Furthermore, in humid air with $\mathrm{RH} \geq 90\%$, relative humidity is prone to errors of about 5%, which can be critical in that regime for measuring super-saturation. While these errors are suggestive of being small, estimating the Richardson number Ri by Eq. 4.10 is difficult because the estimation relies on the assumption of a frozen atmosphere over the entire averaging window. This problem can be mediated by multiple vertically displaced instruments measuring the relevant parameters.

Anisotropy in the Atmosphere

The anisotropy of a turbulent flow is inferred by two invariants η and ξ of the normalized anisotropy tensor. The anisotropy tensor and the invariants in Sec. 4.3 are derived from a high-pass filtered velocity field, which is probed by a sonic anemometer. The sonic anemometer has a limited spatial resolution of $\sim 10\,\mathrm{cm}$, which is insufficient to resolve dissipative scales. However, most of the kinetic energy is stored in large scales (cf. Eq. (4.21) and Fig. 4.32B) so that the sonic anemometer is suited to experimentally measure the (large-scale) anisotropy of turbulent flows in the atmosphere. As the normalized anisotropy is related to the Reynolds stress tensor, it is important that the co-variance estimates $\langle u_i' u_j' \rangle$ are converged. This is achieved by either considering the entire velocity time-record or by choosing the averaging window $\tau = 1800\,\mathrm{s}$ compromising between statistical convergence and unsteady-forcing due to diurnal cycle (cf. Sec. 4.1.2). The cutoff frequency of $f_c = 0.5\,\mathrm{Hz}$ due to platform motion-related filtering corresponds to a scale $l \sim U/f_c \sim 20\,\mathrm{m}$, which is smaller than the average integral length scales of the bulk (Table 4.1).

Measurements in atmospheric flows under various conditions have been conducted revealing that turbulence universally returns to isotropy at scales smaller than the energy-injection scales [206]. However, perfect isotropy in inhomogeneous flows is not expected [5]. In DNS of shear-released turbulence, it has been shown that the flow returns to isotropy on a time scale similar to the large-eddy turnover time [207]. Concerning bulk turbulence characteristics of the marine trade-wind boundary layer, integral and energy injection scales are on the order of magnitude of $\sim 100\,\mathrm{m}$ suggesting isotropic turbulence of scales smaller than 20 m. This is confirmed by balloon-borne measurements with the (tether-mounted) mini-MPCK as shown in Fig. 4.15B. Additionally, this is supported by mean scaling exponents of the longitudinal second-order structure function $D_{LL}(r)$ in the inertial sub-range, which are following K62-scaling ($\zeta_2 = 2/3 + 1/36$). Furthermore, the experimentally obtained invariants derived from the entire velocity time-record are in accordance with invariants inferred from single snapshots of DNS of homogeneous isotropic turbulence. The small-scale isotropy of scales below 20 m is highly relevant for the application of DNS of homogeneous isotropic turbulence suggesting that DNS of homogeneous isotropic turbulence is a useful tool to study atmospheric small-scale processes. Furthermore, it allows for invoking Kolmogorov's phenomenology to infer the energy dissipation rate from velocity statistics.

5.1.2 Cloud droplet statistics

The motivation for characterizing cloud turbulence is to quantify cloud droplet-turbulence interactions at small scales in both non-precipitating and precipitating clouds. The cloud droplet population can be characterized in terms of the cloud droplet size distribution involving quantities like the cloud droplet number concentration. In the following, the main emphasis is discussing the cloud droplet number concentration, the cloud droplet Stokes number St as well as the non-dimensional settling velocity parameter Sv and the spatial distribution of cloud droplets.

One of the most fundamental cloud characteristics is the cloud droplet number concentration n. The cloud number concentration impacts the super-saturation field and thus feedbacks on cloud droplet growth (Sec. 1.3.1). Cloud droplet activation at the cloud base, entrainment and mixing at the cloud edge and cloud droplet evaporation at the cloud top change the cloud droplet number concentration n [208]. Measuring cloud droplet number concentration n by remote sensing is accompanied by uncertainties of more than 50% [208] highlighting the importance of measuring n *in situ*. During EUREC^{4}A , the cloud droplet number concentration n spans three orders of magnitude. Even in cloud-free air, the number concentration does not vanish. In consequence, the CDPs sampled at least one cloud droplet, which causes a cloud droplet number concentration of $n = 1/(uA\Delta t) \approx 0.6/\mathrm{cm}^3$ with $u \sim 10\,\mathrm{m/s}$, $A \approx 0.3\,\mathrm{mm}$ and $\Delta t = 0.5\,\mathrm{s}$. Hence, $n = 0.6/\mathrm{cm}^3$ is the lower bound of PDF(n) as shown in Fig. 4.17.

Furthermore, n decreases sharply before $n = 10/\mathrm{cm}^3$, which is followed by a plateau indicating that number concentrations $n > 10/\mathrm{cm}^3$ are measured inside clouds. This threshold is somewhat arbitrary as it could be chosen also slightly higher. However, as future research involves cloud edge entrainment and mixing, it is important to capture the cloud edge fully. Hence, the minimal cloud threshold is suitable.

Furthermore, the cumulative number concentration provides inside into the altitude dependence of the droplet size distribution (cf. Fig. 4.18). Classifying cloud regions or clouds by the distance from the top of the boundary layer is crude. The accuracy of determining TBL is on the order of 100 m. Additionally, the altitude ranges ($0.8 < z_{\mathrm{PSS8}}/\mathrm{TBL} < 1.2$ and $1.2 < z_{\mathrm{PSS8}}/\mathrm{TBL} < 1.6$) are about 280 m deep for $\mathrm{TBL} \sim 700\,\mathrm{m}$. Hence, the first altitude range might already contain shallow cumulus clouds entirely because of their limited vertical extent on the order of a few 100 m. In the future, altitude regimes could be refined by taking into account simultaneous Radar data and determining the cloud base more accurately.

Despite the rough altitude ranges, bulk properties of clouds are still expected to emerge. At the cloud base, cloud droplets are activated and the time to grow by condensation is limited. Therefore, cloud droplets with a diameter $d_p \geq 20\,\mu\mathrm{m}$ are rare and about 75% of the cloud droplets are even smaller than 10 µm in diameter in the majority of the clouds. In consequence, inertial effects are negligible for droplets with $d_p \leq 10\,\mu\mathrm{m}$ as captured by $\mathrm{St} \propto d_p^2 \sim 0.001$ in case of moderate energy dissipation $\epsilon \sim 1 \times 10^{-3}\,\mathrm{W/kg}$. These cloud droplets behave like tracers following the turbulent flow nearly instantaneously. In case of higher $\epsilon \sim 1 \times 10^{-2}\,\mathrm{W/kg}$, $\mathrm{St} \propto d_p^2 \sim 0.01$, which might be sufficient for initiating cloud voids [39]. Cloud droplets with diameters $d_p \geq 20\,\mu\mathrm{m}$ are more likely to be encountered at larger distances from the cloud base in the altitude regime $1.2 < z_{\mathrm{PSS8}}/\mathrm{TBL}$. Despite that they are rare, these droplets ($d_p \geq 20\,\mu\mathrm{m}$ and $St \sim 0.1$ for $\epsilon \sim 1 \times 10^{-2}\,\mathrm{W/kg}$) are in a regime where sling events can be locally expected [28, 61]. Therefore, these rare but large droplets, being of utmost interest for studying cloud droplet-turbulence interaction, are most likely to encounter 400 m or higher above the cloud base.

It has been established that estimating the energy dissipation rate *in-situ* comes along with difficulties, which can either be mediated or, at least, quantified. Both the cloud droplet Stokes number St as well as the non-dimensional settling velocity parameter Sv depend on the energy dissipation rate. Practically, the energy dissipation rate is an intermittent quantity and can locally fluctuate by more than an order of magnitude depending on R_λ [5]. Therefore, both St and Sv vary locally. Here, the local mean energy dissipation rate is invoked to calculate St and Sv. Invoking Gaussian error propagation, the relative error of $\mathrm{St} \propto \epsilon^{1/2}$ due to the uncertainty in the energy dissipation rate is given by $\delta_\epsilon/2$. Assuming that the error of the local mean energy dissipation rate is $\delta_\epsilon \approx 22\%$, the relative error of St is 11%. Hence, $\mathrm{St} > 0.12$ can be considered to be significantly larger than 0.1. Similarly, the relative error of $\mathrm{Sv} \propto \epsilon^{-1/4}$ due to the uncertainty in the energy dissipation rate is given by $\delta_\epsilon/4$. It follows that the relative error of Sv is 5.5% due to the error of the local mean energy dissipation rate of $\delta_\epsilon \approx 22\%$.

The Sv-St parameter space can be partitioned into four regimes (cf. Figs. 4.20B and 4.26). Regime 1 ($\mathrm{St} < 0.1$, $\mathrm{Sv} < 1$) can be identified as the "tracer" regime. Regime 2 ($\mathrm{St} < 0.1$, $\mathrm{Sv} > 1$) is dominated by gravitation so that (large) cloud droplets sediment on average. In regime 3 ($\mathrm{St} > 0.1$, $\mathrm{Sv} < 1$), inertial effects presumably dominate over gravitation, which is why clustering or even sling events are expected. It is possible, though, that cloud droplets are accelerated downward by vortices, which is known as preferential sweeping [4]. Cloud droplets in regime 4 ($\mathrm{St} > 0.1$, $\mathrm{Sv} > 1$) are large with $d_p \approx 16\,\mu\mathrm{m}$ on average and a few droplets larger than $30\,\mu\mathrm{m}$ in diameter. For high enough Sv, the gravitational collection takes place in regimes 2 and 4. As the non-dimensional settling velocity is still moderate ($\mathcal{O}(\mathrm{Sv}) \sim 1$), it remains questionable whether regime 4 is also associated with preferential sweeping. In a rain event, both regimes 3 and 4 are populated suggesting that both droplet inertia and gravity play an important role in the onset of precipitation. Due to the high accuracy in St and Sv, these results are considered to be significant. It is important to note that the classification of the St-Sv parameter space is most likely not complete, which is due to the size range of the CDPs ($d_p \geq 50\,\mu\mathrm{m}$). As an example, drizzle droplets with $d_p \gtrsim 100\,\mu\mathrm{m}$ have Stokes numbers $\mathrm{St} \gg 1$ in case of $\epsilon \sim 1 \times 10^{-2}\,\mathrm{W/kg}$ leading to significant particle motion relative to the flow.

-particle distances, which is related to lower cloud droplet number concentration n (Fig. 4.28).

Lastly, the accuracy of Δr scales with turbulence intensity. As the turbulence intensity is 7% on average, the error is expected to be small. Another source of measurement error in Δr is the one-dimensional projection [e.g. 62]. In the case of CDP-2, the length of the measurement volume is $\sim \sqrt{A} \approx 0.5\,\mathrm{mm}$ with $A \approx 0.3\,\mathrm{mm}$. This is smaller than the Kolmogorov length scale which is why the effect of one-dimensional projection and finite measurement volume for inter-particle distances $\sim 1\,\mathrm{cm}$ is considered to be small, too. Hence, the strong indications for cloud voids are significant.

5.2 Outlook

In the future, more data analysis and further experiments will provide more insight into cloud microphysical and atmospheric small-scale processes. Here, the focus is mainly on further analysis of cloud droplet statistics.

It has been shown that the Sv-St parameter space is altitude dependent by conditioning individual droplets on altitude regimes. These altitude regimes are related to the depth of the boundary layer. As this estimate is crude and accurate to $\sim 100\,\mathrm{m}$, better results might be obtained by extracting the cloud base from remote sensing data such as Radar reflectivity. Although the information is contained in different altitude regimes as well, a more direct and insightful measure might be cloud depth. It is expected that cloud droplets in deeper clouds have more time to grow by condensation in updrafts. As larger droplets result in larger St and Sv in case of equal energy dissipation rates, it would be interesting to illustrate the Sv-St parameter space as a function of cloud depth. The cloud depth is further affected by the convective activity of the cloud, hence the cloud evolution stage. The latter is determined as a function of vertical velocity and buoyancy [79, e.g.], where both variables have to be taken into account to determine the influence of the cloud evolution stage on the Sv-St diagram. This would link inertial to large-scale processes to the cloud droplet scale, which could hint at their relative importance in warm rain initiation. More events of warm rain have to be analyzed in order to support the conclusions drawn in the scope of this thesis. As warm-rain initiation is associated with rare events, more data is highly welcome.

It has been hypothesized that cloud droplets in regime $\mathrm{Sv} > 1$ pertain to $\mathrm{St} > 0.1$ preferentially fall through strain-dominated regions of the turbulent flow where they collide and coalesce with other cloud droplets. To test this hypothesis, it is favorable to invoke imaging technology such as holography. One requirement is the ability to track particles. Estimating the local energy dissipation rate, given the cloud droplet sizes at each 3D location by holography and applying a tracking algorithm yields cloud droplet paths together with St. Regions of strong vorticity can be identified by regions devoid of cloud droplets. The remaining volume is assumed to be strain dominated. Alternatively, in the presence of small cloud droplets with $\mathrm{St} < 0.01$, these particles can be interpreted as tracers to visualize the flow field. Then, shear can possibly be visualized directly.

The unoccupied region for $\mathrm{St} \lesssim 0.1$ in Fig. 4.20B remains an open question. It might be related to cloud depth because convective, hence deeper clouds, are thought to be more turbulent than shallow clouds. In consequence, one might hypothesize a transition in turbulence level, which is expressed by higher energy dissipation rates. Another reason could be that St depends more stronger on the energy dissipation rate ϵ than Sv. Hence, in low turbulent regions of the cloud such as the cloud base, the cloud droplet motion is dominated by gravity.

In general, a higher resolved local mean energy dissipation rate would be desirable. The only well-suited method to estimate the energy dissipation rate of atmospheric flows based on very short averaging windows, say on a second scale, is the gradient method. Despite its fragility to experimental limitations and imperfections, it converges the fastest. However, the gradient method requires isotropic turbulence, which is generally approximately fulfilled at small scales, and high spatio-temporal resolution below the Kolmogorov scales. Hot-wire measurements with a sampling frequency of at least $\sim 10\,\mathrm{kHz}$ [131] are able to deliver such high-resolution measurements of velocity fluctuations under ideal conditions. In practice, that means low electrical noise, perfect alignment with the mean wind direction and low turbulence intensity. Under ideal conditions and given that the Kolmogorov scales of the flow can be resolved, the hot-wire measurements would allow for determining St and Sv based on more localized energy dissipation rate estimates that better reflect intermittent effects of the flow.

Another important parameter is the super-saturation, which is very challenging to measure *in-situ* and yet more difficult to resolve down to dissipative scales, i.e. the ambient of individual cloud droplets. Quantifying the super-saturation fluctuations at dissipative scales would yield valuable insight into the condensational growth of individual cloud droplets. Especially at the cloud edge and at the cloud top, which is affected by entrainment processes, super-saturation might fluctuate strongly. Moreover, these measurements are of great importance to prove concepts of convective ripening and large-eddy hopping by *in-situ* measurements. However, direct experimental verification requires following droplets along their trajectory.

5.3 Summary

To investigate cloud microphysics and atmospheric turbulence in the trade-wind region, balloon-borne *in-situ* measurements with two specially developed instruments are conducted during the EUREC^{4}A field campaign in the Caribbean from January to February 2020 in the trade-wind region upstream of Barbados over the Atlantic ocean. *In-situ* measurements were conducted aboard two Research Vessels (RV), namely RV Maria S. Merian and RV Meteor where one MPCK+ and one mini-MPCK were deployed on RV Maria S. Merian and one mini-MPCK on RV Meteor. Both instruments, the Max-Planck-Cloudkite+ (MPCK+) and the mini-Max-Planck-Cloudkite (mini-MPCK), are carried by helikites, a helium-filled and kite-stabilized balloon. The helikites carrying one of these instruments, i.e. MPCK+ or mini-MPCK, at a time are launched from the back of the RV Maria S. Merian and RV Meteor, respectively. During EUREC^{4}A field campaign, both instruments recorded 197 h of scientific data in total, out of which 144 h comprise cloud droplet records. During EUREC^{4}A , the helikites performed a variety of flight patterns, among which staircase flights and constant altitude flights were the most frequent. Additionally, measurements were conducted over the entire diurnal cycle with the longest continuous flight of 20 h.

Both cloud droplet characteristics such as the Stokes number St and the non-dimensional settling velocity parameter as well as many turbulence features depend on the mean energy dissipation rate. Therefore, the mean energy dissipation is identified as a central quantity, which is estimated from one-dimensional time-records of the longitudinal velocity. To quantify the accuracy of different methods, among which are the gradient method ϵ_G, the 2nd-order SF (inertial range) method ϵ_{I2}, and the scaling argument ϵ_L, each method is compared to the ground-truth of DNS of homogeneous isotropic turbulence with Reynolds numbers in the range $74 \leq \mathrm{R}_\lambda \leq 321$. In addition, the effect of finite turbulence intensity, misalignment and finite averaging window is assessed. The Reynolds number dependency of the averaging window is investigated with the help of high-resolution one-dimensional velocity measurements in the VDTT wind tunnel with Reynolds numbers in the range $147 \leq \mathrm{R}_\lambda \leq 5864$. In conditions of low turbulence intensity, each method was able to reproduce the global mean energy dissipation on average. However, each method overestimates the ground-truth energy dissipation rate for finite turbulence intensity. Furthermore, misalignment between the probe and the longitudinal direction results in systematic overestimation. In both cases, the 2nd-order SF (inertial range) method ϵ_{I2} is the least affected. However, it has been found that the gradient method ϵ_G converges at least 4 to 5 times faster than

ϵ_{I2}. Due to the robustness of ϵ_{I2}, this method is used to obtain the (local) mean energy dissipation rate from airborne *in-situ* velocity measurements.

To justify the application of the 2nd-order SF (inertial range) method ϵ_{I2} relying on K41, the flow has to be statistically locally isotropic. Therefore, isotropy of length scales below 20 m has been assessed for a high-pass filtered velocity time-record in the platform frame of reference in terms of two invariants of the normalized anisotropy tensor a_{ij} in the Lumley triangle. The comparison to velocity measurements of virtual probes in DNS of homogeneous isotropic turbulence reveals that the flow is statistically and locally isotropic. It is concluded that ϵ_{I2} can be invoked to estimate the mean energy dissipation rate.

Furthermore, the presence of turbulence in the sub-cloud layer and cloud layer was assessed as a function of the Richardson number. Despite that its estimate is rough, the Richardson number rarely exceeds the value of 1 in the lowest 40% of the sub-cloud layer. Close to the top of the boundary layer, which is inferred from the inversion of virtual potential temperature, Ri-values range from negative to about 10 suggesting large-scale variability of atmospheric stratification. In the middle of the sub-cloud layer, Richardson numbers are mostly positive. Overall, turbulence is present in the sub-cloud layer, which is well-mixed most of the time and sampled locations. Turbulence features in the bulk atmosphere have been summarized for an averaging window of $\tau = 1800\,\mathrm{s}$ in Tables 4.1 and 4.8 as well as for the cloud-free atmosphere and inside clouds with an averaging window of $\tau = 60\,\mathrm{s}$ in Tables 4.4 and 4.3, respectively. Generally, the local mean energy dissipation rate was two times higher in clouds than in cloud-free air.

Cloud droplet - turbulence interaction is captured in terms of the Stokes number and the non-dimensional settling velocity parameter Sv. The Sv-St parameter space spans about four orders of magnitude for both parameters and has been classified into four regimes. These regimes can be loosely described by tracers (1), gravitational settling in low turbulence (2), preferential sweeping (3) and gravitational settling in high turbulence (4). The two latter regimes appear predominantly at larger vertical distances from the cloud base, i.e. in deeper clouds. This is related to the fact that the likelihood to encounter cloud droplets larger than 30 µm increases with distance from the cloud base. In addition, regimes 3 and 4 are populated in precipitating clouds where 1% of cloud droplet Stokes numbers had Stokes number $\mathrm{St} > 0.1$ in one rain event. Regimes 1 and 2 are occupied by all altitude regimes as droplets with $d_p < 10\,\mu\mathrm{m}$ exist at all altitudes. Furthermore, regimes 1 and 2 are populated by small cloud droplets in rainy clouds as well as by all cloud droplets in non-precipitating clouds. Statistically, the inter-particle distance of cloud droplets in the cloud core deviates from a Poisson distribution where inter-particle distances at $60\eta_K$ are more likely than expected by a scaled Poisson distribution suggesting for cloud voids. Cloud voids cause an inhomogeneous spatial distribution of cloud droplets in space. In the future, a more detailed analysis of three-dimensional cloud droplet position as well as conditional statistics on cloud evolution stages and different regions in a cloud promise further insight into cloud droplet spatial distributions.

References

[1] A. P. Siebesma, S. Bony, C. Jakob, and B. Stevens. *Clouds and Climate: Climate Science's Greatest Challenge.* Cambridge University Press, 2020.

[2] R. A. Houze Jr. *Cloud dynamics.* Academic press, 2014.

[3] E. Bodenschatz, S. P. Malinowski, R. A. Shaw, and F. Stratmann. "Can we understand clouds without turbulence?" In: *Science* 327.5968 (2010), pp. 970–971.

[4] B. Devenish, P. Bartello, J.-L. Brenguier, L. Collins, W. W. Grabowski, R. IJzermans, S. P. Malinowski, M. Reeks, J. Vassilicos, L.-P. Wang, et al. "Droplet growth in warm turbulent clouds". In: *Quarterly Journal of the Royal Meteorological Society* 138.667 (2012), pp. 1401–1429.

[5] S. B. Pope. *Turbulent flows.* Cambridge University Press, 2000.

[6] S. Bony, B. Stevens, F. Ament, S. Bigorre, P. Chazette, S. Crewell, J. Delanoë, K. Emanuel, D. Farrell, C. Flamant, et al. "EUREC4A: A field campaign to elucidate the couplings between clouds, convection and circulation". In: *Surveys in Geophysics* 38.6 (2017), pp. 1529–1568.

[7] J. S. Malkus. *On the structure of the trade wind moist layer.* Massachusetts Institute of Technology and Woods Hole Oceanographic Institution, 1958.

[8] H. Siebert, M. Beals, J. Bethke, E. Bierwirth, T. Conrath, K. Dieckmann, F. Ditas, A. Ehrlich, D. Farrell, S. Hartmann, et al. "The fine-scale structure of the trade wind cumuli over Barbados–an introduction to the CARRIBA project". In: (2013).

[9] R. Vogel, A. L. Albright, J. Vial, G. George, B. Stevens, and S. Bony. "Strong cloud-circulation coupling explains weak trade cumulus feedback". In: *Authorea Preprints* (2022).

[10] S. Bony, M. Lothon, J. Delanoë, P. Coutris, J.-C. Etienne, F. Aemisegger, A. L. Albright, T. André, H. Bellec, A. Baron, et al. "EUREC 4 A observations from the SAFIRE ATR42 aircraft". In: *Earth System Science Data* 14.4 (2022), pp. 2021–2064.

[11] B. Stevens. "On the growth of layers of nonprecipitating cumulus convection". In: *Journal of the atmospheric sciences* 64.8 (2007), pp. 2916–2931.

[12] S. Bony, B. Stevens, D. M. Frierson, C. Jakob, M. Kageyama, R. Pincus, T. G. Shepherd, S. C. Sherwood, A. P. Siebesma, A. H. Sobel, et al. "Clouds, circulation and climate sensitivity". In: *Nature Geoscience* 8.4 (2015), pp. 261–268.

[13] J. Vergara-Temprado, A. K. Miltenberger, K. Furtado, D. P. Grosvenor, B. J. Shipway, A. A. Hill, J. M. Wilkinson, P. R. Field, B. J. Murray, and K. S. Carslaw. “Strong control of Southern Ocean cloud reflectivity by ice-nucleating particles”. In: *Proceedings of the National Academy of Sciences* 115.11 (2018), pp. 2687–2692.

[14] S. Bony and J.-L. Dufresne. “Marine boundary layer clouds at the heart of tropical cloud feedback uncertainties in climate models”. In: *Geophysical Research Letters* 32.20 (2005).

[15] J. Starr Malkus. “Some results of a trade-cumulus cloud investigation”. In: *Journal of Meteorology* 11.3 (1954), pp. 220–237.

[16] B. Davidson. “The Barbados oceanographic and meteorological experiment”. In: *Bulletin of the American Meteorological Society* 49.9 (1968), pp. 928–935.

[17] E. Augstein, H. Riehl, F. Ostapoff, and V. Wagner. “Mass and energy transports in an undisturbed Atlantic trade-wind flow”. In: *Monthly Weather Review* 101.2 (1973), pp. 101–111.

[18] R. M. Rauber, B. Stevens, H. T. Ochs III, C. Knight, B. A. Albrecht, A. Blyth, C. Fairall, J. Jensen, S. Lasher-Trapp, O. Mayol-Bracero, et al. “Rain in shallow cumulus over the ocean: The RICO campaign”. In: *Bulletin of the American Meteorological Society* 88.12 (2007), pp. 1912–1928.

[19] I. Langmuir. “The production of rain by a chain reaction in cumulus clouds at temperatures above freezing”. In: *Journal of the Atmospheric Sciences* 5.5 (1948), pp. 175–192.

[20] W. W. Grabowski and L.-P. Wang. “Growth of cloud droplets in a turbulent environment”. In: *Annual review of fluid mechanics* 45 (2013), pp. 293–324.

[21] H. Pruppacher and J. Klett. *Microphysics of Clouds and Precipitation.* 18th ed. Atmospheric and Oceanographic Sciences Library. Springer Netherlands, 2010.

[22] K. Lau and H. Wu. “Warm rain processes over tropical oceans and climate implications”. In: *Geophysical Research Letters* 30.24 (2003).

[23] R. A. Shaw. “Particle-turbulence interactions in atmospheric clouds”. In: *Annual Review of Fluid Mechanics* 35.1 (2003), pp. 183–227.

[24] M. Wilkinson. “Convective ripening and initiation of rainfall”. In: *EPL (Europhysics Letters)* 108.4 (2014), p. 49001.

[25] S. Bera, S. Chowdhuri, and T. V. Prabha. “A new methodology for the statistical descriptions of Particle-by-Particle measurements of liquid droplets in cumulus clouds”. In: *Quarterly Journal of the Royal Meteorological Society* 148.743 (2022), pp. 842–859.

[26] A. Pumir and M. Wilkinson. “Collisional aggregation due to turbulence”. In: *Annual Review of Condensed Matter Physics* 7 (2016), pp. 141–170.

[27] S. Glienke, A. B. Kostinski, R. A. Shaw, M. L. Larsen, J. P. Fugal, O. Schlenczek, and S. Borrmann. “Holographic observations of centimeter-scale nonuniformities within marine stratocumulus clouds”. In: *Journal of the Atmospheric Sciences* 77.2 (2020), pp. 499–512.

[28] G. P. Bewley, E.-W. Saw, and E. Bodenschatz. "Observation of the sling effect". In: *New Journal of Physics* 15.8 (2013), p. 083051.

[29] A. Muschinski and D. H. Lenschow. "Future directions for research on meter- and submeter-scale atmospheric turbulence". In: *Bulletin of the American Meteorological Society* 82.12 (2001), pp. 2831–2843.

[30] M. Wilkinson. "Large deviation analysis of rapid onset of rain showers". In: *Physical review letters* 116.1 (2016), p. 018501.

[31] Z. Warhaft. "Turbulence in nature and in the laboratory". In: *Proceedings of the National Academy of Sciences* 99.suppl 1 (2002), pp. 2481–2486.

[32] D. Buaria, A. Pumir, and E. Bodenschatz. "Generation of intense dissipation in high Reynolds number turbulence". In: *Philosophical Transactions of the Royal Society A* 380.2218 (2022), p. 20210088.

[33] F. Hoffmann, H. Siebert, J. Schumacher, T. Riechelmann, J. KATzwINkEL, B. Kumar, P. GöTzFRIED, and S. Raasch. "Entrainment and mixing at the interface of shallow cumulus clouds: Results from a combination of observations and simulations". In: *Meteorologische Zeitschrift 23 (2014)* 23.4 (2014), pp. 349–368.

[34] M. Pinsky, E. Eytan, I. Koren, O. Altaratz, and A. Khain. "Convective and turbulent motions in nonprecipitating Cu. Part I: Method of separation of convective and turbulent motions". In: *Journal of the Atmospheric Sciences* 78.7 (2021), pp. 2307–2321.

[35] M. Pinsky, E. Eytan, I. Koren, and A. Khain. "Convective and turbulent motions in nonprecipitating Cu. Part II: LES simulated cloud represented by a starting plume". In: *Journal of the Atmospheric Sciences* 79.3 (2022), pp. 793–813.

[36] E. Bodenschatz, G. P. Bewley, H. Nobach, M. Sinhuber, and H. Xu. "Variable density turbulence tunnel facility". In: *Review of Scientific Instruments* 85.9 (2014), p. 093908.

[37] G. Bagheri, F. Nordsiek, P. Höhne, O. Schlenczek, M. Schröder, T. Neumann, and E. Bodenschatz. "CloudKite Airborne Atmospheric Measurement Platform: MPCK+". in prep. 2023.

[38] B. Stevens, S. Bony, D. Farrell, F. Ament, A. Blyth, C. Fairall, J. Karstensen, P. K. Quinn, S. Speich, C. Acquistapace, et al. "EUREC 4 A". In: *Earth System Science Data Discussions* (2021), pp. 1–78.

[39] K. Karpińska, J. F. Bodenschatz, S. P. Malinowski, J. L. Nowak, S. Risius, T. Schmeissner, R. A. Shaw, H. Siebert, H. Xi, H. Xu, et al. "Turbulence-induced cloud voids: observation and interpretation". In: *Atmospheric Chemistry and Physics* 19.7 (2019), pp. 4991–5003.

[40] R. B. Stull. *An introduction to boundary layer meteorology.* Vol. 13. Springer Science & Business Media, 1988.

[41] J. C. Wyngaard. *Turbulence in the Atmosphere.* Cambridge University Press, 2010.

[42] P. A. Davidson. *Turbulence: an introduction for scientists and engineers.* Oxford university press, 2015.

[43] A. Kolmogorov. “The Local Structure of Turbulence in Incompressible Viscous Fluid for Very Large Reynolds’ Numbers”. In: *Akademiia Nauk SSSR Doklady.* Vol. 30. 1941, pp. 301–305.

[44] A. N. Kolmogorov. “Dissipation of energy in the locally isotropic turbulence”. In: *Proceedings of the Royal Society of London. Series A: Mathematical and Physical Sciences* 434.1890 (1991), pp. 15–17.

[45] H. Robertson. “The invariant theory of isotropic turbulence”. In: *Mathematical Proceedings of the Cambridge Philosophical Society.* Vol. 36. 2. Cambridge University Press. 1940, pp. 209–223.

[46] G. K. Batchelor. *The theory of homogeneous turbulence.* Cambridge university press, 1953.

[47] K. R. Sreenivasan. “An update on the energy dissipation rate in isotropic turbulence”. In: *Physics of Fluids* 10.2 (1998), pp. 528–529.

[48] K. R. Sreenivasan and R. Antonia. “The phenomenology of small-scale turbulence”. In: *Annual review of fluid mechanics* 29.1 (1997), pp. 435–472.

[49] A. N. Kolmogorov. “A refinement of previous hypotheses concerning the local structure of turbulence in a viscous incompressible fluid at high Reynolds number”. In: *Journal of Fluid Mechanics* 13.1 (1962), pp. 82–85.

[50] J. R. Garratt. “The atmospheric boundary layer”. In: *Earth-Science Reviews* 37.1-2 (1994), pp. 89–134.

[51] M. A. LeMone, W. M. Angevine, C. S. Bretherton, F. Chen, J. Dudhia, E. Fedorovich, K. B. Katsaros, D. H. Lenschow, L. Mahrt, E. G. Patton, et al. “100 years of progress in boundary layer meteorology”. In: *Meteorological Monographs* 59 (2019), pp. 9–1.

[52] S. P. Malinowski, H. Gerber, J.-L. Plante, M. Kopec, W. Kumala, K. Nurowska, P. Chuang, D. Khelif, K. Haman, et al. “Physics of Stratocumulus Top (POST): turbulent mixing across capping inversion”. In: *Atmospheric Chemistry and Physics* 13.24 (2013), pp. 12171–12186.

[53] I. H. Bell, J. Wronski, S. Quoilin, and V. Lemort. “Pure and Pseudo-pure Fluid Thermophysical Property Evaluation and the Open-Source Thermophysical Property Library CoolProp”. In: *Industrial & Engineering Chemistry Research* 53.6 (2014), pp. 2498–2508. doi: 10.1021/ie4033999. eprint: http://pubs.acs.org/doi/pdf/10.1021/ie4033999.

[54] S. Risius, H. Xu, F. Di Lorenzo, H. Xi, H. Siebert, R. Shaw, and E. Bodenschatz. “Schneefernerhaus as a mountain research station for clouds and turbulence”. In: (2015).

[55] J. C. Wyngaard. “Atmospheric turbulence”. In: *Annual Review of Fluid Mechanics* 24.1 (1992), pp. 205–234.

[56] D. Lenschow, J. Mann, and L. Kristensen. “How long is long enough when measuring fluxes and other turbulence statistics?” In: *Journal of Atmospheric and Oceanic Technology* 11.3 (1994), pp. 661–673.

[57] D. Lenschow, J. Mann, and L. Kristensen. “How long is long enough when measuring fluxes and other turbulence statistics?” In: *Journal of Atmospheric and Oceanic Technology* 11.3 (1994), pp. 661–673.

[58] P. Prabhakaran, A. S. M. Shawon, G. Kinney, S. Thomas, W. Cantrell, and R. A. Shaw. “The role of turbulent fluctuations in aerosol activation and cloud formation”. In: *Proceedings of the National Academy of Sciences* 117.29 (2020), pp. 16831–16838.

[59] O. Schlenczek. “Airborne and ground-based holographic measurement of hydrometeors in liquid-phase, mixed-phase and ice clouds”. PhD thesis. Universitätsbibliothek Mainz, 2018.

[60] M. R. Maxey and J. J. Riley. “Equation of motion for a small rigid sphere in a nonuniform flow”. In: *The Physics of Fluids* 26.4 (1983), pp. 883–889.

[61] T. Bätge, I. Fouxon, and M. Wilczek. “Quantitative prediction of sling events in turbulence at high Reynolds numbers”. In: *arXiv preprint arXiv:2208.05384* (2022).

[62] K. Lehmann, H. Siebert, M. Wendisch, and R. A. Shaw. “Evidence for inertial droplet clustering in weakly turbulent clouds”. In: *Tellus B: Chemical and Physical Meteorology* 59.1 (2007), pp. 57–65.

[63] A. B. Kostinski and R. A. Shaw. “Fluctuations and luck in droplet growth by coalescence”. In: *Bulletin of the American Meteorological Society* 86.2 (2005), pp. 235–244.

[64] M. Pinsky, A. Khain, and M. Shapiro. “Collision efficiency of drops in a wide range of Reynolds numbers: Effects of pressure on spectrum evolution”. In: *Journal of the atmospheric sciences* 58.7 (2001), pp. 742–764.

[65] B. Stevens and S. Bony. “What are climate models missing?” In: *Science* 340.6136 (2013), pp. 1053–1054.

[66] E. Bodenschatz. “Clouds resolved”. In: *Science* 350.6256 (2015), pp. 40–41.

[67] T. Schmeissner, R. Shaw, J. Ditas, F. Stratmann, M. Wendisch, and H. Siebert. “Turbulent mixing in shallow trade wind cumuli: Dependence on cloud life cycle”. In: *Journal of the Atmospheric Sciences* 72.4 (2015), pp. 1447–1465.

[68] J. Vial, S. Bony, B. Stevens, and R. Vogel. “Mechanisms and model diversity of trade-wind shallow cumulus cloud feedbacks: a review”. In: *Shallow Clouds, Water Vapor, Circulation, and Climate Sensitivity.* Springer, 2017, pp. 159–181.

[69] M. Satoh, B. Stevens, F. Judt, M. Khairoutdinov, S.-J. Lin, W. M. Putman, and P. Düben. “Global cloud-resolving models”. In: *Current Climate Change Reports* 5.3 (2019), pp. 172–184.

[70] J.-P. Mellado, C. Bretherton, B. Stevens, and M. Wyant. “DNS and LES for simulating stratocumulus: Better together”. In: *Journal of Advances in Modeling Earth Systems* 10.7 (2018), pp. 1421–1438.

[71] J. Mellado. “Using numerical simulations to study the atmospheric boundary layer”. In: *ERCOFTAC Workshop Direct and Large Eddy Simulation.* Springer. 2020, pp. 1–10.

[72] G. Matheou and J. Teixeira. “Sensitivity to physical and numerical aspects of large-eddy simulation of stratocumulus”. In: *Monthly Weather Review* 147.7 (2019), pp. 2621–2639.

[73] V. Dixit, L. Nuijens, and K. C. Helfer. “Counter-gradient momentum transport through subtropical shallow convection in ICON-LEM simulations”. In: *Journal of Advances in Modeling Earth Systems* 13.6 (2021), e2020MS002352.

[74] K. Chang, J. Bench, M. Brege, W. Cantrell, K. Chandrakar, D. Ciochetto, C. Mazzoleni, L. Mazzoleni, D. Niedermeier, and R. Shaw. “A laboratory facility to study gas–aerosol–cloud interactions in a turbulent environment: The Π chamber”. In: *Bulletin of the American Meteorological Society* 97.12 (2016), pp. 2343–2358.

[75] B. Rousset, P. Bonnay, P. Diribarne, A. Girard, J.-M. Poncet, E. Herbert, J. Salort, C. Baudet, B. Castaing, L. Chevillard, et al. “Superfluid high REynolds von Kármán experiment”. In: *Review of Scientific Instruments* 85.10 (2014), p. 103908.

[76] H. Morrison, M. van Lier-Walqui, A. M. Fridlind, W. W. Grabowski, J. Y. Harrington, C. Hoose, A. Korolev, M. R. Kumjian, J. A. Milbrandt, H. Pawlowska, et al. “Confronting the challenge of modeling cloud and precipitation microphysics”. In: *Journal of advances in modeling earth systems* 12.8 (2020), e2019MS001689.

[77] J. Jiménez. “Computing high-Reynolds-number turbulence: will simulations ever replace experiments?” In: *Journal of Turbulence* 4.1 (2003), p. 022.

[78] B. Stevens and D. H. Lenschow. “Observations, experiments, and large eddy simulation”. In: *Bulletin of the American Meteorological Society* 82.2 (2001), pp. 283–294.

[79] J. Katzwinkel, H. Siebert, T. Heus, and R. A. Shaw. “Measurements of turbulent mixing and subsiding shells in trade wind cumuli”. In: *Journal of the Atmospheric Sciences* 71.8 (2014), pp. 2810–2822.

[80] K. Lehmann, H. Siebert, and R. A. Shaw. “Homogeneous and inhomogeneous mixing in cumulus clouds: Dependence on local turbulence structure”. In: *Journal of the Atmospheric Sciences* 66.12 (2009), pp. 3641–3659.

[81] G. Bertens, G. Bagheri, H. Xu, E. Bodenschatz, and J. Moláček. “In situ cloud particle tracking experiment”. In: *Review of Scientific Instruments* 92.12 (2021), p. 125105.

[82] A. Peña. “Østerild: A natural laboratory for atmospheric turbulence”. In: *Journal of Renewable and Sustainable Energy* 11.6 (2019), p. 063302.

[83] O. Schlenczek, J. P. Fugal, G. Lloyd, K. N. Bower, T. W. Choularton, M. Flynn, J. Crosier, and S. Borrmann. “Microphysical properties of ice crystal precipitation and surface-generated ice crystals in a High Alpine environment in Switzerland”. In: *Journal of Applied Meteorology and Climatology* 56.2 (2017), pp. 433–453.

[84] B. R. Dhruva. “An experimental study of high Reynolds number turbulence in the atmosphere.” In: (2001).

[85] A. J. Illingworth, H. Barker, A. Beljaars, M. Ceccaldi, H. Chepfer, N. Clerbaux, J. Cole, J. Delanoë, C. Domenech, D. P. Donovan, et al. “The EarthCARE satellite: The next step forward in global measurements of clouds, aerosols, precipitation, and radiation”. In: *Bulletin of the American Meteorological Society* 96.8 (2015), pp. 1311–1332.

[86] B. Stevens, F. Ament, S. Bony, S. Crewell, F. Ewald, S. Gross, A. Hansen, L. Hirsch, M. Jacob, T. Kölling, et al. “A high-altitude long-range aircraft configured as a cloud observatory: The NARVAL expeditions”. In: *Bulletin of the American Meteorological Society* 100.6 (2019), pp. 1061–1077.

[87] E. J. O’Connor, A. J. Illingworth, I. M. Brooks, C. D. Westbrook, R. J. Hogan, F. Davies, and B. J. Brooks. “A method for estimating the turbulent kinetic energy dissipation rate from a vertically pointing Doppler lidar, and independent evaluation from balloon-borne in situ measurements”. In: *Journal of atmospheric and oceanic technology* 27.10 (2010), pp. 1652–1664.

[88] C. C. Stephan, S. Schnitt, H. Schulz, H. Bellenger, S. P. De Szoeke, C. Acquistapace, K. Baier, T. Dauhut, R. Laxenaire, Y. Morfa-Avalos, et al. “Ship-and island-based atmospheric soundings from the 2020 EUREC 4 A field campaign”. In: *Earth System Science Data* 13.2 (2021), pp. 491–514.

[89] M. Maturilli, D. J. Holdridge, S. Dahlke, J. Graeser, A. Sommerfeld, R. Jaiser, H. Deckelmann, and A. Schulz. *Initial radiosonde data from 2019-10 to 2020-09 during project MOSAiC.* data set. Alfred Wegener Institute, Helmholtz Centre for Polar and Marine Research, Bremerhaven, 2021. DOI: 10.1594/PANGAEA.928656.

[90] A. Theuerkauf, M. Gerding, and F.-J. Lübken. “LITOS-a new balloon-borne instrument for fine-scale turbulence soundings in the stratosphere”. In: *Atmospheric Measurement Techniques* 4.1 (2011), p. 55.

[91] A. Muschinski and C. Wode. “First in situ evidence for coexisting submeter temperature and humidity sheets in the lower free troposphere”. In: *Journal of the Atmospheric Sciences* 55.18 (1998), pp. 2893–2906.

[92] H. Siebert, H. Franke, K. Lehmann, R. Maser, E. W. Saw, D. Schell, R. A. Shaw, and M. Wendisch. “Probing finescale dynamics and microphysics of clouds with helicopter-borne measurements”. In: *Bulletin of the American Meteorological Society* 87.12 (2006), pp. 1727–1738.

[93] G. de Boer, S. Borenstein, R. Calmer, C. Cox, M. Rhodes, C. Choate, J. Hamilton, J. Osborn, D. Lawrence, B. Argrow, et al. “Measurements from the university of colorado raaven uncrewed aircraft system during atomic”. In: *Earth System Science Data* 14.1 (2022), pp. 19–31.

[94] A. Muschinski, R. Frehich, M. Jensen, R. Hugo, A. Hoff, F. Eaton, and B. Balsley. “Fine-scale measurements of turbulence in the lower troposphere: An intercomparison between a kite-and balloon-borne, and a helicopter-borne measurement system”. In: *Boundary-layer meteorology* 98.2 (2001), pp. 219–250.

[95] M. Lonardi, C. Pilz, E. F. Akansu, S. Dahlke, U. Egerer, A. Ehrlich, H. Griesche, A. J. Heymsfield, B. Kirbus, C. G. Schmitt, et al. “Tethered balloon-borne profile measurements of atmospheric properties in the cloudy atmospheric boundary layer over the Arctic sea ice during MOSAiC: Overview and first results”. In: *Elem Sci Anth* 10.1 (2022), p. 000120.

[96] U. Egerer, M. Gottschalk, H. Siebert, A. Ehrlich, and M. Wendisch. “The new BELUGA setup for collocated turbulence and radiation measurements using a tethered balloon: first applications in the cloudy Arctic boundary layer, Atmos”. In: *Meas. Tech* 12 (2019), pp. 4019–4038.

[97] R. Becker, M. Maturilli, R. Philipona, and K. Behrens. “In-situ sounding of radiation flux profiles through the Arctic lower troposphere”. In: *Atmospheric Measurement Techniques Discussions* (2018), pp. 1–18.

[98] G. Canut, F. Couvreux, M. Lothon, D. Legain, B. Piguet, A. Lampert, W. Maurel, and E. Moulin. “Turbulence fluxes and variances measured with a sonic anemometer mounted on a tethered balloon”. In: *Atmospheric Measurement Techniques* 9.9 (2016), pp. 4375–4386.

[99] B. B. Balsley. “The CIRES Tethered Lifting System: a survey of the system, past results and future capabilities”. In: *Acta geophysica* 56.1 (2008), pp. 21–57.

[100] H. Siebert, M. Wendisch, T. Conrath, U. Teichmann, and J. Heintzenberg. “A new tethered balloon-borne payload for fine-scale observations in the cloudy boundary layer”. In: *Boundary-layer meteorology* 106.3 (2003), pp. 461–482.

[101] K. Knapp, M. Jensen, B. Balsley, J. Bognar, S. Oltmans, T. Smith, and J. Birks. “Vertical profiling using a complementary kite and tethered balloon platform at Ferryland Downs, Newfoundland, Canada: Observation of a dry, ozone-rich plume in the free troposphere”. In: *Journal of Geophysical Research: Atmospheres* 103.D11 (1998), pp. 13389–13397.

[102] M. Kitchen and S. Caughey. “Tethered-balloon observations of the structure of small cumulus clouds”. In: *Quarterly Journal of the Royal Meteorological Society* 107.454 (1981), pp. 853–874.

[103] W. Moores. “Direct measurements of radiative and turbulent flux convergences in the lowest 1000 m of the convective boundary layer”. In: *Boundary-Layer Meteorology* 22.3 (1982), pp. 283–294.

[104] A. L. Morris, D. B. Call, and R. B. McBeth. “A small tethered balloon sounding system”. In: *Bulletin of the American Meteorological Society* 56.9 (1975), pp. 964–970.

[105] S. Brönnimann, G. P. Compo, R. Spadin, R. Allan, and W. Adam. “Early ship-based upper-air data and comparison with the Twentieth Century Reanalysis”. In: *Climate of the Past* 7.1 (2011), pp. 265–276.

[106] R. P. Lawson, K. Stamnes, J. Stamnes, P. Zmarzly, J. Koskuliks, C. Roden, Q. Mo, M. Carrithers, and G. L. Bland. “Deployment of a tethered-balloon system for microphysics and radiative measurements in mixed-phase clouds at Ny-Ålesund and south pole”. In: *Journal of Atmospheric and Oceanic Technology* 28.5 (2011), pp. 656–670.

[107] H. Siebert and R. A. Shaw. “Supersaturation fluctuations during the early stage of cumulus formation”. In: *Journal of the Atmospheric Sciences* 74.4 (2017), pp. 975–988.

[108] K. Schmitt, C. Friehe, and C. Gibson. “Humidity sensitivity of atmospheric temperature sensors by salt contamination”. In: *Journal of Physical Oceanography* 8.1 (1978), pp. 151–161.

[109] J. C. Wyngaard and S.-F. Zhang. “Transducer-shadow effects on turbulence spectra measured by sonic anemometers”. In: *Journal of Atmospheric and Oceanic Technology* 2.4 (1985), pp. 548–558.

[110] D. Lenschow. “Micrometeorological techniques for measuring biosphere-atmosphere trace gas exchange”. In: *Biogenic trace gases: Measuring emissions from soil and water* (1995), pp. 126–163.

[111] X. Zhou, T. Gao, E. S. Takle, X. Zhen, A. E. Suyker, T. Awada, J. Okalebo, and J. Zhu. “Air temperature equation derived from sonic temperature and water vapor mixing ratio for turbulent airflow sampled through closed-path eddy-covariance flux systems”. In: *Atmospheric Measurement Techniques* 15.1 (2022), pp. 95–115.

[112] P. Welch. “The use of fast Fourier transform for the estimation of power spectra: a method based on time averaging over short, modified periodograms”. In: *IEEE Transactions on audio and electroacoustics* 15.2 (1967), pp. 70–73.

[113] M. Schröder, T. Bätge, E. Bodenschatz, M. Wilczek, and G. Bagheri. “Estimating the turbulent kinetic energy dissipation rate from one-dimensional velocity measurements in time”. submitted to Atmospheric Measurement Techniques. 2023.

[114] D. Haugen, J. Kaimal, C. Readings, and R. Rayment. “A comparison of balloon-borne and tower-mounted instrumentation for probing the atmospheric boundary layer”. In: *Journal of Applied Meteorology and Climatology* 14.4 (1975), pp. 540–545.

[115] C. C. Lalescu, B. Bramas, M. Rampp, and M. Wilczek. “An efficient particle tracking algorithm for large-scale parallel pseudo-spectral simulations of turbulence”. In: *Computer Physics Communications* (2022), p. 108406.

[116] H. Siebert, K. Lehmann, and R. A. Shaw. “On the use of hot-wire anemometers for turbulence measurements in clouds”. In: *Journal of atmospheric and oceanic technology* 24.6 (2007), pp. 980–993.

[117] H. Siebert and U. Teichmann. “Behaviour of an ultrasonic anemometer under cloudy conditions”. In: *Boundary-layer meteorology* 94.1 (2000), pp. 165–169.

[118] C. Tropea, A. L. Yarin, J. F. Foss, et al. *Springer handbook of experimental fluid mechanics.* Vol. 1. Springer, 2007.

[119] W. M. Organization. “Guide to meteorological instruments and methods of observation”. In: WMO-No. 8 (2008).

[120] W. Wagner and A. Pruss. “International equations for the saturation properties of ordinary water substance. Revised according to the international temperature scale of 1990. Addendum to J. Phys. Chem. Ref. Data 16, 893 (1987)”. In: *Journal of physical and chemical reference data* 22.3 (1993), pp. 783–787.

[121] C. Fairall and S. E. Larsen. “Inertial-dissipation methods and turbulent fluxes at the air-ocean interface”. In: *Boundary-Layer Meteorology* 34.3 (1986), pp. 287–301.

[122] C.-I. Hsieh and G. G. Katul. “Dissipation methods, Taylor’s hypothesis, and stability correction functions in the atmospheric surface layer”. In: *Journal of Geophysical Research: Atmospheres* 102.D14 (1997), pp. 16391–16405.

[123] I. Smalikho, V. Banakh, Y. Pichugina, W. Brewer, R. Banta, J. Lundquist, and N. Kelley. “Lidar investigation of atmosphere effect on a wind turbine wake”. In: *Journal of Atmospheric and Oceanic Technology* 30.11 (2013), pp. 2554–2570.

[124] Z. Warhaft. “Passive scalars in turbulent flows”. In: *Annual Review of Fluid Mechanics* 32.1 (2000), pp. 203–240.

[125] K. Sreenivasan. “Possible effects of small-scale intermittency in turbulent reacting flows”. In: *Flow, turbulence and combustion* 72.2 (2004), pp. 115–131.

[126] S. S. Deshpande, M. J. Sathe, and J. B. Joshi. “Evaluation of local turbulent energy dissipation rate using PIV in jet loop reactor”. In: *Industrial & Engineering Chemistry Research* 48.10 (2009), pp. 5046–5057.

[127] H. E. Gerber, G. M. Frick, J. B. Jensen, and J. G. Hudson. “Entrainment, mixing, and microphysics in trade-wind cumulus”. In: *Journal of the Meteorological Society of Japan. Ser. II* 86 (2008), pp. 87–106.

[128] H. Gerber, G. Frick, S. P. Malinowski, H. Jonsson, D. Khelif, and S. K. Krueger. “Entrainment rates and microphysics in POST stratocumulus”. In: *Journal of Geophysical Research: Atmospheres* 118.21 (2013), pp. 12–094.

[129] K. Fodor and J. P. Mellado. “New Insights into Wind Shear Effects on Entrainment in Convective Boundary Layers Using Conditional Analysis”. In: *Journal of the Atmospheric Sciences* (2020), pp. 1–57.

[130] X.-Y. Li, A. Brandenburg, G. Svensson, N. E. Haugen, B. Mehlig, and I. Rogachevskii. “Condensational and collisional growth of cloud droplets in a turbulent environment”. In: *Journal of the Atmospheric Sciences* 77.1 (2020), pp. 337–353.

[131] A. Muschinski, R. G. Frehlich, and B. B. Balsley. “Small-scale and large-scale intermittency in the nocturnal boundary layer and the residual layer”. In: *Journal of Fluid Mechanics* 515 (2004), p. 319.

[132] D. Buaria, A. Pumir, E. Bodenschatz, and P.-K. Yeung. “Extreme velocity gradients in turbulent flows”. In: *New Journal of Physics* 21.4 (2019), p. 043004.

[133] P. E. Hamlington, A. Y. Poludnenko, and E. S. Oran. “Intermittency in premixed turbulent reacting flows”. In: *Physics of Fluids* 24.7 (2012), p. 075111.

[134] K. R. Sreenivasan. “Turbulent mixing: A perspective”. In: *Proceedings of the National Academy of Sciences* 116.37 (2019), pp. 18175–18183.

[135] N. Lefeuvre, F. Thiesset, L. Djenidi, and R. Antonia. “Statistics of the turbulent kinetic energy dissipation rate and its surrogates in a square cylinder wake flow”. In: *Physics of Fluids* 26.9 (2014), p. 095104.

[136] S. Almalkie and S. M. de Bruyn Kops. “Energy dissipation rate surrogates in incompressible Navier–Stokes turbulence”. In: *Journal of fluid mechanics* 697 (2012), pp. 204–236.

[137] J. Wyngaard and S. Clifford. “Taylor’s hypothesis and high–frequency turbulence spectra”. In: *Journal of the Atmospheric Sciences* 34.6 (1977), pp. 922–929.

[138] J. Elsner and W. Elsner. “On the measurement of turbulence energy dissipation”. In: *Measurement Science and Technology* 7.10 (1996), p. 1334.

[139] R. Antonia. “On estimating mean and instantaneous turbulent energy dissipation rates with hot wires”. In: *Experimental thermal and fluid science* 27.2 (2003), pp. 151–157.

[140] H. Siebert, K. Lehmann, and M. Wendisch. “Observations of small-scale turbulence and energy dissipation rates in the cloudy boundary layer”. In: *Journal of the atmospheric sciences* 63.5 (2006), pp. 1451–1466.

[141] K. Sreenivasan, A. Prabhu, and R. Narasimha. “Zero-crossings in turbulent signals”. In: *Journal of Fluid Mechanics* 137 (1983), pp. 251–272.

[142] M. Wacławczyk, Y.-F. Ma, J. M. Kopeć, and S. P. Malinowski. “Novel approaches to estimating the turbulent kinetic energy dissipation rate from low-and moderate-resolution velocity fluctuation time series”. In: *Atmospheric Measurement Techniques* 10.12 (2017), pp. 4573–4585.

[143] G. I. Taylor. “Statistical theory of turbulence”. In: *Proceedings of the Royal Society of London. Series A-Mathematical and Physical Sciences* 151.873 (1935), pp. 421–444.

[144] W. D. McComb, A. Berera, M. Salewski, and S. Yoffe. “Taylor’s (1935) dissipation surrogate reinterpreted”. In: *Physics of Fluids* 22.6 (2010), p. 061704.

[145] J. C. Vassilicos. “Dissipation in turbulent flows”. In: *Annual Review of Fluid Mechanics* 47 (2015), pp. 95–114.

[146] J. M. Lewis, T. W. Koster, and J. C. LaRue. “On the determination of the dissipation rate of turbulence kinetic energy”. In: *Experiments in Fluids* 62.7 (2021), pp. 1–13.

[147] M. Sinhuber. “On the scales of turbulent motion at high Reynolds numbers”. PhD thesis. PhD thesis, Georg-August-Universität Göttingen, 2015.

[148] R. Frehlich, Y. Meillier, M. L. Jensen, and B. Balsley. “A statistical description of small-scale turbulence in the low-level nocturnal jet”. In: *Journal of the atmospheric sciences* 61.9 (2004), pp. 1079–1085.

[149] J. L. Nowak, H. Siebert, K.-E. Szodry, and S. P. Malinowski. “Coupled and decoupled stratocumulus-topped boundary layers: turbulence properties”. In: *Atmospheric Chemistry and Physics Discussions* (2021), pp. 1–41.

[150] D. S. Dodson and J. D. Small Griswold. “Turbulent and boundary layer characteristics during VOCALS-REx”. In: *Atmospheric Chemistry and Physics* 21.3 (2021), pp. 1937–1961.

[151] M. Chamecki and N. Dias. “The local isotropy hypothesis and the turbulent kinetic energy dissipation rate in the atmospheric surface layer”. In: *Quarterly Journal of the Royal Meteorological Society: A journal of the atmospheric sciences, applied meteorology and physical oceanography* 130.603 (2004), pp. 2733–2752.

[152] H. Siebert, R. Shaw, J. Ditas, T. Schmeissner, S. Malinowski, E. Bodenschatz, and H. Xu. “High-resolution measurement of cloud microphysics and turbulence at a mountaintop station”. In: (2015).

[153] M. Wacławczyk, A. S. Gozingan, J. Nzotungishaka, M. Mohammadi, and S. P Malinowski. “Comparison of Different Techniques to Calculate Properties of Atmospheric Turbulence from Low-Resolution Data”. In: *Atmosphere* 11.2 (2020), p. 199.

[154] E. O. Akinlabi, M. Wacławczyk, J. P. Mellado, and S. P. Malinowski. “Estimating turbulence kinetic energy dissipation rates in the numerically simulated stratocumulus cloud-top mixing layer: Evaluation of different methods”. In: *Journal of the Atmospheric Sciences* 76.5 (2019), pp. 1471–1488.

[155] C. Küchler, G. Bewley, and E. Bodenschatz. “Experimental study of the bottleneck in fully developed turbulence”. In: *Journal of Statistical Physics* 175.3-4 (2019), pp. 617–639.

[156] G. I. Taylor. “The spectrum of turbulence”. In: *Proceedings of the Royal Society of London. Series A-Mathematical and Physical Sciences* 164.919 (1938), pp. 476–490.

[157] H. Nobach and C. Tropea. “A statistical method for transforming temporal correlation functions from one-point measurements into longitudinal spatial and spatio-temporal correlation functions”. In: *Experiments in fluids* 53.6 (2012), pp. 1815–1821.

[158] M. Wilczek, H. Xu, and Y. Narita. “A note on Taylor’s hypothesis under large-scale flow variation”. In: *Nonlin. Processes Geophys* 21 (2014), pp. 645–649.

[159] G. Willis and J. Deardorff. “On the use of Taylor’s translation hypothesis for diffusion in the mixed layer”. In: *Quarterly Journal of the Royal Meteorological Society* 102.434 (1976), pp. 817–822.

[160] R. H. Kraichnan. “Kolmogorov’s hypotheses and Eulerian turbulence theory”. In: *The Physics of Fluids* 7.11 (1964), pp. 1723–1734.

[161] H. Tennekes. “Eulerian and Lagrangian time microscales in isotropic turbulence”. In: *Journal of Fluid Mechanics* 67.3 (1975), pp. 561–567.

[162] J. Lumley. “Interpretation of time spectra measured in high-intensity shear flows”. In: *The physics of fluids* 8.6 (1965), pp. 1056–1062.

[163] F. Champagne. “The fine-scale structure of the turbulent velocity field”. In: *Journal of Fluid Mechanics* 86.1 (1978), pp. 67–108.

[164] D. Donzis, P. Yeung, and K. Sreenivasan. “Dissipation and enstrophy in isotropic turbulence: resolution effects and scaling in direct numerical simulations”. In: *Physics of Fluids* 20.4 (2008), p. 045108.

[165] R. Benzi, S. Ciliberto, R. Tripiccione, C. Baudet, F. Massaioli, and S. Succi. “Extended self-similarity in turbulent flows”. In: *Physical review E* 48.1 (1993), R29.

[166] R. Benzi, S. Ciliberto, C. Baudet, G. R. Chavarria, and R. Tripiccione. “Extended self-similarity in the dissipation range of fully developed turbulence”. In: *EPL (Europhysics Letters)* 24.4 (1993), p. 275.

[167] S. P. Oncley, C. A. Friehe, J. C. Larue, J. A. Businger, E. C. Itsweire, and S. S. Chang. “Surface-layer fluxes, profiles, and turbulence measurements over uniform terrain under near-neutral conditions”. In: *Journal of Atmospheric Sciences* 53.7 (1996), pp. 1029–1044.

[168] K. R. Sreenivasan. “On the universality of the Kolmogorov constant”. In: *Physics of Fluids* 7.11 (1995), pp. 2778–2784.

[169] M. Wilczek and Y. Narita. “Wave-number–frequency spectrum for turbulence from a random sweeping hypothesis with mean flow”. In: *Physical Review E* 86.6 (2012), p. 066308.

[170] C. Fairall, R. Markson, G. Schacher, and K. Davidson. “An aircraft study of turbulence dissipation rate and temperature structure function in the unstable marine atmospheric boundary layer”. In: *Boundary-Layer Meteorology* 19.4 (1980), pp. 453–469.

[171] J. Lumley. “Some comments on turbulence”. In: *Physics of Fluids A: Fluid Dynamics* 4.2 (1992), pp. 203–211.

[172] K. Sreenivasan, S. Deshpande, A. Prabhu, and P. Viswanath. “The energy dissipation in turbulent shear flows”. In: *Symposium on Developments in Fluid Dynamics and Aerospace Engineering.* Interline Publishers, Bangalore. 1995, pp. 159–190.

[173] P. Burattini, P. Lavoie, and R. A. Antonia. “On the normalized turbulent energy dissipation rate”. In: *Physics of fluids* 17.9 (2005), p. 098103.

[174] B. Pearson, P.-Å. Krogstad, and W. Van De Water. “Measurements of the turbulent energy dissipation rate”. In: *Physics of fluids* 14.3 (2002), pp. 1288–1290.

[175] K. R. Sreenivasan. “On the scaling of the turbulence energy dissipation rate”. In: *The Physics of fluids* 27.5 (1984), pp. 1048–1051.

[176] D. Tritton. *Physical Fluid Dynamics.* 1977.

[177] G. P. Bewley, K. Chang, E. Bodenschatz, and (. C. for Turbulence Research). “On integral length scales in anisotropic turbulence”. In: *Physics of Fluids* 24.6 (2012), p. 061702.

[178] K. P. Griffin, N. J. Wei, E. Bodenschatz, and G. P. Bewley. “Control of long-range correlations in turbulence”. In: *Experiments in Fluids* 60.4 (2019), p. 55.

[179] T. Horst and S. Oncley. “Corrections to inertial-range power spectra measured by CSAT3 and Solent sonic anemometers, 1. Path-averaging errors”. In: *Boundary-layer meteorology* 119.2 (2006), pp. 375–395.

[180] L. S. Freire, N. L. Dias, and M. Chamecki. “Effects of path averaging in a sonic anemometer on the estimation of turbulence-kinetic-energy dissipation rates”. In: *Boundary-Layer Meteorology* 173.1 (2019), pp. 99–113.

[181] D. H. Lenschow and L. Kristensen. “Uncorrelated noise in turbulence measurements”. In: *Journal of Atmospheric and Oceanic Technology* 2.1 (1985), pp. 68–81.

[182] C. Lalescu, B. Teaca, and D. Carati. “Implementation of high order spline interpolations for tracking test particles in discretized fields”. In: *Journal of Computational Physics* 229.17 (2010), pp. 5862–5869.

[183] C. Küchler. “Measurements of Turbulence at High Reynolds Numbers”. PhD thesis. Georg-August-Universität Göttingen, 2021.

[184] S. C. Bailey, G. J. Kunkel, M. Hultmark, M. Vallikivi, J. P. Hill, K. A. Meyer, C. Tsay, C. B. Arnold, and A. J. Smits. "Turbulence measurements using a nanoscale thermal anemometry probe". In: *Journal of Fluid Mechanics* 663 (2010), pp. 160–179.

[185] M. Vallikivi, M. Hultmark, S. C. C. Bailey, and A. Smits. "Turbulence measurements in pipe flow using a nano-scale thermal anemometry probe". In: *Experiments in fluids* 51.6 (2011), pp. 1521–1527.

[186] F. E. Jørgensen. *How to measure turbulence with hot-wire anemometers: a practical guide*. Dantec dynamics, 2001.

[187] M. Sinhuber, E. Bodenschatz, and G. P. Bewley. "Decay of turbulence at high Reynolds numbers". In: *Physical review letters* 114.3 (2015), p. 034501.

[188] C. Küchler, E. Bodenschatz, and G. P. Bewley. "Scaling in Decaying Turbulence at High Reynolds Numbers". In: *arXiv preprint arXiv:2006.10993* (2020).

[189] R. B. Stull. *Practical meteorology: an algebra-based survey of atmospheric science*. University of British Columbia, 2015.

[190] A. L. Albright, S. Bony, B. Stevens, and R. Vogel. "Observed subcloud layer moisture and heat budgets in the trades". In: *Journal of the Atmospheric Sciences* (2022).

[191] C. Acquistapace, R. Coulter, S. Crewell, A. Garcia-Benadi, R. Gierens, G. Labbri, A. Myagkov, N. Risse, and J. H. Schween. "EUREC^{4}A's *Maria S. Merian* ship-based cloud and micro rain radar observations of clouds and precipitation". In: *Earth System Science Data* 14.1 (2022), pp. 33–55. DOI: 10.5194/essd-14-33-2022.

[192] J. Vial, R. Vogel, S. Bony, B. Stevens, D. M. Winker, X. Cai, C. Hohenegger, A. K. Naumann, and H. Brogniez. "A new look at the daily cycle of trade wind cumuli". In: *Journal of advances in modeling earth systems* 11.10 (2019), pp. 3148–3166.

[193] J. Vial, R. Vogel, and H. Schulz. "On the daily cycle of mesoscale cloud organization in the winter trades". In: *Quarterly Journal of the Royal Meteorological Society* 147.738 (2021), pp. 2850–2873.

[194] J. Rotta. "Statistische theorie nichthomogener turbulenz". In: *Zeitschrift für Physik* 129.6 (1951), pp. 547–572.

[195] K.-S. Choi and J. L. Lumley. "The return to isotropy of homogeneous turbulence". In: *Journal of Fluid Mechanics* 436 (2001), pp. 59–84.

[196] J. L. Lumley and G. R. Newman. "The return to isotropy of homogeneous turbulence". In: *Journal of Fluid Mechanics* 82.1 (1977), pp. 161–178.

[197] S. Risius. "Investigation of turbulent flows at the Umweltforschungsstation Schneefernerhaus (Zugspitze)". MA thesis. University of Göttingen, Mar. 2012.

[198] B. Stevens, S. Bony, H. Brogniez, L. Hentgen, C. Hohenegger, C. Kiemle, T. S. L'Ecuyer, A. K. Naumann, H. Schulz, P. A. Siebesma, et al. "Sugar, gravel, fish and flowers: Mesoscale cloud patterns in the trade winds". In: *Quarterly Journal of the Royal Meteorological Society* 146.726 (2020), pp. 141–152.

[199] P. Squires. “The microstructure and colloidal stability of warm clouds: Part I—The relation between structure and stability”. In: *Tellus* 10.2 (1958), pp. 256–261.

[200] K. V. Beard and H. T. Ochs III. “Collection and coalescence efficiencies for accretion”. In: *Journal of Geophysical Research: Atmospheres* 89.D5 (1984), pp. 7165–7169.

[201] D. H. Lenschow. “Aircraft measurements in the boundary layer”. In: *Probing the atmospheric boundary layer*. Springer, 1986, pp. 39–55.

[202] J. M. Wilczak, S. P. Oncley, and S. A. Stage. “Sonic anemometer tilt correction algorithms”. In: *Boundary-Layer Meteorology* 99.1 (2001), pp. 127–150.

[203] R. H. Kraichnan. “The structure of isotropic turbulence at very high Reynolds numbers”. In: *Journal of Fluid Mechanics* 5.4 (1959), pp. 497–543.

[204] M. Sinhuber, G. P. Bewley, and E. Bodenschatz. “Dissipative effects on inertial-range statistics at high Reynolds numbers”. In: *Physical review letters* 119.13 (2017), p. 134502.

[205] K. R. Sreenivasan and B. Dhruva. “Is there scaling in high-Reynolds-number turbulence?” In: *Progress of Theoretical Physics Supplement* 130 (1998), pp. 103–120.

[206] I. Stiperski, G. G. Katul, and M. Calaf. “Universal return to isotropy of inhomogeneous atmospheric boundary layer turbulence”. In: *Physical Review Letters* 126.19 (2021), p. 194501.

[207] P.-F. Yang, A. Pumir, and H. Xu. “Return to isotropy of homogeneous shear-released turbulence”. In: *Physical Review Fluids* 6.4 (2021), p. 044601.

[208] D. P. Grosvenor, O. Sourdeval, P. Zuidema, A. Ackerman, M. D. Alexandrov, R. Bennartz, R. Boers, B. Cairns, J. C. Chiu, M. Christensen, et al. “Remote sensing of droplet number concentration in warm clouds: A review of the current state of knowledge and perspectives”. In: *Reviews of Geophysics* 56.2 (2018), pp. 409–453.

Acknowledgements

This work would not have been possible without the support and help of others.

First of all, I would like to express my deepest gratitude to Prof. Dr. Dr. h.c. Eberhard Bodenschatz for initiating the Cloudkite project and giving me the opportunity to work in his group. Coming from the physics of biological systems, I am very grateful for his trust in me, the fruitful and insightful discussions we had and for allowing me to benefit from his enlightening advice. I am also thankful for his support in applying for a scholarship. I would like to extend my sincere thanks to the Konrad-Adenauer-Stiftung for the financial support and for the enriching seminar program in which I was allowed to participate.

I am extremely grateful to Dr. Gholamhossein Bagheri not only for being an outstanding project manager but also for his permanent support and help. I will never forget our joint efforts in designing and assembling two mini-MPCKs within only six months before the EUREC^{4}A field campaign. We succeeded and all the countless hours paid off! I am very thankful for his encouragement and for sharing his extensive scientific experience with me.

Furthermore, I would like to express my gratitude to Prof. Dr. Michael Wilczek and Prof. Dr. Andreas Janshoff for being members of my Thesis Advisory Committee. I am very grateful for your scientific advice and feedback from outside the Cloudkite project. Many thanks to Prof. Dr. Michael Wilczek for the fruitful collaboration on estimating the energy dissipation rate and for supporting my application for a scholarship. I am very grateful to him for his theoretical perspectives and structured approach to complex scientific problems. I would like to extend my sincere thanks to Prof. Dr. Dr.-Ing. habil. Andreas Dillmann, Prof. Dr. Stefan Klumpp and Prof. Dr. Ulrich Parlitz for being members of my examination board.

I am also thankful to Prof. Dr. Bjorn Stevens and Sandrine Bony - representative for all persons involved - for the excellent organization of a one-of-its-kind field campaign. Thanks should also go to Don Lenschow for supporting me on RV Meteor with assembling the mini-MPCK and recommendations on flight strategy. In the context of EUREC^{4}A , I am grateful to Jun.-Prof. Dr. Heike Kalesse-Los, Dr.in Claudia Acquistapace and Dr. Claudia Stephan for sharing Radar and radiosonde data with me. I would also like to thank Prof. Dr. Steffen Risius for providing me with the invariants measured at UFS at Mt. Zugspitze.

The excellent technical support by Dr. Artur Kubitzek, Andreas Kopp, Andreas Renner and Marcel Meyer was essential for the project. Many thanks for handling logistics and persistently solving technical issues of all sorts! Furthermore, I would like to extend my sincere thanks to the in-house machine shop guided by Udo Schminke and the scientific electronics guided by Dr. Holger Nobach. I benefited from your innovative design ideas and I am grateful for the countless hours you spent with me discussing design ideas of mechanical parts and electronics. Without your extraordinary commitment, the mini-MPCK would not have been ready for operation during EUREC^{4}A .

I had the pleasure of working with my colleagues Dr. Freja Nordsiek, Dr. Oliver Schlenczek, Birte Thiede, Dr. Christian Küchler, Dr. Augustinus C. M. Bertens, Dr. Antonio Ibañez Landeta , Dr. Johannes Güttler and Dr. Marcel Wedi and I am thankful for countless helpful discussions and strong support during my PHD. Special thanks to Dr. Freja Nordsiek and Dr. Oliver Schlenczek as well as Tobias Batge and Venecia Chavez Medina for an excellent collaboration and for having the informal journal club. Many thanks should also go to Tobias Bätge, Dr. Florian Spreckelsen, Birte Thiede and Venecia Chavez Medina for proofreading parts of my thesis. Additionally, I thank Lucas Schminke for his excellent work on the revised mini-MPCK.

Finally, words cannot express my gratitude to my dearest family for their endless support, for always believing in me, and for helping me get to where I am now!

Curriculum Vitae

Marcel Schröder

Born: December 3, 1992 — Arolsen, Germany
Nationality: German

Education

since 2018	PhD candidate at Mobile Cloud Laboratory, Laboratory for Fluid Physics, Pattern Formation and Biocomplexity, Max Planck Institute for Dynamics and Self-organization, Göttingen
2016-2018	MSc in Physics, Georg-August-Universität Göttingen, Master thesis: *Cell-Substrate Adhesion and Contact Guidance of D.d. on Surfaces of Varying Curvatures*
2012-2015	BSc in Physics, Georg-August-Universität Göttingen, Bachelor Thesis: *Investigation of the Influence of Vibrations on Coherent X-ray Imaging in the Optical Near Field*
2012	Abitur, Alte Landesschule, Korbach

Publications & talks

Journal articles

2023	**Schröder, M., Bätge, T., Bodenschatz, E.,Wilczek, M. & Bagheri, G.**, “Estimating the turbulent kinetic energy dissipation rate from one-dimensional velocity measurements in time”, *submitted to Atmospheric Measurement Techniques*
2023	**Schröder, M., Schlenczek, O., Nordsiek, F.Ibañez Landeta, A., Bodenschatz, E. & Bagheri, G.**, “mini Max Planck Cloudkite - an Airborne Platform for Characterizing Atmospheric Turbulence and Cloud Microphycis”, *in prep.*

Conference talks

2022	Joint LMD, MPI & friends EUREC4A meetings, online, France, *Airborne Atmospheric and Cloud Measurements with the Max Planck Cloudkite Platforms*
2022	European Geoscience Union, online, Austria, *Energy Dissipation Rate Estimates from Airborne Atmospheric Measurements with the Max Planck Cloudkites*
2021	European Geoscience Union, online, Austria, *Airborne Atmospheric Measurements with the Max Planck Cloudkites*
2020	European Geoscience Union, online, Austria, *Airborne Atmospheric Measurements with the mini Max Planck Cloudkite*
2019	EUREC^{4}A Planning Workshop, Paris, France, *Airborne Atmospheric and Cloud Measurements with the Max Planck Cloudkite Platforms*